Electronic properties of quasi-one-dimensional systems (C60@SWCNTs and InAs nanowires) studied by electronic transport under high magnetic field

Vladimir Prudkovskiy

Université de Toulouse

THÈSE

En vue de l'obtention du

DOCTORAT DE L'UNIVERSITÉ DE TOULOUSE

Délivré par :
Institut National des Sciences Appliquées de Toulouse (INSA Toulouse)

Discipline ou spécialité :

Nanophysique

Présentée et soutenue par :
Vladimir PRUDKOVSKIY

le : vendredi 14 juin 2013

Titre :

Electronic properties of quasi-one-dimensional systems
(C60@SWCNTs and InAs nanowires)
studied by electronic transport under high magnetic field

JURY

Francois LEFLOCH - Directeur de recherche - INAC/SPSMS, CEA (Grenoble)
Catherine JOURNET GAUTIER - Professeur - Université Lyon I (Lyon)
Marc MONTHIOUX - Directeur de recherche - CEMES (Toulouse)
Philippe DEMONT - Professeur - Université Toulouse III (Toulouse)

Ecole doctorale :
Sciences de la Matière (SDM)

Unité de recherche :
Laboratoire National des Champs Magnétiques Intenses

Directeur(s) de Thèse :
Bertrand RAQUET - Professeur - LNCMI, INSA-Toulouse
Michel GOIRAN - Professeur - LNCMI, Université Toulouse III

Rapporteurs :
Francois LEFLOCH - Directeur de recherche - INAC/SPSMS, CEA (Grenoble)
Catherine JOURNET GAUTIER - Professeur - Université Lyon I

Remerciements

Je tiens à remercier en premier lieu mes directeurs de thèse, Bertrand Raquet et Michel Goiran, qui m'ont permis d'effectuer cette thèse et pour leurs conseils pendant toute la durée du travail.

Je suis très reconnaissant envers les membres du jury Francois Lefloch, Catherine Journet Gautier, Marc Monthioux et Philippe Demont d'avoir accepté d'examiner mon manuscrit de thèse et d'avoir jugé mon travail scientifique.

Ce travail a été effectué principalement au LNCMI-Toulouse et je remercie beaucoup le directeur, Geert Rikken, de m'avoir accueilli au sein de son laboratoire. Je remercie tout le personnel du laboratoire, qui ont contribué à la réalisation de ce travail. En particulier, mon arrivée a été grandement facilitée par Walter Escoffier, qui m'avait formé en début de thèse aux nombreuses techniques expérimentales. Un grand travail de développement a été fourni grâce à l'aide de Géraldine Ballon et Sylvie George, sans elles nous n'aurions pas obtenu tous ces résultats. J'ai aussi eu l'opportunité de profiter du talent de l'équipe de l'atelier mécanique. Particulièrement, un grand merci à Thierry Domps pour sa patience et sa compréhension de mes dessins et pour sa capacité de faire tout ce le plus tôt possible et dans la meilleure façon. Je remercie aussi Marc Nardone et Abdelaziz Zitouni pour leur apport en cryogénie. Marc, je vais t'apporter "Shustov Starinnaya", je te le promets. Je tiens également à remercier nos secrétaires Françoise Moes et Séverine Bories pour leur aide concernant toutes les tâches administratives. Je remercie Ludovic Bosseaux et Jean-Pierre Nicolin pour leur aide du côté informatique.

Les conseils et les discussions avec Jean Leotin, Sergey Krishtopenko, Taras Dovzhenko et Revaz Ramazashvili ont également été une aide précieuse.

Je remercie beaucoup mes collaborateurs du :

– LAAS pour m'avoir formé aux techniques de la salle blanche et plus particulièrement Franck Carcenac, Jean-Francois Bobo et Maeva Collet pour les bons moments que nous avons passé en salle blanche et pour leurs compétences en nanotechnologie.

– CEMES : Marc Monthioux, Pascal Puech, Mourad Berd, Ekaterina Pavlenko pour m'avoir formé aux techniques de spectroscopie Raman.

– MEPhI : Konstantin Katin, Mikhail Maslov. J'apprécie vraiment leur travail sur les simulations informatiques.

– Università degli Studi di Pavia : Vittorio Bellani et Francesco Rossella pour leur contribution aux travaux expérimentaux et une aide précieuse à la discussion des résultats.

– IEMN : Leturcq Renaud pour les échantillons exceptionnels.

– CEA : Yann-Michel Niquet pour les calculs de structure de bande de nanofils d'InAs.

Sans aucune exagération toutes ces personnes m'ont permis de profiter de toute la richesse scientifique et humaine que peuvent apporter des collaborations.

Je salue également mes collègues doctorants (anciens et actuels), Rebeca Ribeiro, Fabrice Iacovella (merci pour la lecture et la correction de la partie française de ma thèse !), Anaïs Loubat, Amit Kumar, Jean-Marie Poumirol, David Le Boeuf, Nicolas Ubrig, Sven Badoux, Gernot Scheerer, Xavier Fabreges, Stephane Lepault, Agathe Cadene et Mitiglu Anatolie, Florian Vigneau (courage !) qui m'ont fait partager outre leur expérience, leur soutien et leur bonne humeur. Merci pour tous les bons moments que nous avons passé au laboratoire et ailleurs ! Plus particulièrement je remercie Pierre-Yves Solane avec qui j'ai eu l'honneur de partager le bureau. Nos leçons de la langue russe-français ont laissé une marque dans mon coeur.

Je tiens également à remercier mes anciens directeurs Evgenii Nikolaev et Victor Tsebro, et mes enseignants : Leonid Openov et Igor Rudnev qui ont investi beaucoup d'efforts en moi et m'ont inculqué l'amour de la science.

Je souhaite remercier ma famille, mes parents en particulier qui m'ont toujours soutenu de près et de loin. Merci à tous ceux qui sont venus à ma soutenance de thèse, ça m'a beaucoup touché. Botan, Myshka, Valid - respect !

Et le meilleur pour la fin, merci à ma femme et ma fille. Victoria et Clementina, j'admire votre patience et votre soutien que vous m'avez apporté. Au cours de tout ce temps et pour les années qui vont venir.

List of Acronyms

2DEG	Two-dimensional electron gas
AB effect	Aharonov-Bohm effect
AC	Alternating current
AFM	Atomic force microscope/microscopy
CBE	Chemical beam epitaxy
CNP	Charge neutrality point
CNT	Carbon nanotube
CVD	Chemical vapor deposition
DC	Direct current
DOS	Density of states
DWCNT	Double walled carbon nanotube
FET	Field-effect transistor
HEMT	High electron mobility transistor
HOMO	Highest Occupied Molecular Orbital
HRTEM	High-resolution transmission electron microscope/microscopy
LDOS	Local density of states
LUMO	Lowest Unoccupied Molecular orbital
MBE	Molecular beam epitaxy
MC	Magnetoconductance
MOCVD	Metal-organic chemical vapor deposition
MOSFET	Metal-oxide-semiconductor field-effect transistor
MOVPE	Metal-organic vapour phase epitaxy
NP	Nanoparticle
NW	Nanowire
PMMA	Polymethylmethacrylate
RBM	Radial breathing mode
Sc.	Semiconducting
SEM	Scanning electron microscope/microscopy
SO	Spin-orbit
STM	Scanning tunneling microscope/microscopy
SWCNT	Single walled carbon nanotube
TEM	Transmission electron microscope/microscopy
UCF	Universal conductance fluctuations
UV	Ultra-violet
VLS	Vapor-liquid-solid method
WAL	Weak antilocalization
WL	Weak localization
WZ	Wurtzite
ZB	Zinc-blende

Contents

Chapter 1

Introduction

The word *Nanoscience*, which has been largely spread during the last decade, is not all that young as it may seem at first glance. Its appearance is ascribed to Norio Taniguchi at 1974, but the first ideas in this field were presented even earlier during the famous talk of Richard Feynman at the American Physical Society meeting on December 1959, by the sentence: "There's plenty of room at the bottom". The first device utilizing properties of low dimensional structure – metal-oxide-semiconductor field-effect-transistor, was created in 1960 [Atalla 1959]. As milestones which have paved the development of the nanoscience we can mention the following celebrated events: the discovery of the Quantum-Hall effect in 1980 [Klitzing 1980] which clearly shows precise quantization of the transverse magnetoresistance; the development of a Scanning Tunneling Microscope in 1981 which gave a possibility to create images at the scale of the Nanoworld; the discovery of fullerenes in 1985 [Kroto 1985] a new quasi-zero-dimensional system and more recently the discovery of carbon nanotubes [Iijima 1991] and graphene [Novoselov 2004]. In the same time nanotechnology development pushed forward the electronics miniaturization process. Progress in computer technology and considerable improvement of manufacturing techniques stimulate significant downscaling of the transistor, as a landmark, one can cite the 22 manufacturing process which has been recently developed [Intel 2011].

In this context an important question rises up: Are the physical laws that work in bulk systems applicable to nanosystems? Reducing the structure size enhances the quantum effects that, at some point, begin to dominate the electron properties. For instance, in some nanoscale systems the Boltzmann equation becomes invalid, because it requires that potentials vary slowly on both the spatial scale of the electron thermal wavelength and the temporal scale of the scattering processes.

Other related question comes up: Is there a limit to the downscaling? Is the technology able to obey the Moore's law doubling the number of transistors on the integrated circuits every two years keeping the principles of transport physics or will it demand the next leap of the physical understanding of devices and their operations?

Scientific interest in one-dimensional systems was inspired by their exceptional physical properties which could have extraordinary applications. For example, one can anticipate their use as extremely small interconnections and drain-source channels in electric circuits, as unique tools for nano-scale manipulations for engineering purpose, as a system with a turnable band gap for the laser application, as high

density electron emitters, etc.

The discovery of the Carbon Nanotubes (CNTs) in 1991 [Iijima 1991] gave rise to a huge amount of publications on this completely new quasi-one-dimensional allotropic form of the carbon [Endo 1996, Jorio 2008]. CNT can be described as few layers of graphene rolled up in a cylindrical form having a diameter of several nanometers and length up to several centimeters [Zhang 2011]. Their unusual properties are useful for applications in many different areas: electronics, microscopy, pharmacology, composite material, etc. For example they can exhibit a metallic or semiconducting behaviour depending on the way how they were rolled up - chirality of the nanotube. Another recent application of the CNTs was developed for Nanochromatography, where CNTs with selected chirality are used as a stationary phase to separate the chiral molecules (e.g. peptides, amino acids, etc.).

Another quasi-one-dimension structures – semiconducting nanowires (sc.-NWs) – has attracted the attention of numerous researchers. These are unique systems for exploring phenomena at the nanoscale and promising material for nanoelectronic and optoelectronic devices. Thus, besides all the possibilities offered by a semiconducting material nanowires exhibit additional advantages caused by the confinement. These properties, combined with high carrier mobility and tunable value of the band gap give an opportunity to create high-frequency-operating devices, photodiodes, light-emitting-diodes, etc. To realize these perspectives, a detailed understanding and control of their growth, crystal structure, electronic properties and their combined impact on device performance is essential.

The development of photolithography and e-beam lithography [Rai-Choudhury 1997] has made feasible the creation of nanosystem in a handy way and has allowed the connection of individual nano-objects, opening a possibility to probe their properties by transport techniques. This gave a great opportunity to understand new aspects of nanophysics studying new materials. Different transport regimes, predicted in nanostructures, were evidenced. For example ballistic conductance was revealed in the transistor based on single CNT [Tans 1997].

The aim of the present work is to investigate the electronic properties of quasi-one-dimensional systems: individually connected carbon C_{60} peapods and semiconducting InAs nanowires. Carbon C_{60} peapods as a hybrid of C_{60} fullerenes and CNTs attract attention as well due to their remarkable structure and unusual electronics properties. Preserving all advantages of CNT, peapods present the unique possibility to tune theirs properties by varying the type of the fullerene. InAs NWs attract particular interest because of a small direct band gap, small effective mass, high electron mobility and large Fermi wavelength.

In this work we probe the electronic structure of these systems by transport measurements in field-effect transistor (FET) configuration combined with high magnetic field. In a general case the magnetic field is an efficient tool for the study of the electronic properties as it acts on both the spin and kinetic energy spectra. For high enough magnetic fields the magnetic length becomes smaller than the size of the system, making the magnetic confinement larger than the geometrical confinement

and thus inducing strong modification of the transport regime.

In the first chapter of this thesis, we describe the basic electronic properties of low dimensional systems with different types of confinement and transport regimes in presence of electric and magnetic fields.

In the second chapter, we present the devices preparation process and experimental techniques used in this work.

The third chapter discusses the properties of carbon C_{60} peapods: mainly the influence of the C_{60} fullerenes on the electronic structure. We describe the modification of the transport properties induced by the partial transformation of the peapod into DWCNT obtained by UV irradiation.

The forth chapter is devoted to the properties of InAs NWs. The effects of the magnetic field on the conductance and on the energy spectrum are investigated at different field ranges. In particular, the quench of the conductance in the high magnetic field regime is revealed.

In the last chapter of this thesis, we draw conclusions upon the results obtained herein and we discuss the perspectives of the work.

Chapter 2

Low-dimensional systems

Sommaire

We start this chapter with a brief review of some basic properties of the low-dimensional systems and then we discuss briefly different techniques developed for creating such systems. Subsequently, we continue with a description of the electronic transport regimes and magnetotransport in 1D systems. Some parts of this chapter are based on the books "Electronic transport in mesoscopic System" [Datta 1995], "Transport in Nanostructures" [Ferry 1997] and "Quantum Transport in Semiconductor Nanostructures" [Beenakker 1991].

2.1 Energy dispersion, wave-function and density of states

2.1.1 3D, 2D and 1D free electron gas

In this section, the energy dispersion and the density of states (DOS) of the free electron gas for different dimensionality are recalled.

3D system

Consider a free electron gas in a three dimensional box with volume $V = L_x L_y L_z$. Solving the time-independent Schrödinger equation:

$$\frac{-\hbar^2}{2m} \bigtriangledown^2 \psi(\mathbf{r}) = E\psi(\mathbf{r}) \tag{2.1}$$

the electron wave-functions and energy dispersion can be written as:

$$\psi_{\mathbf{k}}(\mathbf{r}) = \frac{1}{\sqrt{V}} e^{i\mathbf{kr}} \tag{2.2}$$

$$E = \frac{\hbar^2 k^2}{2m} \tag{2.3}$$

where $\mathbf{k}$ is a wave-vector which is defined by periodical boundary conditions as $\mathbf{k} = 2\pi(\frac{n_1}{L_x}, \frac{n_2}{L_y}, \frac{n_3}{L_z})$, n_1, n_2, n_3 are integers.

As electrons have half-integer spin value ($s = 1/2$) they are fermions, and thus obey the Pauli exclusion principle and Fermi-Dirac statistics. This means that in the low temperature limit available states are occupied by pairs of electrons with the opposite spin values up to a maximum value E_f – Fermi energy, according to the Fermi function:

$$f(E) = \frac{1}{1 + e^{(E-E_f)/(k_B T)}} \tag{2.4}$$

There are two temperature limits:

- non-degenerate conductor ($k_B T \gg E_f$) where distribution $f(E) \approx exp[-(E - E_f)/(k_B T)]$ behaves similar to the Boltzmann distribution;

- degenerate conductor ($k_B T \ll E_f$) where distribution $f(E) \approx \vartheta(E_f - E)$ behaves as Heaviside step function.

The Fermi energy can be expressed as:

$$E_f = \frac{\hbar^2 k_f^2}{2m} \tag{2.5}$$

where k_f is Fermi wave-vector. Hence in the reciprocal space all electrons fill up the states up to a sphere with radius k_f, which is called the Fermi surface. The value of the Fermi energy can be derived from the carrier concentration. The total number of the electrons in the system N is equal to the number of the states inside the Fermi surface and the volume of one state in the reciprocal space is $\frac{2\pi}{L_x} \times \frac{2\pi}{L_y} \times \frac{2\pi}{L_z}$:

$$N = 2(\text{for the spin})\frac{4}{3}\pi k_f^3 \frac{V}{(2\pi)^3}$$

substituting the k_f from the equation 2.5 and denoting carrier concentration $n = N/V$:

$$E_f = \frac{\hbar^2}{2m}(3\pi^2 n)^{2/3} \tag{2.6}$$

Electrons at the Fermi surface are characterized by Fermi wave-length λ_f and velocity v_f:

$$v_f = \frac{\hbar k_f}{m}, \quad k_f = \frac{2\pi}{\lambda_f} \tag{2.7}$$

Assuming that dimensions of our box are macroscopic ($L_x, L_y, L_z \gg \lambda_f$), we have a quasi-continuous energetic spectrum. The DOS can be calculated if we introduce the concept of the density of a single-particle state through the Dirac delta function $\delta(x)$. The whole DOS can be obtained if we sum the densities over all states:

$$g_{3D}(E) = \sum_{spin} \sum_{states} \sum_{\mathbf{k}} \delta(E - E_{\mathbf{k}}) = 2\frac{V}{(2\pi)^3} \int d^3k \;\; \delta(E - \frac{\hbar^2 k^2}{2m}) \;\sim\; \sqrt{E} \tag{2.8}$$

2D system

Now we confine the 3D electronic gas along one direction $L_z \ll L_x, L_y$ and $L_z \approx \lambda_f$ (we will come back to this criterion in the section 2.3.1). The electrons are free to propagate in x-y plane but they are confined by some potential $U(z)$ in the z-direction which should be taken into consideration in the time-independent Schrödinger equation:

$$\left[\frac{-\hbar^2 \bigtriangledown^2}{2m} + U(z)\right] \psi(\mathbf{r}) = E\psi(\mathbf{r}) \tag{2.9}$$

Then, the electronic wave-function can be written in the form:

$$\psi_{\mathbf{k}}(\mathbf{r}) = A\varphi_n(z)e^{ik_x x}e^{ik_y y} \tag{2.10}$$

where the vector $\mathbf{k} = 2\pi(\frac{n_1}{L_x}, \frac{n_2}{L_y})$ is a planar vector defined by periodical boundary conditions, and the energy dispersion is:

$$E = \varepsilon_n + \frac{\hbar^2}{2m}(k_x^2 + k_y^2) \tag{2.11}$$

Unlike the 3D case now we have n different subbands each characterized by the wave-function $\varphi_n(z)$ and energy ε_n. In the $x - y$ plane, electron's motion is described by quasi-continuous parabolic energetic spectrum $E_{k_x,k_y} = \frac{\hbar^2}{2m}(k_x^2 + k_y^2)$ with wave-functions:

$$\psi(x, y) = \frac{1}{\sqrt{S}} e^{ik_x x}e^{ik_y y}$$

normalized to the area $S = L_x L_y$. Accordingly the Fermi surface of 2DEG is a circle with the radius k_f. DOS inside one 2D subband can be expressed as:

$$g_{2D}(E') = 2\sum_{\mathbf{k}} \delta(E' - E_{\mathbf{k}}) = 2\frac{V}{(2\pi)^2}\int d^2k \;\; \delta(E' - \frac{\hbar^2 k^2}{2m}) = \frac{m}{\pi\hbar^2}\Theta(E') \quad (2.12)$$

where $E' = E - \varepsilon_n$ is the energy counted from the bottom of the subband and $\Theta(E')$ is a Heaviside function. We see that 2D DOS has a stepwise behaviour (Fugure 2.1b) and as the number of occupied subbands increases.

1D system

We continue to reduce the dimensionality of our system and confine it along the y direction ($L_z, L_y \ll L_x$). The electrons are free to propagate only along the x direction and they are confined by potentials $U_y(y)$ and $U_z(z)$ in y and z directions, thus time-independent Schrödinger equation is:

$$\left[\frac{-\hbar^2\bigtriangledown^2}{2m} + U_y(y) + U_z(z)\right]\psi(\mathbf{r}) = E\psi(\mathbf{r}) \quad (2.13)$$

and the corresponding electronic wave-functions are:

$$\psi_{\mathbf{k}}(\mathbf{r}) = \frac{1}{\sqrt{L_x}} e^{ik_x x}\chi_{n_y}(y)\varphi_{n_z}(z) \quad (2.14)$$

where vector $\mathbf{k} = 2\pi(\frac{n_x}{L_x},\ 0,\ 0)$.

Performing the same operation (Eq. 2.8 and 2.12), it is easy to show that the energy dispersion will be:

$$E = \varepsilon_{n_y} + \varepsilon_{n_z} + \frac{\hbar^2 k_x^2}{2m} \quad (2.15)$$

and DOS for the one 1D subband:

$$g_{1D}(E') \;\sim\; 1/\sqrt{E'} \quad (2.16)$$

where ε_{n_y} and ε_{n_z} are the energy levels defined by the confining potentials $U_y(y)$, $U_z(z)$ and $E' = E - \varepsilon_{n_y} - \varepsilon_{n_z}$. Now, as we approach the bottom of the 1D subband, the DOS diverges (van Hove singularity) (Figure2.1c). This drastic change in the DOS caused by reducing the dimensionality of the system predicts unusual properties of 1D materials and has attracted a lot of attention of the scientists.

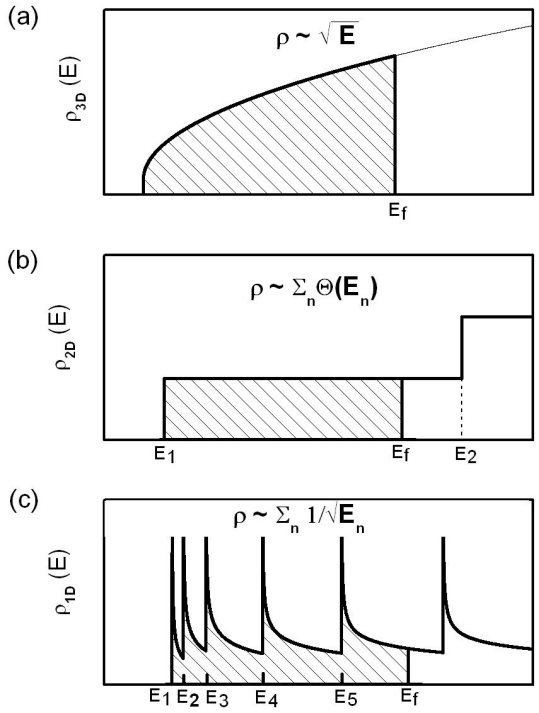

Figure 2.1: DOS as a function of energy fot (a) 3DEG, (b) 2DEG with only the lowest occupied subband, (c) 1DEG with infinite boundary conditions (see section 2.1.2). Dashed areas correspond to the occupied electronic states

The dimensionality of the system influences the DOS and the energy dispersion law. The energy levels ε_{n_y}, ε_{n_z} and the wave-functions $\varphi_{n_z}(z)$, $\chi_{n_y}(y)$ of the electronic states in y and z directions are the eigenvalues and the eigenfunctions of the Schrödinger equation with confining potentials $U_y(y)$ and $U_z(z)$. In general, for arbitrary confinement potential there are no analytical solutions. We will present below several examples of the solution for three particular potentials, which can be used to describe the actual potential in real nanosystems.

2.1.2 Analytical solutions of the eigen energies and wave-functions in the 1D case for different potential profiles

Infinite quantum well potential

Consider free 2DEG in $x-y$ plane confined in y direction by an infinite potential quantum well:

$$U(y) = \begin{cases} +\infty, & y \notin [0, L], \\ 0, & y \in [0, L]; \end{cases}$$

In order to find the wave-functions $\chi(y)$ related with the motion in y direction, we should solve the one-dimensional Schrödinger equation:

$$-\frac{\hbar^2}{2m}\frac{d^2\chi(y)}{dy^2} = E\chi(y) \tag{2.17}$$

with the boundary conditions:

$$\chi(y) = 0 \quad \text{for} \quad y \notin (0, L) \tag{2.18}$$

A solution of the equation 2.17 is a superposition of two planar waves propagating in opposite directions along the axis y:

$$\chi(y) = Ae^{i\frac{2mE}{\hbar^2}y} + Be^{-i\frac{2mE}{\hbar^2}y}$$

From the boundary condition $\chi(0) = 0$ and wave-function normalization $\int_0^L |\chi(y)|^2 = 1$ we can find coefficients A and B. Hence the wave-function can be rewritten as:

$$\chi(y) = \sqrt{\frac{2}{L}} sin\left(\frac{\pi n y}{L}\right) \quad \text{where} \quad n = 1, 2, 3... \tag{2.19}$$

The energy levels can be found from another boundary condition $\chi(L) = 0$:

$$E_n = \frac{\pi^2\hbar^2}{2mL^2}n^2 \tag{2.20}$$

As we can see, the wave-functions are a set of standing waves which are limited by the quantum well and the energy levels have a quadratic distribution. On the Figure 2.1c, we can see the corresponding n^2 spacing of the Van Hove singularities.

Performing similar calculations for the confinement in z direction we can derive the wave-functions and corresponding energy levels for the quasi-1D nanowire with a rectangular cross-section $L_y \times L_z$.

$$\psi_{\mathbf{k}}(\mathbf{r}) = \frac{2}{\sqrt{L_x L_y L_z}} e^{ik_x x} sin\left(\frac{\pi n_y y}{L_y}\right) sin\left(\frac{\pi n_z z}{L_z}\right) \tag{2.21}$$

$$E_{k_x,n_y,n_z} = \frac{\hbar^2 k_x^2}{2m} + \frac{\pi^2\hbar^2}{2mL_y^2}n_y^2 + \frac{\pi^2\hbar^2}{2mL_z^2}n_z^2 \tag{2.22}$$

Infinite cylindrical confining potential

Analytical solution in the infinite cylindrical potential profile can be applied to a big variety of real systems, for example, to quasi-1D nanowires. To obtain the wave-functions and energy spectrum for such kind of system, we should solve the Schrödinger equation with infinite cylindrical confining potential:

$$U(y, z) = \begin{cases} +\infty, & y^2 + z^2 > R^2, \\ 0, & y^2 + z^2 \leq R^2; \end{cases}$$

Schrödinger equation in cylindrical coordinates $\mathbf{r}(\rho,\ z,\ \phi)$ for $\rho \leq R$ can be written as:

$$-\frac{\hbar^2}{2m}\left(\frac{\partial^2\psi(\mathbf{r})}{\partial\rho^2}+\frac{1}{\rho}\frac{\partial\psi(\mathbf{r})}{\partial\rho}+\frac{\partial^2\psi(\mathbf{r})}{\partial z^2}+\frac{1}{\rho^2}\frac{\partial^2\psi(\mathbf{r})}{\partial\phi^2}\right)=E\psi(\mathbf{r}) \tag{2.23}$$

The solution can be presented as $\psi(\varrho,z,\phi)=P(\rho)Z(z)\Phi(\phi)$, thus we can separate the equation and derive $P(\rho)$ and $Z(z)$:

$$Z_n(z)=\frac{1}{\sqrt{L_z}}e^{ik_z z} \quad \text{where} \quad k_z=\frac{2\pi n}{L_z}, \quad n=1,2,3...$$

$$\Phi(\phi)=(2\pi)^{-1/2}e^{im\phi} \quad \text{where} \quad m=0,\pm1,\pm2...$$

and equation for $P(\rho)$ can be reduced to:

$$\rho^2\frac{d^2P(\rho)}{d\rho^2}+\rho\frac{dP(\rho)}{d\rho}+(k^2\rho^2-m^2)P(\rho)=0 \quad \text{,with the boundary condition } P(R)=0$$

The solutions are Bessel functions $J_m(k_{m,p}\rho)$ such that $k_{m,p}R=j_{m,p}$, where $j_{m,p}$ is the p^{th} zero of the Bessel function J_m. Thus, the total wave-functions and corresponding energy levels are given by:

$$\psi(\varrho,z,\phi)=\frac{1}{\sqrt{2\pi L_z}}e^{ik_z z}e^{im\phi}J_m(j_{m,p}\frac{\rho}{R}) \tag{2.24}$$

$$E_{m,p}=\frac{\hbar^2}{2m}\left(\frac{j_{m,p}^2}{R^2}+k_z^2\right) \tag{2.25}$$

Parabolic confining potential

Consider free 2DEG in $x-y$ plane with a parabolic confining potential:

$$U(y)=\frac{1}{2}m\omega_0 y^2 \tag{2.26}$$

We assume that the carrier concentration is low enough, thus only the first energetic z-subband with energy ε_z is occupied, which will be omitted in the further calculations. The Schrödinger equation in this case is:

$$\left[\frac{-\hbar^2\bigtriangledown^2}{2m}+\frac{1}{2}m\omega_0 y^2\right]\Psi(x,y)=E\Psi(x,y) \tag{2.27}$$

or with the substitution $p_x\equiv-i\hbar\frac{\partial}{\partial x}$ and $p_y\equiv-i\hbar\frac{\partial}{\partial y}$:

$$\left[\frac{p_x^2}{2m}+\frac{p_y^2}{2m}+\frac{1}{2}m\omega_0 y^2\right]\Psi(x,y)=E\Psi(x,y) \tag{2.28}$$

Accordingly to the equation 2.14 a solution can be expressed as:

$$\Psi(x,y)=\frac{1}{\sqrt{L_x}}\chi(y)e^{ik_x x} \tag{2.29}$$

where the function $\chi(y)$ satisfies the equation:

$$\left[\frac{\hbar^2 k_x^2}{2m} + \frac{p_y^2}{2m} + \frac{1}{2}m\omega_0 y^2\right]\chi(y) = E\chi(y) \tag{2.30}$$

The eigenfunctions and eigenenergies of this equation are given by:

$$\chi_{n,k}(y) = u_n(q) \quad \text{where} \quad q = \sqrt{\frac{m\omega_0}{\hbar}}y \tag{2.31}$$

$$E(n,k) = \frac{\hbar^2 k_x^2}{2m} + (n+\frac{1}{2})\hbar\omega_0, \quad n = 0,1,2... \tag{2.32}$$

where $u_n(q) = e^{-q^2/2}H_n(q)$ and $H_n(q)$ is the nth Hermite polynomial.

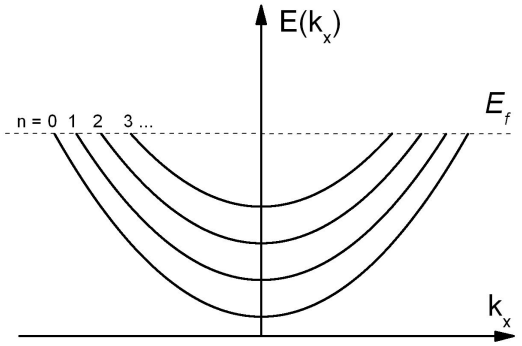

Figure 2.2: Dispersion relation $E(k)$ for electrical subbands due to the parabolic confining potential $U(y) = \frac{1}{2}m\omega_0 y^2$.

The dispersion relation (Figure 2.2) shows that different index n correspond to the different subbands with equidistant spacing of $\hbar\omega_0$. Thus, increasing the confining potential increases the energy splitting of the electrical subbands. We will come back to this type of confinement in the section 2.4.2.

2.2 Creation of 2D and 1D systems

A typical example of a 2D electronic confinement is obtained in an inversion layer in a semiconductor substrate. This is widely used in MOSFET (metal-oxide-semiconductor field-effect transistor). A typical device consists of a SiO_2 layer (a few nanometers thick) grown on a p-type Si substrate, covered by a metallic gate electrode. The 2D electron gas (2DEG) appears in the p-type Si at the oxide–sc. interface as a result of the band-bending which comes from the electrostatic balance caused by the application of a positive voltage V_g on the gate, as shown on the figure 2.3.

The electron concentration n_s of the 2DEG is obtained by the relation $en_sS = C(V_g - V_t)$, where S is the surface of the layer, C is the geometrical capacitance of

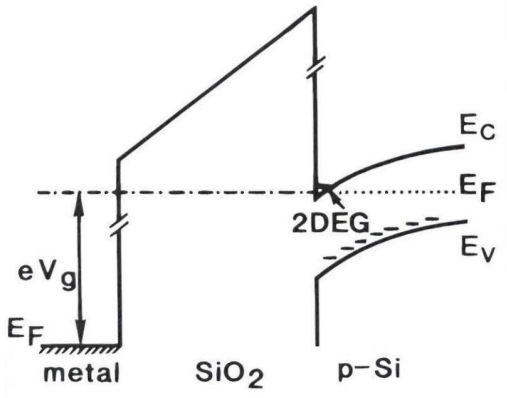

Figure 2.3: The diagram of the band structure of a MOSFET. A 2DEG is formed at the interface between the oxide and the p-type silicon substrate as a consequence of the positive voltage V_g on the gate electrode. Taken from [Beenakker 1991].

the gate electrode and V_t is the threshold voltage beyond which inversion layer is created. We can define $C = \varepsilon_{SiO_2} S/d_{SiO_2}$ (ε_{SiO_2} is the dielectric constant of the SiO_2 layer and d_{SiO_2} its thickness), so

$$n_s = \frac{\varepsilon_{SiO_2}}{e d_{SiO_2}} (V_g - V_t) \tag{2.33}$$

As we can see electronic concentration is linearly proportional to the applied electric field across the oxide layer V_g/d_{SiO_2}.

Inversion layer in $Si/SiO_2/metal$ structure was the first experimental demonstration of quantized electronic states due to the artificial confinement. The success of the Si-based MOSFET is due to the smooth Si–SiO_2 interface, which varies only by a few atomic steps allowing the existence of well-defined quantum states. Later, the development of the molecular beam epitaxy (MBE) and metal organic chemical vapor deposition (MOCVD) has allowed to create more complicated heterostructures with the quantization perpendicular to the substrate, such as the high electron mobility transistor (HEMT), commonly based on GaAs and AlGaAs materials.

HEMT uses a junction between two materials with different band gaps as a conducting channel instead of a doped region, like in MOSFET (Figure 2.4). The electrons are confined at the GaAs–AlGaAs interface by a potential well coming from the conduction band offset between two semiconductors and the electrostatic potential of the positively charged donors in the n-doped AlGaAs layer. To reduce scattering from these donors, the doped layer can be separated from the interface by an undoped AlGaAs spacer layer, which leads to the very high mobility of the 2DEG (up to $3.2x10^7\ cm^2/V/s$ at low temperature) [Kumar 2010].

There are two principal methods to achieve a quasi-one-dimensional structure based on the lateral confinement of the 2DEG: by lithography techniques, one can

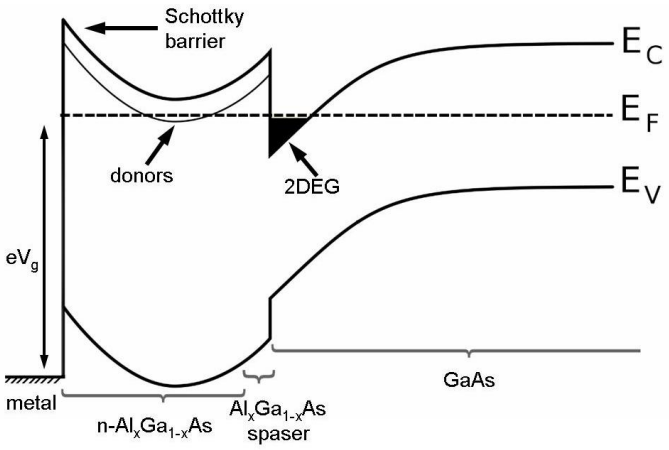

Figure 2.4: Band structure in GaAs/AlGaAs heterojunction based HEMT.

pattern a lateral gate and confine the 2DEG by applying an electrostatic potential, or etch directly the 2DEG, creating a geometrical confining potential. Modern technologies allow to reach a characteristic width of such systems about several tens of nanometers in both cases. The simplest example is presented at Figure 2.5a where narrow channel was defined by scaling down the width of the gate contact. The disadvantages for this type of the devices are some uncertainty in the channel width beyond the gate. This problem is solved in the device Figure 2.5b, fabricated by dry-etching techniques. But the presence of sidewalls may reduce the electron mobility due the sidewall scattering.

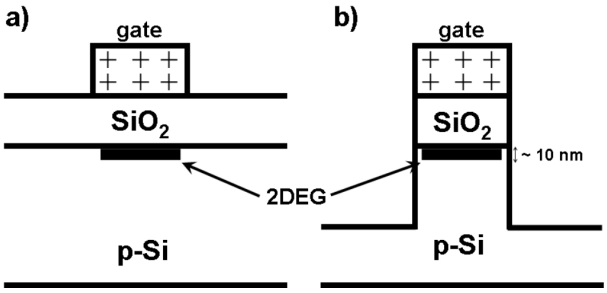

Figure 2.5: Schematic views of two methods used to define a narrow electron accumulation layer. The location of the 2DEG is shown in black.

All techniques mentioned above are referred as a Top–Down approach of the nanodevice fabrication: starting from large 3D patterns we use external tools to reduce the material size and to manufacture the low-dimensional devices. Another approach, called Bottom–Up, in which the properties of single atoms or molecules are used to create nano-objects. The advantage of the second approach is that nano-objects under certain conditions achieve almost ideal crystallinity. This means

that nanodevices based on such kind of nano-objects could reveal unique transport properties. Another advantage of the Bottom–Up technologies is the possibility to produce devices in parallel and much cheaper than Top–Down methods if the self-assembly of these objects is under control at the nanoscale and over wide areas. The problem is that once the object is created it has to be manipulated. We will consider a technique of such manipulation in the chapter 3.

2.3 Electronic transport in quasi-1D systems

In quasi-1D system, electrons are free to move in one dimensions, but they are tightly confined in the two others, which leads to quantized energy levels for motion in these directions. In order to describe the electronic transport in low dimensional systems, and particularly in 1D system, it is necessary to define the characteristic lengths. Characteristic lengths of the electronic transport are the mean free path l_e, the phase relaxation length l_φ and the electron wave-length λ_f at E_f, as only electrons with energies close to the Fermi energy are responsible for the charge transport of the system. When one or more dimensions of the system start to be comparable with these lengths the electronic properties are modified as compared to those of the corresponding bulk system. These systems are called mesoscopic. This term means that the system is still large compared to the microscopic (atomic) scale but its properties cannot be described by a conventional macroscopic model. To define the transport regime, we determine relations between L (characteristic dimension of the system), l_e, l_φ and λ_f. First of all, let us remind the physical meaning of l_e, l_φ and λ_f.

2.3.1 The characteristic lengths

Mean free path (l_e)

An elastic collision is a collision which affects only the direction of the electron momentum and an inelastic collision changes the value of the electron's momentum and thus modifies the electron phase. Denoting the mean time between two adjacent elastic collisions as τ_{els}, we can define a time after which the direction of the momentum will be completely randomized compared to the direction of the initial momentum τ_e (momentum relaxation time) as:

$$\frac{1}{\tau_e} = \alpha_e \frac{1}{\tau_{els}}$$

where $\alpha_e \in [0, 1]$ denotes the efficiency of individual elastic collision to modify the momentum. As the considered electrons have energies close to the Fermi energy, the mean distance that an electron travels before its direction of the initial momentum is completely randomized (mean free path) l_e can be expressed as:

$$l_e = v_f \tau_e \tag{2.34}$$

Phase relaxation length (l_φ)

In analogy with the momentum relaxation time the phase relaxation time can be written as:

$$\frac{1}{\tau_\varphi} = \alpha_\varphi \frac{1}{\tau_{inels}} \quad \text{where} \quad \alpha_\varphi \in [0,1]$$

where τ_{inels} is the mean time between two adjacent inelastic collisions. To define the phase relaxation length l_φ we should consider two cases:

i) $\tau_\varphi \lesssim \tau_e$: the electron motion between two inelastic collisions is ballistic and we can write:

$$l_\varphi = v_f \tau_\varphi \tag{2.35}$$

ii) $\tau_\varphi \gg \tau_e$: the electron motion between two inelastic collisions is diffusive and it consists of $\sim \tau_\varphi/\tau_e$ randomly orientated ballistic segments of length l_e. Thus we can calculate l_φ as a root mean squared distance traveled by the electron in a particular direction:

$$l_\varphi = \sqrt{\frac{\tau_\varphi}{\tau_e} l_e^2 \langle cos^2\theta \rangle} = \sqrt{\frac{1}{2} v_f l_e \tau_\varphi} = \sqrt{D\tau_\varphi} \tag{2.36}$$

where $D = v_f l_e/2$ is the diffusion coefficient.

Fermi-wavelength (λ_f)

Another characteristic length of the system is the Fermi-wavelength λ_f. As we saw in the section 2.1 in the 2D system, allowed values for k_y are spaced by the $2\pi/W$, where W is a characteristic width of the confining potential. Each value of the $k_y \in [-k_f,\ k_f]$ gives a distinct transverse mode, thus the total number of propagating modes N is:

$$N = Round\left(\frac{k_f W}{\pi}\right) = Round\left(\frac{2W}{\lambda_f}\right) \tag{2.37}$$

where *Round* is rounding down to the nearest integer number. When the λ_f is of the order of the width of the system W, we have only few transverse modes and thus we can treat this system as a quasi-1D. Hence another criterion of the low-dimensional system is: the Fermi-wavelength is comparable to the size of the system.

Different transport regimes in quasi-1D system are shown on the figure 2.6 for various ratios of characteristic lengths l_e, l_φ and W; λ_f is of the order of the width of the system W.

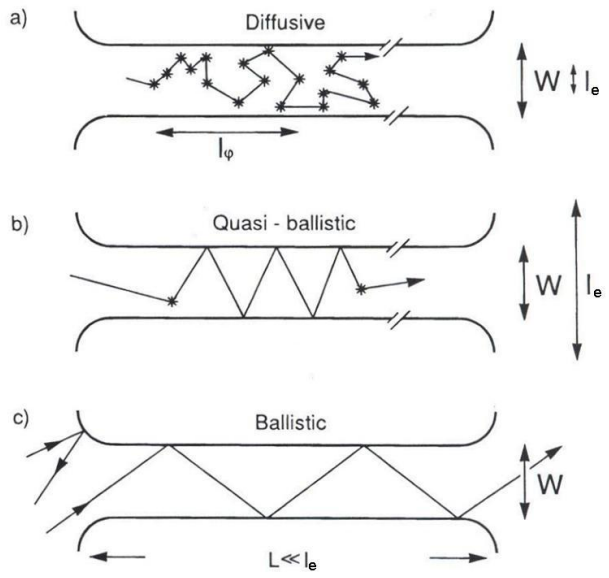

Figure 2.6: Electron trajectories characteristic for the (a) diffusive ($l_e < W, L$), (b) quasi-ballistic ($W < l_e < L$) and (c) ballistic ($W, L < l_e$) transport regimes, in the case of specular boundary scattering. Asterisks are the internal impurity. Taken from [Heinrich 1988].

2.3.2 Classical transport (Drude – Boltzmann model)

The conductor is in the classical transport regime if $L \gg l_e \gg l_\varphi$ and $k_f l_e \gg 1$. The first condition means that an electron passing through the conductor is subjected to a large number of collisions and at the same time there is no interference between electrons wave-functions, so they behave as a classical particles. The second inequality, called criterion of Ioffe-Reggel, avoid the localization of the electrons due to the scattering centers (Anderson localization) [Anderson 1958]. It should be noticed that the Boltzmann description is semi-classical, as we treat electrons as a classical particles and in the same time the band structure and Fermi-Dirac statistics, deduced from the Schrödinger equation are introduced into the model.

In the periodic potential of the crystal lattice, electrons can be represented by Bloch wave-functions with a wave-vector k. Hence the group velocity can be defined as:

$$v(k) = \frac{1}{\hbar}\frac{\partial E}{\partial k} = \frac{\hbar k}{m^*} \tag{2.38}$$

where m^* is the effective electron mass and $\hbar k$ is the electron momentum. Since there are no interference effects ($l_e \gg l_\varphi$) between the collisions we can use the classical law for describing the dynamics of electrons:

$$\mathbf{F} = \frac{\partial(\hbar \mathbf{k})}{\partial t} \quad \Longrightarrow \quad \mathbf{F} = m^* \frac{\partial \mathbf{v}}{\partial t} \tag{2.39}$$

where $\mathbf{F}$ is the sum of external forces applied to the electron. In the presence of an electric field E, there are two forces: force of the electric field and the "friction" force caused by the collisions.

$$\mathbf{F} = -e\mathbf{E} - \left(\frac{d\mathbf{p}}{dt}\right)_{scattering} \tag{2.40}$$

If we assume that an electron after being scattered receives its momentum due to the external field and looses it completely at the next scattering, so the system reaches an equilibrium and we can say that all the electrons have a mean velocity value v_d, which is called drift velocity. Hence:

$$e\mathbf{E} = -\frac{m^*\mathbf{v}_d}{\tau_e} \quad \Longrightarrow \quad \mathbf{v}_d = -\frac{e\tau_e}{m^*}\mathbf{E} = -\mu\mathbf{E} \tag{2.41}$$

where μ is the electron mobility.

The Boltzmann model describes the evolution of the electron energy distribution in the presence of external forces. At the thermodynamic equilibrium electrons obeys the Fermi-Dirac statistic $f(E)$ (Eq. 2.4), thus to determinate its evolution in time we should resolve the Boltzmann equation:

$$\frac{df}{dt} = \frac{\partial f}{\partial t} + \frac{1}{\hbar}\frac{\partial f}{\partial \mathbf{k}}\mathbf{F} + \frac{\partial f}{\partial \mathbf{r}}\mathbf{v}(\mathbf{k}) \tag{2.42}$$

Electric field shifts the Fermi-Dirac distribution by a vector $\mathbf{k}_d = -e\mathbf{E}\tau_e/\hbar$, thus:

$$[f(\mathbf{k})]_{\mathbf{E}\neq 0} = [f(\mathbf{k}\text{-}\mathbf{k}_d)]_{\mathbf{E}=0}$$

In the k-space, it can be seen as a shift of the Fermi surface by the vector $\mathbf{k}_d$ (Figure 2.7).

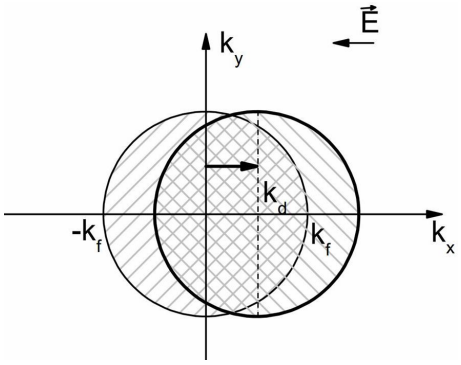

Figure 2.7: At low temperatures all the states within a circle of the radius k_f are occupied at equilibrium (left-handed shading). In the presence of the electric field the circle is shifted in the direction of $-\mathbf{E}$ (right-handed shading). Taken from [Datta 1995].

Now, the number of the electrons propagating along the x axis is not compensated by electrons moving in the opposite direction. For the weak electric field ($k_d \ll k_f$), nothing happens deeply inside the Fermi surface. It is only near $-k_f$ the states that used to be full become empty, while near $+k_f$ the states that were empty become full. So, only a small number of electrons with energy states from $k_f - k_d$ to $k_f + k_d$ are carrying the current and the current density can be written as:

$$\mathbf{J} = -e \int_{E(k_f - k_d)}^{E(k_f + k_d)} f(E)\mathbf{v}(E)DOS(E)dE = \sigma \mathbf{E} \tag{2.43}$$

where

$$\sigma = en\mu \tag{2.44}$$

is the Drude conductivity and f obeys the Boltzmann equation. If we substitute the $\mu = e\tau_e/m^*$ and denote diffusion coefficient $D = \tau_e/m^*$, we obtain the Einstein relation for the conductivity:

$$\sigma = e^2 nD \tag{2.45}$$

In order to show the agreement of derived conductivity with the Ohm's law, we can calculate the current in the conductor with length L and cross-section S under the bias voltage V:

$$I = JS = \sigma ES = \sigma \frac{V}{L} S \tag{2.46}$$

If we denote system resistivity $\rho = 1/\sigma$ we obtain the Ohm's law:

$$I = \frac{V}{\rho \frac{L}{S}} = \frac{V}{R}$$

2.3.3 Ballistic regime

A system is in a ballistic regime if the electrons propagate without collisions. As a consequence from this definition, the system should satisfy the inequality $L \ll l_e, l_\varphi$. From the classical conductance equation $G = \sigma S/L$, where σ is the conductivity, a parameter specified by the material of the sample, we should expect an infinite increase of the conductance with the reduction of the length L. But experimentally it was found, that once the system's length becomes shorter than the mean free path, the conductance is limited by some value G_0. The Landauer-Büttiker model allows to understand this discrepancy considering the conductance as a probability that electron can be transmitted through the system.

Consider a quasi-1D system with N electronic conduction channels connected by two perfect contacts at zero temperature (Figure2.8) and polarized by a tension V. Denoting the chemical potential of the left and right contacts μ_1 and μ_2 respectively, we can write $eV = \mu_1 - \mu_2$.

As we have an asymmetry in the electron energy distribution, the flow of electrons emitted from the left contact to the right one is not equal to the opposite flow emitted by right contact and we can calculate the current as:

$$I = e \int_{\mu_2}^{\mu_1} v(E) D(E) dE \tag{2.47}$$

replacing the velocity of the electrons by $v = \frac{1}{\hbar}\frac{\partial E}{\partial k}$ and DOS of electrons propagating in one direction by $D(E) = \frac{N}{\pi}\frac{\partial k}{\partial E}$ we have:

$$I = \frac{2eN}{h}(\mu_1 - \mu_2) = \frac{2e^2 N}{h} V \tag{2.48}$$

and the conductance

$$G = \frac{I}{V} = \frac{2e^2 N}{h} = N G_0 \tag{2.49}$$

where $G_0 = 2e^2/h \approx 7.75\ 10^{-5}\Omega^{-1}$ is called the quantum of conductance.

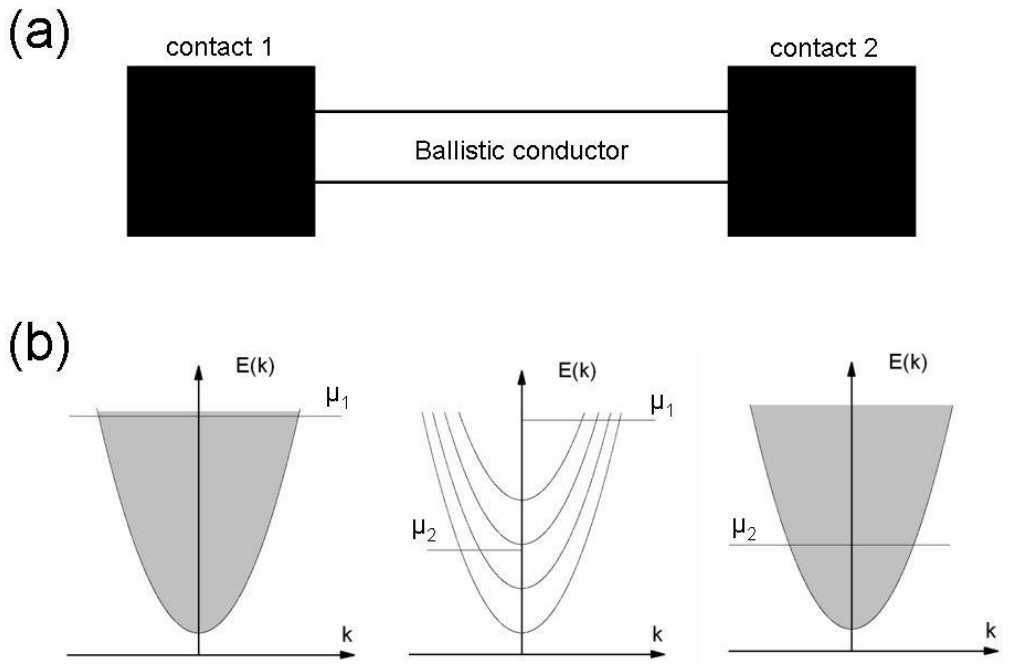

Figure 2.8: (a) A conductor under external bias between two contacts. (b) Band diagram under bias. In the contacts there is a high DOS - indicated by shading, thus $+k$ stated and $-k$ states have nearly the same quasi-Fermi level μ_1 and μ_2 correspondingly.

We derived the conductance of the 1D system in the ballistic regime, which behaves as multi-moded waveguide: electrons propagate between the contacts with

a constant energy defined by the initial state. The conductance is independent of the length L of the sample, and it increases proportionally to the number of conducting bands (modes) N involved in the process. Consequently, the resistance of the ballistic conductor with a single mode is $\sim 12.9k\Omega$, if we assumed that there are no collisions in the system. This resistance comes from the contacts and can be explained by the fact that in the metallic contacts we have a 3D electronic gas with the quasi-continuous energy distribution while in the 1D conductor we have a discrete energy distribution in y-z plane. Thus some of the electrons from the contacts will be reflected by the interface contact/conductor, because there is no "place" (in energetic space) for such electrons in the 1D system.

2.3.4 Conductor as a waveguide with a finite transmission probability

We consider a diffusive system where $l_e \ll L$ in the incoherent regime ($l_\varphi \ll l_e$) and we consider propagation of electrons in the conductor as a transmission of wave-functions through a waveguide. A simple approach to define a diffusive conductor is to introduce a transmission probability of the system. Consider as previously a quasi-1D system with N conduction electronic bands below E_f, contacted by two ideal contacts at zero temperature, with a probability $T \leq 1$ that an electron injected in the contact 1 will be transmitted to the contact 2 (Figure2.9).

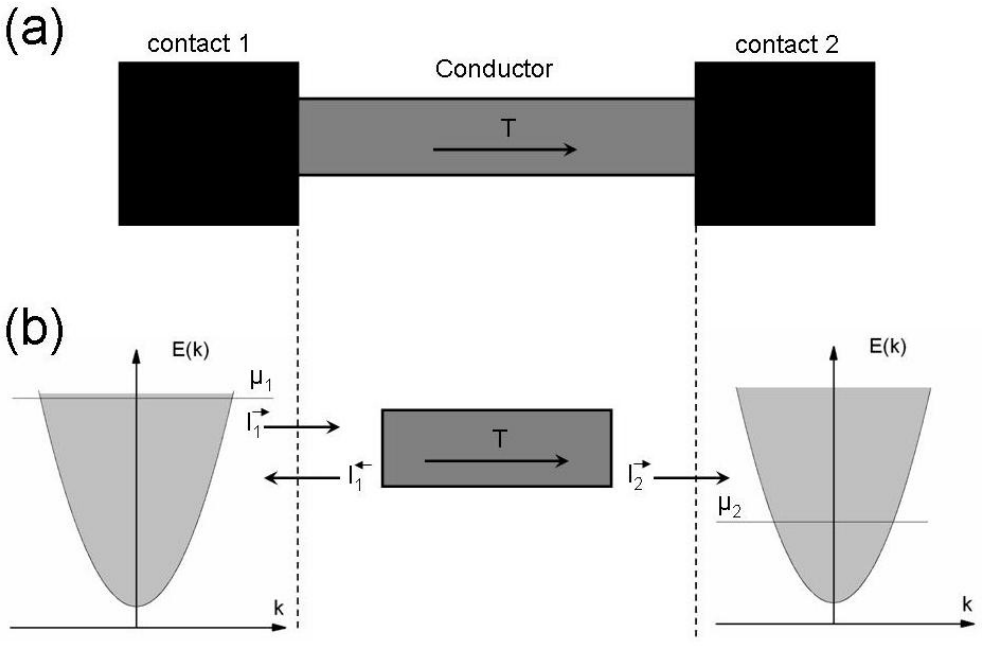

Figure 2.9: a) A conductor having a transmission probability T under external bias between two contacts. b) Band diagram under bias with ingoing and outgoing currents at the interfaces contact/conductor.

By polarizing the system with the potential $V = (\mu_1 - \mu_2)/e$, we write the current ingoing from the contact 1 to the conductor as (see Eq. 2.48):

$$I_1^{\rightarrow} = \frac{2eN}{h}(\mu_1 - \mu_2)$$

and the current outgoing from the conductor $I_2^{\rightarrow}$ to the contact 2 as $I_1^{\rightarrow}$ times a transmission probability T:

$$I_2^{\rightarrow} = \frac{2eN}{h}T(\mu_1 - \mu_2)$$

and the reflected part of the current as:

$$I_1^{\leftarrow} = \frac{2eN}{h}(1 - T)(\mu_1 - \mu_2)$$

Thus the full current flowing from left contact to right contact is:

$$I = I_1^{\rightarrow} - I_1^{\leftarrow} = I_2^{\rightarrow} = \frac{2eN}{h}T(\mu_1 - \mu_2)$$

Hence the conductance is equal to:

$$G = \frac{I}{V} = \frac{2e^2N}{h}T = G_0NT \tag{2.50}$$

This equation, called the Landauer formula, describes the properties of low-dimensional conductor, with a length-independent contact resistance and the steps-like conductance behaviour versus the number of filled channels. In the same time it recovers the Ohm's law for large conductors.

From the equation 2.50, the resistance of the conductor R can be written as:

$$R = \frac{h}{2e^2N}\frac{1}{T} = \frac{h}{2e^2N} + \frac{h}{2e^2N}\frac{1-T}{T} \tag{2.51}$$

where the first term comes from the contact resistance of the ballistic system and the second term is due to the presence of reflection inside the system and proportional to the ratio of reflected to propagated electrons $(1 - T)/T$. It can be shown that this ratio has an additive property for incoherent electrons. This means that the transmission probability $T(X)$ of the system with X scatterers, each having a transmission probability T, is given by

$$\frac{1 - T(X)}{T(X)} = X\frac{1-T}{T} \;\Rightarrow\; T(X) = \frac{T}{X(1-T)+T}$$

and if we rewrite the number of scatterers X trough the linear density of scatterers ν in a conductor of length L as: $X = \nu L$, we can write:

$$T(L) = \frac{L_0}{L + L_0}$$

where $L_0 \equiv \frac{T}{\nu(1-T)}$ is of the order of mean free path l_e (in case $T \sim 1$). The last is easy to see if we remember that l_e is the average distance that an electron can pass before it is scattered. So the probability to be scattered on the distance l_e is:

$$(1-T)\nu l_e \sim 1 \Rightarrow l_e \sim \frac{1}{\nu(1-T)} \sim L_0$$

Hence the equation 2.50 can be rewritten as:

$$G = G_0 N \frac{l_e}{L + l_e} \quad \text{, or in case where } l_e \ll L \text{ as } \quad G \approx G_0 N \frac{l_e}{L} \tag{2.52}$$

For the resistance, accordingly with equation 2.51, we can write:

$$R = \frac{h}{2e^2 N} + \frac{h}{2e^2 N} \frac{L}{l_e} = R_c + R_{cl} \tag{2.53}$$

The number of the conduction electronic subbands N is proportional to the width of the sample W (Eq. 2.37): $N \sim k_f W/\pi$. Hence the resistance of the conductor (Eq. 2.53) consists of the resistance of the contacts R_c, which becomes negligible with the increase of W, and thus:

$$R \approx \frac{1}{\sigma} \frac{L}{W} \quad \text{where} \quad \sigma = e^2 n \frac{v_f l_e}{\pi} \tag{2.54}$$

where n is a carrier concentration. If we define diffusion coefficient as $D = v_f l_e/\pi$ we obtain the Einstein relation $\sigma = e^2 n D$ for the conductivity. Thus, the Landauer formula recovers the Ohm's law as we increase the size of the system.

2.3.5 Coherent transport

At low temperature, the phase relaxation length l_φ can be comparable or larger than the mean free path l_e, and the quantum nature of the electrons, represented by their wave function, in particular its phase, should be taken in to account. First we will describe the case where l_φ exceeds the length of the system L.

Consider a single mode conductor connected to ideal contacts with two scattering centers in series with probabilities T_1 and T_2 and reflection probabilities R_1 and R_2 respectively.

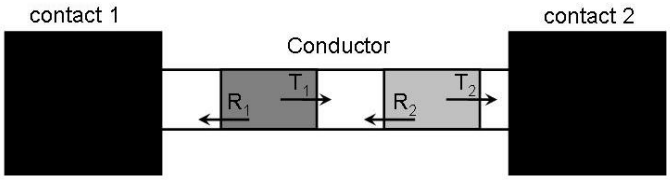

Figure 2.10: A conductor with two scatterers in series with transmission probabilities T_1 and T_2 and reflection probabilities R_1 and R_2 respectively under external bias between two contacts.

The transmission probability through the system is [Datta 1995]:

$$T = \frac{T_1 T_2}{1 - 2\sqrt{R_1 R_2} cos\theta + R_1 R_2} \tag{2.55}$$

where θ is the phase shift acquired in one round-trip between the scatterers. Before we write down the resistance of such a system, it should be noted, that interference effects depend on the scatterers configuration and on the electron wavelength, so the resistance could be defined only through an ensemble averaged over many conductors having different configurations but the same number of scattering centers.

$$\rho_{12} = \left\langle \frac{1-T}{T} \right\rangle$$

here ρ_{12} is the resistance normalized to $h/2e^2$. If we substitute T from equation 2.55 and realize the ensemble averaging as integration over all possible phase shifts θ:

$$\rho_{12} = \int \frac{1}{2\pi} \frac{1 + R_1 R_2 - T_1 T_2 - 2\sqrt{R_1 R_2} cos\theta}{T_1 T_2} d\theta = \frac{1 + R_1 R_2 - T_1 T_2}{T_1 T_2}$$

we see that there is no more additivity for the ratio $(1-T)/T$. Hence if we define the resistances of the individual scatterers as

$$\rho_1 \equiv \tfrac{1-T_1}{T_1} \text{ and } \rho_2 \equiv \tfrac{1-T_2}{T_2}$$

we can write:

$$\rho_{12} = \rho_1 + \rho_2 + 2\rho_1\rho_2 \tag{2.56}$$

To obtain the resistance as a function of the conductor length L we consider what happens if to the conductor of length L and resistance $\rho_1(L)$ we add a short section of length ΔL, with resistance $\rho_2(\Delta L)$. As this section is small it has a ballistic conductance and its resistance can be derived from equation 2.53:

$$\rho_2(\Delta L) = \frac{\Delta L}{L_0}$$

where L_0 is in the order of the mean free path. Here we ignore the contact resistance, as we are interested only in the intrinsic resistance of short section ΔL. From the equation 2.56:

$$\rho(L + \Delta L) = \rho(L) + [1 + 2\rho(L)] \frac{\Delta L}{L_0}$$

reducing ΔL we can write the differential equation:

$$\frac{d\rho}{dL} = \frac{\rho(L + \Delta L) - \rho(L)}{\Delta L} = \frac{1 + 2\rho}{L_0} \tag{2.57}$$

This equation was solved by Landauer [Landauer 1970] and the solution is:

$$\rho(L) = \frac{1}{2}(e^{2L/L_0} - 1) \tag{2.58}$$

The derived quantum resistance dependence $\rho(L)$ differs drastically from the Ohm's law, because the electron interference was taken into the account.

2.3.6 Universal Conductance Fluctuations

In the previous section, we derived the resistance of a single-moded conductor in the phase-coherent regime. It was shown [Thouless 1977] that multi-moded conductor resistance can be described by this solution as well, if it is long enough that the resistance is of the order of $h/2e^2$. From the equation 2.53 we can see that this requires that the length exceeds NL_0, which is called localization length L_c. According to the relation between the length of the phase-coherent conductor and the localization length we can divide the conductance regimes into two types:

- regime of strong localization ($L \geq L_c$): the resistance no longer scales linearly with L but diverges exponentially;

- regime of weak localization ($L \ll L_c$): the resistance from equation 2.58 can be expressed as a Taylor series up to second order:

$$\rho(L) \sim \left[\frac{L}{L_c} + \left(\frac{L}{L_c}\right)^2\right]$$

where the first term $\rho_{cl} = L/L_c$ is the classical Ohm's behaviour and the second term $\Delta\rho = (L/L_c)^2 = \rho_{cl}^2$ represents the deviation due to the interference. Thus the related correction to the conductance ΔG (in $2e^2/h$ units) is:

$$\Delta G = \Delta\left(\frac{1}{\rho}\right) = -\frac{\Delta\rho}{\rho^2} \simeq -1$$

Taking into account this correction we derive the ensemble averaged conductance of the system in the weak localization conduction regime:

$$< G >= G_{cl} - G_0 \tag{2.59}$$

We see that interference effects lead to the reduction of the conductance by G_0 and this correction is universal and independent of the system's characteristics while $L < l_\varphi$. If $L > l_\varphi$ the conductor can be consider as a L/l_φ series of phase-coherent blocs, each of which contains many elastic scatterers. This type of transport is called quantum diffusive regime. Inside the blocs, we can use the equation 2.59 for weak localization conduction regime and in between them we can apply Ohm's law and treat them as a series of resistances r:

$$r = (G_{cl} - G_0)^{-1} \tag{2.60}$$

where $G_{cl} = \sigma\frac{W}{l_\varphi}$ and W is the width of the conductor. Thus:

$$< G_{tot}^{-1} >= \frac{L}{l_\varphi}(G_{cl} - G_0)^{-1} \Rightarrow < G_{tot} >= \sigma\frac{W}{L} - G_0\frac{l_\varphi}{L} \tag{2.61}$$

the correction to the Ohm's law is the same up to a ratio of the phase relaxation length to the length of the system.

We want to pay attention to the fact that corrections derived in equations 2.59 and 2.61 are the corrections to the ensemble average value of the conductance - *Universal Conductance Fluctuations* (UCF). This means that the conductance will vary from sample to sample due to different configurations of scattering sites. These fluctuations can be achieved as well by varying of the electron density or applying a magnetic field and thus changing the Fermi wavelength of the electrons. For the microscopic system ($L < l_\varphi$), these fluctuations are universal and the value is in the order of [Datta 1995]:

$$\delta G \approx \frac{e^2}{h} \tag{2.62}$$

and for the macroscopic system ($L > l_\varphi$) the value of fluctuations is reduced by the number of the coherent blocs in the system l_φ/L [Datta 1995]:

$$\delta G \approx C\frac{e^2}{h}\left(\frac{l_\varphi}{L}\right)^{3/2} \tag{2.63}$$

where parameter C depends on the geometry of the system.

2.4 Magnetotransport

The magnetic field may have a profound effect on the electronic and transport properties of the nanostructures and leads to the appearance of new fundamental behaviors, such as the quantum hall effect (QHE) and fractional quantum hall effect(FQHE).

2.4.1 Classical magnetotransport

Conductivity measurement in a weak magnetic field is an effective tool to characterize the semiconducting system, as it provide the carrier density n and the mobility μ individually, whereas the conductivity only derives their product $\sigma \sim n\mu$. This can be shown if we assume that an electron, after scattering, receives its momentum due to the external field and looses it completely at the next scattering:

$$\frac{m\mathbf{v}_d}{\tau_m} = e[\mathbf{E} + \mathbf{v}_d \times \mathbf{B}] \tag{2.64}$$

where v_d is the drift velocity of the electrons. After some calculations we obtain a resistivity as a second-order tensor:

$$\mathbf{E} = \rho^{[2]}\mathbf{J} \tag{2.65}$$

where

$$\rho_{xx} = \sigma^{-1} \tag{2.66}$$

and

$$\rho_{yx} = -\rho_{xy} = \frac{\mu B_z}{\sigma} = \frac{B_z}{en} \tag{2.67}$$

We derived the longitudinal and the Hall resistances in the Drude model. These values can be measured in a sample with 2DEG in a Hall bar configuration (see Figure 2.11)

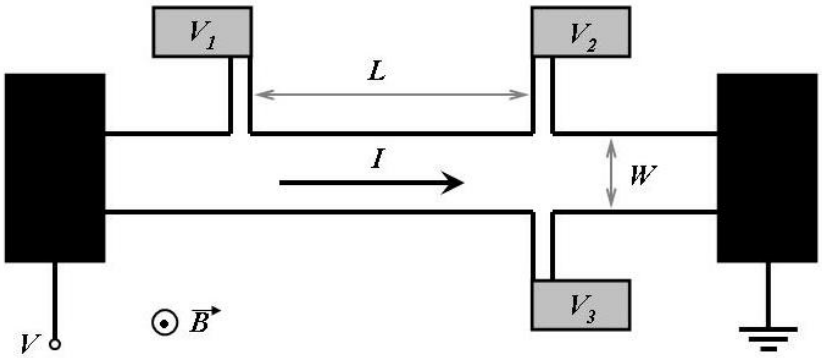

Figure 2.11: Hall bar configuration for magnetoresistance measurements.

Where the longitudinal voltage drop is $V_x = (V_1 - V_2)$ and the Hall voltage drop is $V_H = (V_2 - V_3)$. Hence from the equation 2.65:

$$E_x = \rho_{xx} J_x \quad \text{and} \quad E_y = \rho_{yx} J_x$$

Taking into the account the configuration of the sample wee can express the resistivity as:

$$\rho_{xx} = \frac{V_x W}{IL} \quad \text{and} \quad \rho_{yx} = \frac{V_H}{I}$$

Thus we can derive the carrier concentration n and the mobility μ from the equations 2.66 and 2.67 :

$$n = \frac{IB}{eV_H} \tag{2.68}$$

$$\mu = \frac{IL}{enV_x W} \tag{2.69}$$

The Drude model predicts that the longitudinal resistance is constant and the Hall resistance increases linearly with the magnetic field. This prediction holds quite well at low magnetic fields, however at high magnetic fields in low temperatures were observed oscillations of the longitudinal resistivity, called Shubnikov-de Haas oscillations, and the Hall resistance exhibits plateaus corresponding to the minima in the longitudinal resistance. Understanding of these features involves the quantum effects such as formation of Landau levels.

2.4.2 2DEG under quantizing magnetic field

We consider a 2D rectangular conductor in a constant magnetic field applied perpendicular to the plane of the conductor. We assume that the carrier concentration is low enough, thus they occupy only the first electronic z–subband with energy ε_z which will be omitted in the further calculations. Schrödinger equation for this system in the effective mass approximation is:

$$\left[\frac{(i\hbar \bigtriangledown + e\mathbf{A})^2}{2m^*}\right]\Psi(x,y) = E\Psi(x,y) \tag{2.70}$$

where $\mathbf{A}$ is a vector potential of the magnetic field, which in the Landau gauge is expressed as:

$$A_x = -By \quad \text{and} \quad A_y = 0$$

Performing the substitution $p_x \equiv -i\hbar\frac{\partial}{\partial x}$ and $p_y \equiv -i\hbar\frac{\partial}{\partial y}$ equation 2.70 can rewritten as:

$$\left[\frac{(p_x + eBy)^2}{2m^*} + \frac{p_y^2}{2m^*}\right]\Psi(x,y) = E\Psi(x,y) \tag{2.71}$$

The solutions of this equation can be expressed in the form of plane waves:

$$\Psi(x,y) = \frac{1}{\sqrt{L_x}}\chi(y)e^{ikx} \tag{2.72}$$

where L_x is the length of the system and the function $\chi(y)$ satisfies the equation:

$$\left[\frac{(\hbar k + eBy)^2}{2m^*} + \frac{p_y^2}{2m^*}\right]\chi(y) = E\chi(y) \tag{2.73}$$

The last one can be rewritten in the form:

$$\left[\frac{p_y^2}{2m^*} + \frac{1}{2}m^*\omega_c^2(y + y_k)^2\right]\chi(y) = E\chi(y) \tag{2.74}$$

where

$$y_k \equiv \frac{\hbar k}{eB} \quad \text{and} \quad \omega_c = \frac{eB}{m^*} \tag{2.75}$$

Equation 2.74 is the equation of the harmonic oscillator centered at $y = -\frac{\hbar k}{eB}$ and not at $y = 0$ as it was for 1D system with the parabolic confining potential (eq. 2.30). Hence the eigenfunctions and eigenenergies are similar to the equations 2.31, 2.32:

$$\chi_{n,k}(y) = u_n(q + q_k) \tag{2.76}$$

$$E(n,k) = \left(n + \frac{1}{2}\right)\hbar\omega_c\ , \quad n = 0, 1, 2, ... \tag{2.77}$$

$$\text{where} \quad q = \sqrt{m^*\omega_c/\hbar}y \quad \text{and} \quad q_k = \sqrt{m^*\omega_c/\hbar}y_k$$

States with different n belong to the different magnetic subbands, which are spaced equidistantly by $\hbar\omega_c$ (see Figure 2.12).

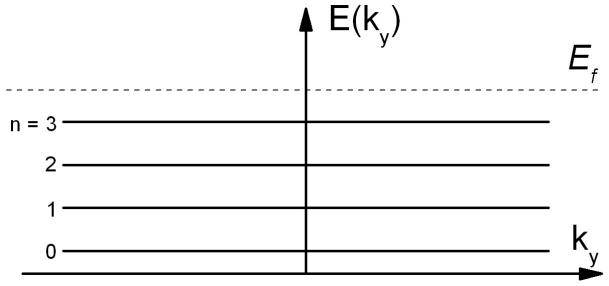

Figure 2.12: Dispersion relation $E(k)$ for Landau levels (magnetic subbands) in 2DEG.

The description is similar to the one-dimensional system with the parabolic confining potential except the fact that the energy is independent of k, which leads to a velocity $v(n,k) \sim \partial E/\partial k = 0$ associated with these states and not $\hbar k/m^*$ as it was for electrical subbands. Thus wave-functions $\chi_{n,k}$ are localized along the y direction near the $y = y_k$ values. And if we construct a wave-packet localized in x it would not move. This reminds us a solution for electron in magnetic field from classical dynamics, where electrons execute a circular movements in $x-y$ plane and don't move in any particular direction.

Hence the presence of the magnetic field splits the 2DEG subbands with constant DOS into discrete Landau levels. The number of states in one Landau level (degeneracy of the Landau level) can be calculated if we remind that the allowed k values are spaced by $2\pi/L$, so the corresponding wave-functions are spaced along y direction by:

$$\Delta y_k = \frac{\hbar\Delta k}{eB} = \frac{2\pi\hbar}{eBL}$$

To obtain the whole number of states we can divide width of the sample W by Δy_k (taking spin into the account):

$$N = \frac{eBS}{\pi\hbar}, \text{ so the degeneracy is:} \quad n = \frac{N}{S} = \frac{eB}{\pi\hbar} \tag{2.78}$$

Thus we can write the DOS for 2DEG in a perpendicular magnetic field as:

$$N(E,B) = \frac{eB}{\pi\hbar}\sum_n \delta\left[E - \left(n + \frac{1}{2}\right)\hbar\omega_c\right] \tag{2.79}$$

2.4.3 Toward 1D conductor under high magnetic field

Now we consider the same system as in previous section 2.4.2 additionally confined by a parabolic potential $U(y) = \frac{1}{2}m^*\omega_0 y^2$. We start from the equation 2.73 we and add the potential:

$$\left[\frac{(\hbar k + eBy)^2}{2m^*} + \frac{p_y^2}{2m^*} + \frac{1}{2}m^*\omega_0 y^2\right]\chi(y) = E\chi(y) \tag{2.80}$$

and rewrite it in the form of a one-dimensional Schrödinger equation with a parabolic potential:

$$\left[\frac{p_y^2}{2m^*} + \frac{1}{2}m^*\frac{\omega_0^2\omega_c^2}{\omega_{c0}^2}y_k^2 + \frac{1}{2}m^*\omega_c^2\left[y + \frac{\omega_c^2}{\omega_{c0}^2}y_k\right]^2\right]\chi(y) = E\chi(y) \tag{2.81}$$

where $\omega_{c0}^2 = \omega_c^2 + \omega_0^2$

Thus, the eigenfunctions and eigenenergies are given by:

$$\chi_{n,k}(y) = u_n\left(q + \frac{\omega_c^2\omega_{c0}^2}{q}_k\right) \tag{2.82}$$

$$E(n,k) = \frac{1}{2}m^*\frac{\omega_0^2\omega_c^2}{\omega_{c0}^2}y_k^2 + \left(n + \frac{1}{2}\right)\hbar\omega_{c0} \tag{2.83}$$

$$\text{where} \quad q = y\sqrt{m^*\omega_{c0}/\hbar} \quad \text{and} \quad q_k = y_k\sqrt{m^*\omega_{c0}/\hbar}$$

and the velocity:

$$v(n,k) = \frac{1}{\hbar}\frac{\partial E(n,k)}{\partial k} = \frac{\hbar k}{m^*}\frac{\omega_0^2}{\omega_{c0}^2} \tag{2.84}$$

The dispersion relation $E(n,k)$ (Figure 2.13) shows the appearance of the magneto-electric subbands. We can notice that the ratio

$$\frac{\omega_0^2}{\omega_{c0}^2} = \left(1 + \frac{\omega_c^2}{\omega_0^2}\right)^{-1}$$

governs the transformation of the magneto-electric subbands to purely magnetic subbands when $\omega_0 \ll \omega_c$ or to purely electric subbands for $\omega_c \ll \omega_0$.

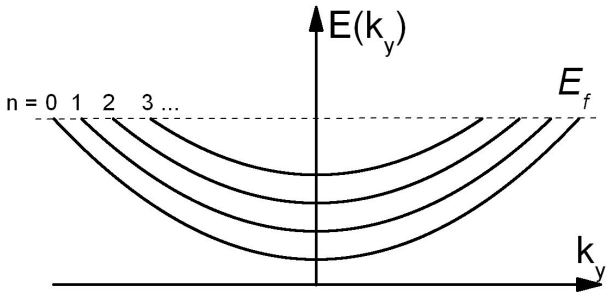

Figure 2.13: Dispersion relation $E(k)$ for magneto-electric subbands in a parabolic potential.

So at the first glance, it seems that the effect of the magnetic field can be taken into account through the increase of the effective electron mass:

$$m^* \longrightarrow m^* \left(1 + \frac{\omega_c^2}{\omega_0^2}\right)$$

making the subbands more flat as B increases. It can also be noticed that the presence of the magnetic field influences the location of the electronic wave-function. From the previous section (2.4.2) we saw that the magnetic field affects the wave-function corresponding to a state (n,k) in the same way as a parabolic confinement potential with center $y = -y_k$, thus localizing it in the y direction near y_k. Using the definition (Eq. 2.75) $y_k \equiv (\hbar k)/(eB)$, if we substitute $\hbar k$ from equation 2.84 it comes:

$$y_k = v(n,k)\frac{m^*}{eB}\frac{\omega_{c0}^2}{\omega_0^2} = v(n,k)\frac{1}{\omega_c}\frac{\omega_0^2 + \omega_c^2}{\omega_0^2} \tag{2.85}$$

We derived that the location of the wave-function is proportional to its velocity. Thus the presence of the magnetic field shifts the states carrying the current in x direction to one side of the sample and states carrying the current in the opposite direction to another side of the sample. This spatial gap in the y direction between the forward and backward propagating states increases with the field (Figure 2.14).

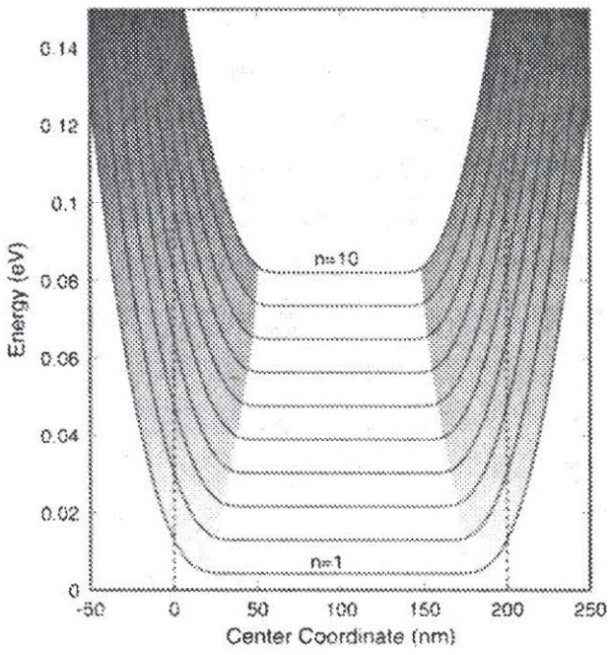

Figure 2.14: Calculated energy versus center coordinate x_0 for a 200-nm-wide wire and a magnetic field intensity of 5 T. The shaded regions correspond to skipping orbits associated with edge state behavior. Taken from [Ferry 1997].

At the boundaries of the wire, we see the increase of the DOS, while at the middle of the wire (approximately 50–150 nm) the energy states are broadly dispersed and the corresponding values of k vectors are close to zero. Thus, the current is carried by only the edge states. This again reminds us the solution from classical mechanics, where the Lorentz force $e\mathbf{v} \times \mathbf{B}$ is opposite for the electrons moving in opposite directions, leading to the appearance of the Hall voltage across the sample.

2.4.4 Magneto size effects

According to the Drude formula the longitudinal resistivity is independent of the magnetic field. This starts to be violated once the size of the system becomes comparable with the magnetic length $L_B = \sqrt{\frac{\hbar}{eB}}$. This size effect can be illustrated using a classical approach. Consider a ballistic 2D system with a width W and diffuse boundary scattering (Figure 2.15).

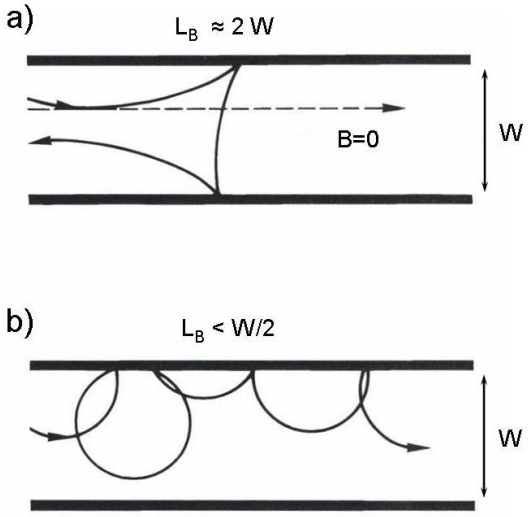

Figure 2.15: Illustration of the effect of a magnetic field on motion though a channel with diffuse boundary scattering. a) Electrons which in a zero field move nearly parallel to the boundary can reverse their motion in weak magnetic fields. b) Suppression of back scattering at the boundaries in strong magnetic fields. Taken from [Beenakker 1991].

At low magnetic field ($L_B \sim 2W$), the curvature of electron trajectories are large and the diffuse reflection at the sample border can enhance the backscattering processes (Figure 2.15a) and therefore we observe the positive magnetoresistance. At high magnetic field ($L_B < W/2$), the small curvature radius combined with the diffuse reflection results in the suppression of the backscattering (Figure 2.15b) and leads to a negative magnetoresistance.

In the same classical approach we can discuss a negative magnetoresistance in a diffusion transport regime - figure 2.16.

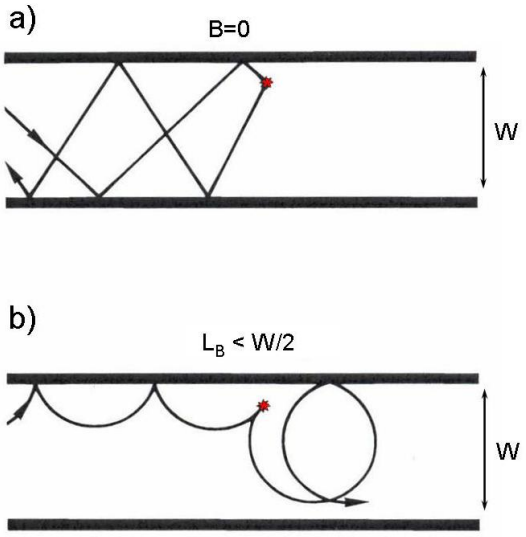

Figure 2.16: Electron trajectories in a 2D channel with specular boundary scattering with one isolated diffusive center close to a boundary. a) Backscattering effect in zero magnetic field. b) Illustration of the backscattering suppression induced by the strong magnetic field. Taken from [Beenakker 1991].

It is notable, that in the presence of a magnetic field the positions of the impurities should be taken into account with respect to the channel boundaries. An increase of the magnetic field ($L_B \leq W/2$) "excludes" the contribution of the impurities to the scattering process, if they are close to the boundaries. Thereby we can say that magnetic field forms the conducting channels along the edges of the sample.

This reminds us the solution obtained in the previous section 2.4.3, when we saw that the magnetic field separates the states carrying the current along the sample to the opposites sides of the sample according to the current direction (Figure 2.14).

2.4.5 Suppression of weak localization by a magnetic field

In section 2.4.4 we discussed the negative magnetoresistance in the classical approach. Here we will examine the case of the coherent transport, when l_φ is not negligible compared to system length L. We recall that in zero magnetic field the conductance value in the weak localization regime is lover than conductance value in the ballistic regime by δG:

$$\delta G \sim \frac{e^2}{h} \left(\frac{l_\varphi}{L} \right)^{3/2} \tag{2.86}$$

The cause of this effect is the constructive interference of the clockwise and anticlockwise propagating waves in a closed-loop trajectory (Figure 2.17).

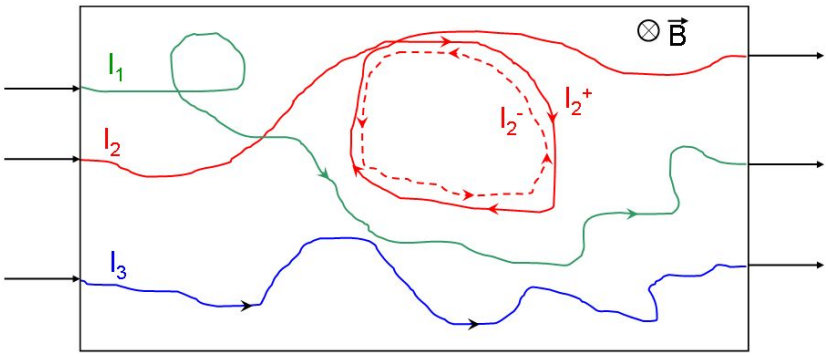

Figure 2.17: Schematic electron diffusion in a disordered system. The curves represent different electron trajectories with (l_1, l_2) and without (l_3) closed-loop regions. For the trajectory l_2 the clockwise (l_2^+) and the anticlockwise (l_2^-) propagations are shown.

Now, as we apply a magnetic field, the electron momentum should we written as:

$$\mathbf{p} = \hbar\mathbf{k} - e\mathbf{A} \tag{2.87}$$

Hence the acquired phase difference for clockwise (+) and anticlockwise (-) propagation around the close loop is:

$$\Delta\varphi = \frac{1}{\hbar}\left(\oint_+ \mathbf{p}^+ d\mathbf{l} - \oint_- \mathbf{p}^- d\mathbf{l}\right) = \frac{2e}{\hbar}\int(\bigtriangledown \times \mathbf{A})d\mathbf{S} = \frac{2eBS}{\hbar} \equiv \frac{2S}{L_B^2} \equiv 4\pi\frac{\Phi}{\Phi_0} \tag{2.88}$$

where L_B is a magnetic length, $\Phi_0 \equiv h/e$ is an elementary quantum flux and S is an area enclosed by the closed-loop trajectory. Thus, the constructive interference of these wave is broken and the weak localization is suppressed. Further increase of the magnetic field affects the phase difference and the constructive interference can be restored. Hence we will see fluctuations of the conductance, which varies from one sample to another, depending on the particular configuration of impurities. A measure for the typical magnetic field scale of these fluctuations is called correlation field B_c. It can be estimated from the first expression for the acquired phase difference (Eq. 2.88) $\Delta\varphi = 2S/L_B^2$. The largest existing area that can be enclosed by the coherence wave functions is proportional to the l_ϕ^2, thus the magnetic field begins to have a significant effect on the weak localization when $l_\phi \sim L_B$.

Finally, we have four different characteristic lengths for the system: channel width W, mean free path l_e, phase relaxation length l_φ and magnetic length l_B. Depending on the relative magnitude of this lengths we can distinguish different regimes listed in the Table 2.1 [Beenakker 1991]

	Dirty metal ($l_e \ll W$)		Pure metal ($l_e \gg W$)	
Cond. regime	2D ($l_\varphi \ll W$)	1D ($l_\varphi \gg W$)	1D weak field ($L_B^2 \gg W l_e$)	1D strong field ($W l_e \gg L_B^2 \gg W^2$)
B_c	$\frac{\hbar}{e}\frac{1}{2l_\varphi^2}$	$\frac{\hbar}{e}\frac{\sqrt{3}}{W l_\varphi}$	$\frac{\hbar}{e}\frac{1}{W}\sqrt{\frac{C_1}{W v_f l_\varphi}}$	$\frac{\hbar}{e}\frac{C_2 l_e}{W^2 v_f l_\varphi}$

Table 2.1: Magnetic characteristic field B_c for the weak localization suppression in different regimes.

For all cases, we assume a channel length $L \gg l_\varphi$, channel width $W \gg \lambda_f$ and $l_\varphi \gg l_e$. The constants are given by $C_1 = 9.5$ and $C_2 = 24/5$ for specular boundary scattering, and $C_1 = 4\pi$ and $C_2 = 3$ for diffusive boundary scattering. For pure metals, the case $L_B < W$ is out of the diffusive transport regime for weak localization.

2.4.6 Influence of the 1D band structure on the conductance of the system.

Large research efforts have been made to analyze the electronic transport properties of 1D systems [van Wees 1988, Bogachek 1993, Bogachek 1994, Bogachek 1996, Scherbakov 1996, Debald 2005, Tserkovnyak 2006]. In the absence of magnetic field and if one neglects the coherence effects, the conductance of a confined system, like a conductance of a NW, is defined by the Landauer formula:

$$G = \frac{2e^2}{h} NT \tag{2.89}$$

It depends on the transmission probability T and on the number of propagating modes N, which is determined by the cross-section of the NW. Thus, assuming a ballistic transport regime, the conductance is quantized in $2e^2/h$ units when the cross-section is varied.

The effect of the magnetic field on the conductance can be taken into account as a time independent perturbation of the system through the Kubo formula [Kubo 1966]. In this approach the conductance can be written as:

$$G(E_f, B) = \frac{2e^2}{h} D(E_f, B) DOS(E_f, B) \tag{2.90}$$

In a weak magnetic field the magnetoconductivity is mainly governed by the diffusion coefficient $D(E_f, B)$. In the high magnetic field regime ($\sqrt{\hbar/eB} \ll W$ - system width), the modulation of the density of states at the Fermi energy may significantly impact the magnetoconductivity. For example, a shift of the electronic energy levels under the influence of an applied magnetic field may lead to significant

changes in the conductance. Bogachek et al. [Bogachek 1993, Bogachek 1994] predicted a step-like variations of the conductance in longitudinal magnetic field. These calculations were performed for relatively wide wires, characterized by a large number of conducting channels. The step-like structures on the magnetoconductance smothed by the temperature (Figure 2.18), track the number of conducting channels at E_f.

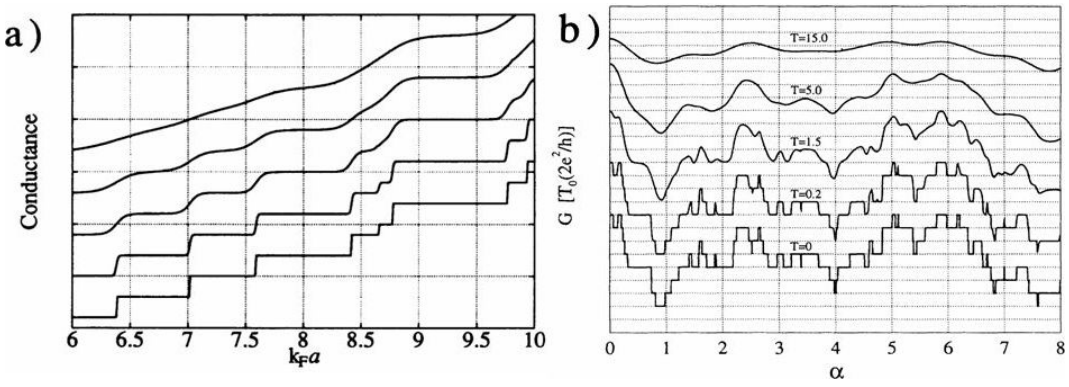

Figure 2.18: a) Conductance as a function of $k_f a$ (a is the NW diameter, k is a momentum along the NW axis) at different temperatures $T = 0, 0.1, 0.5, 1.0, 1.5$ and 2.0 (in unites of $\hbar^2/(m^* a^2 k_B)$), from [Bogachek 1994]. b) Conductance as a function of normalized magnetic flux ($\alpha = \Phi/\Phi_0$) through the NW at different temperatures $T = 0$, 0.2, 1.5, 5.0 and 15.0 (in unites of $\hbar^2/(m^* a^2 k_B)$). From [Bogachek 1993].

It was predicted that, at low temperatures sharp modulations should appear on the scale of a fraction of a flux quantum Φ_0, a new scale for mesoscopic phenomena. These sharp conductance steps (Figure 2.18b) are caused by the shift of electronic levels through the Fermi level in a magnetic field. Thus, the scale of this phenomena is related to the separation of energy levels in the system. At finite temperature these steps are broadened and will be smoothed when kT becomes comparable with the average energy level spacing. As expected the conductance steps are broadened at finite temperatures, as can be seen in Figs. 2 and 3. The temperature scale for the broadening is related to the average energy level spacing.

At low doping levels, Bogachek et al. [Bogachek 1996] predicted a magnetic switch effect and the occurrence of a magnetic quench of the quantum transport in nanowires (Figure 2.19a).

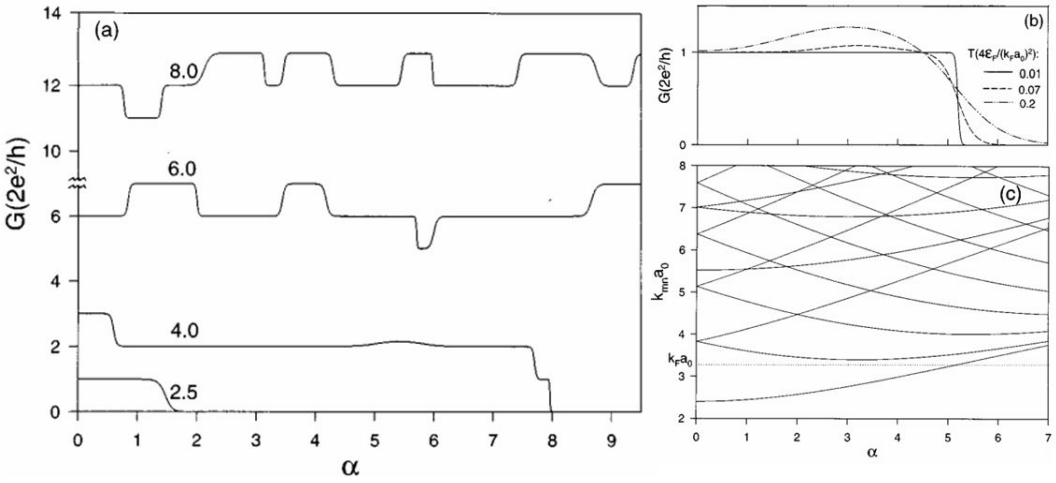

Figure 2.19: a) Conductance of a NW as a function of normalized magnetic flux ($\alpha = \Phi/\Phi_0$). The different curves correspond to the marked values of $k_f a_0$ (a_0 is the NW diameter). b) Conductance of a NW versus α for $k_f a_0$=3.3 for different temperatures, measured in $4E_f/(k_f a_0)^2$ units. c) Dependence of the electromagnetic subbands ($k_{mn}^2 = 2m^* E_{mn}(a_0)/\hbar^2$) versus α. The dotted line corresponds to $k_f a_0$=3.3. From [Bogachek 1996].

The two lower curves on the figure 2.19a ($k_f a_0$=2.5, 4.0) reveal a conductance quench, since all the electromagnetic subbands crossed the Fermi level due to the magneto-induced shift toward higher energies. The conductance modulations on the two upper curves ($k_f a_0$=6.0, 8.0) occur due to changes in the number of electromagnetic subbands crossing the Fermi level. Additionally, using the band structure calculation, another effect has been predicted: the enhancement of the magnetoconductance along with the increase of the temperature under appropriate conditions (Figure 2.19b,c). This effect originates from the thermally activated increase of the transmission probability of a quantum channel located above the Fermi level.

These theoretical investigations unveil the direct link between the magnetoconductance behaviour in the high field regime and the electronic band structure.

2.4.7 Conclusion

In this section, the influence of the magnetic field on the transport properties of mesoscopic systems was described. Started from the classical Drude model, we presented the band structure of the 2D and 1D under magnetic field, where it can be considered as an additional confinement of the system. The application of the magnetic field suppresses weak localization in the system, once it exceeds the values of the correlation magnetic field B_c. The B_c value depends on the purity of the system (pure and duty metal limit) and express differently for coherent and

noncoherent regimes. The following increase of the magnetic field causes strong modifications of the band structure, which influence the conductance of the system. These band structure modifications lead to conductance modulations followed by the conductance quench at high magnetic field.

Chapter 3

Experimental methods

Sommaire

In this chapter, we present the sample fabrication process and the experimental techniques that have been used to study the electronic properties of individual nano-objects. The are several difficulties related to the electric contacts, which should provide an ohmic behaviour and must present good mechanical characteristics. In addition, nano-objects are very sensitive to electric discharges, thus, once connected, all further manipulations require special protection of the sample. These issues will be discussed in this chapter.

3.1 Device fabrication and characterization

During the work on this thesis, more than 60 samples were produced and characterized. The most part of the samples fabrication was done in the clean room of the Laboratory for Analysis and Architecture of Systems (LAAS) with the invaluable help of the LAAS technical staff.

3.1.1 InAs nanowires

In the present work, we have studied the transport properties of the InAs NWs with two different diameters: 30 nm and 80 nm.

30 nm diameter nanowires. The 30 nm diameter NWs were manufactured and electrically contacted by Renaud Leturcq and Philippe Caroff from Institut d'Electronique, de Microelectronique, et de Nanotechnologie (IEMN). InAs nanowires, grown by Au-assisted metal organic vapor phase epitaxy, were provided in a FET configuration: deposited on a Si/SiO_2 substrate connected by the Ti/Au (10nm/100nm) contacts. The distance between the electrodes is 380 nm and the thickness of the SiO_2 layer (l_{ox}) is 310 ± 5 nm. According to the TEM observations NWs are monocrystals of wurtzite crystallographic structure with <0001> growing direction. The preliminary measurements of the conductance versus gate voltage reveal the unipolar n-type behaviour. For more details, see [Pfund 2006].

80 nm diameter nanowires. The 80 nm diameter NWs were manufactured and electrically contacted by Lucia Sorba and colleagues from NEST laboratory of Istituto Nanoscienze CNR and Scuola Normale Superiore. InAs nanowires have been grown by Chemical Beam Epitaxy (CBE) in a Riber Compact-21 system by Au-assisted growth on InAs(111)B substrates. Trimethylindium $In(CH_3)_3$ (TMIn) and tertiarybutylarsine $AsH_2(CH_3)_3$ (TBAs) were employed as metal-organic (MO) precursors for InAs growth. The InAs segment was grown for 90 min at a temperature of $(430 \pm 10°C)$, with MO line pressures of 0.3 and 1.0 Torr for TMIn and TBAs, respectively. Subsequently, samples were prepared in a FET configuration on a Si/SiO_2 ($l_{ox} = 300nm$) substrate via e-beam lithography. Electrodes made of Ti/Au (10nm/100nm) and were spaced by 600 nm. The wire diameters were estimated by SEM to be about 80 nm. For more details, see [Heun 2010].

3.1.2 Peapod fabrication process

The peapods were fabricated by the process discovered by M. Monthioux in 2002 [Monthioux 2002]. First, SWCNTs are passed through a purification step: various procedures of acid treatments (HCl, HNO_3, H_2SO or theirs mixes), assisted by cross-flow filtration and sonication. The major goal of this step is to remove catalyst particles and impurity carbon phases such as amorphous carbon, polyaromatic shells and graphite particles. At the same time, during the purification, the SWCNTs are opened, removing their caps as demonstrated by Monthioux et al. [Monthioux 2001]. Then open SWCNTs and fullerene material are inserted into glass ampoule, sealed under vacuum, and heat-treated beyond the fullerene sublimation temperature during 24h. Capillary forces pull C_{60} inside the SWCNT, creating peapods (Figure 3.1).

This method is specifically well adapted to prepare C_{60} peapods due to the rather low sublimation temperature of fullerenes ($\sim 350°C$) and the exceptional thermal stability of the isolated C_{60} molecules ($\sim 3000 - 4000\ K$) [Dresselhaus 1995].

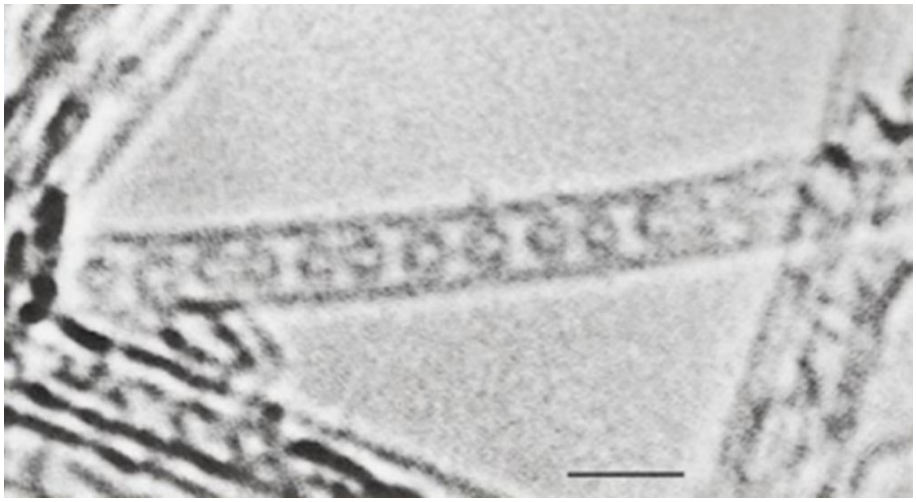

Figure 3.1: HRTEM image of SWCNT containing a row of C_{60} fullerenes concentric with the tubule axis. Scale bar, 2.0 nm. [Monthioux 2001])

The fabrication process is successful since the filling rate reaches almost 100% [Hirahara 2000]. The resulting peapods are subjected to an $800°C$ heat treatment in vacuum for 1 h, in order to remove the excess fullerenes.

The C_{60} peapods for our experiments were provided by the research group of Marc Monthioux from the Centre d'Elaboration de Matériaux et d'Etudes Structurales (CEMES), in a form of suspension with sodium dodecyl sulfate (SDS) surfactant.

3.1.3 Substrate preparation and deposition

As back gate of the peapod-based FET, we used n-doped silicon substrate with an approximate carrier concentration $n \approx 10^{21} cm^{-3}$, which gives a resistivity on the order of several $m\Omega/cm$, as a back gate. For this purpose, it is covered with 300 nm of thermally oxidized SiO_2 layer.

The first step is a photo-lithography on a four-inch Si/SiO_2 substrate in order to define large contacts and to create reference marks for the e-beam lithography. Following development, metallization and lift-off processes determine 161 areas of the 6×6 mm size with nine contact zones inside, with twelve contacts in each zone (Figure 3.2). The contacts consist of two metallic layers: Cr 10 nm as an adhesive layer and Au 40 nm. Below we refer to these contacts as to macroelectrodes. Then the four-inch substrate is diced into the 6×6 mm areas, which are ready for the sample deposition.

Prior to deposition, nano-objects are usually put into solution. Solvent should be chosen in accordance with the type of the nanomaterial, taking into account such parameters as viscosity, solubility, surface tension, hydrophobicity or hydrophilicity of the nano-objects, etc. Due to the Van der Waals forces, nano-particles tend

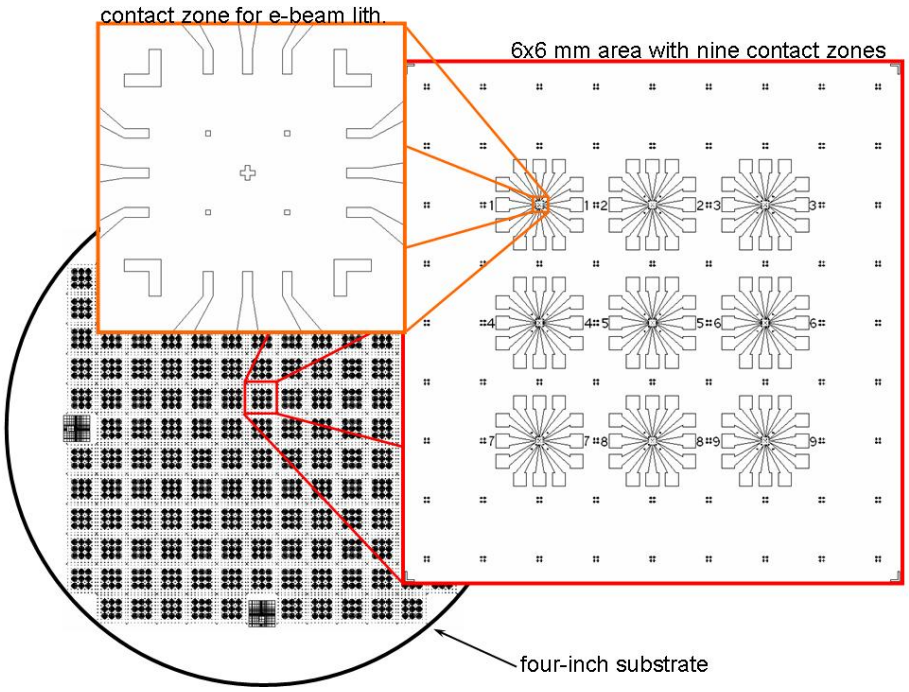

Figure 3.2: Four-inch substrate consist of 161 areas of the $6 \times 6mm$ size with nine contact zones inside, each zone have twelve macroelectrodes.

to stick together and form big clusters. There are several techniques to create a homogeneous suspension and thus achieve isolated individual nano-objects after deposition. The most widely used are the ultrasonic dispersion (sonication) and the use of surfactants. Particularly for the peapods we use SDS surfactant to avoid CNTs bundling.

The suspension is deposited on the substrate in a form of droplet using micropipette, after a short time (∼30 sec.) the substrate is rinsed with ethanol and a flow of nitrogen. This cleaning process does not remove nano-particles, as they stick to the substrate by Van der Waals forces. Then, individual nano-objects are detected using atomic force microscope (AFM), in case of peapods, or using scanning electron microscope (SEM), in case of nanowires (see section 3.1.5). In addition, the peapods chosen for the transport experiment are studied by micro-Raman spectroscopy to ensure that we are working with a single object and not with a bundle (see section 3.3).

3.1.4 Electron-beam lithography

Electron-beam lithography is the most widely used technique for nano-device fabrication. It is a lithographic technique where a finely focused electron beam emitted in a patterned fashion across a surface. The surface of the sample is covered with a film of a e-beam-sensitive resist. Subsequent selectively removing of either

exposed or non-exposed regions of the resist (developing procedure) is performed.

In our case, we use polymethylmethacrylate (PMMA) (30 mg/l) as a positive resist. We deposit it on top of the substrate by spin coating with a resulting layer height of 300 nm. E-beam lithography is performed by the "Raith 150" lithography system. In general, the exposure time or the rate of e-beam lithography in strongly dependent on the substrate material, type of the resist and geometry of the contacts.

In order to calibrate the system for our samples we performed multiple tests, varying the width of the contacts (resolution correction), distance between them (shadow effect correction) and angle orientation (astigmatism correction). As a result, we are able to create 200 nm-thick contacts spaced by 300 nm. Exposing time and geometry are taken into account in the contact design made by the AutoCAD software application (see Figure 3.3).

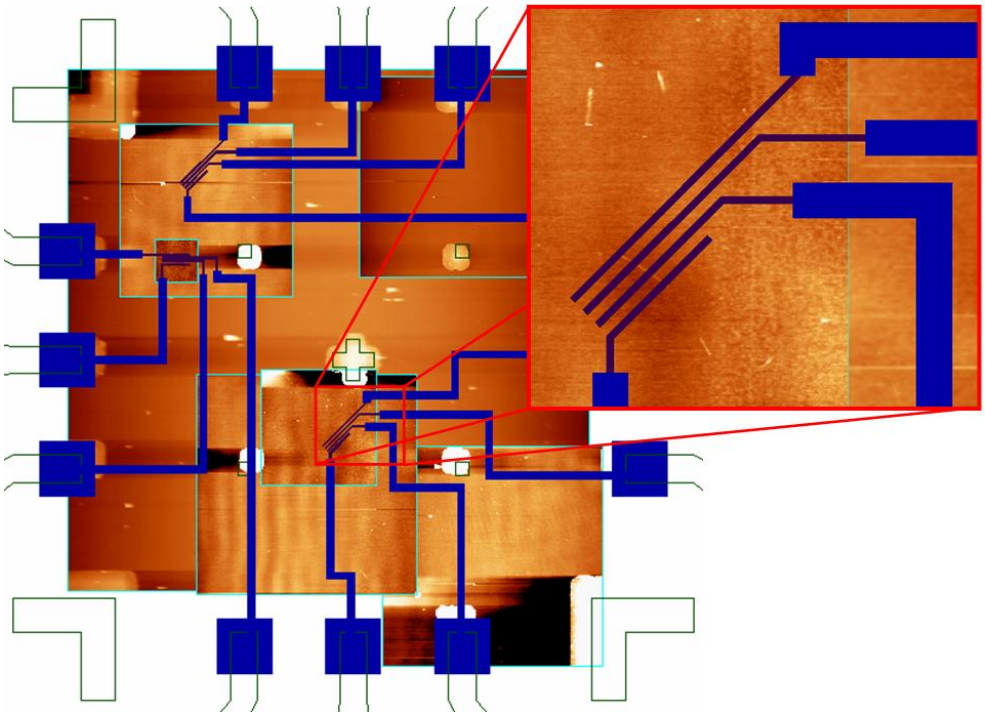

Figure 3.3: Snapshot of a contact design with aligned AFM images. Filled rectangles are the contacts to be defined by e-beam lithography. Different colors correspond to the different exposition doses (blue – 280 $\mu A/cm^2$, violet – 336 $\mu A/cm^2$). The zoomed part presents an AFM image of the individual peapod that will be crossed by four contacts.

After e-beam lithography, the exposed parts of the PMMA polymers are chopped up and thus start to be solvable with mix of methyl isobutyl ketone and isopropyl alcohol. Metallization is made in a vacuum chamber where a chosen type of metal is heated up until it evaporates. This evaporated metal then condenses on the

substrate as a thin metallic film. The metal for the contacts is chosen in order to obtain a weak Schottky barrier. The height of the metallic film should be less than one third of the PMMA thickness to ensure the disconnection of the contact areas from the other part of the metallic layer (see Figure 3.4). For the peapods we use a 50 nm-thick layer of Pt and, for the InAs nanowires a 10 nm-thick layer of Ti, which plays the role of an adhesive layer, followed by a 100 nm-thick layer of Au.

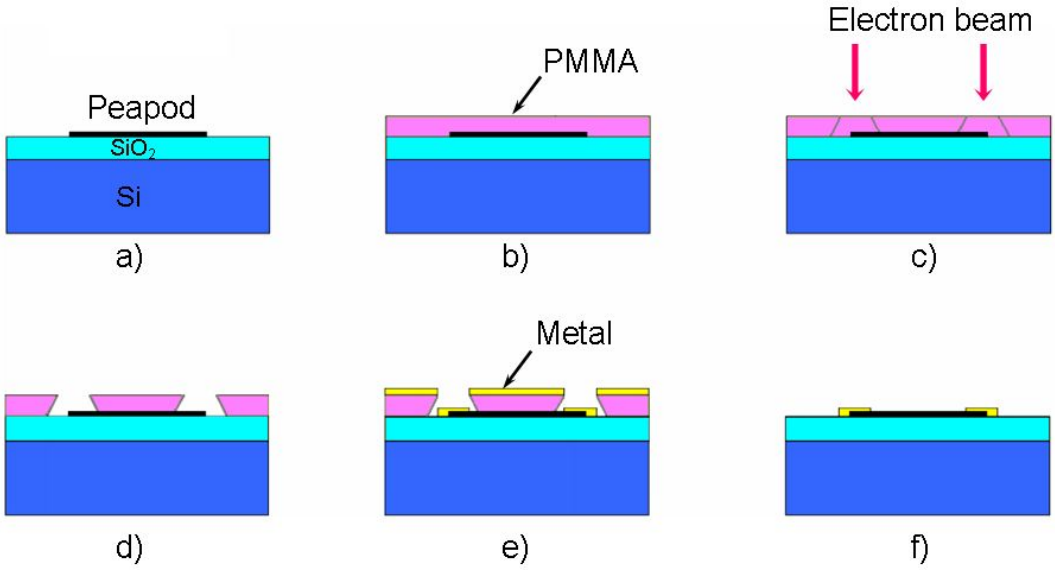

Figure 3.4: Sketch of the e-beam lithography with positive resist following by lift-off process: a) sample deposition, b) PMMA spin coating, c) e-beam exposition, d) PMMA developing, e) metallization, f) lift-off.

The lift-off process is made by immersing the sample into the thrichloroethylene heated up to 60^oC for several minutes. Then the sample is rinsed with acetone, alcohol, deionized water and a flow of nitrogen. The result can be controlled by optical microscopy. This procedure shall be repeated until the PMMA is completely removed from the substrate.

The final step is a rapid thermal annealing in order to passivate the contacts and thus to improve their quality. It is carried out at $300°C$ for three minutes in the gas mixture H_2 (5%) and N_2 (95%). Created contacts, which make the connection between a nano-object and macroelectrodes, will be referred below as microelectrodes. A schematic peapod device is shown in Figure 3.5.

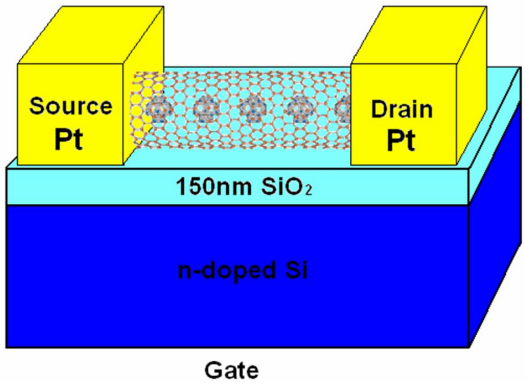

Figure 3.5: Schematic drawing of the substrate with connected peapod device in FET configuration.

3.1.5 AFM and SEM microscopy

Atomic force microscopy is a high-resolution type of scanning probe microscopy which is used to determine the surface topography. Atomic force microscope (AFM) contains a cantilever with a sharp tip that scans the sample surface (see Figure 3.6). The tip curvature is of the order of several nanometers. As the tip is brought close to the sample, the surface forces between the tip and the samples (such as Van der Waals forces, capillary forces, chemical bonding, electrostatic forces, etc.) deflect the cantilever. This deflection is measured using a laser spot reflected from the cantilever's top surface into a photodetector. Feedback mechanism is employed to maintain a constant tip-to-sample distance and thus to avoid the collision of the tip with the surface. The sample is mounted on a table, which performs the scanning in the $x - y$ plane by piezoelectric motors. The cantilever is placed on top of the sample and is governed by piezoelectric motor in the z direction. The resulting map of the area $z = f(x, y)$ represents the topography of the sample. AFM can be operated in a number of modes, depending on the application. We use the close-contact (tapping) mode where the cantilever is oscillating with a frequency close to its resonant frequency. The deviations from this value, caused by the sample's surface, are detected by the laser reflection into the four-sector photodetector. The oscillation frequency is controlled by proportional-integral-derivative (PID) control loop feedback. The AFM, used in this work, allows to observe a surface up to $100 \times 100\ \mu m^2$ (which is limited by the linearity of the $x - y$ piezo-motors) with a height resolution of about 1 nm. The lateral resolution is much lower, being limited by the number of pixels in the AFM image.

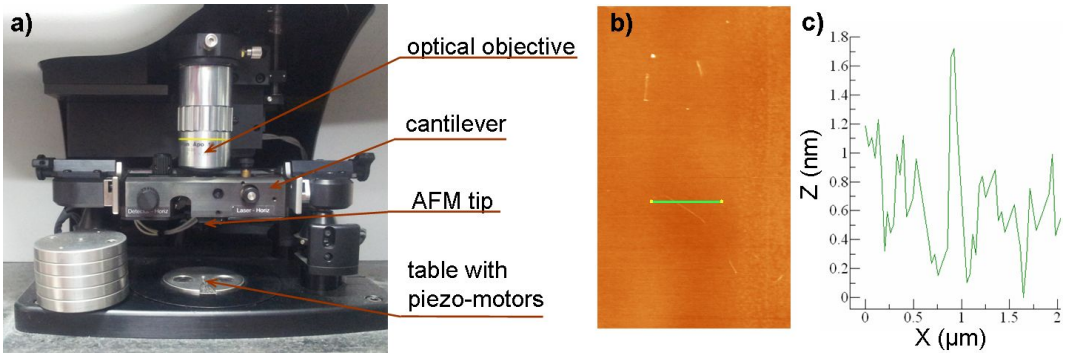

Figure 3.6: a) Atomic force microscope "Pacific Nanotechnology". b)AFM scan plotted with a contrast proportional to the height. The green line indicates the place of the profile – c). Signle peapod is clearly seen at the contract plot, and its diameter can be estimated as $d = 1.2 \pm 0.3$ nm.

We used AFM as a preliminary test to check the quality of the sample deposition and to locate the peapods. AFM images are used further for the electric contacts design (see section 3.1.4). Since the horizontal resolution of the AFM is much lower than the vertical one, AFM cannot provide information whether the detected object is a single peapod or it is a small bundle of peapods. In order to resolve this issue we used micro-Raman microscopy (see section 3.3). After e-beam lithography we used AFM in order to check the contacts quality and the device configuration.

Another widely used technique to define the position of nano-objects is the electronic microscopy. Scanning electron microscope (SEM) images a sample by scanning it with a beam of electrons in a raster scan pattern. The advantage is that image of a sample can be obtained in several seconds almost as a snapshot, which avoids the non-linearity effects of the AFM images caused by the long scanning time (from 20 to 80 minutes) and by piezo-motors calibration. As disadvantages, we note i) the probability of defect creation by a high power e-beam in the understudy structures; ii) the lack of the image contrast for some pairs substrate–sample. For example, it is impossible to see CNTs on the Si substrate.

3.1.6 Electric micro-connection of the sample

The first test, which should be done before the mounting of the sample on the set-up for the transport measurements, is to check the device's conductance as a function of the gate voltage. A sample may not conduct current for several reasons: bad electric contacts, break-down of the SiO_2 layer, electric disconnection (e-beam misalignment, electric discharge), or mechanical break-down of the nano-object.

This check is performed on the probe station, where the sample is fixed on the movable table, which provides the back gate voltage, and the drain-source voltage is applied through the thin needles contacted to the macroelectrodes. Details of the

conductance measurements will be described in the next section.

After we verified the quality of the sample, we glued it to the ceramic support with golden pads (Figure 3.7) by silver paste. Thus the bottom of the Si substrate is connected with the back-gate contact.

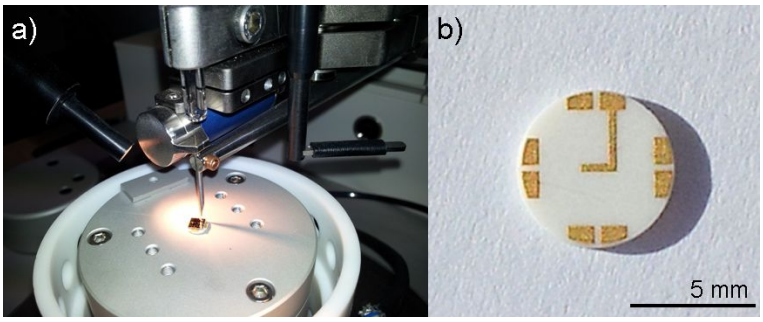

Figure 3.7: a) Bonding machine, b) ceramic support with a gold pads. The 100 μm-diameter golden wires are used for bonding.

We used a bonding machine to make the interconnections between the macro-contacts and gold pads. Further connections to the sample holder are made by golden wires and silver paint. The figure 3.8 presents the insert for the transport measurements. The sample is installed on the rotating plateau surrounded by twelve pins, which are connected by twisted pairs to connectors at the top of the insert. The temperature diode is placed on the plateau near the sample. The magnetic field is measured by a pick-up coil, reeled around the end of the insert.

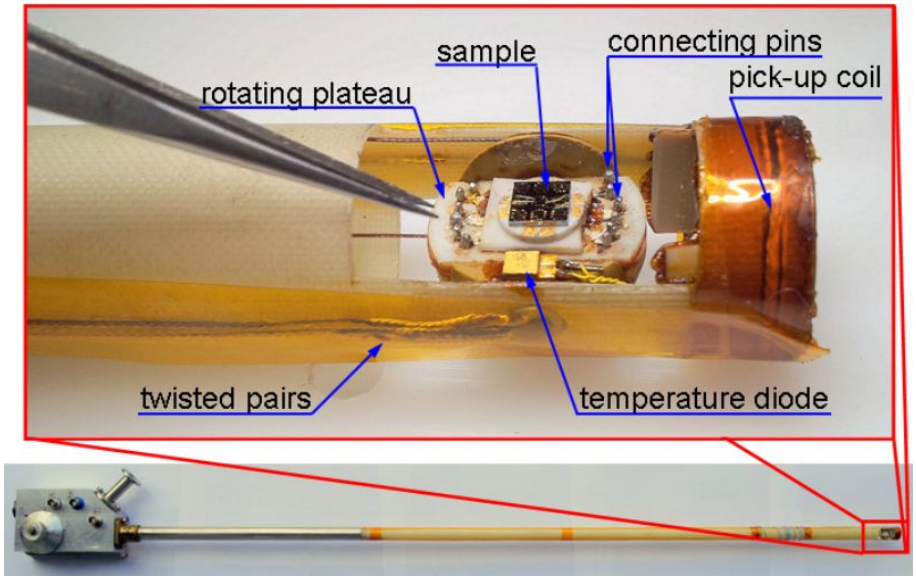

Figure 3.8: Insert for magnetotransport measurements.

The magnetotransport experiments are carried under "pulsed" magnetic fields, thus when establishing electric connections, it is important to avoid wire loops, that feed the induced voltage back into the measurement.

Once the sample is connected, we perform the annealing procedure in order to desorb water and other impurities from the sample surface, which plays the role of an additional sample doping. The sample holder is inserted into hermetic glass tubing and pumped continuously for 24 hours at the temperature $110°C$. The effect of the annealing can be observed as a shift of the conductance curve's $G(V_g)$ minimum toward the zero back gate voltage. Then we fill the volume between the insert and the glass tubing with He gas and insert this system into the cryostat.

For the magnetotransport measurements, it is important to limit use of any metallic details in the set-up, as they may heat the sample environment during the pulse of magnetic field because of induced currents.

3.2 Electronic transport measurements

Transport measurements were performed at the Laboratoire National des Champs Magnétiques Intenses de Toulouse (LNCMI-T).

3.2.1 Generation of high magnetic field

There are three main ways to generate a high magnetic field for experimental purpose:

- the use of resistive, superconducting or hybrid coils to produce a static magnetic field up to 45 Tesla.

- the use of nondestructive resistive coils to produce a pulsed magnetic field up to ∼80–100 Tesla. The pulse time $\Delta\tau_{pulse} \sim 20\ ms$.

- the use of destructive resistive coils to produce an short pulsed ($\Delta\tau_{pulse} \sim 1\ ms$) magnetic field up to 120 Tesla.

- the use of destructive resistive coils with additional external compression to produce an ultra short pulsed (($\Delta\tau_{pulse} \sim 1\ \mu s$)) magnetic field up to 2800 Tesla [Boyko 1999].

According to the research goals one should chose between the needed value of the magnetic field and the duration of the time necessary for the measurements.

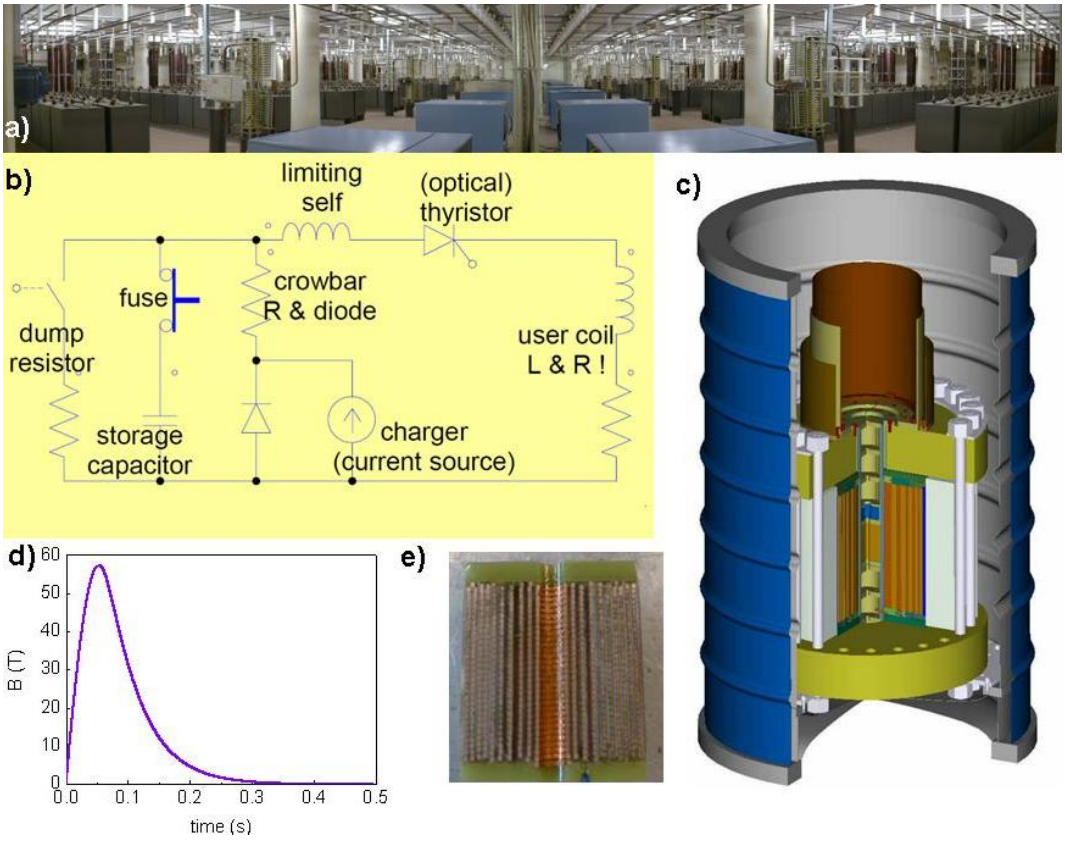

Figure 3.9: a) Capacitor bank at LNCMI-Toulouse. b) General electric scheme for a pulsed magnetic field creation. c) Sectional scheme of the set-up with the coil and the nitrogen cryostat. d) A typical magnetic field pulse profile as a function of time. e) Sectional view of a coil with Zylon reinforcement. Partly taken from [Nanot 2009].

In this work the pulsed magnetic field was produced by nondestructive resistive coil. LNCMI-T has a 14 MJ capacitor bank (Figure 3.9a), which can be charged up to 24 kV. A subsequent fast discharge through the coil creates a pulse of magnetic field with a maximum value of 80 T and duration about ~300 ms. We mainly use them in the 55–60 T regime (Figure 3.9d) in order to reduce the wear and to extend the life-time of the coils. The general electric scheme for a pulsed magnetic field creation is presented on the figure 3.9b.

At such magnetic field values, much attention shall be paid to the reinforcement of the coil. For this purpose, a coil is made of copper-silver alloy winding surrounded by the Zylon strengthening (Figure 3.9e). Another important point is heating of the coil. The resistive coil is placed into the liquid nitrogen (see Figure 3.9c) and inside the coil winding, channels are made to enable nitrogen circulation. The waiting time

between two pulses is about 45 minutes for the fast-cooling coils of latest generation.

An important point in the coil's construction is the usable space – the inner bore of the coil, where the magnetic field is maximal and its distribution is homogeneous. In our experiments we use coils with a 27 mm hole diameter. As we were working at low temperatures, some place inside is used by a helium cryostat, thus the final diameter available for the insert for transport measurements is about 20 mm.

3.2.2 Measurements at zero magnetic field

As discussed in the previous sections, the sample is installed on the rotating plateau at the end of the transport insert, which is surrounded by the glass tubing with exchange gas (He), and inserted into the helium cryostat at the center of the magnetic field. The top of the insert is connected with the measuring stand through a low-pass filter, in order to protect the sample from static electric discharges or voltage jumps.

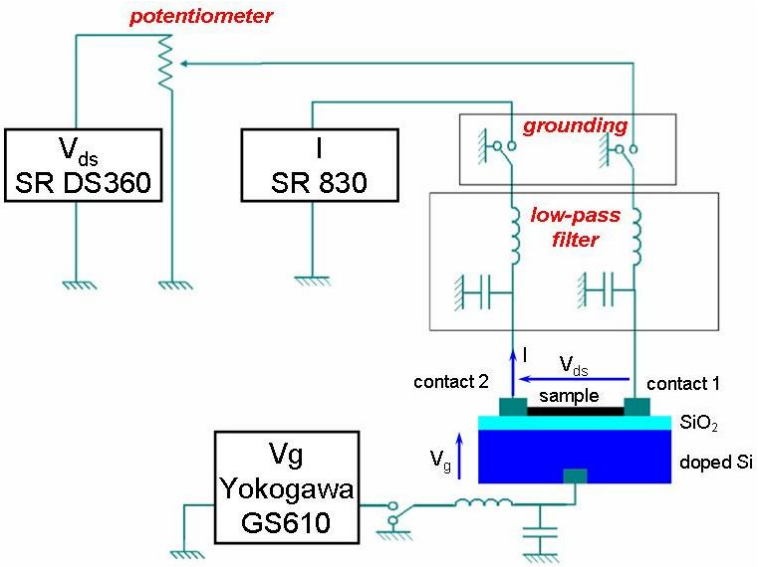

Figure 3.10: General electric schema of transport measurements. Partly taken from [Nanot 2009].

We use the three main types of transport measurements:

– Current versus drain-source voltage $I(V_{ds})$ at different values of the gate voltage (V_g) in order to check the ohmic behaviour of the contacts. For this we use Stanford Reasearch DS360 as a voltage source and Stanford Research SR560 as current amplifier.

– Conductance versus gate voltage $G(V_g)$. Applying the AC drain-source voltage (frequency $\sim$ 30 Hz) we measure the current with the lock-in current amplifier Stanford Reasearch 830. For the gate voltage sweep we use the Yokogawa GS610 voltage source, which allows to sweep from -110 V to 110 V.

– Differential conductance versus gate voltage $dI/dV_{ds}(V_g)$. We apply a DC drain-source voltage combined with relatively low AC voltage (ratio is about the 100), and we measure the differential conductance of the sample using the lock-in current amplifier. The gate voltage sweep, as previously, is made by the Yokogawa GS610 voltage source.

For all measurements we choose the drains-source voltage in order to keep a temperature equilibrium $eV_{ds} < k_BT$ in the system. Temperature during the measurements was controlled by the Lakeshore 330 or 332 using the calibrated silicon diode, placed at the plateau near the sample, and electric heater, winded at the end of the cryostat. Thus, the available temperature range is from 1.8 K to 300 K.

As mentioned above, nano-objects are very sensitive to all kinds of abrupt voltage changes. Thus, to prevent such incidents, we use different safety devices in the measurement's schema (Figure 3.10): potentiometer to ground the sample during the parameters modification, loss-pass frequency filter to cut high frequency voltage peaks during the measurements, and grounded bracelets for the operator's hand to avoid static electricity discharges.

3.2.3 Measurements at high magnetic field

The specificity of magnetotransport measurements is that the time of the experiment is limited by the duration of the magnetic pulse. Thus, the conductivity recording rate shall be much larger than the characteristic variation rate of the magnetic field and the sample conductance $G(B)$. We use two types of transport measurements:

DC. We apply DC drain-source voltage and we measure the current with the current amplifier with high dynamic range. In this case induced currents, which are added to the signal, can be removed during the data treatment using the signal of the pick-up coil as a reference.

AC. We apply a high-frequency drain-source voltage and measure the current by the lock-in amplifier. The frequency should exceed the characteristic variation rate of the magnetic field and the sample conductance $G(B)$, thus we have about $\sim 1kHz$ as a lower limit. Increasing the frequency, we increase an out-of-phase signal, as our circuit has capacitance and inductance. In order to keep it relatively small compared with the in-phase signal we get a upper limit for the frequency. For our samples it was $\sim 9kHz$. In AC case we have no induced currents in the measured signal, as their frequency does not coincide with the detecting frequency.

For all magnetotransport measurement, we monitor the sample temperature.

3.3 Raman spectroscopy

The Raman spectroscopy was used in this work in order to characterize the CNTs of the peapods. The measurements were performed at the Centre d'Elaboration de Matériaux et d'Etudes Structurales (CEMES) with the invaluable help of Pascal Puech, Mourad Berd and Ekaterina Pavlenko.

3.3.1 Resonant Raman spectroscopy

Raman scattering is the inelastic scattering of light. During a scattering event, a photon excites the system from the ground state to a virtual energy state. When the system relaxes it emits a photon and it returns to a different rotational or vibrational state. The difference in energy between the original state and this new state leads to a shift in the emitted photon's frequency away from the excitation wavelength. A Raman spectrum is the intensity of the scattered light plotted as a function of frequency shift of the scattered light. Generally, Raman spectra are observed for scattered photons whose energy is smaller by the phonon energy – Stokes scattering, as their sensitivity is bigger than photons whose energy is bigger by the phonon energy – anti-Stokes scattering.

In resonance Raman spectroscopy, the energy of the incoming laser is adjusted such that it coincides with an electronic transition of the system. So, rather than exciting the molecule to a virtual energy state, it is excited to near one of its excited electronic transitions. This technique became to be broadly applicable after the development of the tunable lasers. Thus, the frequency of the laser beam could be tuned to be near a particular resonance of the system, which leads to a strong amplification of the Raman signal. This is the main advantage of resonant Raman spectroscopy, which allows study an extremely small quantity of the material. In the current work we observe the Raman spectra from a single SWCNT.

3.3.2 Resonant Raman spectroscopy of CNTs

Raman spectra of CNTs consists of many features, that can be identified with specific phonon modes and with specific Raman scattering processes that contribute to each feature. Raman spectra of CNTs provides information about their phonon structure, electronic structure and structural defects.

Certain parts of the following chapter are based on the books "Physical Properties of Carbon Nanotubes" [Saito 1998] and [Dresselhaus 2005].

3.3.2.1 Vibration modes in the nanotubes

The understanding of the vibration modes of SWCNTs can be addressed through the graphene modes, taking into account the particular symmetry of the tubes. The phonon dispersion relation for a SWCNT can be determined by folding the phonon dispersion of a graphene layer. Using this folding method, one can show how the out-of-plane tangential acoustic mode in graphene gives rise to the radial breathing mode (RBM) in CNT (Figure 3.11a).

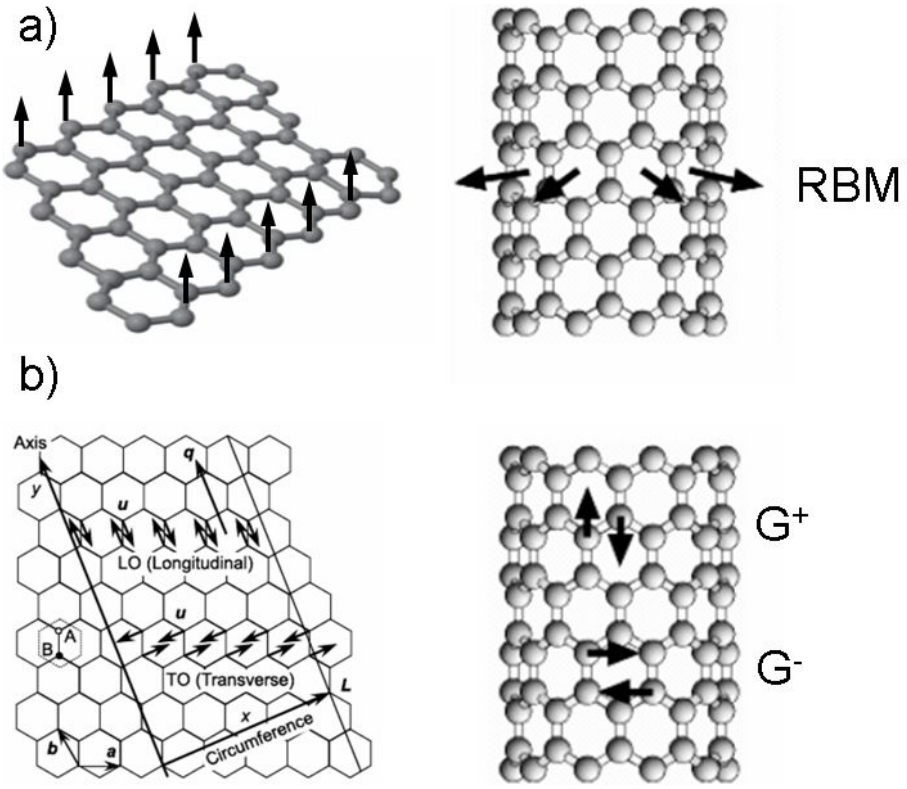

Figure 3.11: a) The out-of-plane tangential acoustic mode in graphene transforms into the RBM in the SWCNT. b)Transverse and longitudinal optical modes in graphene and in SWCNT.

Another peculiar vibration mode in the SWCNT originates from the in-plane transverse and longitudinal optical modes in graphene (Figure 3.11b). In a SWCNT they are splitted into in-plane vibrations along the tube axis (G^+ band) and in-plane vibrations along the circumferential direction (G^- band). This specific structure of the G bands is an easily recognizable sign of single-wall tubes and it does not exist for a multiwall tubes.

Further, if we consider a tube with a specific chirality, we can derive the fine structure of the vibration modes. For example, the most intense modes for a (10,10) nanotube are shown on the figure 3.12.

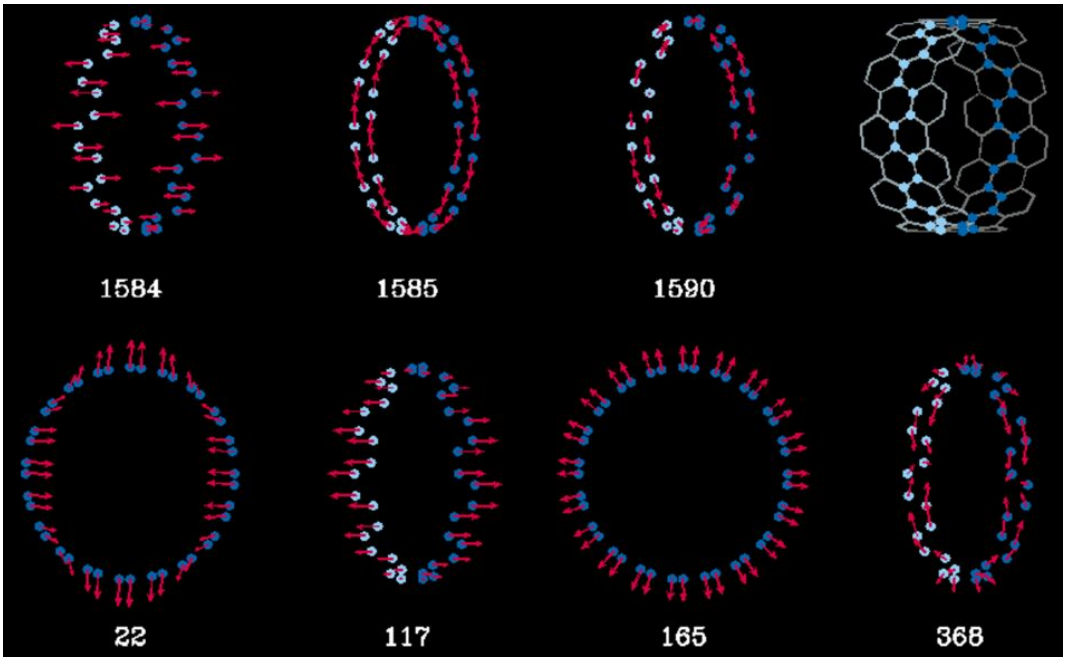

Figure 3.12: Seven most intense Raman modes and corresponding frequencies (cm^{-1}) for a (10,10) nanotube. The red arrows indicate the magnitude and direction of the appropriate C-atom displacements. The unit cell (blue atoms) is shown schematically in the upper right-hand corner. Taken from [Rao A. M. 1997]

3.3.2.2 Raman spectrum of CNTs

The unique spectroscopic properties of CNTs are largely due to the 1D confinement, resulting in the van Hove singularities (vHS) in the nanotube DOS. When the energy of incoming photons matches a difference between vHS of the valence and conduction bands, one expects resonant enhancement of the corresponding Raman signal.

In scattering process the number of emitted phonons before relaxation can be different, thus we can define one-phonon, two-phonon and multi-phonon Raman processes. The order of a scattering event is defined as its number in the sequence of the total scattering events, including elastic scattering by defects of the structure (see Figure 3.13).

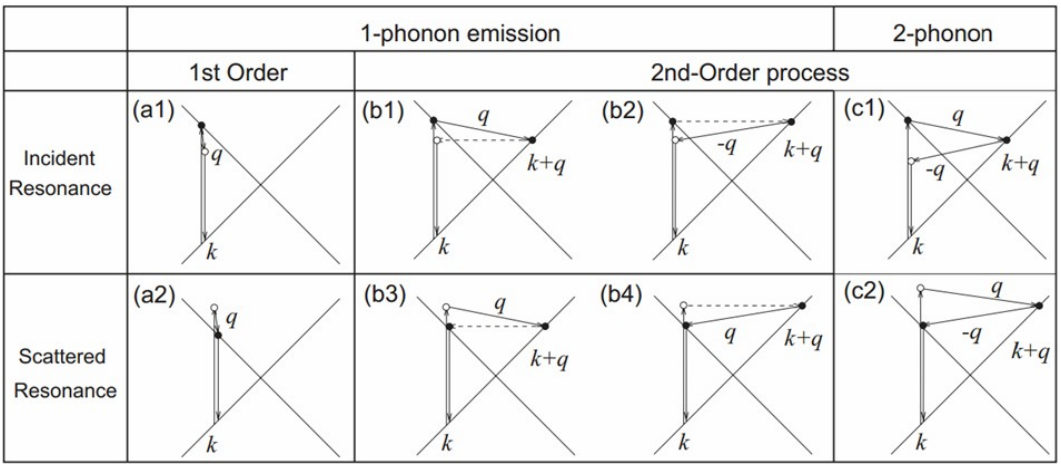

Figure 3.13: a) First-order and b) one-phonon second-order, c) two-phonon second-order, resonance Raman spectral processes. For one-phonon, second-order transitions, one of the two scattering events is an elastic scattering event (dashed lines). Resonance points are shown as solid circles. Taken from [Dresselhaus 2005].

In SWCNTs first-order Raman modes are the radial breathing mode (RBM) and the G band spectra, which is splits into two peaks (G^+ and G^-) around 1580 cm^{-1}. The second-order Raman modes includes the D band (or G') and the 2D band.

Here we list briefly the physical parameters which can be extracted from the different resonant Raman peaks for a given excitation energy:

– position of the RBM peak gives a diameter of the SWCNT;

– shape of the G band points out the type of SWCNT (metal or semiconducting);

– ratio of the intensities D/G bands gives the relative disorder in the system;

– value of the G^- and G^+ band splitting gives a diameter of the SWCNT;

– shape of the G and 2D bands allows distinguish the SWCNT and DWCNT.

As well the positions of the RBM peak as a function of the excitation energy define the conducting type of the SWCNT – Kataura plot (see Figure 3.14).

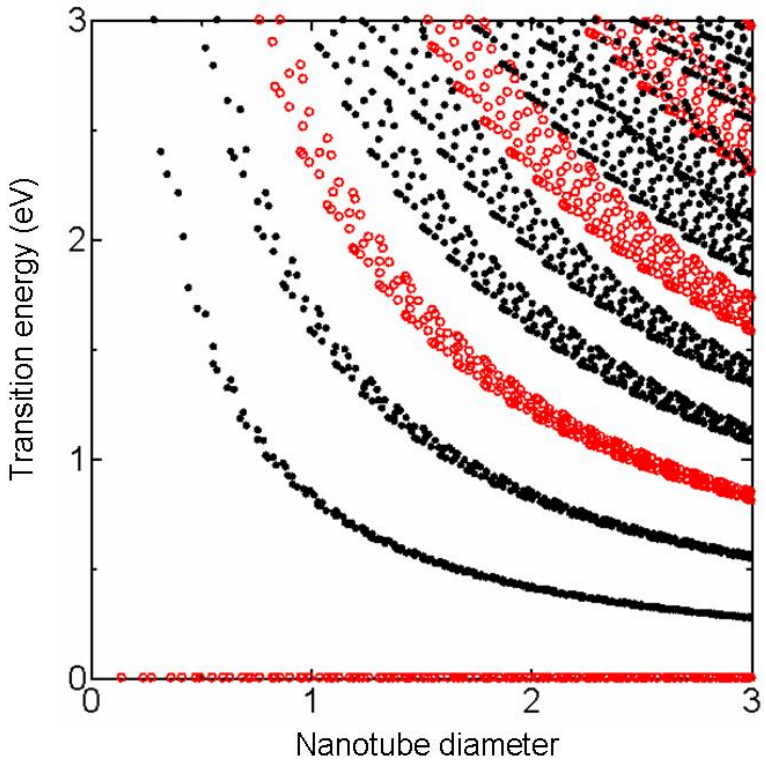

Figure 3.14: Kataura plot for resonant Raman spectroscopy: red points are metallic CNTs, black points are semiconducting CNTs.

More detailed information on Raman spectroscopy of CNTs can be found in [Dresselhaus 2005].

3.3.3 Experimental set-up

Resonance Raman spectra from SWCNTs is acquired using "Xplora-MV2000" and "T64000" micro-Raman spectrometer (Figure 3.15). Measurements are performed in a back-scattering configuration with $100\times$ objective lenses which gives $\sim$ 1 μm size for a laser spot. In order to place the spot over a single peapod we use a table with piezo-motors for $x - y$ displacement.

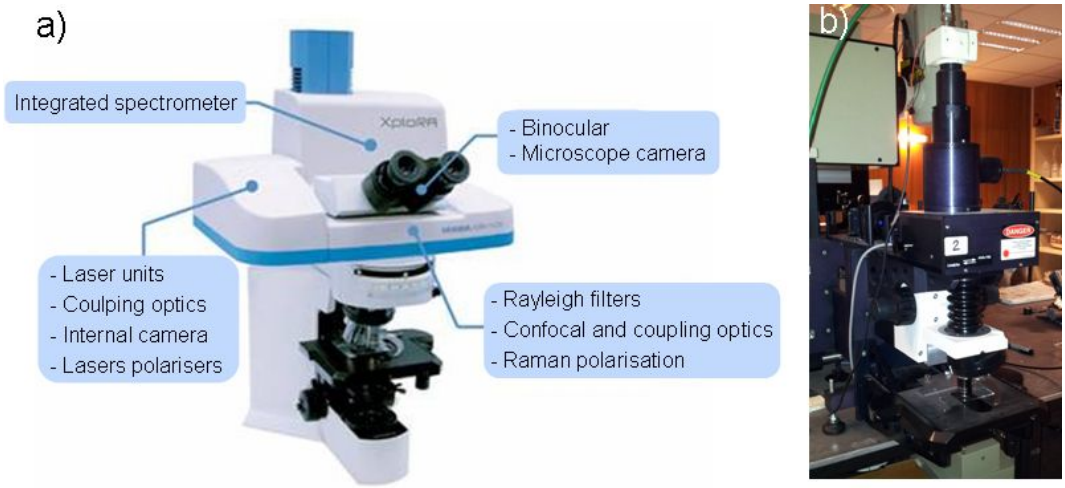

Figure 3.15: Micro-Raman spectrometers used in this work: a) Xplora-MV2000, b)T64000.

Measured Raman spectra from peapods are taken with different excitation energies: 1.58 eV, 1.94 eV, 2.33 eV, 2.60 eV. Raman data treatment is done using the "LabSpec 5" software.

Chapter 4

Electronic transport in individual C_{60} peapods

Sommaire

This chapter is devoted to the influence of the C_{60} fullerenes on the electronic transport in individual peapods. In the first part, we introduce the state of the art and theoretical background of carbon peapods. In the second part, we present experimental results of the transport measurements on the several individual C_{60} peapods combined with a micro-Raman spectroscopy on the same devices. The experiments are consistently supported by numerical simulations of the Density of States (DOS) and the conductivity of the peapods developed by K.P. Katin and M.M. Maslov from National Research Nuclear University (MEPhI).

4.1 Introduction

The possibility of doping carbon nanotubes was a subject of intensive studies in the past decade. It was reported that their electronic and transport properties are significantly altered by materials encapsulated in nanotubes [Miyake 2002, Georgakilas 2007]. Thus, a new class of hybrid nanomaterials composed of CNTs and different nanoparticles (NPs) attracts a lot of interest as a system, combining the unique properties of both CNTs and NPs, and exhibiting novel physical and chemical properties arising from NP–CNT interactions. Of great interest is the specific structure of these materials and especially the NP-CNT bounds, which provide an opportunity to tune the size, shape and the chemical properties of this

heterostructures and thus exceed the properties of isolated constituent components. For example, electron transfer across the NP-CNT bound could be very sensitive to surrounding molecular species or photon illumination [Peng 2009]. In another field, a significant attention was focused at the use of the CNTs filled with different molecules or NPs for biosensing [Wang 2005] and drug delivery [Foldvari 2008]. CNTs can also act as a support for the dispersion and stabilization of NPs.

Various applications have been recently proposed for these hybrid nanomaterials, such as transparent conductive electrodes [Kong 2007], solar cells [Kongkanand 2007, Lee 2007], gas sensors [Lu 2009], hydrogen storage [Yildirim 2005], fuel cells [Robel 2006], electrode material for rechargeable Li-ion batteries [Liu 2012], etc.

Two main principles are used to stabilize NPs on CNTs: first a growth of the NPs directly on the CNT surface; second a subsequent connection of separately grown NPs to CNTs. For such subsequent connection various techniques were developed, including the chemical modification of one (or both) components, the electrostatic force-directed assembling, capillary effect encapsulation, etc. In terms of CNT structure, there are two configurations for NP connection – on the inner and on the outer CNT surface. Most of the present-day researches are focused on the study of the outer decorated CNTs, as they are expected to have hybridization synergetic effect. Systems with NPs encapsulated inside CNTs, among which are the fullerene@CNT complexes, known as fullerene peapods, are nevertheless of scientific interest. Produced by the simple encapsulation induced by the capillary effect, they show a tunable structure and unusual electronics properties [Hornbaker 2002, Pichler 2003, Eliasen 2010].

The influence of the encapsulated fullerenes on the SWCNT energy band structure and their role in the peapod electronic transport is an important issue for both fundamental research and technical applications. This problem was a subject of controversial investigations both for theoretical and experimental studies for a long time (see part 4.2.2.2). We address this issue of the energy band structure of peapods through electronic transport and micro-Raman spectroscopy performed on the same and individual peapods. We bring evidence that the encapsulated C_{60} strongly modify the electronic band structure of semiconducting nanotubes in the vicinity of the Charge Neutrality Point (CNP), including a rigid shift and a partial filling of the energy gap.

4.2 State of the art and theoretical background

4.2.1 Single Walled Carbon Nanotubes

The basic parameters of carbon nanotubes are nowadays well described in several books. The properties of these objects will be only briefly discussed in this section. A deeper information about structure or properties of carbon nanotubes can be found in [Saito 1998].

4.2.1.1 Geometrical structure of SWCNTs

The properties of the SWCNT strongly depend on their structure along the circumference, in other words, on the rolling vector (*chiral vector*) of the nanotube:

$$\mathbf{C}_h = n\mathbf{a}_1 + m\mathbf{a}_2 \tag{4.1}$$

where $\mathbf{a}_1$ and $\mathbf{a}_2$ are the unit vectors of the real space lattice of the graphene sheet and n, m are integer parameters – *indexes of chirality*. The chiral vector $\mathbf{C}_h$ and the translational vector $\mathbf{T}$, parallel to the tube axis, define the unit cell of a SWCNT (see Figure 4.1a). All the variety of different chiral tubes arranges between two limiting cases: *zigzag* and *armchair* with indexes type (n,0) and (n,n) respectively. The name arises from the shape of the cross-sectional ring of the tube (see Figure 4.1b).

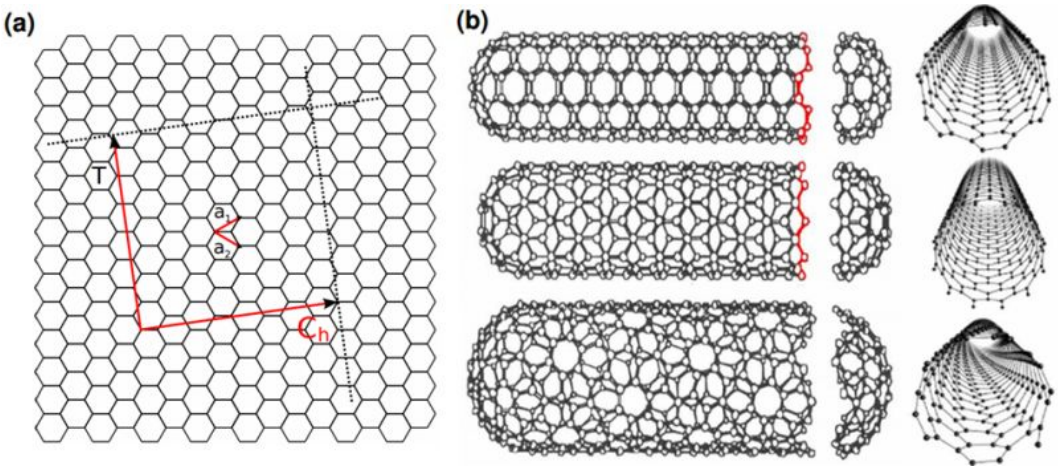

Figure 4.1: a)Unrolled carbon nanotube which is equivalent to a graphene sheet. The vectors $\mathbf{C}_h$ and $\mathbf{T}$ define the unit cell of SWCNT. b) Three particular cases: armchair (5,5); zigzag (8,0) and chiral (8,4). In red highlighted the cross-section ring and its armchair/zigzag shape. Taken from [Dresselhaus 1995].

Knowing the chirality of the tube, we can deduce its diameter d as:

$$d = \frac{\mid \mathbf{C}_h \mid}{\pi} = \frac{a\sqrt{n^2 + nm + m^2}}{\pi} \tag{4.2}$$

where a is a unit vector $a = \sqrt{3}a_{C-C} = 0.249\ nm$; here, a_{C-C} is the bond length between two carbon atoms.

4.2.1.2 Band structure of SWCNTs

The electronic properties of SWCNT are based on those of graphene. The unit cell of nanotubes on a sheet of graphene is presented in figure 4.1a. The unit vectors

of this cell are chiral vector $\mathbf{C}_h$ and translational vector $\mathbf{T}$. The reciprocal lattice vectors are obtained from the relation:

$$\mathbf{R}_i\mathbf{K}_j = 2\pi\delta_{ij} \tag{4.3}$$

where $\mathbf{R}$ and $\mathbf{K}$ are the real space and reciprocal lattice vectors respectively. Hence, the reciprocal lattice vectors of SWCNT can be expresses as:

$$\mathbf{K}_1 = \frac{1}{N}(-t_2\mathbf{b}_1 + t_1\mathbf{b}_2) \quad \text{and} \quad \mathbf{K}_1 = \frac{1}{N}(m\mathbf{b}_1 - n\mathbf{b}_2) \tag{4.4}$$

where $\mathbf{b}_1$ and $\mathbf{b}_2$ are the reciprocal lattice vectors of the graphene sheet, N is a number of Carbon hexagons present in a SWCNT unit cell and t_1,t_2,n,m are the integers of translational vector $\mathbf{T} = t_1\mathbf{a}_1 + t_2\mathbf{a}_2$ and chiral vector $\mathbf{C}_h = n\mathbf{a}_1 + m\mathbf{a}_2$. The Brillouin zones of graphene and SWCNT are shown on the figure 4.2. The SWCNT Brillouin zone is one dimensional, it is shown on the figure 4.2 by a line segment WW' parallel to the $\mathbf{K}_2$ vector.

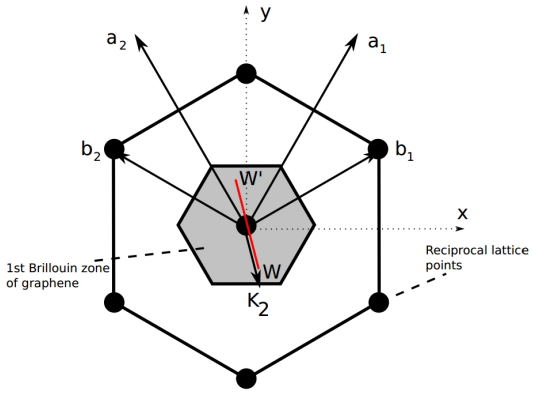

Figure 4.2: The first Brillouin zone of graphite (the grey area) and of SWCNT (red line segment WW'). $\mathbf{a}_1$ and $\mathbf{a}_2$ are the unit vectors of real space and $\mathbf{b}_1$ and $\mathbf{b}_2$ are the reciprocal lattice vectors of the graphene sheet. Taken from [Dresselhaus 1995].

Depending on chirality SWCNTs can exhibit metallic or semiconducting properties. The ratio of metallic to semiconducting tubes is 1:2. This can be seen for example in Figure 4.3 where the different electronic states are attributed to their specific chirality. The main criterion to define SWCNT's nature is:

$$(n - m) \bmod 3 = 0 \quad \text{for metallic tube} \tag{4.5}$$

$$(n - m) \bmod 3 = 1, 2 \quad \text{for semiconducting tube} \tag{4.6}$$

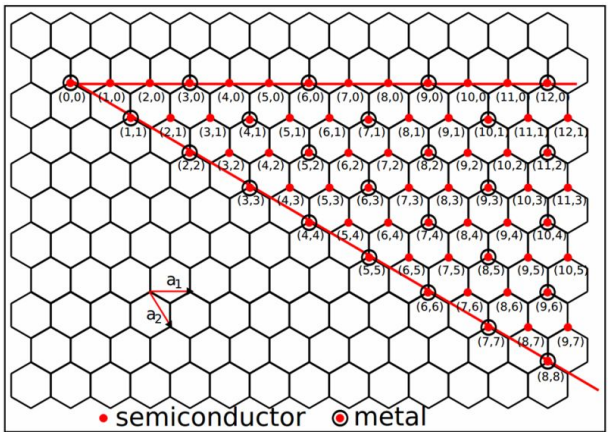

Figure 4.3: Map of the electronic state of SWCNTs as a function of the chiral vector. a_1 and a_2 are the real space lattice vectors of the honeycomb structure. Taken from [Dresselhaus 1995].

The band structure of SWCNT can be derived from the graphene dispersion relation in the tight-binding model:

$$E_{graphene} = \pm\gamma_0 \sqrt{1 + 4cos\left(\frac{\sqrt{3}k_x a}{2}\right) cos\left(\frac{k_y a}{2}\right) + 4cos^2\left(\frac{k_y a}{2}\right)} \tag{4.7}$$

where γ_0 is the overlap integral of the nearest neighbours in the graphene honeycomb lattice.

The band structure of SWCNT is obtained by introducing a periodic boundary condition, as the graphene sheet is rolled up. The wave function has to be continuous along the circumference:

$$\psi(\mathbf{r}) = \psi(\mathbf{r} + \mathbf{C}_h) \tag{4.8}$$

Which gives a 1-D dispersion relation:

$$E_q(k) = E_{graphene}\left(q\mathbf{K}_1 + k\frac{\mathbf{K_2}}{K_2}\right) \quad \text{where } q = 0, ..., N-1 \text{ and } \frac{-\pi}{T} \leq k \leq \frac{\pi}{T} \tag{4.9}$$

Here, N is the number of pairs of dispersion relation representing each a cross-section of the Brillouin zone and $\mathbf{K}_1$, $\mathbf{K}_2$ are the basis vectors of the reciprocal lattice. From the electronic dispersion relation, deduced from equation 4.9, we can calculate the density of states in carbon nanotubes in the vicinity of the Fermi energy [Mintmire 1998]:

$$g(E) \propto \frac{E}{\sqrt{E^2 - E_p^2}} \tag{4.10}$$

where E_p represents extremal values of each band of the band structure $E_q(k)$. This formula works well for energies within about 1 eV of the Fermi level ($|E/\gamma_0| \ll 1$). As we can see, this is a typical DOS for a 1-D material with Van-Hove singularities around the E_p values. For the metallic SWCNTs the DOS value is constant near the CNP (Figure 4.4d) and can be estimated as:

$$g_{CNP} = \frac{8}{\sqrt{3}\pi a \gamma_0} \tag{4.11}$$

Thus the conduction and valence bands are touching in the K (or K') point of Brillouin zone, and energy dispersion law has a linear dispersion (Figure 4.4b). For semiconducting SWCNT the DOS presents a band gap (Figure 4.4c), which can be estimated as:

$$E_g = \frac{\gamma_0 a_{C-C}}{d} \tag{4.12}$$

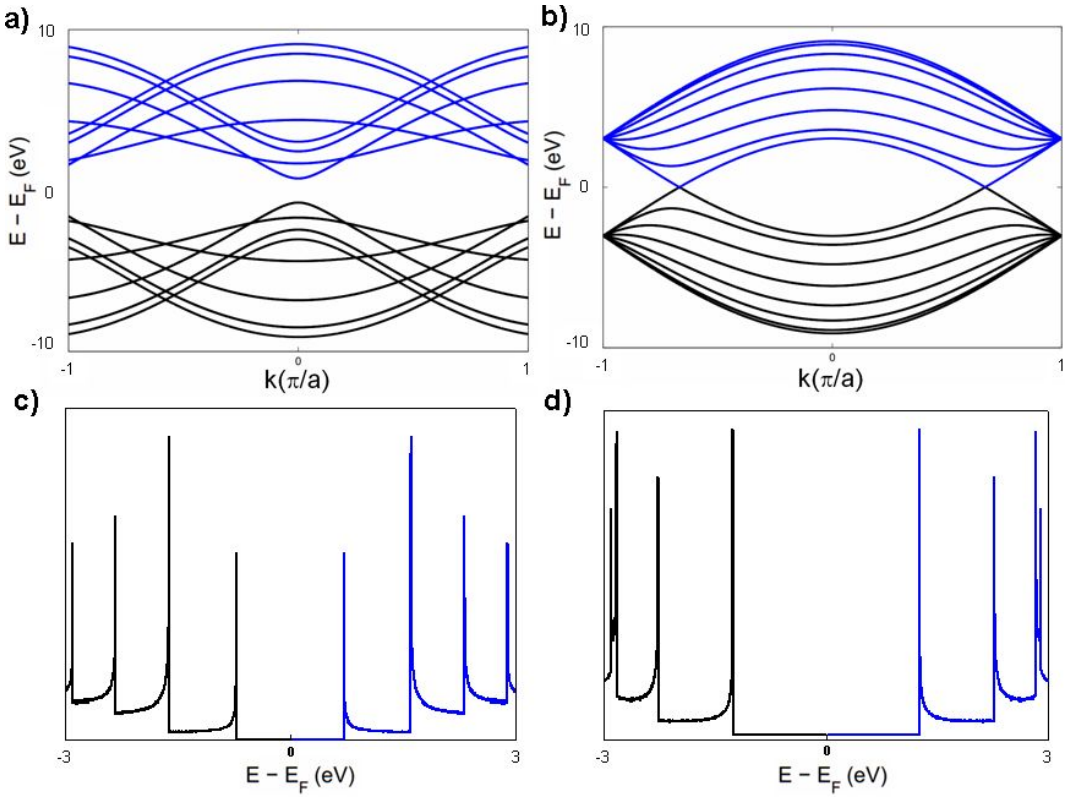

Figure 4.4: The band structure (a,b) and DOS (c,d) for semiconducting SWCNT (7,0) and for metallic SWCNT (7,7) respectively.

One can derive the conductance of a SWCNT ($G(E)$) in the ballistic transport regime at zero temperature, based on its band structure. Each energy subband lying

under the Fermi energy gives one conducting channel, leading to a step-like conductance behaviour (Figure 4.5). In a proximity of the CNP the subbands are four-fold degenerated in case of semiconducting SWCNTs and are two-fold degenerated in case of metallic SWCNTs. Thus, in the vicinity of the CNP, for a semiconducting SWCNT conductance is zero and then increases to $2e^2/h$ and for a metallic SWCNT $G = 2e^2/h$ followed by a rise to $6e^2/h$. As the temperature increases, these step-like features are gradually smoothed. A ballistic transmission in CNTs was observed experimentally in the FET configuration [Kong 2001, Javey 2003].

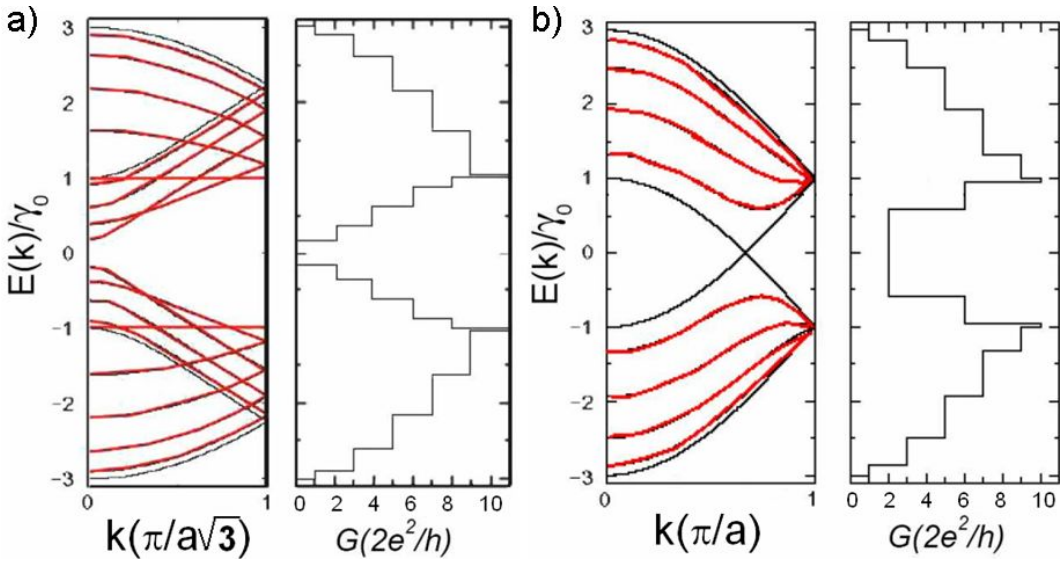

Figure 4.5: Band structure and corresponding conductance versus energy dependence for (a) semiconducting SWCNT and (b) metallic SWCNT in the ballistic transport regime. The four-fold degenerate subbands are shown in red and the two-fold degenerate subbands are shown in black. Adopted from [Nanot 2009].

4.2.1.3 Sensibility of SWCNTs to the environment.

Sensibility of SWCNTs to the environment is an important issue for both fundamental research and technical applications. Several research groups [Philip G. Collins 2000, Jing Kong 2000] demonstrated that the electrical conductance of the CNTs can be changed dramatically upon exposure to different molecules species. For example, it was shown that, nanotube based sensors can detect ppm or sub-ppm levels of gas molecules at room temperature, which opens a possibility of developing high quality gas sensors.

Attractive sensing mechanism may be provided by the perturbations on the nanotube electronic structure induced by different molecules, which can give direct information, easy to read-out and to interface with conventional electronic architec-

tures. This may be useful for the high integration solutions for lab-on-a-chip applications. Thus chemisorption and physisorption on individual carbon nanotubes and nanotube bundles is indeed an important issue, due to the large surface area (up to 1587 m^2/g [Cinke 2002]), that allows a high capability of interaction between molecules and SWCNTs.

4.2.2 From C_{60} fullerenes to $C_{60}@SWCNT$ - peapods

Since the first observations of complexes C_{60}@SWCNT, or C_{60} carbon peapods, in 1998 [Smith 1998], they are referred to as promising components for nanoelectronic devices due to their tunable structure and unusual electronics properties [Hornbaker 2002, Pichler 2003, Eliasen 2010]. Possibility to create a hybrid structure of one-dimensional CNTs with zero-dimensional fullerenes opens a route for designing of new materials in controlled way. Before going further into the peapods properties, I would like to remind the reader the main properties of C_{60} fullerenes.

4.2.2.1 Fullerenes crystallographic and electronic structure

The World became aware of the fullerenes after the Nobel Prize of 1996 which has been won by Harold W. Kroto, Robert F. Curl and Richard E. Smalley for their discovery in 1985 [Kroto 1985] of a new allotrope of carbon, in which the atoms are arranged in closed shells. The new form was named Buckminsterfullerene, after the architect Buckminster Fuller who designed geodesic spheres.

Buckminsterfullerene (C_{60}) consists of 20 hexagonal and 12 pentagonal rings as the basis of an icosahedral symmetry closed cage structure (Fig.4.6). Each carbon atom belongs simultaneously to one pentagon and to two hexagons, which makes all atoms equivalent; this was confirmed by the NMR spectrum of the C^{13} that contains only one line. All the bonds are not equivalent, a common edges of two hexagons consist of double C=C (0.139 nm) bond, as opposed to a pentagons-hexagons edges which contain a single C-C bond (0.144 nm).

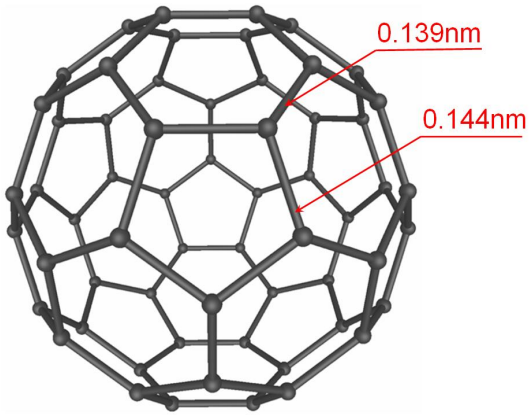

Figure 4.6: C_{60} fullerene in pentagon-face centered orthogonal projection.

Buckminsterfullerene is an electron acceptor, sustaining up to six reversible one-electron reductions to C_{60}^{-6}, further oxidizing is irreversible. Electron delocalization is weak according to the C_{60} tendency to avoid double bond inside the pentagons. In solid state (fullerite), buckminsterfullerenes stick together via the Van der Waals forces forming face-centered cubic structure [Haluska 1993]. Fullerite is a n-type semiconductor with a band gap of 1.6 eV [Katz 2006]. The discrete levels of a free C_{60} (Fig.4.7a) molecule are only weakly broadened in the solid (Fig.4.7b), which leads to a set of non-overlapping subbands with a narrow width of about 0.5 eV.

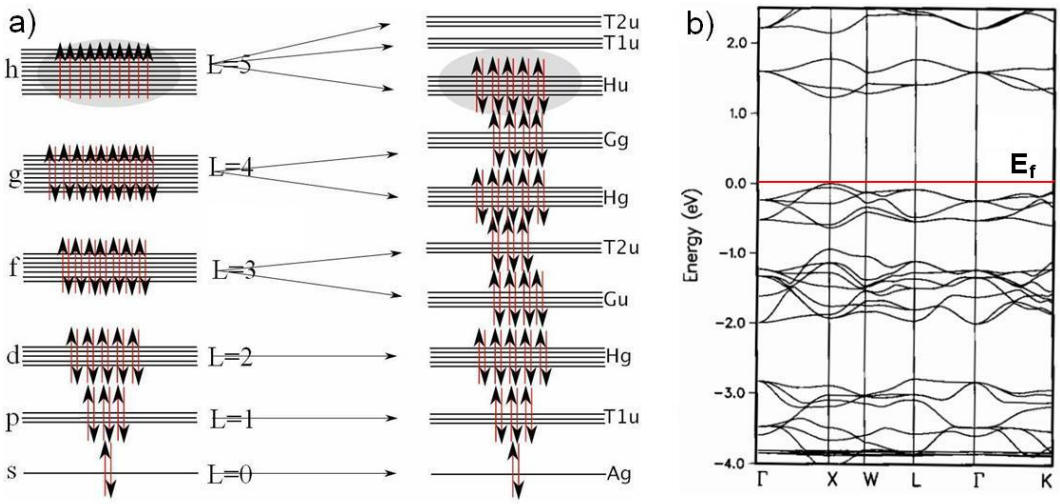

Figure 4.7: a) Electronic structure of C_{60} under "ideal" spherical (left) and "real" icosahedral (right) symmetry. b) Band structure around the Fermi energy for solid C_{60}. The bands at about -0.5eV are the h_u bands, which are occupied in solid C_{60}, and the bands at about 1.5eV are the t_{1u} bands. (From [Gunnarsson 1997])

As we can see from Fig.4.7a the Highest Occupied Molecular Orbital (HOMO level) of C_{60} is presented by the 5-fold h_u band and the Lowest Unoccupied Molecular Orbital (LUMO level) by the 3-fold t_{1u} band.

4.2.2.2 Band structure modification

The strength of the hybridization of the C_{60} states with the CNT band structures depends in a complex manner on the tube radius and helicity, on the fullerene distribution inside the tube and on their orientation with respect to the tube axis.

Review of theoretical studies on C_{60} peapods

The first studies in this area include a number of theoretical calculations [Okada 2001, Cho 2003, Lu 2003], which show, that the presence of fullerenes gives an additional

conducting path in a vicinity of the Fermi level. According to the study of armchair peapods [Okada 2001], four bands cross the Fermi level in the C_{60}@(10, 10) peapod (Figure 4.8a): two of them with a large linear dispersion, corrsponding to the π orbitals in empty SWCNT(10,10), and two other bands with a weak dispersion, resembling the π state in the C_{60} band structure – LUMO. DFT calculations have predicted that C_{60}@(10, 10) is a metallic system with multi-carriers states at the CNP, originating from SWCNT and C_{60}-chain orbitals. However this prediction does not hold for all armchair peapods. Once the tube's diameter becomes smaller than Van der Waals diameter of the C_{60} fullerene, the encapsulating process (Equation 4.13) starts to be endothermic, showing substantial structural distortion of the SWCNT and the position of C_{60} LUMO does not match with the Fermi level of the SWCNT.

$$SWCNT(n,n) + C_{60} \;\rightarrow\; C_{60}@(n,n) - \Delta E \tag{4.13}$$

Here, ΔE is the reaction energy per fullerene in the encapsulation reaction. Thus, the resulting band structure are not only the consequence of hybridization of the electronic states of the constituents, but also the effect of the structural distortion of the system. It was found, that the minimum diameter of the SWCNT, which is capable to encapsulate the C_{60} fullerenes without structural distortions is 1.28 nm (Figure 4.8b).

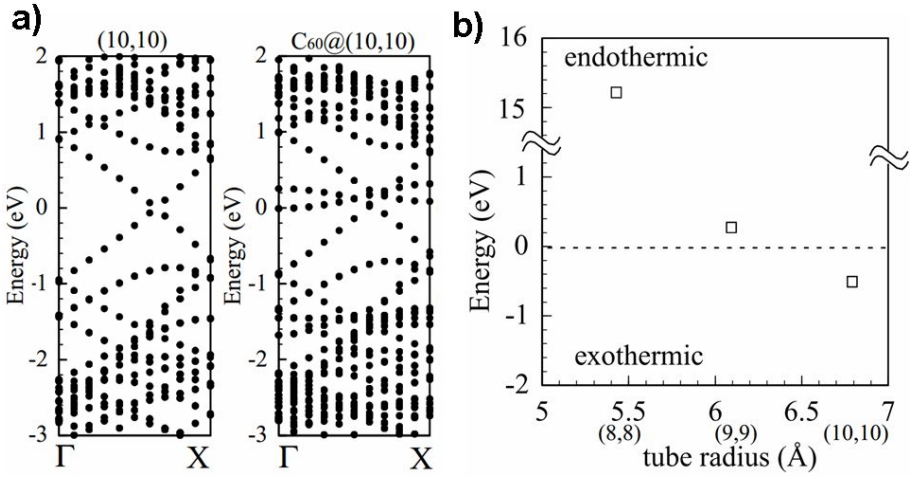

Figure 4.8: a) Energy band structures of encapsulated C_{60}@(10, 10) and of isolated (10,10) SWCNT. Fermi energy is adopted to zero. b) Reaction energies ΔE per C_{60} in the encapsulation reaction for the (8,8), (9,9), and (10,10) SWCNTs. [Okada 2001]

The study of the armchair peapods [Lu 2003] with smaller fullerenes C_{20}@(n, n) confirms this trend, showing that the position of the fullerene orbitals matches well with the Fermi level of the SWCNT, till its structural distortions are not inessential.

The impact of this additional conductivity path in a metallic SWCNT was analyzed by Kondo et al. [Kondo 2005] through the theoretical study of the transport properties on the armchair peapod with calculations based on Green function approach within a tight-binding model. Varying the distance l between centers of encapsulated C_{60}s in the (10,10) SWCNT, the authors found the distance l_0, below which the chain of fullerenes starts to contribute to the transmission at the Fermi energy. This means that the fullerene orbitals create continuous energy band, providing conducting path all along the system (Figure 4.9a,b). For larger intervals, $l > l_0$, only the (10,10) nanotube contributes to the transmission of the system. It was also found that an aperiodicity in the fullerene distribution acts as a defect, providing back-scattering and altering the electronic transport (Figure 4.9c,d).

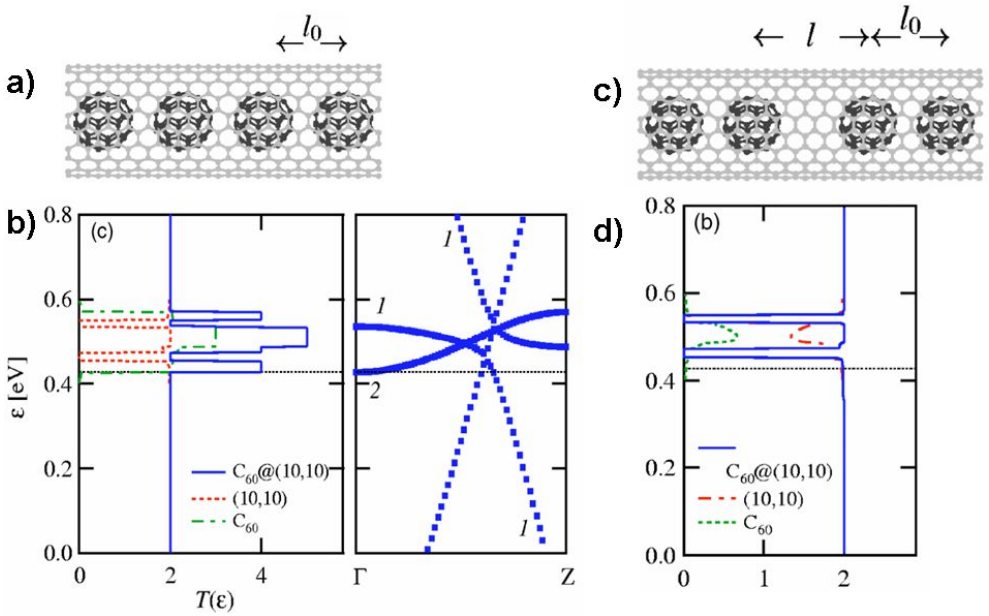

Figure 4.9: a) Model of the periodic C_{60}@$(10, 10)$ peapod, $l_0 = 0.9845$ nm. b) The transmission (left) and the band structure (right) of periodic C_{60}@$(10, 10)$ around Fermi energy. c) Model of the nonperiodic C_{60}@$(10, 10)$ peapod. d) The transmission of nonperiodic C_{60}@$(10, 10)$ ($l = 1.2036$ nm) around Fermi energy. Dashed and dashed-dotted lines show contributions to the transmission from (10,10) nanotube and C_{60}, respectively. Dotted lines show Fermi energy. [Kondo 2005]

For peapods derived from semiconducting SWCNT, a similar picture is observed. The first prominent result was obtained on the zigzag peapods C_{60}@$(n, 0)$ [Lu 2003], showing that C_{60} orbital energies partly fill the initial band gap for semiconducting SWCNTs (19,0) and (17,0), (Figure 4.10).

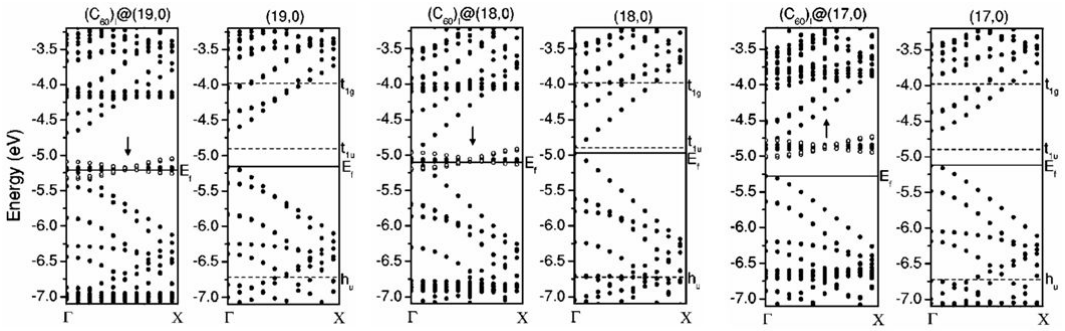

Figure 4.10: Energy band structures of encapsulated C_{60}@$(19,0)$, $(18,0)$, $(17,0)$ and of isolated SWCNTs. The open circles ($\circ$) represent the broadened C_{60} t_{1u} bands in peapods, the dash lines represent the isolated C_{60} levels. [Lu 2003]

The peapod band structure also exhibits a hybridization of the initial C_{60} orbitals with the lowest unoccupied and highest-occupied bands of the SWCNT, which can be seen on the figure 4.10, as a relative shift from the initial fullerene states (indicated by the arrows). The local DOS (LDOS) calculations [Cho 2003], as well, present similar results for zigzag peapods (Figure 4.11a).

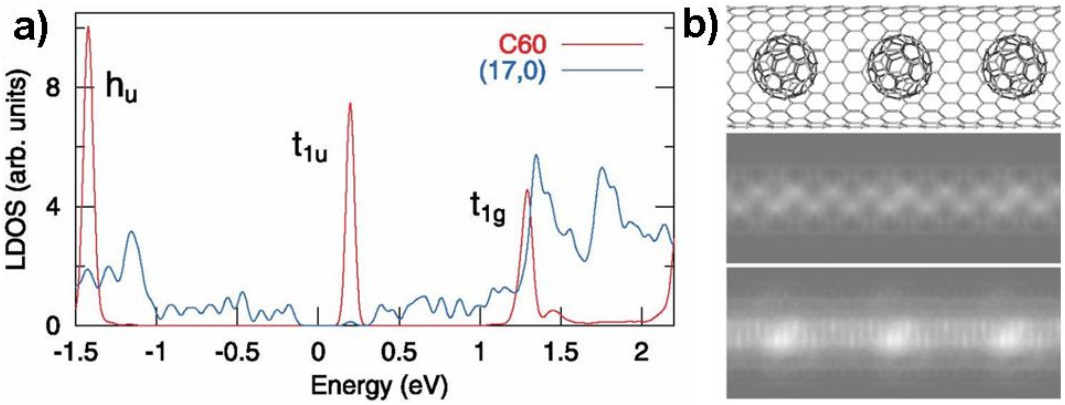

Figure 4.11: a) Local density of states of C_{60}@$(17,0)$ decomposed into the constituents. b) (top – down) Model of C_{60}@$(17,0)$ peapod and simulated STM images for -1.5 V and 1.5 V sample bias. [Cho 2003]

By analyzing this LDOS we see that the LUMO of the fullerene chain reduces the value of the band gap. This should strongly impact the peapod transport properties. Besides, the HOMO and LUMO+1 orbitals give rise to non-zero LDOS at energies accessible by the STM measurements (Figure 4.11b). These results were supported by subsequent detailed calculations of the hybridization C_{60} orbitals with nanotube

band structure for various chiral SWCNTs [Dubay 2004]. The fact that the t_{1u} states of fullerene are located close to the Fermi level was explained as a consequence of the strong electron affinity of the C_{60} molecule. For semiconducting SWCNT, it has been theoretically predicted that the contribution of the t_{lu} orbital depends on the azimuthal symmetry of the tube states and goes decreasing with the tube diameter. This is consistent with an another study of the electronic transport properties of peapods by A. Rochefort [Rochefort 2003], which predicts that the charge transfer between the host SWCNT and the C_{60} molecule decreases with the tube's diameter and starts to be negligible when $d > 2\ nm$. But contrary to what was reported previously, Rochefort in his study highlighted that only minor changes, ascribed to a small structural deformation of the nanotube walls, were observed. Thus, because of the small electron charge transfer (less than 0.10 electron) from the CNT to the C_{60} molecules, he predicted a poor mixing of the C_{60} orbitals with those of the CNT. This contradiction reveals a question: Do encapsulated fullerenes provide strong alterations of the electron transport properties of SWCNTs? Particularly it is interesting for a diameter range $[1.2; 2]\ nm$, when the diameter of the nanotube is sufficiently large to exothermically encapsulate C_{60} and narrow enough to induce the hybridization of C_{60} orbitals with the nanotube band structure.

Theoretical calculations of the conductance for such kind of systems with a large number of atoms are a complicated and computer time consuming problem. Thus till now, there are only a limited number of papers, dealing with this issue. The latest one [Kojima 2012] presents first-principles calculations of the electron transport properties on a 1.23 nm - length armchair (10,10) SWCNT with one C_{60} fullerene inside, which is suspended between Au(111) contacts (Figure 4.12a). Comparison between the conductance spectra of the peapod and the empty nanotube exibits some relevant features (Figure 4.12b).

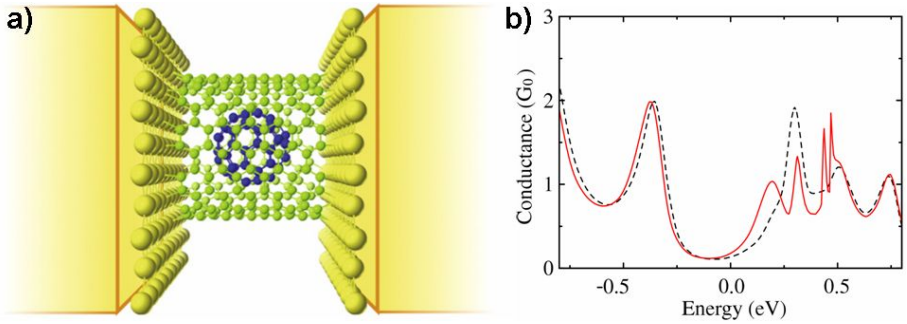

Figure 4.12: a) Schematic computational model of C_{60}@$(10,10)SWCNT$ suspended between Au(111) electrodes. b) Conductance spectra as function of energy. The dashed curve represents the conductance of the SWCNT and the solid curve that of the peapod. Fermi energy adopted to zero. [Kojima 2012]

1. The peapod spectrum unveils few sharp peaks in the $[0.2; 0.5]\ eV$ energy range, arising from the coupling of the threefold degenerate t_{1u} orbitals with the

CNT states. Additionally, it was found that the t_{1u} orbital with an azimuthal quantum number $m = 0$ is responsible for the onset of an additional transport channel, resulting to a higher conductance than the one of the SWCNT for some given energies.

2. The peapod's spectrum is shifted to the lower energies, following the overall shape of the nanotube's one. This is well seen in the $[-0.75; 0]$ eV energy range where the spectrum is not any more disturbed by the t_{1u} orbitals. This effect originates from the charge transfer – a shift of electrons from SWCNT to the C_{60}, leading to down-shift of E_f toward lower energies.

For the best of our knowledge, there are no similar conductance calculations performed on semiconducting SWCNT based peapods.

Thus, reviewing the theoretical studies performed on C_{60} peapods we can notice a contradiction concerning the contribution of the encapsulated fullerenes to the transport properties of the SWCNT. The discrepancy in the estimates of the C_{60}s contribution varies from significant alterations, that could change the overall behavior of the system, to minor modifications of the band structure, barely accessible by experimental techniques.

Review of experimental studies on C_{60} peapods

Experimental characterizations of peapod band structures and electronic transport remain unfortunately puzzling. Early STM experiments demonstrate that the encapsulated C_{60}s strongly modify the electronic structure far from the Fermi level [Hornbaker 2002]. This can be seen on the figure 4.13b. STM images under positive bias $+1$ V show characteristic features of C_{60}s, as variations of LDOS between and on the top the fullerenes (Figure 4.13c).

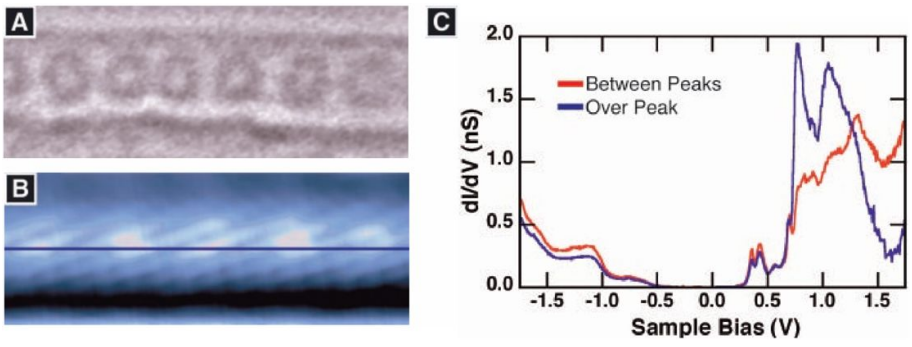

Figure 4.13: a) Room temperature TEM image of one peapod, showing the SWCNT cage and the encapsulated C_{60}s. b) STM image under a positive sample bias ($+1.5$ V, 700 pA), showing bright spots originating from the encapsulated C_{60}s. c) Variation of LDOS. The relatively small variation of the differential conductance dI/dV observed for negative bias can be attributed to the initial difference in STM tip heights. [Hornbaker 2002]

In the same time, the photoemission spectroscopy performed on an assembly of C_{60} peapods does not confirm the presence of extra bands crossing the Fermi energy [Shiozawa 2006] in sharp contrast with the theoretical calculations [Okada 2001, Lu 2003, Cho 2003, Kojima 2012]. On the other hand, the photoluminescence spectroscopy [Okazaki 2008] unveils shifts of the first (E_{11}) and the second (E_{22}) interband transition energies (Figure 4.14), attributed to the local strain and the hybridization between C_{60} states and those of the nanotube.

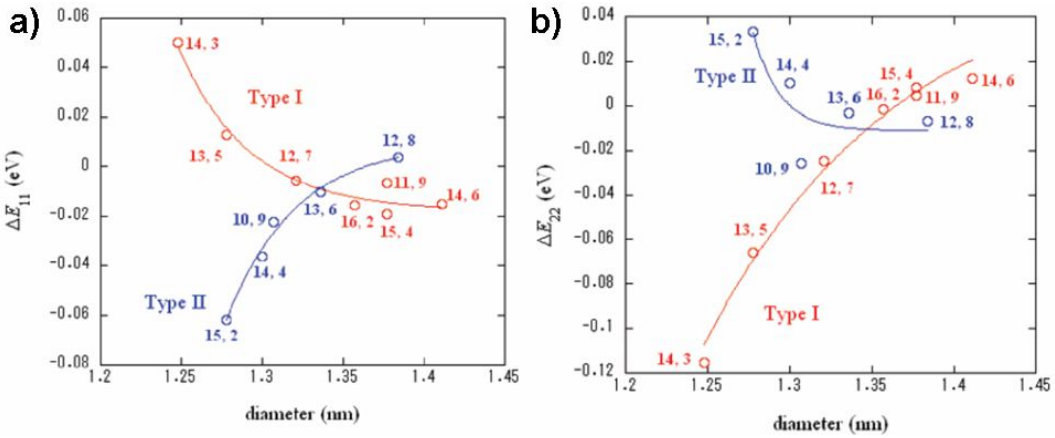

Figure 4.14: Differences in optical transition energies in a) E_{11} and b) E_{22} (ΔE_{11} and ΔE_{22}, respectively) between C_{60} peapods and SWCNTs as a function of tube diameter. [Okazaki 2008]

The first electronic transport experiments [Pichler 2001, Vavro 2002] were performed on buckypapers or mats of bundled tubes, so these results represent some kind of average over a large number of tubes with different chirality along with intertube resistance contribution to the overall conductance. In addition, it is difficult to completely degas these samples, leaving open the question of the probable p-doping by the adsorbed oxygen and moisture. Thus, such fascinating results, as a strong decrease of the resistivity of the peapods compared to the initial SWCNTs, or even transitions from semiconducting to metallic states due to the C_{60} encapsulation, could be hardly linked with the particular features of the peapods band structure. This emphasizes the necessity of the studies performed on individual peapods.

Electronic transport experiments on individual peapods in the Coulomb blockade regime started to reveal the electronic states close to the Fermi energy. Pioneer experiments gave evidence of highly regular quantum dots, identical to those obtained with defect-free and empty SWCNTs [Utko 2006, Quay 2007] (Figure 4.15). Thus, it was concluded that C_{60} peapods do not differ from nanotubes in their electronic transport characteristics. Nevertheless more recent results unveil anomalous resonance states, caused by a C_{60} chain inside the tube [Eliasen 2010]. It was shown (Figure 4.16), that the regular Coulomb blockade diamonds are perturbed by

a weakly gate-dependent feature superimposed on the entire structure, originating from the C_{60} coupling to the nanotube. The presence of a nanoelectromechanical coupling between electronic states of the nanotube and mechanical vibrations of fullerenes was also confirmed by Utko et al. [Pawel Utko 2010].

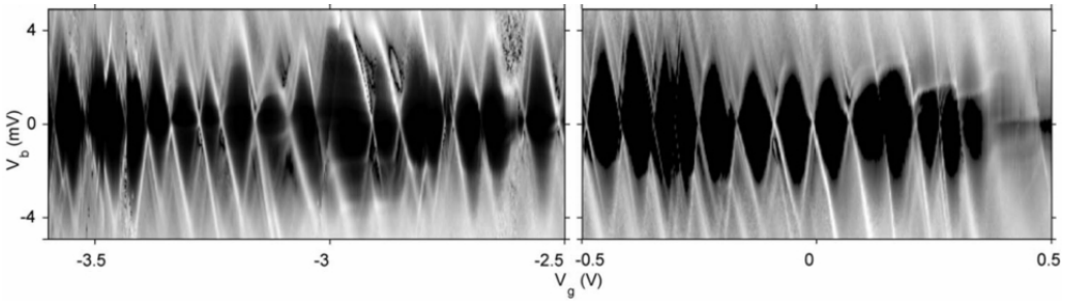

Figure 4.15: Conductance versus bias and gate voltage of peapod at 250 mK. The color scale is black (low) to white (high conductance). Regular Coulomb blockade diamonds indicate that device acts as a single quantum dot. [Quay 2007]

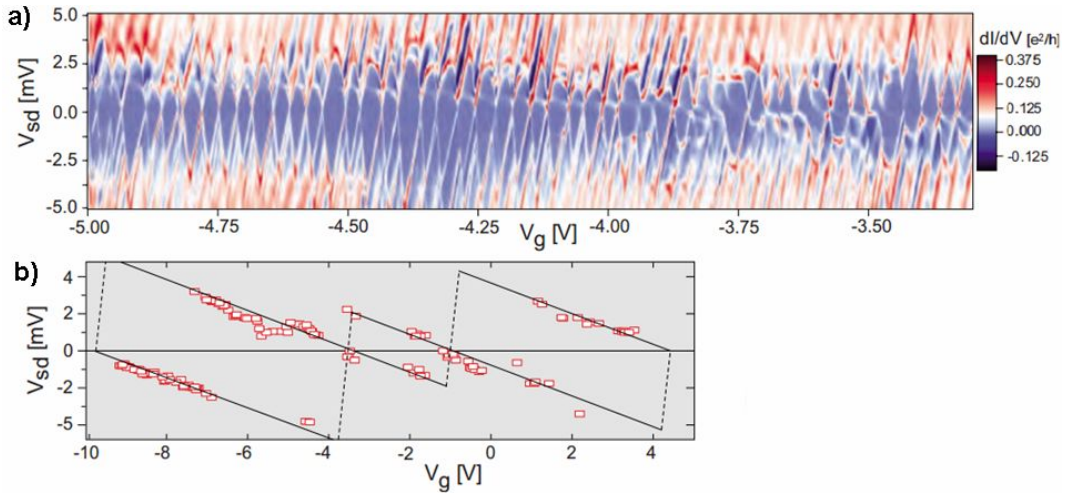

Figure 4.16: a) Conductance versus bias and gate voltage of peapod at 300 mK. b) Observed avoided crossings over the entire gate-range (red rectangles). Black lines are guides to the eye, outlining the edges of the "impurity diamond". [Eliasen 2010]

Reviewing the experimental studies performed on C_{60} peapods, we can notice a lack of structural characterization of the encapsulating tubes. The experimental results of the transport measurements remain hardly comparable to the electronic structure simulations, as the theoretical studies indicate a big impact of the partic-

ular chirality of nanotube on the peapod electronic transport.

This problem has prompted us to study electronic structure of individual peapods by transport measurements combined with the micro-Raman spectroscopy. Thus, this allows to probe transport properties and independently characterize the external SWCNT on the same devises, providing the necessary structural information.

4.2.3 Transformation from Peapod to DWCNT

An attractive aspect of the peapods for the nanoengineering is the possibility to use them as precursors for double-walled carbon nanotubes (DWCNT) [Bandow 2001]. Under heat treatment [Bandow 2001, Suarez-Martinez 2010], electron irradiation [Smith 1998, Hernandez 2003, Luzzi 2000], or both mild temperature and electron irradiation combined [Sakurabayashi 2003, Arrondo 2005], peapods can be transformed to DWCNTs, in which coalesced C_{60}s form the internal tube and the outer tube templates the formation of the inner one. It provides an efficient technique for fabricating high-quality DWCNTs [Bandow 2004]. Recently, a new way of directly promoting the coalescence of encapsulated fullerenes into an inner tube by subjecting the peapod to an appropriate ultra violet (UV) laser irradiation with wavelength 335.8 nm was proposed [Berd 2012]. The fact that C_{60} fullerenes have a peak in the absorption spectrum at λ=335.8 nm, while SWCNTs absorption remains relatively small (Figure 4.17), allows to adjust the laser power to keep the outer tube weakly affected by heating effects (for laser powers $< 1\ W\mu m^{-2}$).

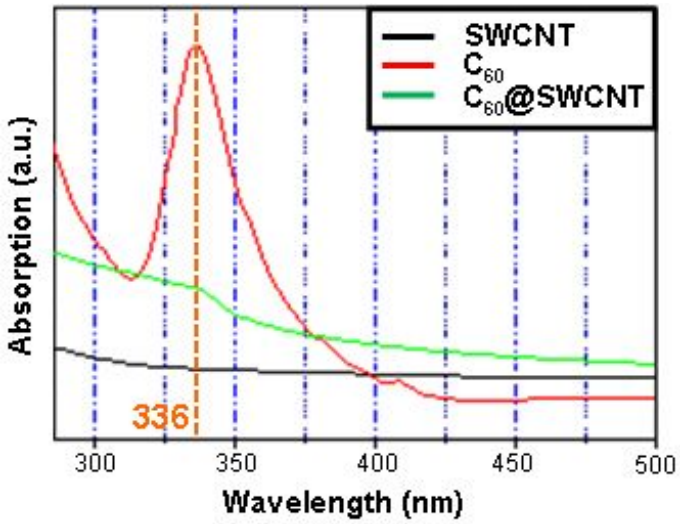

Figure 4.17: Absorption spectra for SWCNTs, C_{60}@SWCNTs (peapods), and C_{60} fullerenes versus the laser irradiation wavelength. [Berd 2012]

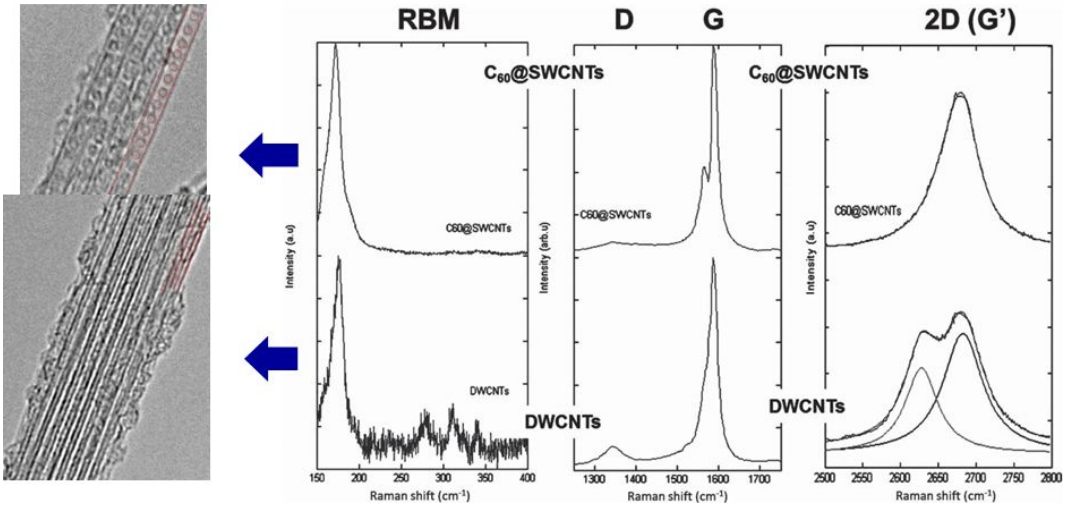

Figure 4.18: HRTEM images and Raman spectra (λ=515 nm) of the starting peapod material (top) and the same after irradiation for 120s with the 335.8 nm laser probe at 0.25 mWμm^{-2} (bottom). [Berd 2012].

The transformation of the former peapods into DWCNTs (Figure 4.18) is marked by: 1) the occurrence of new RBM bands corresponding to smaller SWCNTs; 2) merging of the formerly split G^+ and G^- bands into a single, broader, asymmetric G band; and 3) the occurrence of a low-wavenumber contribution to the 2D band.

This method provides a selective excitation of fullerenes, while the containing SWCNT is only weakly heated by the laser and as a consequence tubular structure remains free from defects on the contrary to the former methods.

4.3 Electronic transport in individual C_{60} peapods

As it was mentioned before (part 4.2.2.2), the electronic structures of encapsulated C_{60}s in carbon nanotubes have been subject to controversial theoretical studies during the last ten years. But till now, the results remain unfortunately puzzling and hardly comparable with experiment. To address this issue, we performed transport measurements on the several individual C_{60} peapods combined with a micro-Raman spectroscopy on the same devices. Our results suggest that the encapsulated C_{60}s induce a profound modification of the energy spectrum of the semiconducting external tube in the vicinity of the CNP. The experiments are consistently supported by numerical simulations of the Density of States (DOS) and the conductivity of the peapods developed by K.P. Katin and M.M. Maslov from National Research Nuclear University (MEPhI). Finally, on the very same devices, we investigate the effects on the electronic properties of a partial coalescence of C_{60} induced by UV irradiation.

4.3.1 Transport measurements and Raman spectroscopy

Samples were prepared and measured in accordance with the experimental methods described in the chapter 3. More than 40 samples were measured. AFM observations combined with Raman spectroscopy revealed that after deposition peapods with a metallic external SWCNT were presented in a small bundles or clusters and never as a single peapods, whereas those with semiconducting SWCNT have been found in bundles and as single peapods as well. Only individual peapods were chosen for the transport experiments in order to associate the C_{60}s influence on the transport properties with intrinsic structure of the SWCNT. The results are presented by four representative samples named here A, B, C and D.

AFM imaging used for the patterning of the electrical connection (Figure 4.19a) allows to measure the SWCNT diameters. The figure 4.19b illustrates this by showing the AFM z-profiles obtained at three different locations along the connected peapod, confirming a regular diameter of the order of 1.5 nm and then the presence of a single SWCNT.

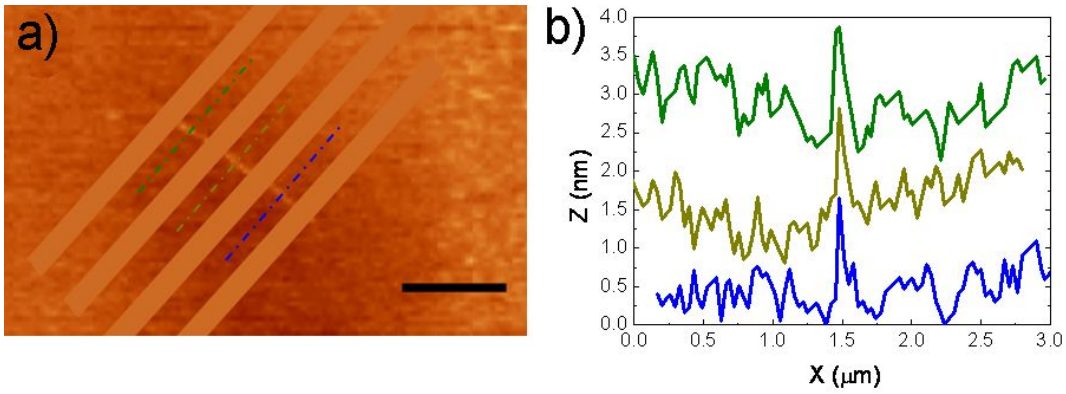

Figure 4.19: a) AFM image of an individual peapod connected to Pt electrodes (Sample A). The black bar corresponds to 500 nm. (b) AFM z-profiles have been measured between the contacts at three different locations marked by the dashed-dotted lines of corresponding colors. Profiles are up-shifted for clarity.

In addition to the AFM measurements, Raman spectroscopy with various excitation energies (2.33 eV, 1.94 eV and 1.58 eV) was used to determine the diameter and the nature, i.e. semiconducting or metallic, of the individual encapsulating SWCNTs. Indeed, it was proved by Shen et al. [Shen 2012] that by means of Raman spectroscopy using 1.94 eV and 2.33 eV excitation energies (532 nm and 638 nm wavelengths respectively), it is possible to discriminate metallic from semiconducting individual nanotubes respectively and this Raman-based determination was always consistent with the transport behaviours.

The four samples A to D exhibit a Raman fingerprint consistent with an individual semiconducting SWCNT (typically, the presence of a small G^- band (low

energy side) nearby a prevalent G^+ band (high energy side) see figure 4.21a-c-e-g). All of them exhibit clear Raman resonances under a 2.33eV excitation (black curves) while the spectra performed at 1.94eV (red curves) and 1.58eV (not shown) remain flat. The lack of Raman signal when using the 1.94eV and 1.58eV excitation energies truly means that no metallic CNT is present [Krupke 2003]. For sample A (Figure 4.21a), we deduce from the RBM and the G band splitting [Jorio 2002] a diameter value of 1.51±0.04 nm and 1.48±0.04 nm, respectively, in agreement with the AFM image. The presence of the resonant Raman response only under 2.33 eV excitation combined with the peapod diameter allow to identify, by using the Kataura plot (Figure 3.14), the external SWCNT as a semiconducting tube with a band gap E_g=0.54±0.02 eV. The same conclusion holds for all the samples (Figure 4.21). All parameters for these peapods are summarized in Table 4.1.

Sample	AFM ($\pm 0.5\ nm$)	RBM peak ($\pm 0.04\ nm$)	G band ($\pm 0.04\ nm$)	E_g ($\pm 0.03\ eV$)
A	1.5	1.51	1.48	0.54
B	1.4	1.41	1.47	0.56
C	1.5	1.40	1.46	0.56
D	1.5	–	1.53	0.53

Table 4.1: Diameters of the peapods obtained from AFM measurements and Raman spectroscopy (calculated from RBM and G peaks positions). The last column shows the values of band gaps for empty SWCNTs with the same diameters.

On the other hand, it is worth mentioning that our Raman spectra cannot provide evidence of the encapsulated fullerene. Indeed, the encapsulated C_{60}s can give a signal corresponding to the fullerene - Ag mode, located at 1462 cm^{-1} when excited with a wavelength lower than 488 nm [Rafailov 2003], however with an intensity of about 1% only of the intensity of the G^+ band of the containing SWCNT for the same wavelength. Hence, even for 488 nm, the signal/noise ratio is too low to expect to distinctly reveal the encapsulated fullerenes for individual peapods. Moreover, as the resonance of the individual containing-SWCNTs is checked with both 532 and 638 nm excitation wavelengths (instead of 488 nm), the fullerene signal definitely cannot be visible in our spectra.

Previously to the transport measurements, all devices were passed through the annealing procedure ($T = 100°\ C$) combined with continuous pumping during 12 hours ($P \approx 10^{-4}$ mbar). The general trend of the annealing effect is a slight decrease of the conductance along with a shift of the $G(V_g)$ curves toward the negative back-gate voltage. This can be seen on the figure 4.20, a zoomed view of the conductance versus gate voltage of the A sample.

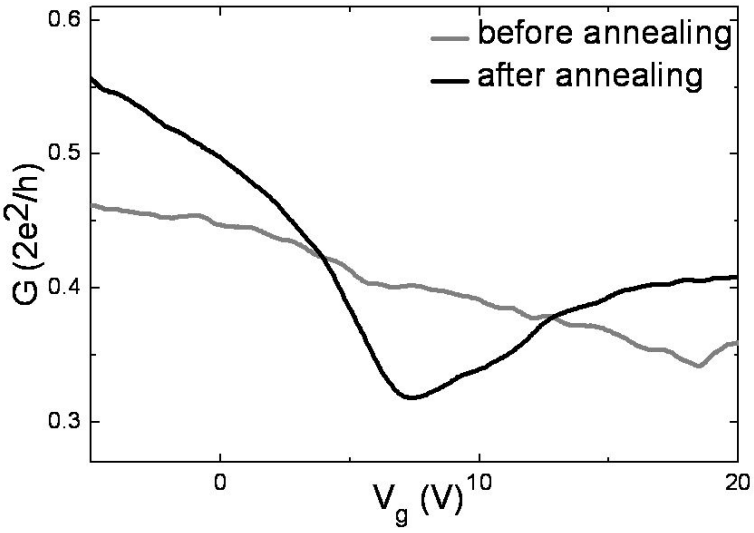

Figure 4.20: Sample A, conductance versus the gate voltage at 300 K before (gray curve) and after (black curve) annealing.

This is the expected consequence of the removal of p-doping adsorbates, most likely moisture and oxygen on to the device [Nanot 2009]. The conductance measurements $G(V_g)$ of the four samples are presented in the Figure 4.21b-d-f-h at various temperatures. The grey curves are the conductance at 300 K under ambient atmosphere, prior to the in-situ thermal annealing.

As it can be seen on the figure 4.21h, the annealing effect is out of the general trend for the sample D: the doping level of this sample was probably too high, which leaded to the increase of the scattering centers, this explains the low conductivity level before annealing. After annealing, the conductivity rises up by almost one order of magnitude, revealing a stronger back gate dependence and a minimum of conductance around 70 V, attributed to the CNP.

Remarkably, the devices exhibit a moderate gate voltage dependence of the conductance with no off-state of the peapod transistor, even at 4.2 K (shown for sample A, Figure 4.21b). The V-shape curves at 300 K and 77 K with their minima of conductance are not consistent with the aforementioned energy gap of the order of 0.8 eV/d(nm) (about 0.5 eV for our diameter range) deduced from Raman spectroscopy. Since the measurements are performed under controlled He atmosphere after thermal annealing, we rule out the possibility of a rigid shift of such an energy gap out of our gate voltage window (extended in some case to ± 70 V) due to unintentional doping by adsorbates. For most of the measured devices, the conductance at room temperature, under a negative back-gate voltage, reaches 0.6-0.8 G_0, with G_0, the quantum of conductance, equal to $2e^2/h$.

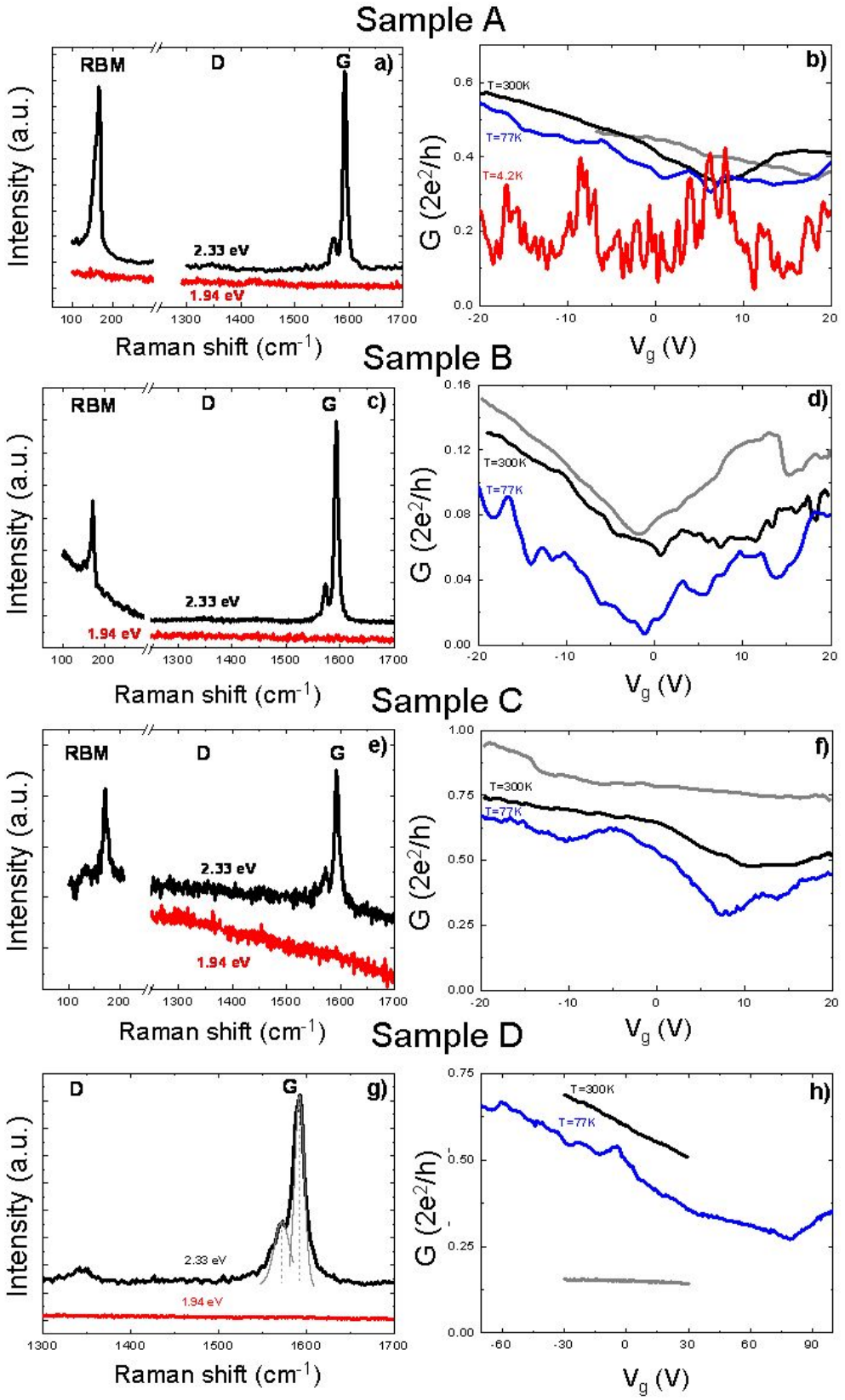

Figure 4.21: Raman spectra at 1.94 eV and 2.33 eV performed on samples A (a), B (c), C (e) and D(g) (zoomed on the G band, accenting G^+, G^- splitting). Conductance measurements of the same samples A (b), B (d), C(f) and D(h), versus back-gate voltage at different temperatures. The grey curves are the room temperature conductance measured before the in-situ annealing. The other measurements are performed under He atmosphere.

Using the Landauer formula [Datta 1995], we extract an underestimate value of the product $N \times l_e \approx 210$ nm, neglecting the contact resistance (N is the number of 1D sub-bands and l_e, the electronic mean free path). Considering a constant density of states between two Van Hove singularities and a back-gate coupling C_g between the tube and the substrate defined by

$$C_g = \frac{\pi \varepsilon_0 \varepsilon_{ox} L}{ln\,(4l_{ox}/d)} \tag{4.14}$$

we roughly estimate an electrostatic coupling of 20 meV/V for a twofold degenerate channel and deduce $N \approx 6$ at $V_g = -20\ V$, giving rise to a low limit of l_e equal to 35 ± 5 nm. Note that if one considers a contact resistance in the range of few kOhm, the electronic mean free path would be 25% larger but its order of magnitude remains the same. The large aperiodic oscillations that develop at 4.2 K (Figure 4.21b) are strongly thermal cycling dependent, signature of Universal Conductance Fluctuation (UCF). Assuming a 1D system, we consider [Beenakker 1988]

$$\delta G_{rms} = \sqrt{6} \left(\frac{L_\varphi}{L} \right)^{3/2} \frac{e^2}{h} \tag{4.15}$$

from which we deduce a phase coherence length $L_\varphi \approx 50\ nm$. Both l_e and L_φ unveil a diffusive regime and are rather standard values for unfilled semiconducting SWCNT. This demonstrates that the chemical steps to open the tubes prior to the filling process and encapsulating the C_{60} do not significantly enhance the electronic scattering. However, the Raman spectroscopy analysis along with the absence of the expected transport gap on the devices directly address the longstanding controversy of doping effects of fullerenes in the vicinity of the CNP.

4.3.2 Calculation of the DOS

DOS has been calculated by K.P. Katin and M.M. Maslov from National Research Nuclear University (MEPhI) in the case of empty and partially filled nanotube, with very close geometrical characteristics (diameter) compared to the peapod investigated here.

Nonorthogonal tight-binding method [Maslov 2009], which correctly describes a band gap in graphene and graphene nanoribbons [Podlivaev 2011] can be used to explore peapods electronic structure. In this case peapods conductivity can be calculated as a transmission of the system using the Green's function approach combined with the extended Hückel model [Hoffmann 1963]. This model, less demanding of computer cost, can not provide sufficient accuracy in absolute values of electronic energy levels, but ensure their regular alternation. Despite of its simplicity, this approach provides almost as accurate results of transport calculations as more sophisticated ab initio approaches [Tian 1998]. The computations details can be found in the Annex A.1.

To deeply understand the peapod electronic structure the DOS of an unfilled (10,12) SWCNT (black curves) and a (10,12) SWCNT filled with C_{60} (red curves)

was investigated (Figure 4.22). The (10,12) indexes are chosen as possible chirality in accordance with the nanotube radius deduced from the resonant micro-Raman spectroscopy. The length of the SWCNT is optimized at L=2 nm for convergence. Edge carbon atoms are passivated by hydrogen to avoid dangling bonds at the nanotube ends. Thus, the empty nanotube is represented as a $C_{476}H_{44}$ cluster. The energy band gap for this system estimated from the black curve (Figure 4.22) is around 0.54 eV, which is close to the expected value for (10,12) SWCNT.

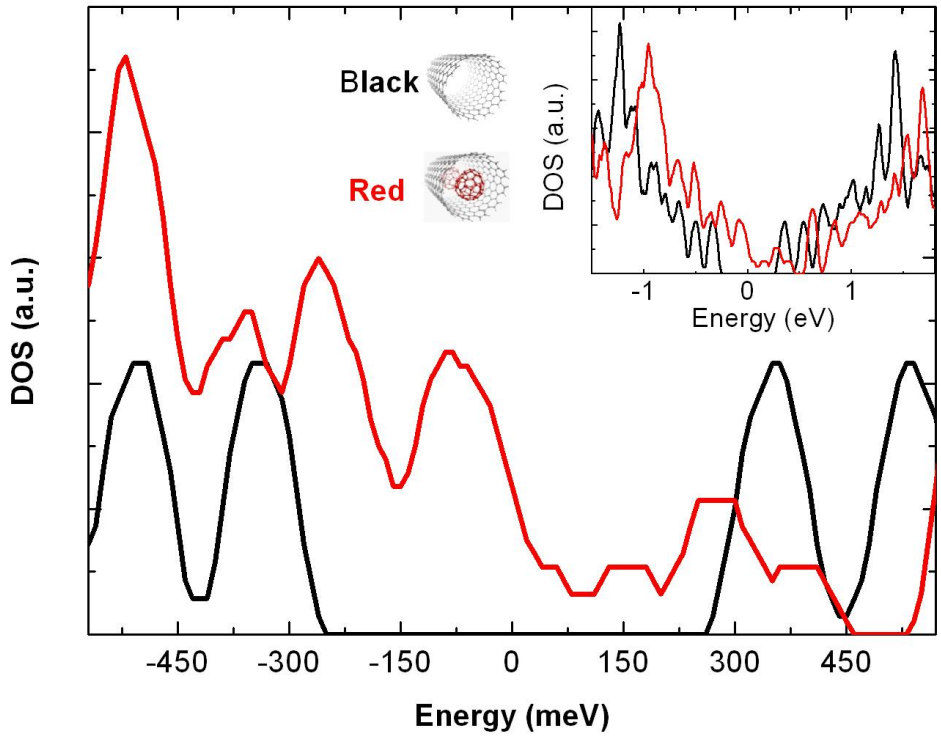

Figure 4.22: The DOS calculated for an empty (12,10) SWCNT (black curve) and for the same tube filled with two C_{60} (red curve). The inset is an extended scale over a larger energy range.

Then, the system is filled by one fullerene. The simulation clearly demonstrates that the encapsulation of C_{60} significantly influences the DOS, showing both a charge transfer and the occurrence of new states partially filling the energy gap of the tube. It was considered a set of different C_{60} isomers obtained from the ideal buckminsterfullerene by the Stone-Wales transformations. The energy shift induced by the electron transfer from the tube to the fullerene varies from 0.1 to 0.3 eV as a function of the type of C_{60} isomer. Adding one more fullerene into the nanotube enhances

this trend. As a result, the simulation strongly supports a shift of the electronic structure toward higher energies along with the appearance of an impurity band that significantly shrinks the energy gap of the SWCNT, as a consequence of the encapsulated C_{60}.

4.3.3 Magnetotransport

We next address the electronic band structure of our devices by magneto-transport experiments. Magneto-resistance measurements under a large magnetic field parallel to the carbon nanotube axis reveal its 1D electronic sub-bands and their magnetic field modulation, through the well-know Arahonov-Bohm (AB) effect [Bachtold 1999]. The expected energy band gap modulation for a pristine metallic and a semiconducting CNT are depicted on the figure 4.23.

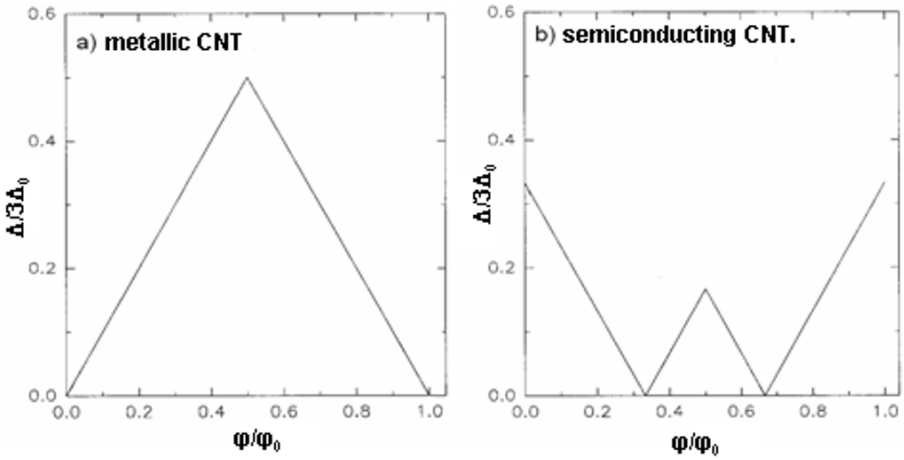

Figure 4.23: Modulation of the energy band gap as a function of the magnetic flux threading for a) a metallic, b) a semiconducting CNT. Here, Δ is a magnetically induced gap, $\Delta_0 = \gamma_0 a_{C-C}/d$ (see eq. 4.12) and $\varphi_0 = h/e$ is the magnetic flux quantum. Taken from [Jiang 2000].

In our study, we apply a 55T magnetic field on two samples, A and D at 77 K, under various back-gate voltages (Figure 4.24, left and right). A drastic reduction of the conductance in the high field regime is observed around the minimum of conductance, 5 V (Figure 4.21b) and 70 V (Figure 4.21h) for sample A and D, respectively.

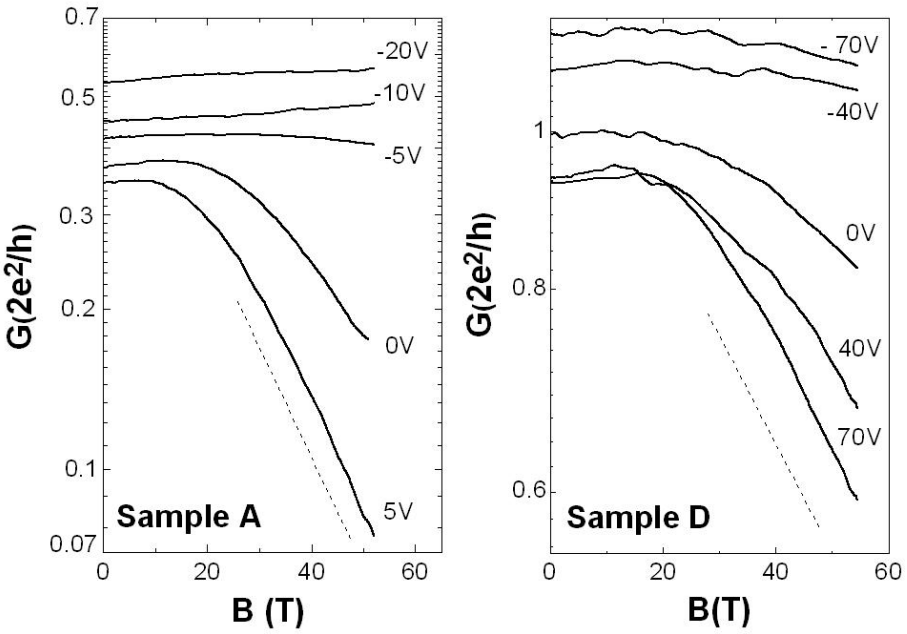

Figure 4.24: Magnetoconductance measurements under a magnetic field parallel to the tube axis, at 77 K for different back-gate voltages (left and right panels correspond to sample A and D). The dotted lines illustrate the exponential decrease of the conductance in the vicinity of the CNP.

At lower V_g, the magnetoconductance (MC) is almost insensitive to the magnetic field. At first glance, a large negative MC in the vicinity of the CNP may suggest an energy gap opening $E_g(B)$ due to AB modulation of the allowed $k\perp$ states of a metallic tube. For a diameter of 1.5 nm, $E_g(B)$ equals to 0.7 meV/T [Fedorov 2007]. Here, assuming a flat band model, the slope of the linear decrease of the logarithm of the conductance (dotted lines, Figure 4.24), corresponds to an energy gap opening of 0.6 and 0.2 meV/T for samples A and D, respectively. These values are comparable but lower than the expected one in the AB picture. Nevertheless, the AB scenario for a negative MC around zero energy requires a metallic CNT, which is excluded from the Raman spectroscopy. At this stage, we tentatively explain the magnetoconductance by a magnetic field-induced shrinkage of the C_{60} wave functions.

This effect, observed in the hopping regime of doped semi-conductors [Shklovskii 1984], is the result of the contraction of the impurity wave-function in the plane perpendicular to the magnetic field. It is responsible for an exponential decrease of the magneto-conductance [Mikoshiba 1962]. Close to the CNP, the conduction occurs through the electronics states induced by the encapsulated C_{60}s. The magnetic field squeezes the associated orbitals reducing thus the overlap with the CNT states and giving rise to the observed exponential decrease of the conductance, gradually

restoring the energy gap of the semiconducting shell. Away from the CNP, the electronic states involved in the conduction process are band states which are much less sensitive to the magnetic field.

4.3.4 UV irradiation effects

Coalescence of the C_{60}s induced by UV-laser irradiation (see part 4.2.3) can be used as a powerful tool for redistribution of fullerenes inside the peapod. The C_{60}s configuration has a strong impact on the electronic transport properties of the peapod, as it was shown by Kondo et al. [Kondo 2005]. To explore this effect we undertake to modify the structure of the encapsulated fullerenes by UV-irradiation.

4.3.4.1 Coalescence of C_{60} revealed by Raman spectroscopy

For this purpose, we irradiate the connected peapods (samples A and D) with a $4.5mW$ UV laser at 335 nm and a $\times$ 40 objective during 20 s and under ambient conditions. Using Raman spectra from the work of Berd et al. (figure 4.18 [Berd 2012]) as reference, we study the Raman spectra of the peapods before and after the irradiation (Figure 4.25, sample A).

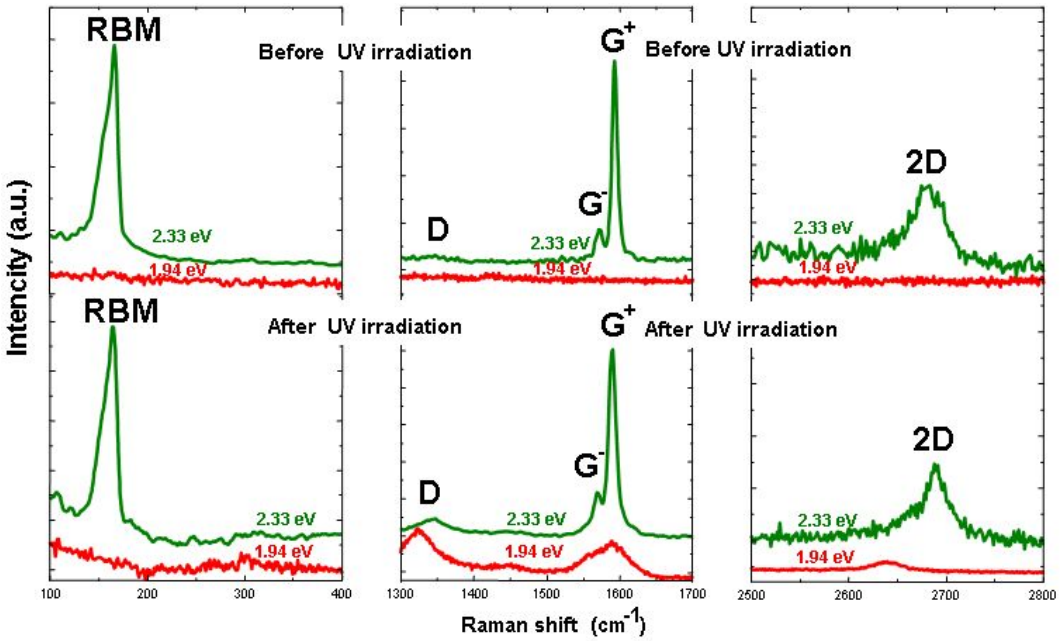

Figure 4.25: Raman spectra at 2.33 eV (green) and 1.94 eV (red) excitation energies before and after UV irradiation on the sample A.

We see that, after irradiation, the Raman spectra for 2.33 eV excitation energy still confirms the semiconducting external shell.

RBM: the RBM peak keeps its position and we do not observe any new peaks corresponding to the inner tube. This is not so much surprising, as RBM signal is relatively weak and not always easy to observe. Additionally, as we are working with an individual peapod, amount of the material may be not enough to obtain a good signal/noise ratio. For example, appearance of the 7 nm-length or shorter inner tubes is too close to the resolution limit of the Raman spectroscopy and could be hardly seen.

D and G bands: for 2.33 eV excitation energy, we notice the increase of the D-band, which reveals the emergence of a laser-induced disorder related to the partial coalescence and the redistribution of the C_{60} inside the peapod. Together with the D band increase the G-band manifests the very beginning of the G^+ – G^- bands merging, confirming the beginning of the fullerenes coalescence [Puech 2007]. For a 1.94 eV excitation energy we see the appearance of the resonant Raman signal, which did not exist before, associated with a modification of the fullerenes. The large D-band over G^- band ratio indicates the incompleteness and defectiveness of the created inner structure.

2D band: the $2D$ band modification for the 2.33 eV excitation energy are not so remarkable, but still, we can notice the elongation of the left shoulder toward 2650 cm^{-1}. For the 1.94 eV excitation energy, we also clearly see the appearance of the $2D$ band signal.

Thus, the most prominent modifications of the Raman spectra for irradiated peapods were observed for the D and G bands. By increasing the laser power three times (Figure 4.26, Sample D, left panel), we achieve the very beginning of the C_{60} coalescence unveiled by the more pronounced G^+ – G^- bands merging.

At the same time, the two irradiated samples undergo a huge decrease of their conductance by more than two orders of magnitude whatever the back-gate voltage, signature of a strongly diffusive regime. For Sample A, the very low conductance goes along with more pronounced temperature dependence and some fingerprint of an ambipolar behavior versus V_g at the edges of our energy window.

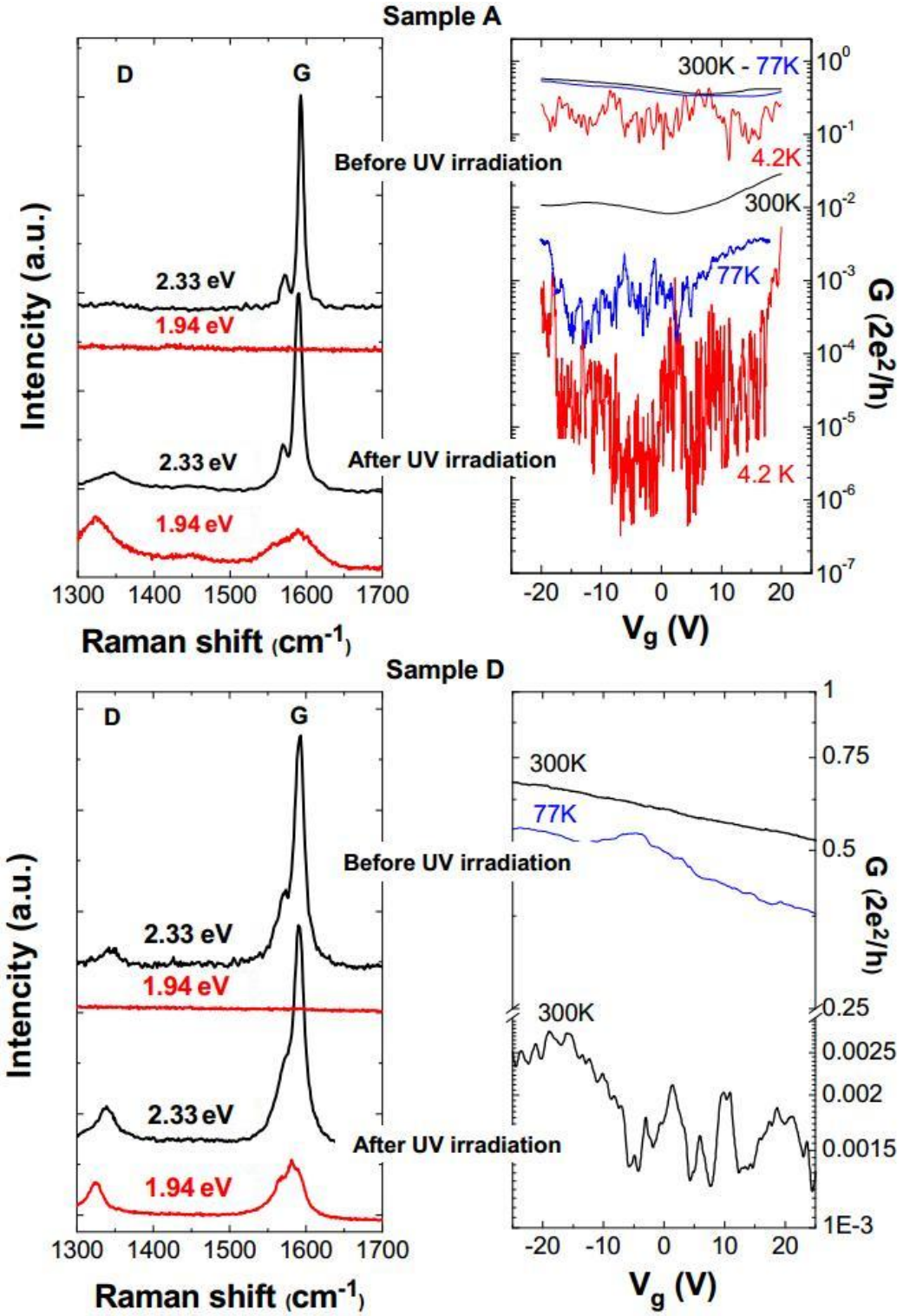

Figure 4.26: Raman spectra at different excitation energies and conductance measurements versus V_g at different temperatures, before and after UV irradiation on two samples A and D (top and lower panels, respectively).

4.3.4.2 Fullerenes redistribution effect on the electronic transport

K.P. Katin and M.M. Maslov simulated the impact of the coalescence of the C_{60} on the electronic transport by calculating the conductance at zero energy for two model systems: (i) a C_{60}@(10, 12)SWCNT peapod of diameter d=1.51 nm, length l=4.5 nm and containing five C_{60} fullerenes and (ii) a similar system for which the five fullerenes are replaced by one dimer and one trimer as illustrated in Figure 4.27.

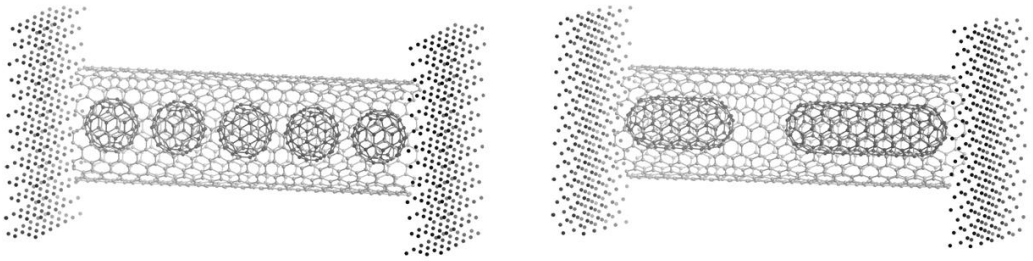

Figure 4.27: Illustration of the simulated system for the calculation of the conductance, before (left panel) and after UV irradiation (right panel) responsible for the partial coalescence of the C_{60}.

The platinum contacts are included in the simulation; each contact consists of 322 atoms. Huckel Hamiltonian is calculated within the program package [Landrum 2006] (2S, 2P orbitals for carbon atoms and 6S, 5P, 5D orbitals for platinum atoms are considered). The parameters describing the orbital extensions and energies for carbon and platinum atoms are taken from [Maslov 2009] and [Ditlevsen 1993], respectively. We obtain a conductance of 0.6 G_0 for the ideal peapod with equispaced C_{60}, while the presence of a dimer and a trimer inside the tube (Figure 4.27) yields to a drastic drop of conductance down to 0.006 G_0. These simulated values qualitatively support the scenario that the low conductance, after irradiation, is related to the C_{60} coalescence into short and irregular segments, which was confirmed by the HRTEM images. Because of the periodicity break, the segments of coalesced C_{60} inside the tube do not contribute any more to an impurity band and they mainly behave as scattering centers [Kondo 2005]. In between the coalesced C_{60}, the local DOS of the semiconducting tube is restored. Note that it is also likely that the presence of defects on the outer shell induced by the irradiation performed under ambient condition, as confirmed by the emergence of the D-band, contributes to the strong diffusive regime.

4.4 Conclusion

We have measured Raman spectra and transport properties on individually connected peapods. A majority of the devices exhibit a semiconducting type resonant Raman spectrum while the conductance shows no hint of an energy gap in the range

of a fraction of eV. Our experimental results, supported by numerical simulations, bring evidence of a significant doping effect of the encapsulated C_{60}, including a rigid shift of the band structure and a partial filling of the energy gap. The drop of the high magnetic field conductance close to the CNP could be the signature of the field-induced shrinkage of the electronic states generated by the C_{60}. UV irradiation induces a partial coalescence of the C_{60}s onto segments of various lengths which drastically modify the electronic coupling between the C_{60}s and the carbon nanotube. The loss of the periodic distribution of the C_{60}s inside the CNT results in a reduced conductance.

Chapter 5

Magnetotransport in indium arsenide nanowires

Sommaire

This Chapter is devoted to the investigation of the band structure of InAs nanowires through high field magnetotransport. The interpretation of the experimental data is supported by numerical simulations performed by Yann-Michel Niquet from Institut Nanoscience and Cryogénie (INAC/CEA). The measurements were performed on nanowires with two diameters, 30 nm and 80 nm, in a wide temperature range, applying a magnetic field up to 55 T in a FET configuration.

5.1 Introduction on semiconducting nanowires

Semiconducting nanowires have unveiled a wide range of interesting optical and transport properties that have allowed to create various NW-based devices such as $p-n$ and resonant tunneling diodes, bipolar and field-effect transistors, detectors, etc [Cui 2001, Ohlsson 2002, Doh 2005]. Besides all specific properties of semiconducting material NWs exhibit additional features caused by the confinement. For example, strong alterations of the band structure lead to the transition from nondirect to direct bandgap semiconductor for certain materials. These properties combined with high carrier mobility and a tunable band gap give an opportunity to create single electron transistors, resonant-tunneling diode, high-frequency-operating devices, photodiodes, light-emitting-diodes, etc.

Another interesting aspect of the semiconducting NWs is their potential application in the field of spintronics. Spin degrees of freedom attract researcher's attention for a long time, since the electron spin, being a superposition of two states, can represent a unit of quantum information - qubit. This idea of spin logic was formulated

in the second part of the last century but still was not realized due to the absence of effective mechanisms to control the spin of charge carriers by the light or applied electric field. The spin-orbit (SO) interaction, which couples the translational motion and the spin rotation of the quasiparticle, gives such opportunity to influence the spin by electromagnetic radiation or electric current. On the basis of these ideas, a new area emerged and has been widely developed during the last ten years - semiconductor based spin electronics. The building block of the semiconductor spintronics are low-dimensional quantum structures: quantum wells, nanowires, and quantum dots. These structures can be produced with specific electronic properties, which makes possible to control the orbital and spin degrees of freedom of carriers.

A distinctive feature of the bulk InAs is a large value of the SO interaction, a high electron mobility (up to 30000 $cm^2/(Vs)$ at room temperature), a small effective mass of charge carriers (m^*=0.023m_e) [Dayeh 2010] and the presence of the surface accumulation layer, which makes it interesting for electronic applications with high-speed performance and low power operation. Low-dimensional structures based on InAs are characterized by a spin splitting in the energy spectrum, which is higher than in the structures based on semiconductors with lager band gap as Si and GaAs. This spin splitting exists even in the absence of a magnetic field and originates from the large value of the SO interaction in InAs. Nonparabolic energy-momentum law leads to new spin-dependent effects, which is inaccessible for a classical structures with parabolic subbands [Golubev 1985, Zawadzki 2004, Krishtopenko 2012]. An important feature of the InAs structures is the possibility to control various spin-dependent phenomena by applying an electric field to the structure via Bychkov-Rashba effect, which makes them attractive for the spintronic application such as construction of spin filters and spin transistors. Thus, quasi-1D electronic confined system such as InAs NWs are promising materials as versatile building blocks for future application in spintronics. Experimental and theoretical studies of such structures are one of the current problem in semiconductor physics.

A detailed investigation of the band structure is a key issue to understand the electronic transport in InAs nanowires. In this work, we perform magnetotransport measurements on individual InAs NWs in order to unveil the signature of the 1D electronic band structure on the conductance.

5.2 State of art on InAs NWs

5.2.1 Growth process and crystallographic structure of InAs NWs

The first report on InAs whiskers synthesis via vapor growth was done by Antell and Effer in 1959 [Antell 1959]. Later, in 1966, InAs whiskers were obtained using Au and Ag catalysis through chemical vapor deposition (CVD) technique [Takahashi 1966]. Furthers, a variety of growing techniques were proposed: chemical and molecular beam epitaxy, laser ablation, metalorganic vapor phase epitaxy (MOVPE) and low-temperature solution techniques. The discovery of the vapor-

liquid-solid (VLS) mechanism by Wagner and Ellis [Wagner 1964], gave a significant boost to the understanding of the whiskers synthesis. The VLS approach allowed the synthesis of high-quality NWs from the variety of usual semiconductor materials and, moreover, it enables to modulate the NW composition along the growth axis, which allows to embed quantum dots into NW or to create core-shelled one-dimensional structures. VLS grown NWs have quickly attracted the attention of numerous researchers, offering the possibility to investigate the physical properties of quasi-1D systems. For example, MOVPE technique, which allowed to fabricate high quality nanowires with diameters down to 20 nm [Koguchi 1992, Yazawa 1993], is based on the VLS mechanism. Among others, such as vapor-solid-solid, solution-liquid-solid, vapor-solid, this is the most widely used mechanism to grow InAs NWs.

The vapor phase, consisting of $In(CH_3)_3$ and AsH_3, forms a supersaturated liquid alloy inside a metallic nanoparticle catalyst (mostly In or Au). It precipitates at the liquid-solid interface and forms the NW crystal. Additional material fluxes contribute to the longitudinal and to the lateral growth (Figure 5.1).

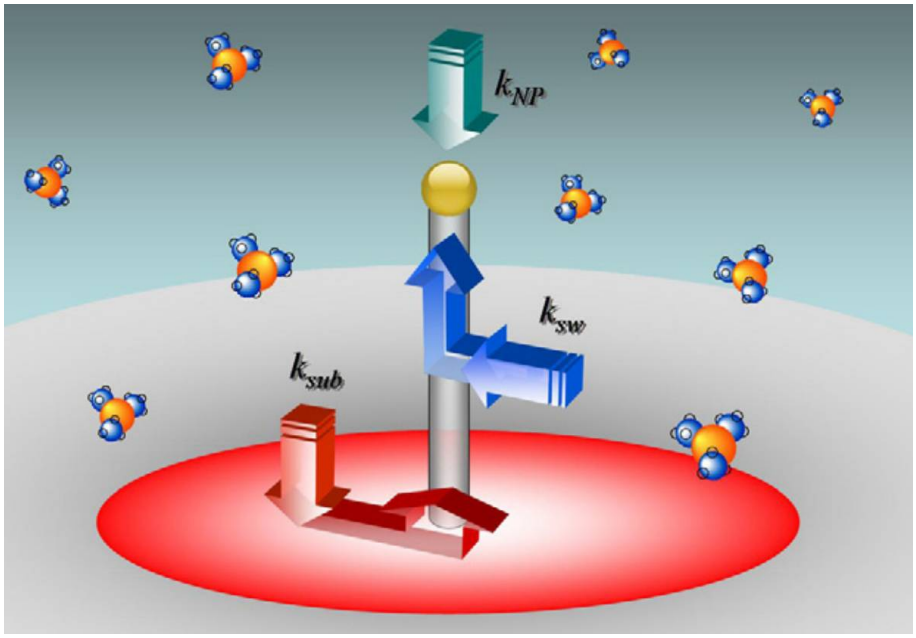

Figure 5.1: VLS growing mechanism with three types of material contribution: via the nanoparticle, the NW sidewalls, and the substrate growth; k_{NP}, k_{sw}, and k_{sub} are the growth rate of each contribution respectively. From [Dayeh 2009a].

The impact of each flux is proportional to the collection area and also depends in a complex manner on different growth parameters such as the molar ratio of $In(CH_3)_3/AsH_3$, the growing time, the temperature, the pressure, etc.

The crystallographic structure of InAs NWs depends also on these parameters and can change from zinc-blende (ZB), face-centered cubic lattice (Figure 5.2a), to wurtzite (WZ), hexagonal close packed lattice (Figure 5.2c). The dark and bright

regions on the cross-sectional TEM images of InAs NW (Figure 5.2d,e) correspond to these two crystal structures. The crystallographic change is caused by a [111] rotating twin. The ZB structure with one [111] rotating twin is presented at the figure 5.2b: atomic arrangements on the (111) plane are 180° rotated around [111] axis at the twin boundary. Thus, we obtain a monolayer of the WZ type crystal in ZB structure. If such rotating twins occur at every (111) ZB plane, these planes become (001) WZ planes and the crystal type changes completely from ZB to WZ. The lattice constants for ZB and WZ III-V crystals and the potential energy of (111) ZB planes and (001) WZ planes are very close to each other [Koguchi 1992], which allows the co-existence of WZ and ZB structures under same growth conditions.

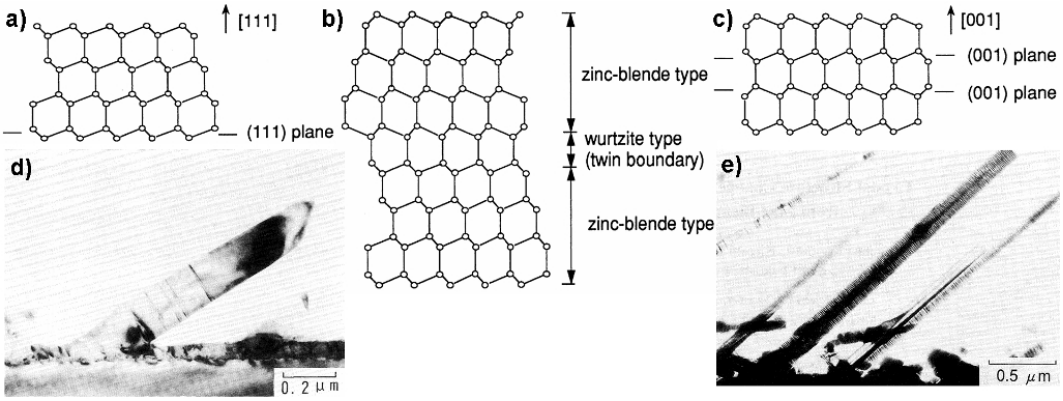

Figure 5.2: Crystal structure: a) zinc-blende type, b) twin structure of zinc-blende type and c) wurtzite type; d) and e) cross-sectional TEM images of InAs NW grown at different substrate temperatures and gas molar flow ratio. From [Koguchi 1992].

Properly selected growth parameters allow to produce single crystal InAs NWs containing only one crystallographic structure, that is of interest for transport experiments.

5.2.2 Electronic transport properties of InAs NWs

5.2.2.1 Accumulation layer and electron mobility problem

The first transport studies on InAs NWs (d=60 nm) were performed by Ohlsson and co-workers [Ohlsson 2002] on a two terminal FET configuration. The obtained mobility of those wires was of the order of 100 $cm^2V^{-1}s^{-1}$. Such low value compared to the bulk one (30 000 $cm^2V^{-1}s^{-1}$) was explained by the presence of impurities and staking faults. A technical progress of the growing technologies improved the crystal quality of the InAs NWs, which led to an increase of the electron mobility. In 2005, reports of high electron mobility observed on the vertical wrap-gated and flat

top-gated transistors based on InAs NWs [Bryllert 2005, Dayeh 2005, Dayeh 2007a] were published. Lower bound of the mobility in both cases was estimated as 3000 $cm^2V^{-1}s^{-1}$.

The near-surface accumulation layer, which existence was well known for bulk InAs material, provides the possibility to make good ohmic contacts for the InAs based devices. Once the structure's size shrinks down and the thickness of this layer starts to be comparable to the NW diameter, a significant impact on the NW transport properties is expected [Ford 2009, Dayeh 2009a]. The depth of this layer was estimated from 10 to 20 nm depending on the NW diameter (Figure 5.3a).

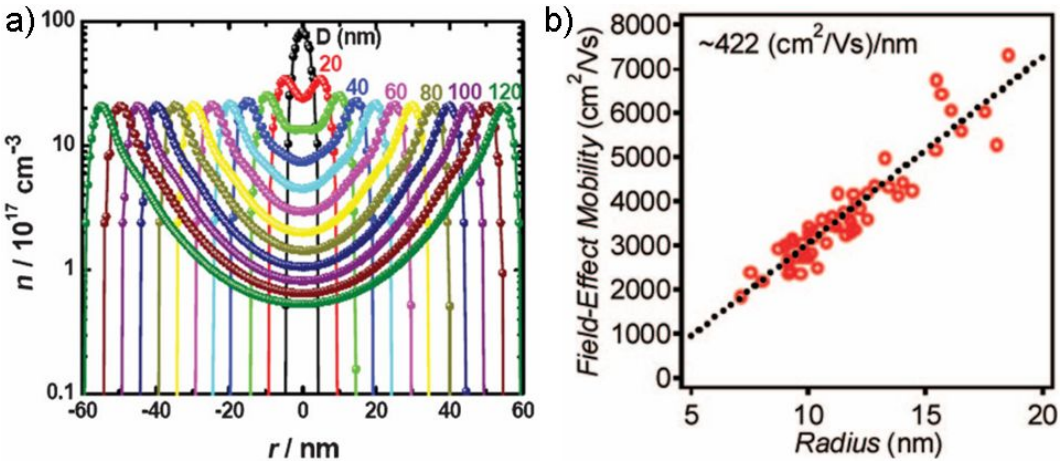

Figure 5.3: a) Free carrier distribution along the channel for different NW diameters obtained by the Schrödinger–Poisson solver in one dimension. From [Dayeh 2009b]. b) Field–effect mobility as a function of radius measured on more than 50 different InAs Nw-based devices. From [Ford 2009].

The presence of the accumulation layer led to an idea, that the carrier transport mainly takes place in a tube-like 2D surface electron gas like in InN nanowires [Richter 2008]. This model was also supported by the lower values of mobility and higher average carrier densities n_{av} obtained on small-diameter NWs, explained by the increase of the scattering effect in the electron surface accumulation layer. While larger-diameter NWs, having more bulk-like transport properties, show higher mobility and lover n_{av} values.

Thus, surface-state effects requires a detailed consideration, as they play an important role in the transport properties of nano-devices. From the one side, the surface-states can introduce coulomb scattering centers and thus reduce the field effect mobility (Figure 5.3b). On the other side, the presence of the accumulation layer reduces the gate capacitance, which leads to lower transconductance and lower switching rate of the NW-based devise. In addition, the charge capture and emission from interface states during the gate sweep alter the threshold gate value, induce

a hysteresis in the FET transfer curves and smooth the on/off switching characteristics. The above-mentioned effects cause a problem for an accurate estimation of the field-effect mobility and carrier concentration in semiconductor NWs, taking into account the accumulation layer, leakages and interface-state capacitance. The influence of these parameters on the InAs FET transport properties is considered in details in the publications of S. A. Dayeh and A. C. Ford [Dayeh 2007b, Ford 2009]. As a positive side, we can notice strong changes of conductance depending on the NW environment due to the presence of the surface states, which can be desirable for NW applications as photodetectors and highly sensitive sensors [Cui 2001].

5.2.2.2 Phase-coherent transport and spin-orbit interaction

Electronic transport measurements at low temperatures in low dimensional systems or in a weakly diffusive materials usually reveal the phase coherence of the electronic wave functions participating to the transport. The phase coherence manifest itself through the universal conductance fluctuations (UCF) and the quantum corrections to the conductance (weak localization and weak anti-localization).

The phase-coherent transport in InAs NWs, studied through the universal conductance fluctuation as a function of electric and magnetic fields, reveal a large phase-coherence length L_φ, reaching 450 nm at 0.5K [Blömers 2011], confirming the good crystallinity of the NWs. Indeed the stacking faults revealed in NWs by HRTEM are responsible for elastic scattering and reduce L_φ only indirectly through the reduction of the diffusion coefficient. A large value of $L_\varphi \sim 250$ nm at 8 K was also confirmed by the study of the weak localization in perpendicular magnetic field on 60 nm diameter InAs NWs [Hansen 2005].

The observation of a crossover from weak localization (WL) to weak anti-localization (WAL) regime in InAs NWs (Figure 5.4) driven by a back gate voltage [Hansen 2005] induced a lot of studies devoted to spin relaxation effects [Dhara 2009, Roulleau 2010, Liang 2012]. The spin relaxation length in InAs NWs has been estimated from several tens of nm to more than one hundred nm, depending on the gate voltage (L_{SO} from 40 nm to 160 nm [Liang 2012]).

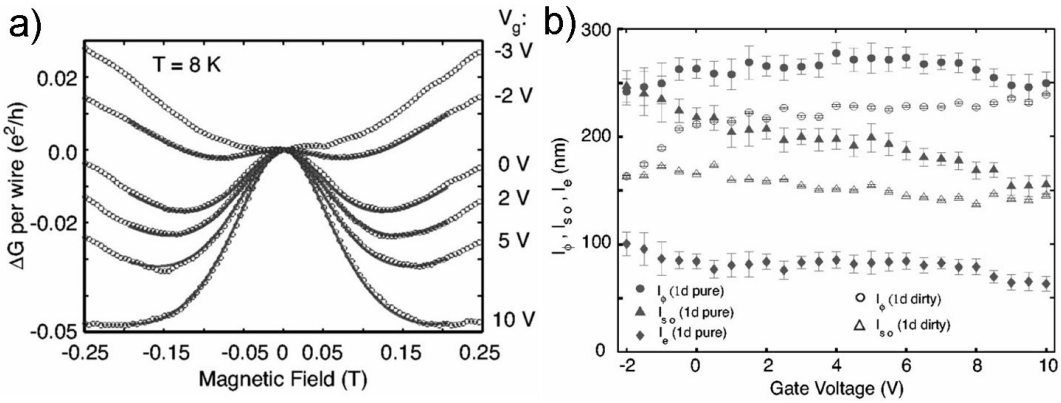

Figure 5.4: a) The average magnetoconductance per NW, measured on an array of 45 InAs NWs, offset to zero at zero magnetic field. A crossover from WAL to WL takes place as the gate voltage is decreased. b) The L_φ, L_{SO} and l_e extracted from the fits of the measured magnetoconductance, as a function of the applied back gate voltage. The filled symbols are obtained using "pure" limit approach ($l_e \ll d_{NW}$) and the open symbols using "dirty" limit approach ($l_e \gg d_{NW}$). From [Hansen 2005].

The WL–WAL crossover and the spin relaxation length L_{SO} are generally attributed to the Dyakonov-Perel spin relaxation mechanism due to the lack of inversion center [Hansen 2005, Roulleau 2010]. This lack of inversion symmetry combined with the spin-orbit interaction creates an effective magnetic field, which changes in random directions when the electron scatters to a state with a different momentum. In a more general case, we should consider both types of asymmetry: bulk-induced asymmetry, which leads to the Dresselhaus spin splitting effect [Dresselhaus 1955] and structure inversion asymmetry induced by the electric field, which leads to the Bychkov-Rashba spin splitting effect [Rashba 1960, Bychkov 1984b, Bychkov 1984a]. For InAs NWs, the contribution of the Dresselhaus effect is negligible compared to the Bychkov-Rashba effect or vanishes completely along the <111> directions of the NW axis [Žutić 2004].

Among others spin relaxation mechanisms in the absence of magnetic impurities (Elliott-Yafet, Bir-Aronov-Pikus and Hyperfine-interaction mechanisms), the Elliott-Yafet mechanism [Elliott 1954] may be relevant in our system, as it is important for small-gap semiconductors with large spin splitting [Žutić 2004]. In this mechanism, the electron wave function is considered to contain a mixture of two opposite-spin states, due to the spin-orbit coupling induced by the lattice ions. This provides a spin-flip scattering mechanism via momentum scattering on phonons or impurities.

Additionally, the transition from low to high electron density changes the relative contribution of bulk and surface electrons in InAs NW. This was proposed as a

possible explanation of the L_{SO} tunability by the gate voltage [Dhara 2009].

5.2.2.3 Band structure effects on the electronic magnetotransport properties

As it has been mentioned (part 2.4.6), large research efforts have been made to analyze the electronic transport properties of nanowires [van Wees 1988, Bogachek 1993, Bogachek 1994, Bogachek 1996, Scherbakov 1996, Debald 2005, Tserkovnyak 2006]. Sharp modulations of the conductance have been predicted at low temperatures on the scale of a fraction of a flux quantum Φ_0 – a new scale for a mesoscopic phenomena. Moreover, at low doping levels, Bogachek et al. [Bogachek 1996] predicted a magnetic switch effect and the occurrence of a magnetic quench of the quantum transport in nanowires.

The magnetotransport behaviour, in a simplified approach, may be considered through the Einstein relation for the conductivity:

$$\sigma(E,B) = e^2 D(E,B) DOS(E,B) \tag{5.1}$$

In a weak magnetic field the magnetoconductivity is mainly governed by the diffusion coefficient $D(E,B)$. Conductance measurement constitutes a well known technique to unravel the electronic transport regimes and the related characteristic lengths, like the electronic mean free path and the phase coherence length. During the last 10 years, magnetotransport experiments on InAs NWs under weak magnetic fields ($L_m \gtrsim d_{NW}$), were mainly focused on the magnetic field dependence of UCF and on the weak antilocalization (WAL) - weak localization (WL) crossover [Hansen 2005, Dhara 2009, Liang 2009, Estévez Hernández 2010, Roulleau 2010, Liang 2010, Blömers 2011, Liang 2012]. In the high magnetic field regime ($L_m \ll d_{NW}$), the modulation of the density of states at the Fermi energy may significantly impact the magnetoconductivity.

An additional parameter complicating the problem is the fact that, the carrier concentration in semiconducting InAs NWs is not homogeneous in the NW cross-section and tends to create a surface accumulation layer. The group of Tserkovnyak et al. [Tserkovnyak 2006] addressed this issue considering the conductance of quasi-1D NWs with electronic states confined to a surface-charge layer in both parallel and perpendicular magnetic fields. They unveiled the prominent magnetoconductance features, which are related to the positions of Van Hove singularities in 1D DOS (Figure 5.5).

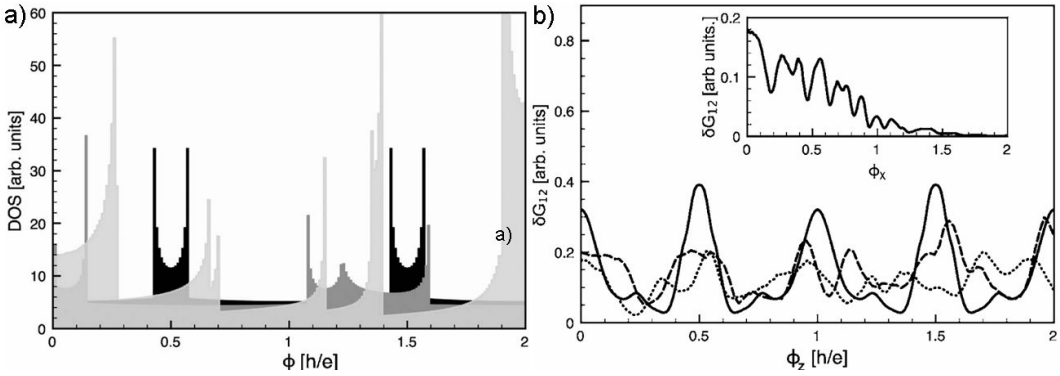

Figure 5.5: a) The total density of states as a function of the parallel and perpendicular magnetic field. $B_{\|}$: black histogram – an idealized shell modell; dark-gray histogram – a shell model including Zeeman splitting and spin-orbit coupling. $B_{\perp}$: light-gray histogram – triangular-well model . b) The main panel shows the MC in the parallel magnetic field calculated using the same parameters as the histogram in the a-panel: the solid line corresponds to the black histogram, the dashed line – the dark-gray histogram, and the dotted line – the light-gray histogram. The inset shows a calculation similar to the dotted line in the main panel but for the perpendicular magnetic field. From [Tserkovnyak 2006].

It was also determined, that the aperiodicity of magnetoconductance fluctuations is caused by the Zeeman splitting, which is vanishing in the case of very narrow confinement. At large magnetic fields, a quench of the conductance is also predicted in agreement with previous studies [Bogachek 1996].

Among the theoretical studies of InAs NWs, the work of Debald et al. [Debald 2005] should be mentioned. It considers the influence of a perpendicular magnetic field on the transport properties of a ballistic NWs, taking into account the Zeeman splitting and the Rashba effect. It evidenced that the magnetoconductance behaviour is strongly linked to the relation between three length scales: the geometrical confinement l_0, the magnetic length $l_B = \sqrt{\hbar/(m\omega_c)}$, and the relaxation length due to the spin-orbit interaction $l_{SO} = \hbar^2/(2m\alpha)$.

These theoretical investigations unveil the direct link between the magnetoconductance behaviour in the high field regime and the electronic band structure. To the best of our knowledge, there is no published data on high magnetic field experiments, requiring the pulsed magnetic field technique, to explore the electronic density of the states and the related 1D band structure in semiconducting NW.

5.3 Experimental study of the electronic transport in InAs NWs

In this work, we studied the transport properties of the InAs NWs with two range of diameters, 33 ± 5 nm and 80 ± 5 nm. The 30 nm and 80 nm diameter InAs NWs were grown using epitaxy techniques and electrically contacted in a FET configuration on a Si/SiO_2 substrate by Renaud Leturcq and Philippe Caroff from Institut d'Electronique, de Microelectronique, et de Nanotechnologie (IEMN) and by Lucia Sorba and colleagues from NEST laboratory of Istituto Nanoscienze CNR and Scuola Normale Superiore, respectively. According to the TEM observations (Figure 5.6), in both cases the InAs NWs are single crystals of wurtzite crystallographic structure with <0001> growing direction. More detailed description can be found in the part 3.1 and in the works of Pfund et al. [Pfund 2006] and Heun et al. [Heun 2010].

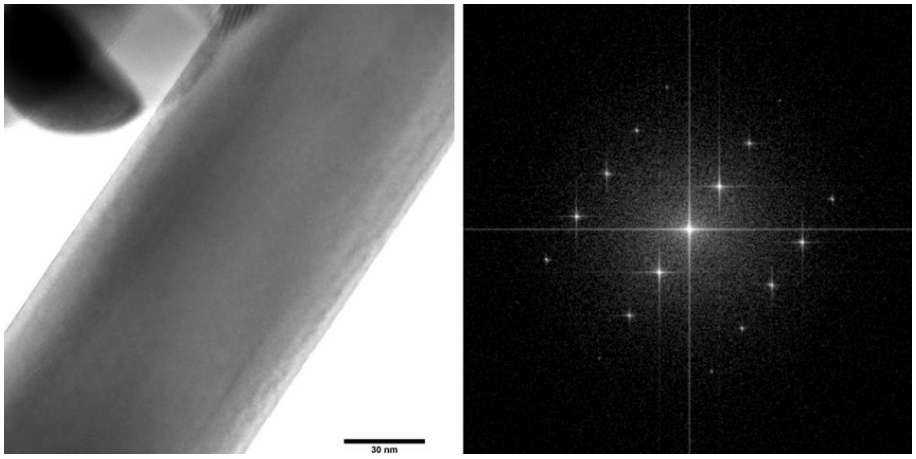

Figure 5.6: The TEM image of a typical InAs NW ($d \sim 80$ nm) reveals a wurtzite single crystal structure.

Transport measurements were performed on more than 30 individual InAs NW based devices. TEM image of a typical NW (Figure 5.6) confirms a wurtzite single crystal structure with a high crystalline perfection and a high purity. The results of the measurements are presented here by five representative samples, named A, B, C, D, and E. The parameters of these samples are summarized in a Table 5.1.

Sample	Diameter ($\pm 0.5\ nm$)	Length ($\pm 5\ nm$)	Mobility at 4.2K ($cm^2/(Vs)$)	L_φ at 4.2K ($\pm 5\ nm$)
A	33.1	377	3000	130
B	34.7	375	1000	120
C	29.8	386	900	125
D	37.8	372	1500	110
E	80 ± 5 nm	600	840	200

Table 5.1: Geometrical dimensions and transport characteristic lengths of the InAs NW based devices.

For both types of the NWs, the back gate capacitance coupling between the NW and the Si/SiO_2 substrate is approached by the following expression:

$$C_g = \frac{\pi \varepsilon_0 \varepsilon_{ox} L}{cosh^{-1}\left(\frac{l_{ox}+r}{r}\right)} \tag{5.2}$$

where ε_{ox} is the dielectric constant of the SiO_2, L and r is the length and the radius of the NW. One can notice that this formula is slightly different from the standard expression of the capacitance of a wire parallel to a plane (C_{wire}). It has been shown [Ford 2009] by comparing the measured values of C_g with the standard expression, that the last one overestimates the effective capacitance approximately by a factor of two for the considered range of diameters and oxide thickness. Therefore, we use the aforementioned formula, $C_g = C_{wire}/2$, which gives 0.03 nF/m and 0.04 nF/m for 30 nm and 80 nm, respectively.

5.3.1 Electronic transport characterization at zero magnetic field

5.3.1.1 Evidence of the 1-D band structure on the $G(V_g)$ curves

Before the transport measurements, all devices are preliminary exposed to low pressure He atmosphere ($P \approx 10^{-4}$ mbar) during 12 hours in order to desorb molecules (mostly moisture) from the sample surface. After this procedure, the conductance increases between 10 and 100 times.

The figure 5.7 presents the measurement of the conductance G of the sample A versus the applied back gate voltage V_g for different temperatures. The InAs NW remains in its off-state ($G \approx 10^{-4} G_0$), close to the experimental resolution, for gate voltages smaller than the threshold value V_t and then increases up to the saturation value, $G_s \approx 2e^2/h$, at high gate voltages. The on/off transition starts to be more abrupt with decreasing of the temperature, unveiling the increase of the electron mobility at lower temperature.

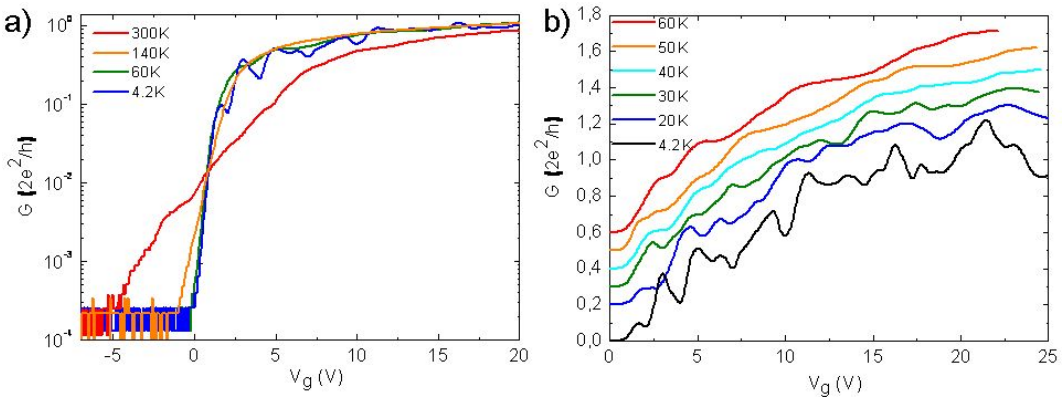

Figure 5.7: Sample A. Conductance as a function of the gate voltage V_g measured at different temperatures. Drain-source voltage is $V_{ds} = 1$ mV for all the curves. On the right panel the curves are shifted for clarity.

In addition, at low temperatures we observe the onset of large modulations in $G(V_g)$ (Figure 5.7b), which are superimposed to an overall monotonous increase. We extract the field-effect mobility value μ using the standard expression from the averaged slope of the $G(V_g)$ at $V_g \sim V_t$:

$$\mu = \frac{L^2}{C_g} \frac{dI}{dV_g} \frac{1}{V_{ds}} \tag{5.3}$$

here, V_{ds} is a drain-source voltage. The extracted mobility versus temperature for the five InAs NWs are presented on the figure 5.8.

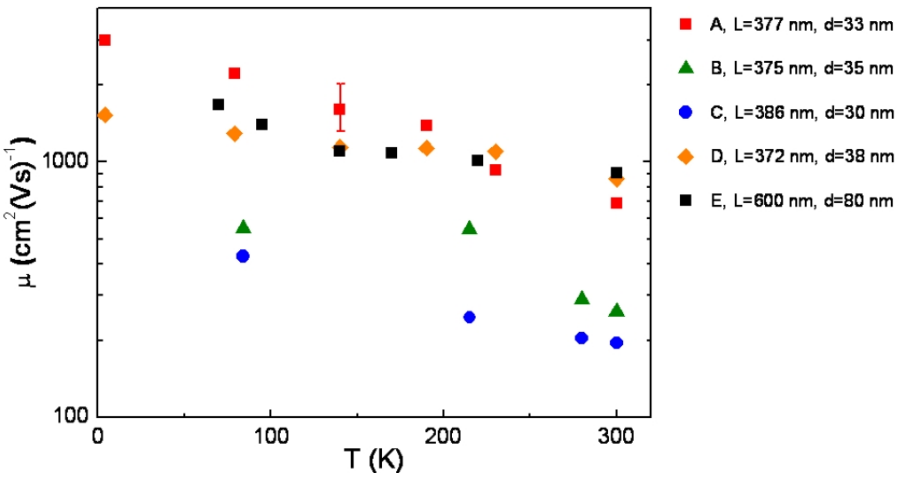

Figure 5.8: Field-effect mobility as a function of the temperature in a semi-logarithmic scale for the five samples.

At room temperature our samples exhibit a mobility in order of several hundreds $cm^2/(Vs)$, which strongly rises at low temperatures up to a few thousands $cm^2/(Vs)$. The highest mobility at 4.2 K was obtained for the sample A ($\mu \approx$ 3000 $cm^2/(Vs)$). This values are in good agreement with a mobility in InAs NWs, reported previously [Bryllert 2005, Dayeh 2005, Dayeh 2007a].

The conductance modulations at low temperatures consist of two components: some fluctuations, which are strongly temperature dependent and other, with step-like features, which persist up to T=60 K and which are reproducible for different thermal cycles. The physical origin of the first contribution is attributed to the universal conductance fluctuations (UCF) originating from changes in the electronic interference pattern due to the variation in the Fermi wavelength. The second contribution, the step-like features, are attributed to the 1-D band structure of the NWs [Ford 2012]. In order to give an evidence of this band structure effect, the calculation of the band structure of a 33 nm and a 80 nm diameter InAs NW has been made by Yann-Michel Niquet (Institut Nanoscience and Cryogénie – INAC/CEA) (see appendix A.2 for more details). The figure 5.9a presents the energy-momentum law $E(k)$ for a 33 nm diameter InAs NW.

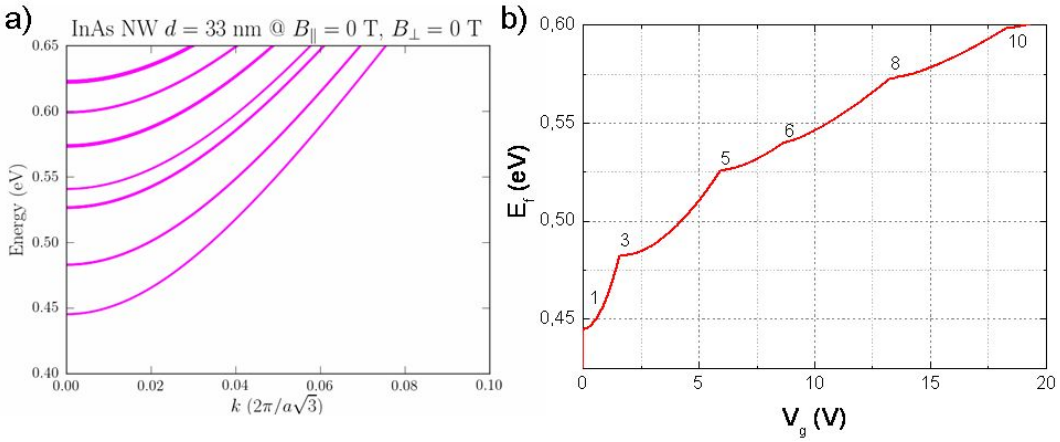

Figure 5.9: a) The energy-momentum law $E(k)$ for 33 nm diameter InAs NW calculated in a frame of tight-binding model at zero temperature. b) Dependence of the Fermi energy versus the applied voltage calculated from the equation 5.5. Values mark the number of the subbands under the Fermi energy, spin is not taken into account.

The DOS(E) calculations are based on the band structure computation:

$$DOS(E) = \frac{\sqrt{2m^*}}{\hbar} \frac{\sum_i H(E - E_i)}{\sqrt{E - E_i}} \tag{5.4}$$

where E_i are the minima of the subbands $E_i(k)$ and $H(x)$ is the Heaviside step function. Thus, the applied gated voltage V_g could be converted into the Fermi level

(Figure 5.9b) under assumption, that the carrier density n depends linearly on the V_g:

$$\int_{E_c}^{E_f} DOS(E)dE = n_{1D}(E_f) = \frac{V_g C_g}{eL}; \tag{5.5}$$

here, E_c is the energy minimum of the conduction band and L is the sample length. The figure 5.10 presents the DOS as a function of the applied gate voltage together with the conductance curves at different temperatures for two different samples.

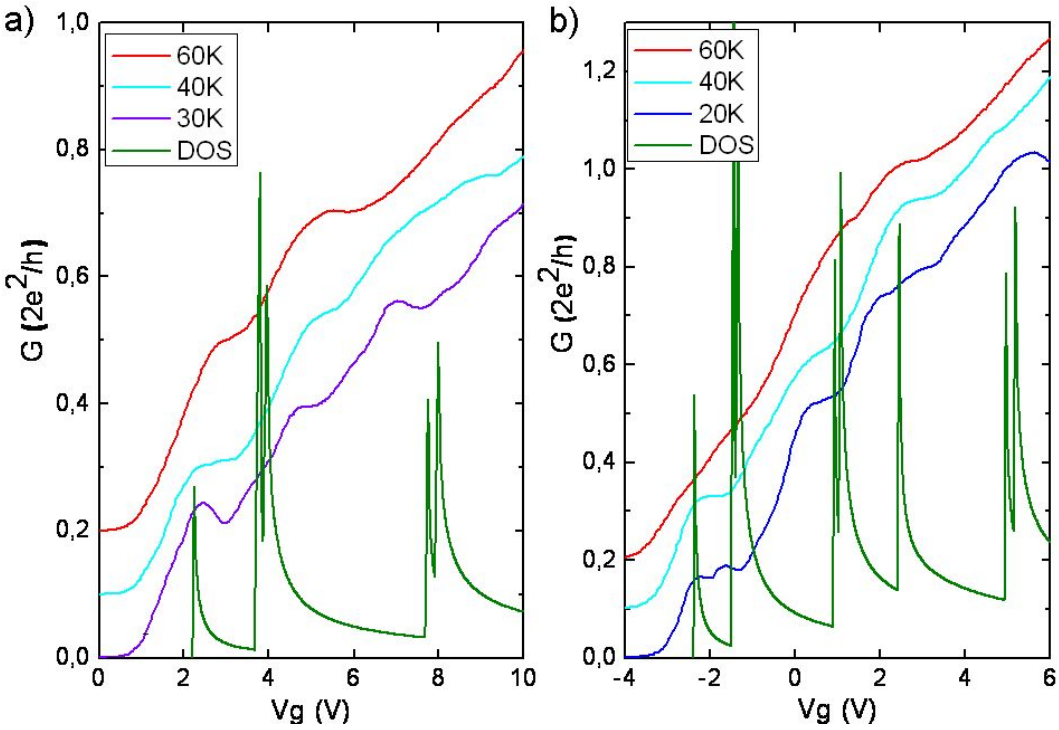

Figure 5.10: Conductance versus the back gate voltage at low temperatures and corresponding DOS (green curves) in arbitrary units for a) sample A and b) sample D.

We are assuming the intrinsic nature of the charge carriers of the NW, thus the increase of the conductance for $V_g > V_t$ is attributed to the crossing of E_f with the first 1D subband.

The step-like conductance features (Figure 5.10) are in a pretty good agreement with the location of the Van Hove singularities of the DOS, calculated directly from the dispersion law without any free parameters. Thus, we observe the influence of the individual 1D subbands on the electronic transport. Such a result indicates that

our NWs are clean enough to exhibit band structure effects on the conductance at zero field. It also validates the estimation of the conductance coupling. And finally, $E_f(V_g)$ relation (Figure 5.9b) will be very useful to tune the number of conducting 1D subbands for magnetotransport experiments.

The same measurements performed for 80 nm InAs NWs show much less pronounced step-like behaviour (Figure 5.11).

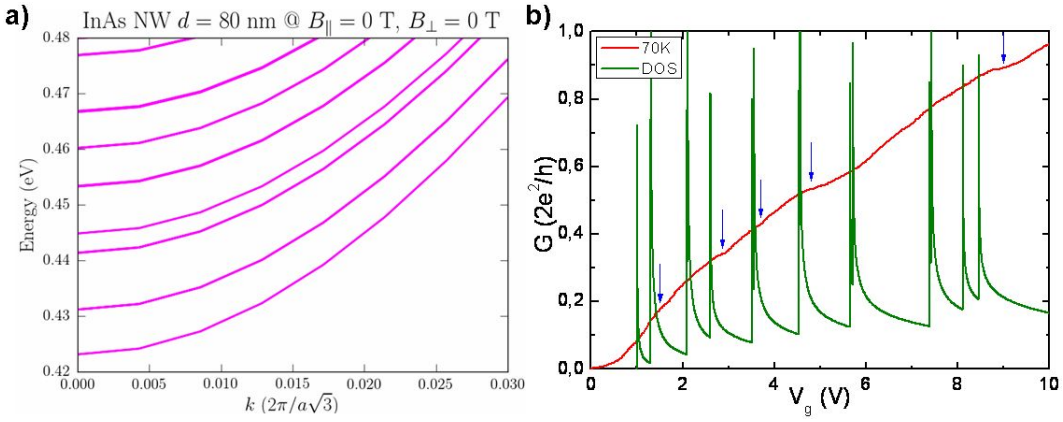

Figure 5.11: a) The energy-momentum law $E(k)$ for 80 nm diameter InAs NW calculated in a frame of tight-binding model at zero temperature. b) Conductance versus the back gate voltage at 77 K (red curve) and corresponding DOS in arbitrary units (green curve) for 80 nm NW (sample E). Arrows indicate the step-like features on the conductance curve.

Nevertheless, we can see some modulations that may coincide with the location of the Van Hove singularities (marked by arrows). Note that the much weaker signature of the band structure for the 80 nm diameter NW is not surprising, as the 1-D subbands energy separation is less than in the 33 nm diameter NW. The distance between the subbands $\Delta E \sim 10\ meV$ ($\sim 40\ meV$ for the 33 nm diameter NW), starts to be comparable with kT at 70 K ($6\ meV$). At lower temperature the onset of the UCF makes the band structure effects imperceptible.

The mean free path L_e was estimated through the Landauer formula in the weakly diffusive regime, for $L_e < L$:

$$G = \frac{2e^2}{h}\frac{NL_e}{L + L_e} \tag{5.6}$$

We use the mean value of the conductance in between of the two first Van Hove singularities, thus only one subband is involved in the electronic transport ($N = 1$). We obtain a mean free path of the order of 60 nm for 30 nm and 80 nm diameter NWs. Since the contact resistance is not taken into account, this value underestimates the mean free path. Thus, we can conclude on the presence of a diffusive regime for 80 nm NWs ($L_e < d < L$) and a weakly diffusive regime for both 30 nm

NWs ($d < L_e < L$). Note that a similar L_e value can be extracted by considering the simple Drude formula ($L_e = \hbar(3\pi^2 n)^{1/3}/(\rho n e^2)$) for an equivalent doping level. Here, n is the electron concentration and $\rho = 1/\sigma$ is the resistivity of the sample.

5.3.1.2 Universal conductance fluctuations

Equilibrium regime. Now let's turn to the second part of the signal - universal conductance fluctuations (UCF). These fluctuations are clearly seen in the temperature range from 4.2 to 30 K and then, they are gradually suppressed with the following increase of the temperature. The drain-source voltage for this experiments was fixed at 50 μV in order that $eV_{ds} \ll kT$. Several characteristic lengths have been deduced from this low drain-source voltage regime. We estimate a diffusion coefficient from the Einstein relation for the conductivity:

$$\sigma = e^2 D \times DOS \tag{5.7}$$

as $D \approx 200\ cm^2 s^{-1}$ and a thermal length $L_T = \sqrt{\hbar D/k_B T} \approx 190$ nm at 4.2 K.

The expected electronic phase coherence length L_φ for such InAs NWs is of the order of 200 nm [Blömers 2011]. Thus, L_T and L_φ might be comparable. For this reason we derive L_φ from the amplitude of the UCF through the following expression [Beenakker 1988]:

$$\delta G_{rms} = \beta \frac{e^2}{h} \left(\frac{L_\varphi}{L}\right)^{3/2} \left[1 + \frac{9}{2\pi}\left(\frac{L_\varphi}{L_T}\right)^2\right]^{-1/2} \tag{5.8}$$

Here, δG_{rms} is a root mean square value of the UCF amplitude and β is a constant of the order of one. The extracted values of the L_φ at 4.2 K are ≈ 120 nm and ≈ 200 nm for 30 nm and 80 nm diameter NWs, respectively. As we can see from the table 5.1, for the all samples, the coherence length is smaller than the NW length L and in a good agreement with previously reported values on similar InAs NWs [Hansen 2005, Dhara 2009, Liang 2010, Liang 2012].

In order to unveil the electron dephasing mechanism in InAs NWs, the temperature behaviour of the coherence length $L_\varphi(T)$ was investigated. The UCF are subtracted from a monotonous part of the conductance curves measured at different temperatures (Figure 5.12a) and L_φ is estimated from the equation 5.8. The $L_\varphi(T)$ dependence is presented in the figure 5.12b for samples A, D and E.

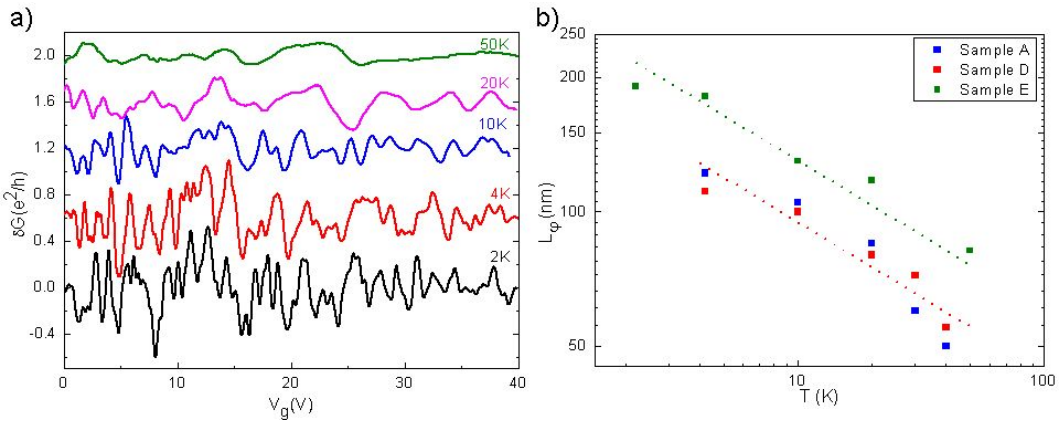

Figure 5.12: a) UCF in e^2/h units measured on the sample E at $V_{ds} = 50\ \mu V$ versus V_g for different temperatures. Curves are up-shifted for clarity. b) Electron phase coherence length L_φ versus temperature for the samples A, D and E. Dotted lines show a $T^{-1/3}$ power law dependence.

The decrease of L_φ with temperature is close to the $T^{-1/3}$ power law for all samples. This indicates that the Nyquist dephasing (the interaction of an electron with the time and space dependent fluctuating electromagnetic fields, produced by all the other electrons in the system) is the major source of decoherence in measured InAs NWs [Altshuler 1982, Blömers 2011].

Non-equilibrium regime. In addition, a non-equilibrium regime of UCF has been investigated, when the applied drain-source voltage V_{ds} exceeds both $k_B T$ and the coherence energy (Thouless energy) defined by:

$$E_T = eV_c = \hbar D/L_\varphi^2 \tag{5.9}$$

The root mean square values of the conductance fluctuations δG_{rms} are extracted from the conductance curves mesured at different V_{ds} and we clearly see a drastic decrease of the UCF at large bias voltages (Figure 5.13a). The $\delta G_{rms}(V_{ds})$ dependence is presented on the figure 5.13b for samples A, D and E. Samples B and C exhibit the same behaviour and are not shown for clarity.

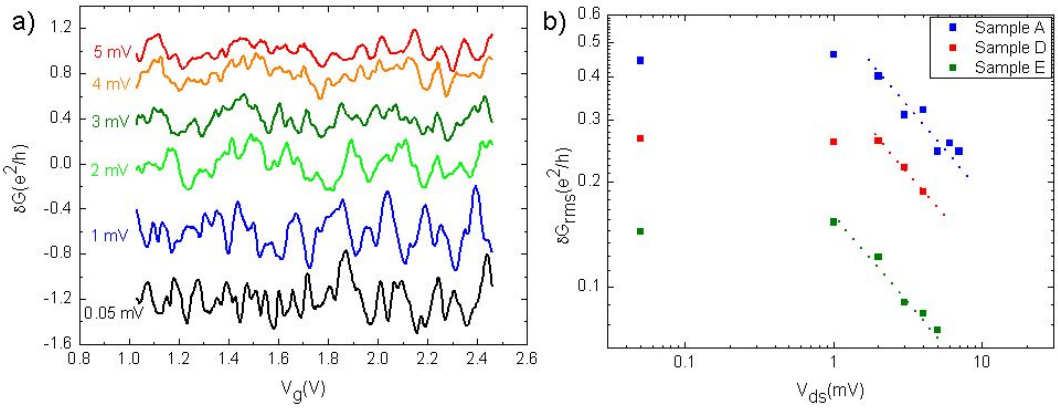

Figure 5.13: a) UCF in e^2/h units measured on the E sample at 4.2 K versus V_g for different V_{ds}. Curves are up-shifted for clarity. b) δG_{rms} in e^2/h units versus V_{ds} for sample A, D and E. Dotted lines show a $V^{-0.5}$ power law dependence for large V_{ds}.

The δG_{rms} plotted versus V_{ds} clearly reveals a $V^{-0.5}$ power law dependence once the V_{ds} exceeds the critical voltage $\sim 1.5\ mV$. This critical voltage is consistent with the Thouless energy $\sim 1.3\ meV$ estimated from the equation 5.9. Ludwig et al. [Ludwig 2004] showed that, for large drain-source voltage, UCF are dominated by the largest quantum-coherent region of the nanowire adjacent to the contacts. The voltage dependence of these coherent segments was predicted to vary as $V^{-0.25}$ when electron-electron interaction dominates the inelastic scattering, giving rise to $\delta G_{rms} \sim V_{ds}^{-0.5}$ dependence. These predictions are favorably compared to our experimental results (Figure 5.13). Thus we can conclude that, for measured InAs NWs in the non-equilibrium regime the electron-electron scattering is the main mechanism responsible for the phase decoherence.

5.3.2 Magnetotransport experiments on InAs NWs

5.3.2.1 Study of the magnetic field dependence of the UCF

In this paragraph, we study the magnetic field dependence of the UCF in InAs NWs. Magnetoconductance curves of 30nm InAs NWs are shown on the figure 5.14 for different values of the gate voltage. The threshold value V_t is adopted to zero.

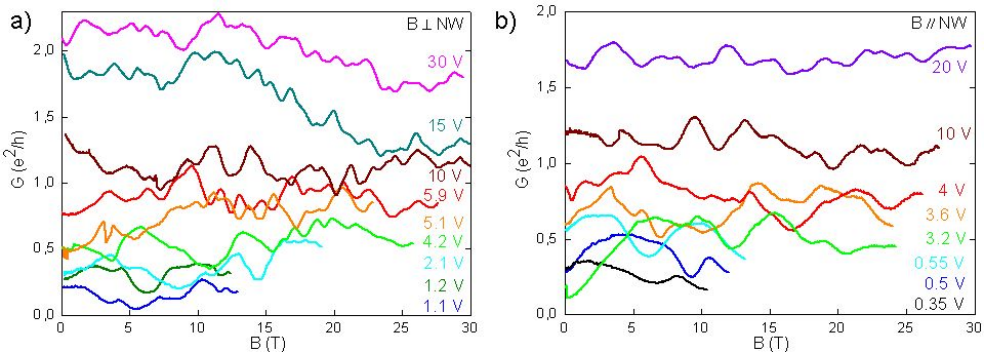

Figure 5.14: Magnetoconductance as a function of a) a perpendicular and b) a parallel magnetic field for different V_g, measured at T=4.2 K on the sample A.

Pronounced conductance fluctuations versus magnetic field are observed in the two magnetic field configurations. These conductance fluctuations are analyzed through the correlation magnetic field B_c, which is defined by the autocorrelation function of conductance given by [Lee 1987]:

$$F(\Delta B) = \langle \delta G(B + \Delta B) \delta G(B) \rangle \tag{5.10}$$

with B_c corresponding to the half maximum of the autocorrelation function:

$$F(B_c) = \frac{1}{2} F(0) \tag{5.11}$$

The values of the correlation magnetic field as a function of V_g for two magnetic field configurations are presented on the figure 5.15.

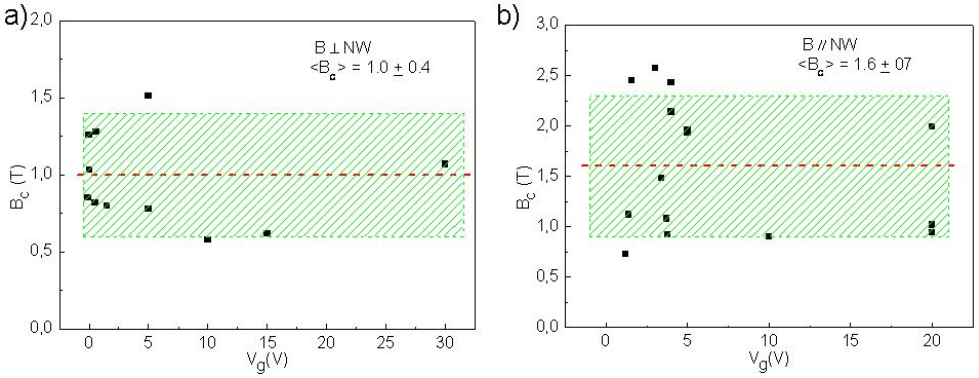

Figure 5.15: The correlation magnetic field B_c as a function of the applied gate voltage in a) perpendicular and b) parallel magnetic field at T=4.2 K for the sample A. The red dashed line is the mean value of the B_c and the green dashed rectangle is the estimated error of the B_c.

The average values of the correlation magnetic field over the different gate voltages are $B_{c\perp} = 1 \pm 0.4\ T$ and $B_{c\parallel} = 1.6 \pm 0.7\ T$ for the perpendicular and the parallel magnetic field, respectively. It has been shown [Beenakker 1988], that for quasi-1D systems ($d \ll L_\varphi \ll L$), under the dirty metal approximation, the correlation magnetic field B_c is defined:

$$B_c = \gamma \frac{\Phi_0}{A_\varphi} \tag{5.12}$$

where $\Phi_0 = h/e$ is the quantum flux, γ is a constant which equals 0.95 for $L_\varphi \gg L_T$ and 0.42 for $L_\varphi \ll L_T$, and A_φ can be interpreted as the maximum area, perpendicular to B, which is enclosed by the phase coherent length. Taking into the account that for the 30 nm diameter NWs, $d < L_\varphi < L$, we can estimate $A_{\varphi\perp} = L_\varphi d$ and $A_{\varphi\parallel} = \pi d^2/4$ for normal and axial magnetic field, respectively. Thus, we determinate the γ constant using the B_c values defined by the autocorrelation function: $\gamma_\perp = 1 \pm 0.2$ and $\gamma_\parallel = 0.5 \pm 0.2$.

These γ values for InAs NW in our case ($L_\varphi \lesssim L_T$) are in satisfactory agreement with the range [0.42; 0.95] predicted by the theory. This confirms the validity of the applied requirements for one dimensionality $d \ll L_\varphi \ll L$ for our systems.

The phase coherence length estimated from the correlation magnetic field (Eq. 5.12) is consistent with the $L_\varphi \approx 120$ nm deduced from the UCF at zero magnetic field.

The application of the dirty metal approximation may raise doubts, as for 30 nm diameter InAs NWs the mean free path and the nanowire diameter are in the same order of magnitude. In order to clarify this point, we additionally performed the B_c estimation under the pure metal approximation ($L_e \gg d$) (see equation in the appendix A.3). The obtained values exceed the experimental B_c (eq. 5.11) by 3 and 8 times for axial and normal magnetic field respectively, which points out the inconsistency of this approach for our system.

5.3.2.2 Magnetoconductance in the low field regime: a crossover from WL to WAL

In this paragraph, we study the crossover from weak antilocalization (WAL) to the weak localization (WL) in our InAs NW-based devices. The presence of the UCF makes difficult to extract the weak localization and antilocalization contribution to the magnetoconductance (MC). In order to subtract the UCF, we averaged from 10 to 20 different $G(B)$ curves measured in the vicinity of a given V_g at $T = 4.2$ K. The averaged $\Delta\bar{G}(B)$ curves for different back gate voltages are presented on figure 5.16 for the perpendicular and the parallel magnetic field (sample A). We clearly observe a strong back gate voltage dependence of the low magnetic field behaviour of the MC, that we attribute to a crossover from the WAL (MC<0) to WL (MC>0) as the carrier concentration decreases.

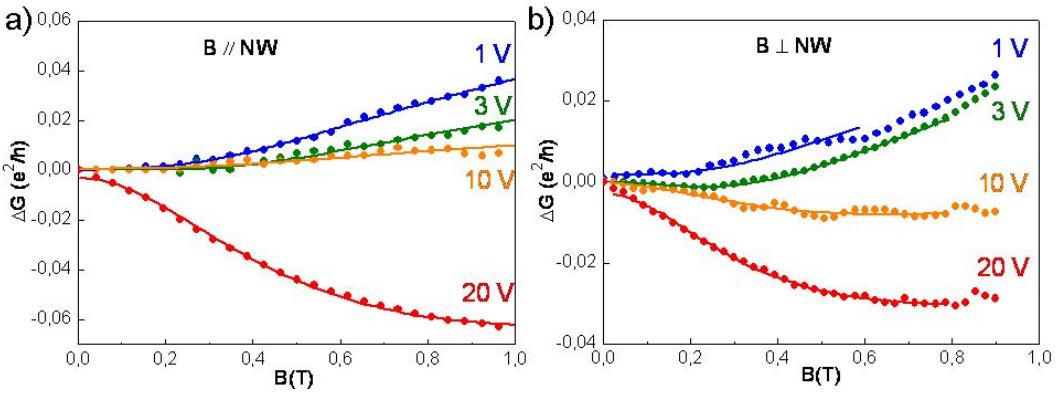

Figure 5.16: The conductance correction $[G(B) - G(0)]$ in e^2/h units in a) parallel and b) perpendicular magnetic field measured at T=4.2 K on the sample A. Solid lines are fits to the equation 5.13

We notice that the WAL effect seems to be more efficient in the perpendicular configuration compared to the parallel one: at $V_g = 20\ V$ in the perpendicular configuration the main MC decrease takes place below $B \sim 0.7$ T and MC is almost constant above this value, as the WAL is completely suppressed by the magnetic field, while in the parallel configuration MC continues to decrease up to $B \sim 1$ T. To understand this angular dependence, we must consider the electronic time reversed paths, which are responsible for the quantum correction in both cases. In the perpendicular orientation, the shape of the relevant time reversed trajectories can cover an area up to $L_\varphi d$ perpendicular to B, which will be strongly affected by the magnetic field. On the other hand, in the parallel orientation, the area covered by the relevant paths cannot exceed the NW cross-section $\pi d^2/4$ and, thus, will be less affected by the magnetic field. Our results on the angular dependence of WAL–WL crossover are in a good agreement with the experimental work of Roulleau et al. [Roulleau 2010].

To demonstrate the WL and WAL contribution to the MC curves and to extract the relevant characteristic length, we directly compare the experimental data to the theoretical expression of the quantum correction to the conductance under a magnetic field. As we showed previously, our InAs NWs are in the 1D regime with $d < L_\varphi \ll L$. However, for the 30 nm diameter, since $L_e \gtrsim d$, both expressions for the dirty and the pure metal approximation need to be considered.

The conductance correction $\Delta G(B)$ in a weak magnetic field ($d < L_m = \sqrt{\hbar/eB}$) under the dirty limit is expressed as [Altshuler 1982, Hansen 2005]:

$$\Delta G(B) = -\frac{2e^2}{h}\frac{1}{L}\left[\frac{3}{2}\left(\frac{1}{L_\varphi^2}+\frac{4}{3L_{so}^2}+\frac{1}{L_B^2}\right)^{-1/2} - \frac{1}{2}\left(\frac{1}{L_\varphi^2}+\frac{1}{L_B^2}\right)^{-1/2}\right] \quad (5.13)$$

where L_{so} is the relaxation length due to the spin-orbit interaction, L_B is the

magnetic relaxation length which depends on the field orientation [Altshuler 1981, Liang 2010]:

$$L_{B\perp}^2 = \frac{12}{\pi}\frac{L_m^4}{d^2} \tag{5.14}$$

$$L_{B//}^2 = 8\frac{L_m^4}{d^2} \tag{5.15}$$

The expression for the conductance correction in the pure limit additionally takes into account the mean free path L_e [Beenakker 1988]:

$$\Delta G(B) = -\frac{2e^2}{h}\frac{1}{L}\left[\frac{3}{2}\left(\frac{1}{L_\varphi^2}+\frac{4}{3L_{so}^2}+\frac{1}{L_B^2}\right)^{-1/2} - \frac{1}{2}\left(\frac{1}{L_\varphi^2}+\frac{1}{L_B^2}\right)^{-1/2} - \frac{3}{2}\left(\frac{1}{L_\varphi^2}+\frac{1}{L_e^2}+\frac{4}{3L_{so}^2}+\frac{1}{L_B^2}\right)^{-1/2} + \frac{1}{2}\left(\frac{1}{L_\varphi^2}+\frac{1}{L_e^2}+\frac{1}{L_B^2}\right)^{-1/2}\right] \tag{5.16}$$

See appendix A.3 for L_B description. The fitting parameters are L_φ and L_{so} for the dirty limit expression and L_φ, L_{so} and L_e for the pure limit expression. A comparison of these models applied to our data is presented on the figure 5.17 as a difference between the theoretical curves and the measured conductance for optimized parameters.

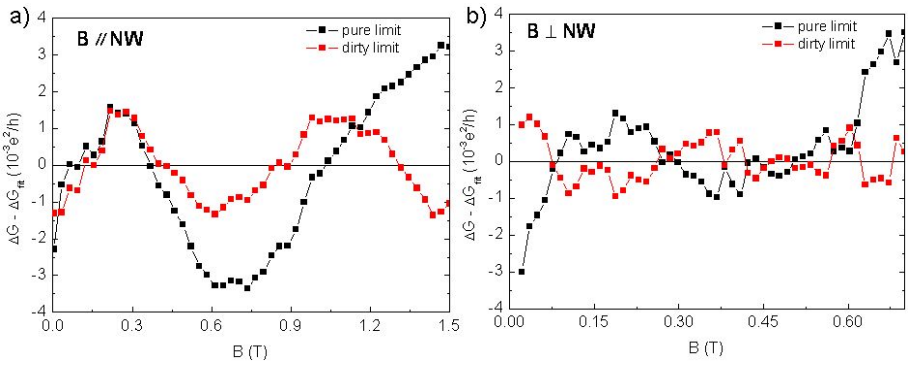

Figure 5.17: Difference between the fitted curves and measured conductance for the two models used: Eq. 5.13 (dirty limit) and Eq. A.5 (pure limit) versus magnetic field. The presented data were measured on the sample A at V_g=20 V in a) parallel and b) perpendicular configuration at T=4.2 K.

Both models describe the measured data reasonably well, however, the dirty limit gives a better fit for the whole range of magnetic field. Taking into account that the correlation magnetic filed was also better described in the dirty metal limit, we therefore refer to the results obtained from the dirty limit model in the following discussion. The theoretical curves in the dirty limit (Eq. 5.13) for different V_g in

both perpendicular and parallel magnetic field (solid lines) are directly compared to the experimental data (dot symbols) on the figure 5.16. The fitting parameters L_{so} and L_{φ} for different gate voltages are shown on the figure 5.18.

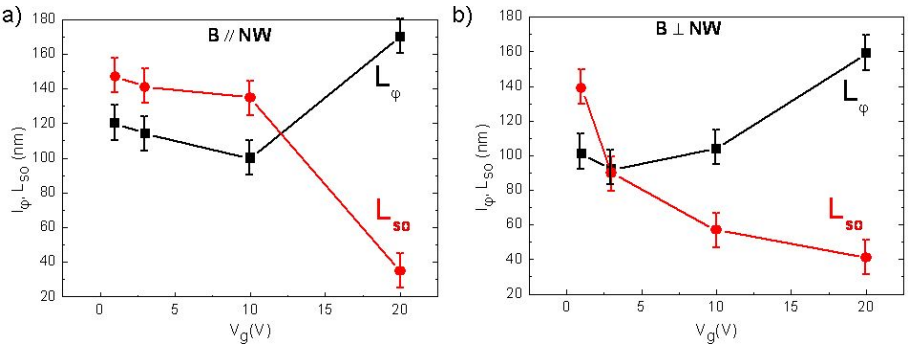

Figure 5.18: The spin relaxation length L_{so} and phase coherence length L_{φ} extracted from the fits to the measured magnetoconductance are plotted against the back gate voltage for c) axial and d) normal magnetic field. Sample A, T=4.2 K.

Note that the 1D requirement ($L_{\varphi} > d$) is indeed satisfied. Besides, the L_{φ} values obtained here are in a good agreement with the $L_{\varphi} \approx 120\ nm$ previously extracted from UCF at zero and low magnetic fields at 4.2 K. The crossover from WAL to WL occurs when L_{so} starts to be larger than L_{φ}. Since we consider the field orientation through the magnetic relaxation length we should obtain the same values of L_{so} and L_{φ} in both configurations. Indeed, this is well satisfied for L_{φ} and less for L_{so}. As it was mentioned in the introduction of this chapter (part 5.2.2), mainly the Dyakonov-Perel and the Elliott-Yafet mechanisms contribute to the spin relaxation in InAs NWs.

First, let's consider the Elliott-Yafet mechanism, where momentum scattering gives rise to the spin relaxation due to the spin-splitting of the valence band. The spin relaxation length for this case is estimated from the bulk InAs in a three-band kp-approximation and is expressed as [Chazalviel 1975]:

$$L_{so} = \sqrt{\frac{3}{8}} l_e \frac{E_g}{E_f} \frac{(E_g + \Delta_{so})(3E_g + 2\Delta_{so})}{\Delta_{so}(2E_g + \Delta_{so})} \tag{5.17}$$

where $\Delta_{so} = 0.38$ eV is the valence band splitting and $E_g = 0.445$ eV is the band gap of InAs NW. In the frame of this mechanism, we deduce a spin relaxation length $L_{so} \in [110; 80]$ nm for $V_g \in [1; 20]$ V. Hence, this mechanism may be of importance in our system, but it does not address completely the full range of the L_{so} values we extract.

Considering the Dyakonov-Perel mechanisms, we know that the bulk-induced asymmetry is absent in <111> direction of the InAs NWs, suppressing the Dresselhaus spin splitting effect. Thus, only Bychkov-Rashba spin splitting effect, induced by the electric field across the wire, should be taken into the account. The contri-

bution of the Bychkov-Rashba effect to the spin-orbit relaxation length L_{so} can be estimated by [Bychkov 1984a]:

$$L_{so} = \frac{\hbar^2}{2m^*\alpha_R} \tag{5.18}$$

here, α_R is the Rashba coupling parameter and $m^* = 0.023m_e$ is the InAs effective mass. Considering the obtained values of L_{so} (Figure 5.18), we deduce the Rashba coupling parameter α_R from 1.2×10^{-11} to 4.1×10^{-11} eVm, varying V_g from 1 to 20 V, respectively. The derived Rashba coupling parameter is surprisingly large comparing to the previously reported results, obtained on InAs NWs in similar FET configuration (Figure 5.20).

The same analysis of the low field magnetoconductance $\Delta\bar{G}(B)$ has been performed for the 80 nm diameter InAs NW (Sample E, figure 5.19).

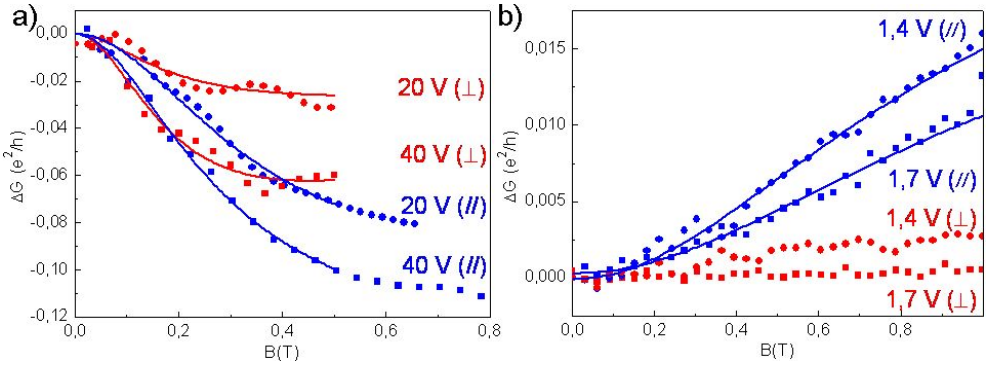

Figure 5.19: The a) WAL (high V_g) and b) WL (low V_g) conductance correction $[\Delta G(B) - G(0)]$ in e^2/h units in parallel and perpendicular configuration, measured at T=4.2 K on the sample E. Solid lines are the fits to the equations a) 5.13 and b) 5.19.

For low gate voltages, we obtain a positive magnetoconductance behaviour (Figure 5.19b). One notes, that in parallel magnetic field we obtain a steeper conductance slope than for perpendicular configuration. At the first glance, this behaviour is not consistent with aforementioned WL behaviour: in the perpendicular orientation the shape of the relevant back-scattering paths can cover a bigger area affected by the magnetic field than in the parallel one, which leads to a steeper positive magnetoconductance slope in the perpendicular orientation [Liang 2010]. However, for the proper analysis of this data the surface accumulation layer should be taken into account. For the cylindrical sample with a diameter d, length L and a wall thickness Δd the WL conductance corrections is expressed as [Aronov 1987]:

$$\Delta G(B) = -\frac{2e^2}{h}\frac{d}{L}\left[ln\left(\frac{L_\varphi(B)}{L_\varphi}\right) + 2\sum_{n=1}^{\infty}\left[K_0\left(\frac{n\pi d}{L_\varphi(B)}\right) \times cos\left(2\pi n\frac{2\Phi}{\Phi_0}\right)\right]\right] \tag{5.19}$$

here, $K_0(x)$ is the Macdonald function, $\Phi = B \times \pi d^2/4$, $\Phi_0 = h/e$, L_φ is the coherence length at the zero magnetic field and $L_\varphi(B)$ is expressed as:

$$L_\varphi(B) = L_\varphi \left[1 + \frac{1}{3}\left(\frac{L_\varphi \Delta d}{L_m^2}\right)^2\right]^{-\frac{1}{2}} \tag{5.20}$$

We use this expression to fit the positive magnetoconductance in parallel magnetic field. The phase coherence is $L_\varphi \approx 200$ nm (extracted at zero magnetic field from the UCF amplitude) and the thickness Δd of the accumulation layer is a fitting parameter. The resulting curves are presented on the figure 5.19b. The extracted thickness of the accumulation layer $\Delta d \approx (12 \pm 3)$ nm is in good agreement with the calculated carried distribution in 80 nm diameter InAs NWs [Dayeh 2009b], which estimates the accumulation layer to be in the order of 10 nm.

For $G(B)$ curves measured at high gate voltage we obtain the WAL conductance behaviour (Figure 5.19a), which fits well with the aforementioned theoretical equation 5.13. The extracted phase coherence length $L_\varphi \approx 130$ nm is in the same range of magnitude as the value obtained through the UCF amplitude $L_\varphi \approx 200$ nm for 80 nm diameter NWs. The spin relaxation length derived from this fit is $L_{so} \approx 30$ nm, which gives a Rashba coupling parameter $\alpha_R \approx 5.5 \times 10^{-11}$ eVm.

The values of Rashba coupling parameter for 30 nm and 80 nm diameter InAs NWs are surprisingly large comparing to the previously reported results, obtained on InAs NWs in similar FET configuration (Figure 5.20).

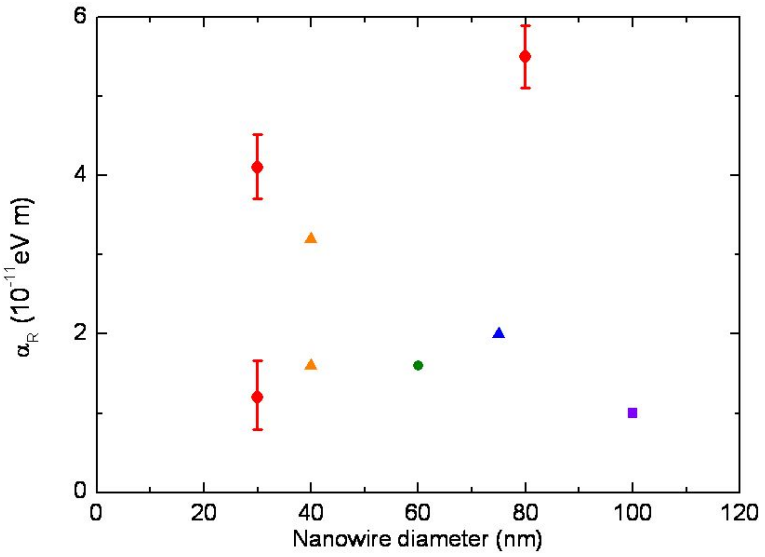

Figure 5.20: Rashba coupling parameter α_R versus InAs NW diameter reported by different groups: violet $d = 100$ nm [Dhara 2009]; blue $d = 75$ nm [Roulleau 2010]; green $d = 60$ nm [Hansen 2005]; orange $d = 40$ nm for $V_g \in [0 - 30]$ V [Liang 2012]; red - current work ($d = 33$ and 80 nm) for $V_g \in [1 - 20]$ V.

One can note, that Rashba coupling parameter α_R stay in the range of $\sim 10^{-11}$ eVm with the decrease of the NW diameter. These results are in sharp contrast with the prediction of weak antilocalization suppression in narrow quantum wires ($\alpha_R \sim 1/d$) due to the geometrical confinement [Schäpers 2006, Roulleau 2010]. Clarification of this issue requires additional measurements in smaller diameters range in order to approach indeed the 1D system properties.

5.3.2.3 High magnetic field experiment: onset of magnetoelectric subbands

As it was discussed previously (part 5.2.2.3), the theoretical investigations [Bogachek 1996, Debald 2005, Tserkovnyak 2006] predicted a strong influence of the high magnetic field on the transport properties of NWs. To the best of our knowledge, there is no published data on high magnetic field experiments on semiconducting NWs.

The figure 5.21 presents, in a semi-logarithmic scale, typical magnetoconductance behaviour for 33 nm diameter NWs, measured at $T = 4.2$ K on sample A for different values of the applied gate voltage and in different configuration of the magnetic field with respect to the NW axis.

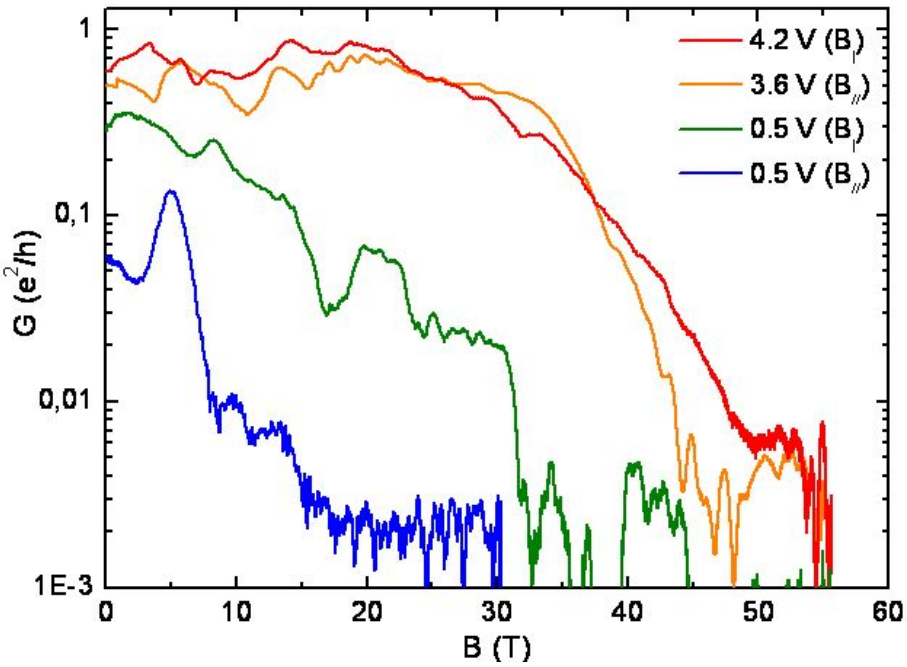

Figure 5.21: Magnetoconductance in parallel (orange and blue) and perpendicular (red and green) magnetic field for two ranges of V_g corresponding to different positions of E_f. $T = 4.2$ K, sample A.

For both perpendicular and parallel magnetic fields, the conductance displays

large fluctuations in the low and intermediate field range followed by a vanishing at high magnetic field. Above a critical field, which clearly rises with the Fermi energy, the conductance rapidly decreases down to values, which are close to the experimental resolution. A similar behaviour has been obtained on 80 nm diameter NW also. This effect can be associated to the loss of conducting channels once all the magnetoelectric subbands, shifted toward the high energy range by the magnetic field, have crossed the Fermi energy. Moreover, it will be shown that for both types of wires, the quench of the conductance occurs in slightly different ways in the two configurations, the effect being more abrupt in the B perpendicular geometry than in the parallel one. This qualitative observation points towards the distinct behaviors of the magnetoelectric subbands expected for the different configurations of the magnetic field with respect to the NW axis. In order to understand this behaviour, the electronic band structure calculations of 33 nm and 80 nm diameter InAs NWs were performed by Yann-Michel Niquet and colleagues, taking into account the lateral and magnetic confinements (see appendix A.2). The band structure was calculated for each value of magnetic field from 0 to 50 T with a step of 1 T (d=33 nm) and 2 T (d=80 nm) for both perpendicular and parallel configurations of the magnetic field. The results of these calculations are partly depicted on the figure 5.22.

Magnetic field applied along the NW (Figure 5.22d) tends to strengthen the confinement along their axis and the energy dispersion remains close to a parabolic law. The application of the magnetic field perpendicular to the wire axis leads to the formation of Landau-like levels with weak dispersion close to the Brillouin zone center (Figure 5.22e). These calculations take into account the Zeeman effect and SO coupling; spin-splitted subbands are shown in red (spin up) and blue (spin down). The calculations show that the wave function is confined in the plane perpendicular to the magnetic field.

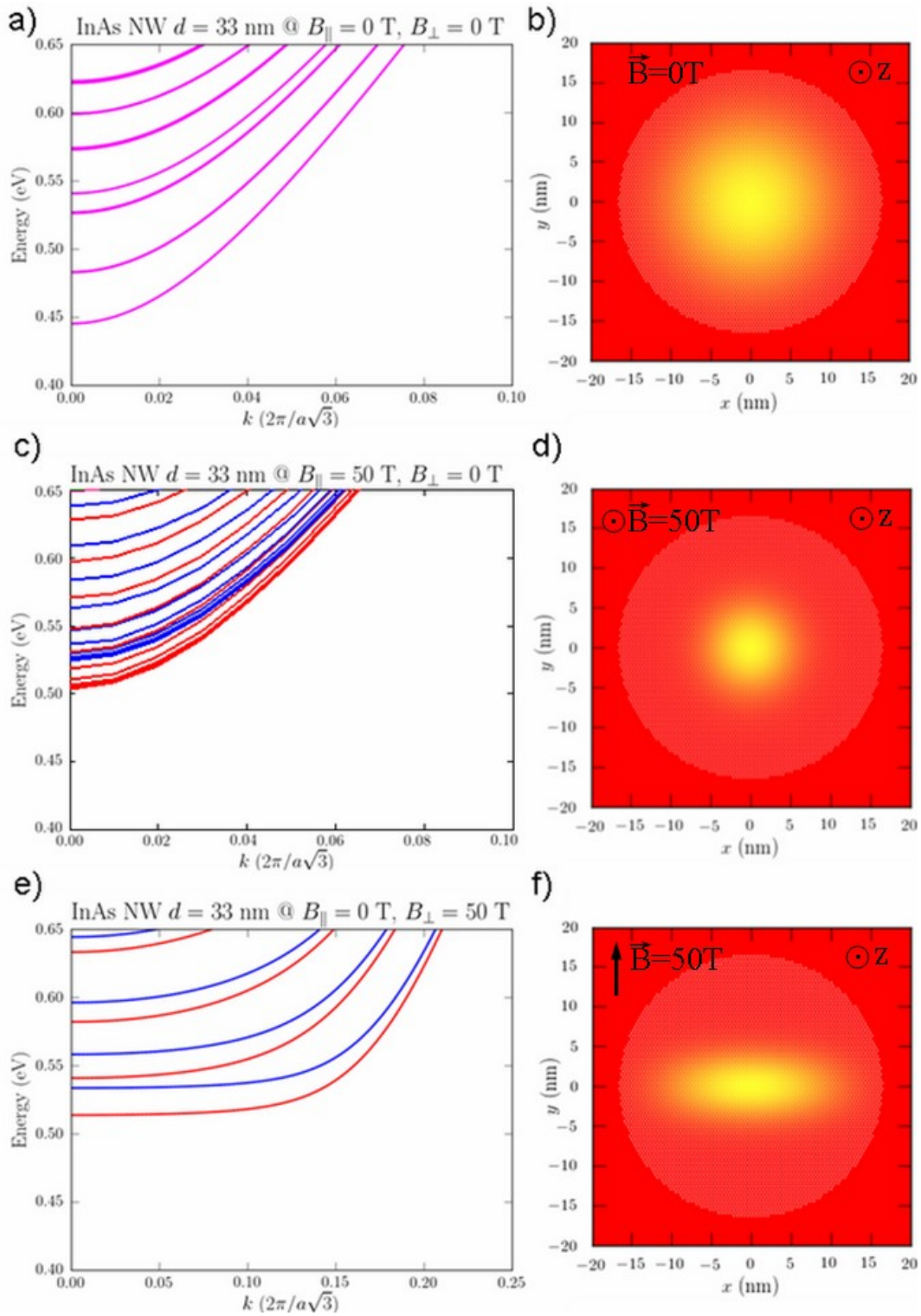

Figure 5.22: (a) Energy-momentum law $E(k)$ (k// NW axis) and (b) conduction band wave function of the first energetic subband of a 33 nm diameter InAs NW (NW axis //z) at zero magnetic field, (c) and (d) at 50 T parallel magnetic field (B//z), (e) and (f) at 50 T perpendicular magnetic field ($B \perp x, z$). Red and blue lines are spin splitted subbands with the spin "up" and "down" respectively.

In order to analyze the magnetotransport results, from one side, the position of the Fermi energy and thus the number of occupied subbands at zero magnetic field are evaluated from the $G(V_g)$ plots. From the other side, the magnetic fields (B_q) corresponding to the conductance quench together with fields corresponding to large decrease of $G(B)$ were evaluated as shown on the figure 5.23. The corresponding data (B_q, $E_f(B = 0)$) are then transferred on the plot of the calculated energy levels as a function of magnetic field (Figure 5.24).

The figure 5.23 presents the magnetotransport measurements on the sample A in the perpendicular magnetic field orientation.

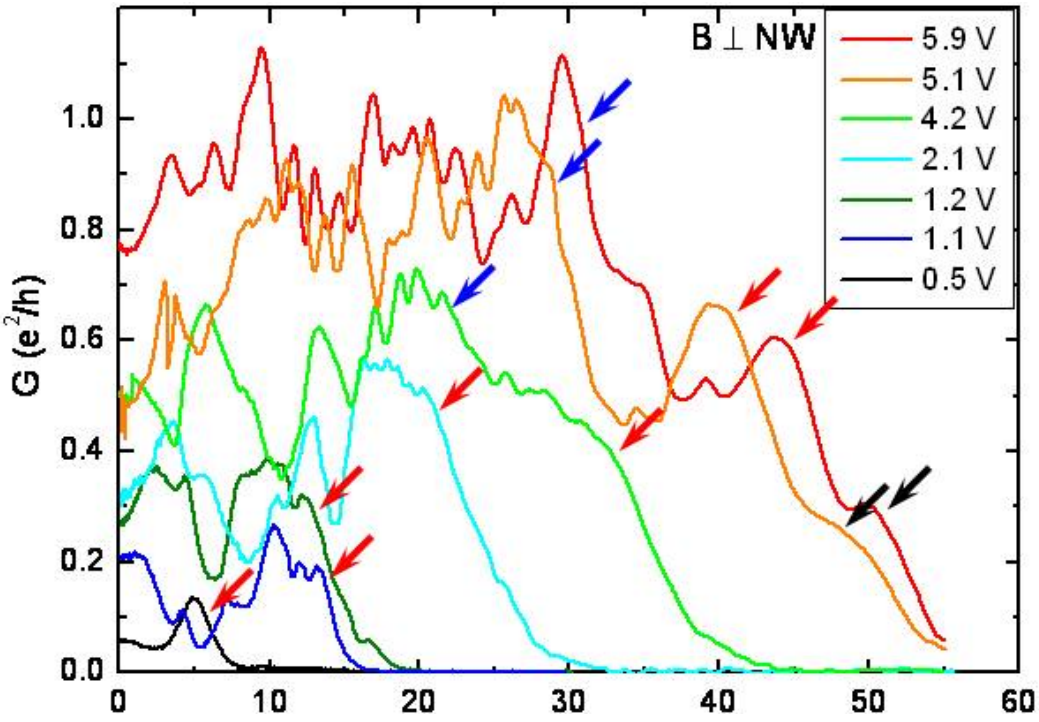

Figure 5.23: Magnetoconductance for different applied gate voltages in the perpendicular magnetic field at $T = 4.2$ K, sample A. Conductance drops corresponding to the loss of conducting channels marked by the arrows.

On the figure 5.23 the magnetoconductance at low gate voltages (V_g= 0.5, 1.1, 1.2, 2.1 V) exhibits large fluctuation followed by a sharp drop and a quench of the conductance. The position of this drop shifts to higher values of the magnetic field with the increase of the gate voltage. At higher gate voltages (V_g= 4.2, 5.1, 5.9 V) this conductance quench occurs in several stages. The beginning of each conductance drop is marked by the arrow.

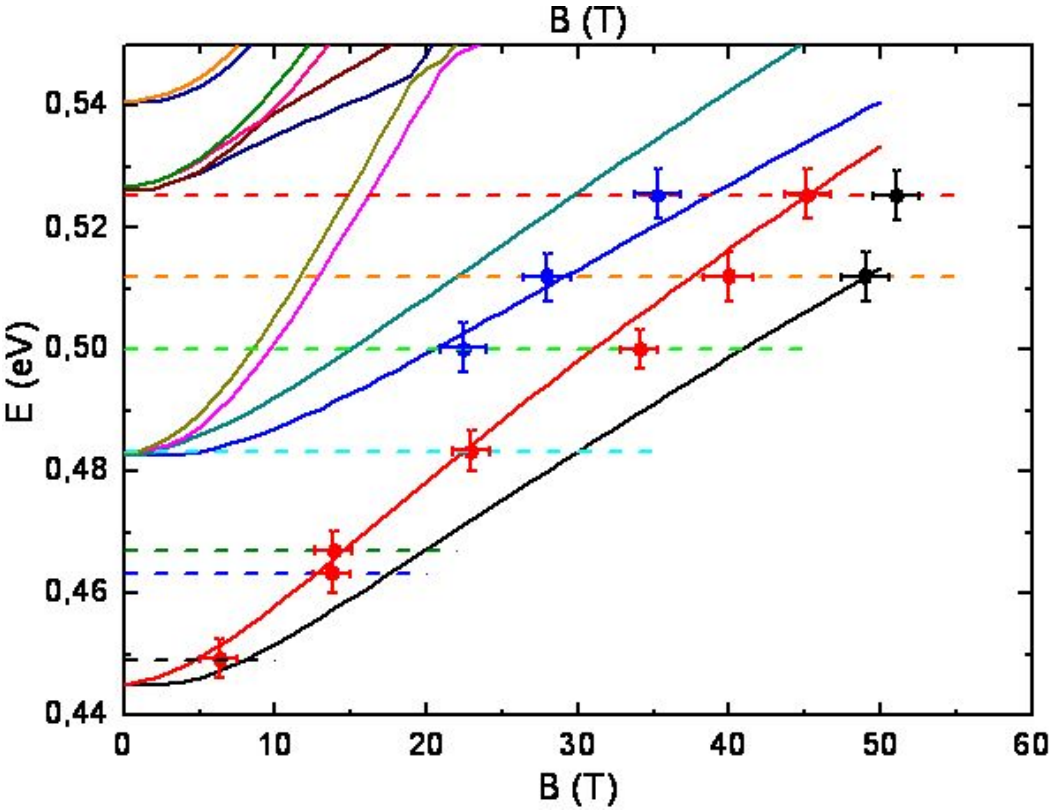

Figure 5.24: Calculated magneto-electric subbands as a function of magnetic field. The dashed lines point the Fermi level for $G(B)$ curves with corresponding colors from Fig.5.23. The filled circles correspond to the positions of the arrows on the Fig.5.23 (color corresponds to the lost subband).

On the figure 5.24 the drops of the conductance are marked by the filled circle at the Fermi level of the corresponding $G(B)$ curve. On this plot a good agreement between conductance drops and the crossings of $E_f(B = 0)$ with the magneto-electric subbands is obtained. Thus, we attribute the $G(B)$ behaviour to the loss of conducting channels, shifted toward high energy by the applied magnetic field. In order to highlight this, the color of the circles at the bottom panel (arrows at the top panel) corresponds to the color of the subband, which crosses the Fermi level of the given $G(B)$ curve. The quench of the conductance correlates with the loss of the last magnetoelectric subband. The same analysis was performed for the parallel orientation of the magnetic field for the sample A (Figure 5.25).

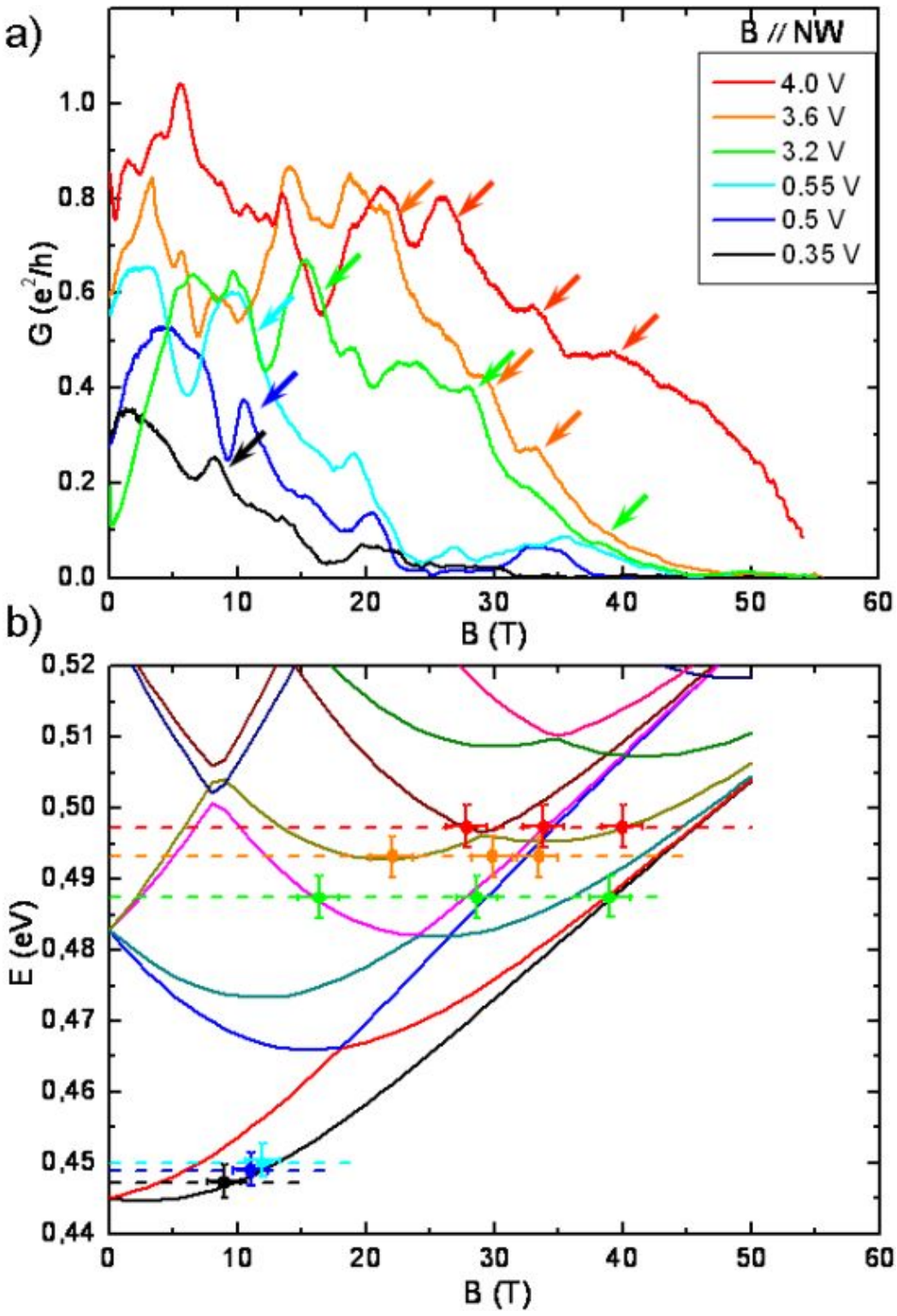

Figure 5.25: a) Magnetoconductance for different applied gate voltages in the parallel magnetic field at $T = 4.2$ K, sample A. Conductance drops corresponding to the loss of conducting channels are marked by the arrows. b) 1D electronic subbands E_i as a function of parallel magnetic field. The dashed lines point the Fermi level for $G(B)$ curves with corresponding colors. The filled circles correspond to the positions of the arrows on the top panel (color corresponds to the applied gate voltage).

The $G(B)$ curves in parallel orientation (Figure 5.25a) also exhibit large fluctuation followed by a quench of the conductance. It is much more difficult to associate the conductance drops with the loss of conducting channels (Figure 5.25b). The band structure of the InAs NW in the parallel magnetic field is indeed more complicated, as: i) the 1D subbands may have an upward or downward energy shift, depending on the spin orientation, when the magnetic field is increased and ii) the resulting energy versus B spectra may exhibit a level anticrossing due to the symmetry of the subbands. Nevertheless, the conductance quench is in a satisfactory agreement with the position of the last magnetoelectric subband. The relatively smoothed decrease of the conductance above the value of magnetic field expected from the calculations can be explained by the pinning of the Fermi level at the bottom of the conduction band. Indeed, in axial magnetic field, the number of 1D subbands increases sharply in the vicinity of the bottom of the conducting band Figure 5.22c), which might pin the Fermi level.

In order illustrate this effect, the 1D carrier concentrations was calculated as a function of the Fermi energy for both orientations of the magnetic field (Figure 5.26).

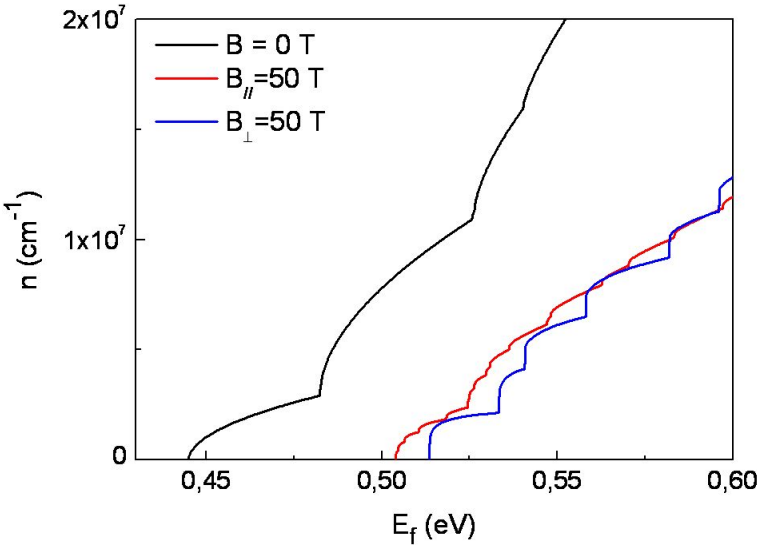

Figure 5.26: 1D carrier concentrations n as a function of the Fermi energy for zero magnetic field (black curve), parallel $B_{\|}$=50 T (red curve) and perpendicular $B_{\perp}$=50 T (blue curve) orientation of the magnetic field.

The increase of the magnetic field, causes the decrease of the concentration for a given Fermi energy, which in our case is fixed by the applied back gate voltage. In the parallel case, when the Fermi level approaches the bottom of the conduction band, the carrier concentration decreases smoothly, due to the large density of the 1D magneto-subbands. Whereas, in the perpendicular magnetic field, a sharp drop of the carrier concentration is observed.

The magnetoconductance of the 80 nm diameter InAs NWs was also studied at high magnetic field regime. Since the geometrical confinement is less, the density of states is considerably larger, thus the aforementioned Fermi level pinning effect should be more pronounced for 80 nm diameter NWs. The calculated energy-momentum laws $E(k)$ for these NWs are presented on the figure 5.27 for both orientations of the magnetic field.

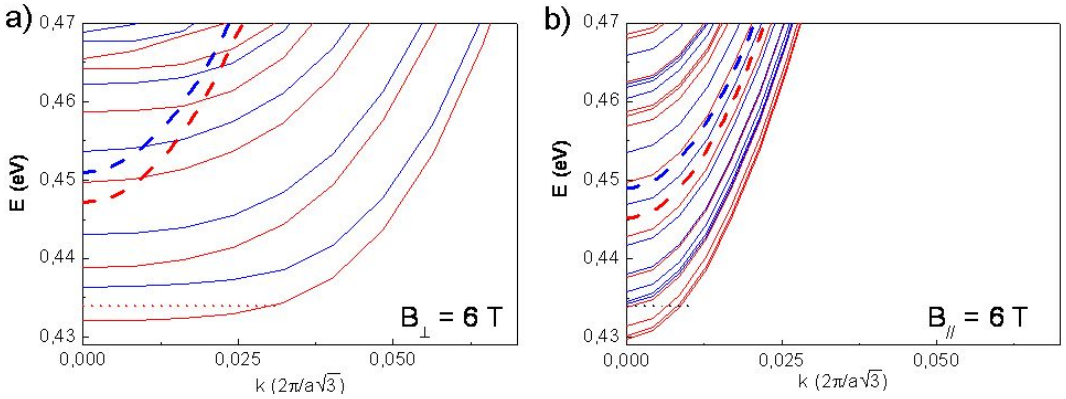

Figure 5.27: Energy-momentum law $E(k)$ (k// NW axis) for 80 nm diameter NWs at B=6 T for (a) perpendicular and (b) parallel configuration, red and blue lines are spin "up" and "down" subbands respectively. The energy-momentum law of the 33 nm diameter NWs is shown for comparison (dashed lines). The dotted lines in the bottom point the Fermi level for the V_g=1.4V and will be discussed in text.

The application of the magnetic field modifies the 1D subbands in the same qualitative way as it does for 33 nm diameter NW: formation of Landau-like levels for B $\perp$NW axis and nearly parabolic low energy dispersion for B//NW axis. Comparing the $E(k)$ for the two types of NWs (solid and dashed lines on the figure 5.27), we notice a strong increase of the density of states for both configurations and a weaker dispersion relation for perpendicular magnetic field. In order to compare magnetoconductance behaviour in parallel and perpendicular magnetic fields, sample E, mounted on a rotating holder, was measured successively in both configurations, keeping the value of the applied gate voltage, thus we assume to have the same Fermi level at $B = 0$ for both measurements. The figure 5.28 (bottom panels) presents the magnetoconductance behaviour of the sample E.

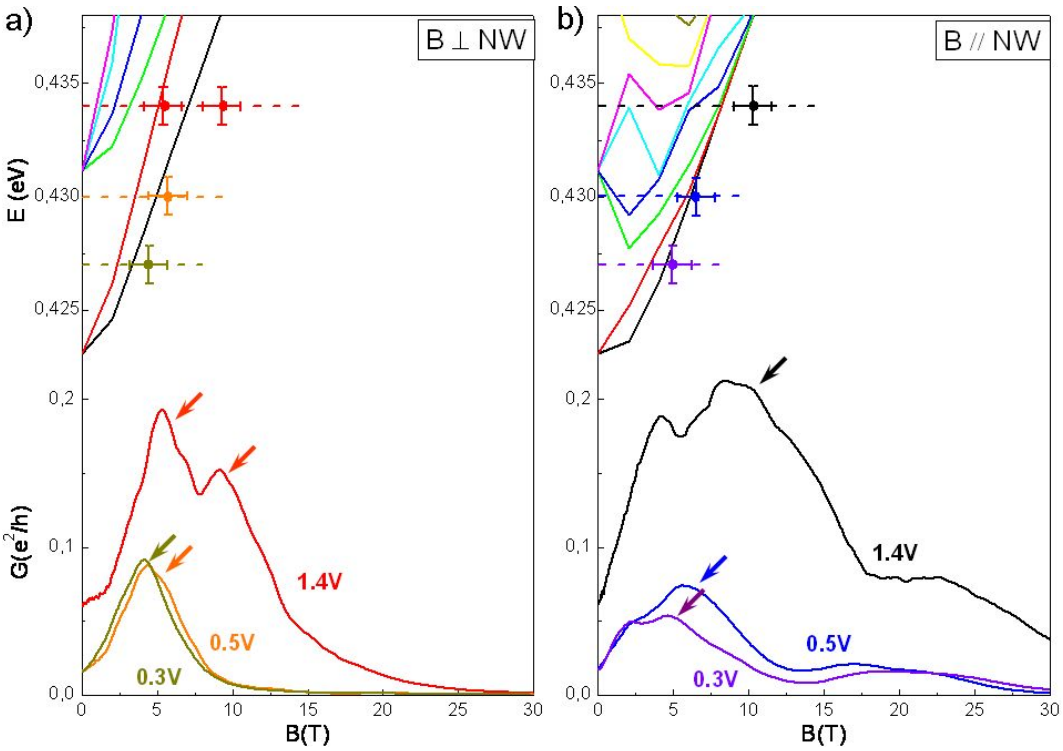

Figure 5.28: Magnetoconductance for different applied gate voltages in the a)(bottom panel) perpendicular and b) (bottom panel) parallel magnetic field for sample E at $T = 4.2$ K. Conductance drops (corresponding to the loss of conducting channels) are marked by arrows. 1D electronic subbands E_i as a function of a)(top panel) perpendicular and b) (top panel) parallel magnetic field. The dashed lines point the Fermi level for $G(B)$ curves with corresponding colors. The filled circles correspond to the positions of the arrows on the top panel (color corresponds to the applied gate voltage).

For perpendicular magnetic field, at low Fermi energy, the field range where the drop of the conductance occurs, corresponds to the crossing of the last 1D subband with the Fermi energy at $B = 0$. At higher Fermi energy $G(B)$ clearly exhibits a structure made of two peaks before total conductance quench. This two peaks structure could be attributed to the spin splitting of the magneto-electric subbands, which become larger for a higher values of E_f. For parallel magnetic field the drop of the conductance also coincides with the loss of the last 1D subband, but, compared to the perpendicular orientation, we observe a larger tails of the magnetoconductance after the expected loss of the last conducting channel. This is in agreement with the significant increase of the DOS close to the bottom of the conduction band for the parallel case compared to the perpendicular one. For example, on the figure 5.27 we see dispersion and distribution of the 1D subbands

in both configurations under the Fermi level corresponding to the V_g=1.4 V (dotted lines). Several close-packed subbands in parallel magnetic field may pin the Fermi level more effectively, than the last subbands in perpendicular orientation, which leads to the shift of the conductance quench toward higher values of the magnetic field. This is also in agreement with the smoother conductance quench observed for the 33 nm diameter NWs in parallel configuration compared to the perpendicular one.

This pinning effect starts to be more efficient with the increase of the gate voltage, since the DOS increases in the vicinity of the bottom of the conduction band in higher magnetic field. To explore the angular dependence of this effect we undertake to measure the conductance with respect to the relative orientation between magnetic field and the NW axis (Figure 5.29).

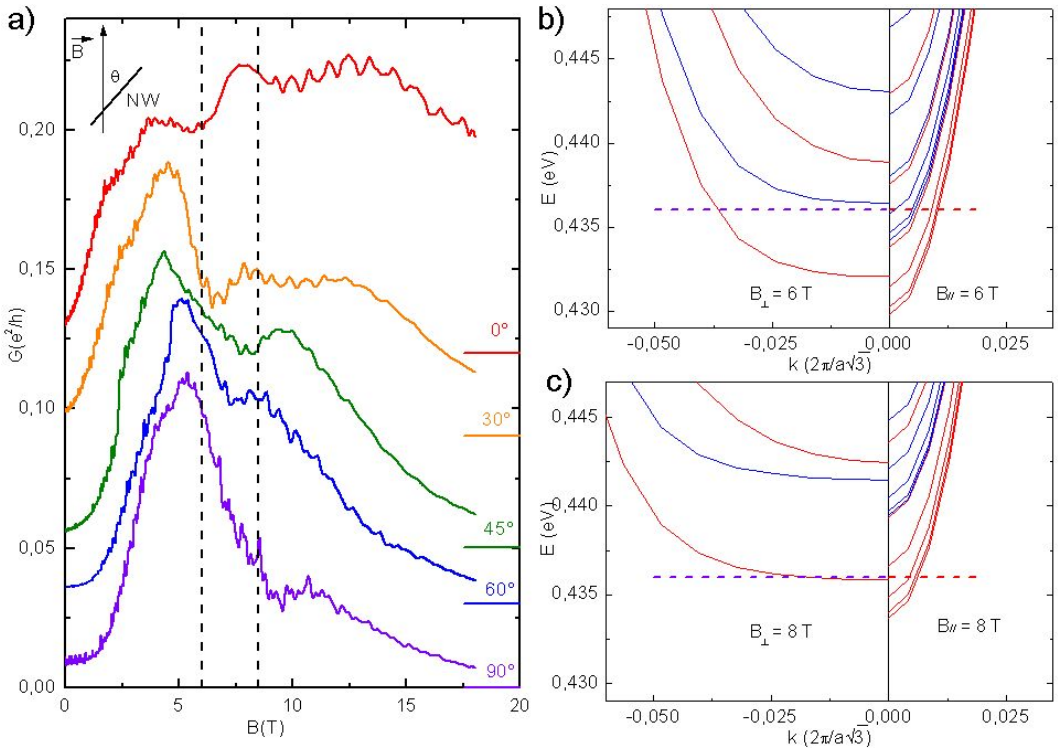

Figure 5.29: a) Angular dependence of the conductance at T=4.2 K, V_g=1.7 V, sample E; θ is the angle between the direction of the magnetic field and the NW axis. Curves are up-shifted for clarity, zero level for each curve is marked by the solid line of the corresponding color on the right side of the figure. Vertical dashed curves point the B=6 and 8 T. The energy-momentum law $E(k)$ for b) B=6 T and c) B=8 T for perpendicular (left panel) and parallel (right panel) orientation. Dashed line points the Fermi level corresponding to V_g=1.7 V at zero magnetic field.

All these measurements were done successively, keeping the value of the applied

gate voltage constant, thus we assume to have the same Fermi level at B=0 for all the magnetoconductance curves. The $G(B)$ curve in the perpendicular orientation shows a first conductance drop at B ~6 T, when the Fermi level crosses the last spin "down" subband (Figure 5.29b left panel). The second conductance drop (less pronounced) occurs in the vicinity of B ~8 T, when the Fermi level crosses the last spin "up" subband (Figure 5.29c left panel). With the decrease of the angle θ the second conductance drop gradually shifts toward the higher values of the magnetic field. At θ=0 (parallel orientation) the conductance drop starts at about B ~15 T, when the initial Fermi energy is much lower than the last 1D subband. In order to show this more clearly we plot the two extreme cases along with the minima of the subbands E_i versus magnetic field (Figure 5.30).

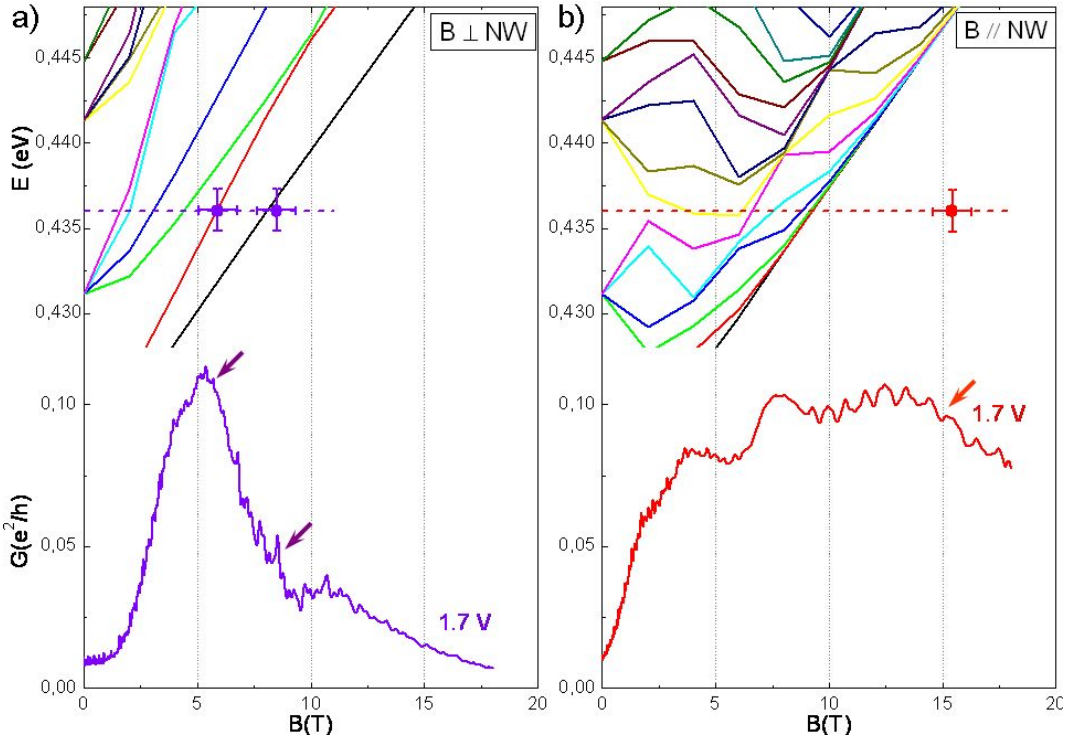

Figure 5.30: 1D subbands E_i as a function of a) (top panel) perpendicular and b) (top panel) parallel magnetic field. Dashed lines point the Fermi level corresponding to V_g=1.7 V at zero magnetic field. The filled circles correspond to the positions of the arrows on the bottom panels. Magnetoconductance in the a) (bottom panel) perpendicular and b) (bottom panel) parallel magnetic field for the sample E at V_g=1.7 V, T=4.2 K. Conductance drops corresponding to the loss of conducting channels marked by the arrows.

The top panels present the 1D electronic subbands E_i as a function of the magnetic field. For the perpendicular configuration the drop of the conductance can be

associated to the loss of the last spin "up" and spin "down" electronic subband. For the parallel orientation the beginning of the conductance decrease is shifted to $B \sim$15 T, which is much larger than the expected loss of the last conducting channel ($B \sim$9 T). Thus, the angular dependence evidences the shift of the conductance quench toward higher values for parallel orientation of the magnetic field. We tentatively propose the pinning effect of the Fermi level as a possible mechanism for the observed conductance behaviour. Indeed, in parallel case the number of 1D subbands increases sharply in the vicinity of the bottom of the conducting band (Figure 5.27), which might pin the Fermi level. As long as the Fermi level is pinned, the number of the conducting channels are conserved, this maintains the conductance level and postpones the conductance quench.

5.3.2.4 Conductance quench

Once we speak about the quench of the conductance at high values of the magnetic field, an important question rises up: what happens to the charge carriers in InAs NW? To answer this question we should consider the quantum capacitance and the chemical potential of the NW. As it was discussed previously, the back gate capacitance coupling between the NW ans Si/SiO_2 substrate was estimated through the geometrical parameters of the system (Eq. 5.2). This expression works well if both plates of a capacitor have a high DOS. In case, one of the capacitor plates has a low DOS, a shift of the chemical potential $\delta\mu$ in this plate caused by the applied voltage should be taken into account. The capacitance of such system expressed as:

$$\frac{1}{C_{system}} = \frac{1}{C_{ox}} + \frac{1}{C_q} \tag{5.21}$$

Here C_{ox} is a gate independent geometrical capacitance of the oxide layer defined as previously bu the equation 5.2 and C_q is a quantum capacitance:

$$C_q = e^2 \times DOS = e^2 \frac{\partial n}{\partial \mu} \tag{5.22}$$

where n is a carrier concentration and μ is a chemical potential. This provides a well known technique to probe the DOS of the system in case the low electronic compressibility dominates the electrostatic one ($C_q > C_{ox}$) [Ponomarenko 2010].

The quantum capacitance of InAs NWs was derived from the electronic band structure calculations for both orientation of the magnetic field.

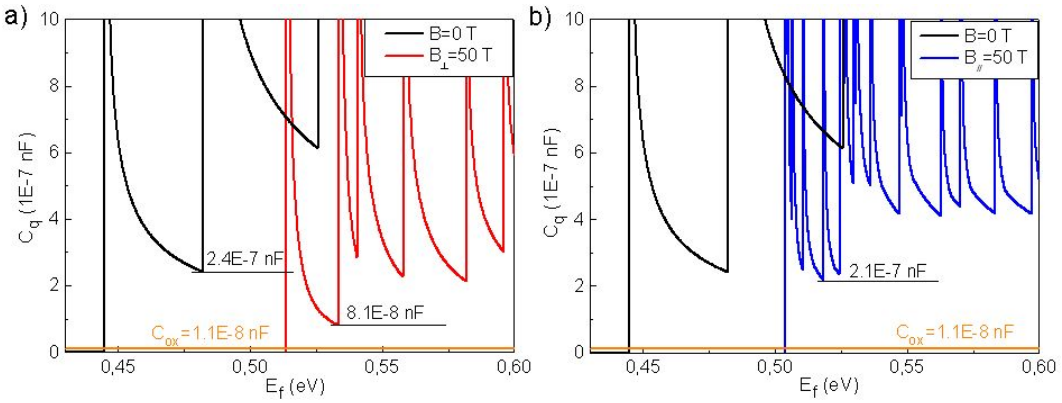

Figure 5.31: Comparative plot of the quantum capacitance C_q a) for B=0 T (black curve) and $B_\perp$=50 T (red curve) b) for B=0 T (black curve) and $B_\parallel$=50 T (blue curve) as a function of the Fermi energy for 33 nm diameter NWs. Orange line marks the geometrical capacitance of the oxide layer C_{ox}.

On the figure 5.31 the quantum capacitance as a function of the Fermi energy is plotted together with the geometrical capacitance of the oxide layer. The Fermi level in the InAs NW is defined by the chemical potential in the contacts. The NW band structure is altered by the application of the back gate voltage and the magnetic field but in a different way: the increase of the gate voltage upshifts the entire band structure, while the increase of the magnetic field additionally modifies the band structure (Figure 5.22). Thus, for a fixed V_g we can determine the Fermi level relative to the bands structure and the following application of the magnetic will modify the electrical subbands together with a general upshift of the band structure. One can see that $C_{ox} \ll C_q$ as long as the Fermi level is above the last magneto-electric subband. Thus, the carrier concentration and accordingly the Fermi level of our system is defined by the geometrical capacitance and variations of the quantum capacitance are negligible for all range of the applied magnetic field and gate voltages. Once the last magneto-electrical subband crosses the Fermi level, the NW passes to an insulation state, as there are no more conducting channels to transmit the current, or, in terms of charge carriers, the quantum capacitance tends to zero and $\partial\mu/\partial n \longrightarrow \infty$, preventing the electron transition from the contacts, due to a high value of the chemical potential in the NW.

5.4 Conclusion

We have studied the transport properties of single InAs nanowires. Investigations at zero magnetic field have evidenced the influence of the individual 1D electrical subbands on the electronic transport, which allows to monitor the number of the

populated subbands per given gate voltage. The electron phase coherence length was estimated through the UCF behaviour versus applied gate voltage and low magnetic field. The obtained value of $L_\varphi \sim 120$ nm and $L_\varphi \sim 200$ nm for 30 nm and 80 nm diameter InAs NWs, respectively, demonstrate a weakly diffusive regime of the carrier transport in these wires. The investigation of the UCF at different temperatures evidenced the Nyquist dephasing to be the major source of the electron phase decoherence. The study of the non-equilibrium UCF regime confirms the prediction of Ludwig et al. [Ludwig 2004], unveiling the prevalence of the electron-electron scattering over the inelastic scattering and, thus becoming the main phase decoherence mechanism in non-equilibrium regime.

Magnetotransport measurements were performed in both perpendicular and parallel orientations of the magnetic field with respect to the NW axis. At low magnetic field magnetoconductance fluctuations were observed. They originated from the phase modulation of the electronic wave functions induced by the magnetic field. The study of the correlation magnetic field B_c confirmed the validity of the 1D dirty metal approximation application. Observed WAL–WL crossover fitted by a 1D dirty metal limit expression revealed the strong SO interaction. The contribution to the spin relaxations was found to be due Dyakonov-Perel and Elliott-Yafet mechanisms.

The high field investigations have revealed a drastic conductance drop above a critical field, which clearly rises with the Fermi energy. This effect is interpreted by the loss of conducting channels once all the magneto-electric subbands, shifted toward the high energy range by the magnetic field, have crossed the Fermi energy. Preliminary band structure calculations, performed by Y-M Niquet (CEA-INAC), taking into account the lateral and magnetic confinements, are in fairly good qualitative agreement with the observed result in the high field regime. This result is the first observation of band structure effects in magneto-transport experiments on sc-NWs.

Chapter 6

Summary

The scope of this thesis is related to the electronic properties of quasi 1D systems probed by high field magnetotransport. Two different systems exhibiting quasi-1D confinement have been considered: carbon C_{60}@SWCNT and InAs semiconductor nanowires. The magnetotransport measurements on single nano-objets have been used to investigate the specific electronic structure of these 1D systems. In both cases, the high magnetic fields experiments have been supported by structural characterisation and conductance measurements at zero field.

The encapsulation of various molecules inside carbon nanotubes (CNTs), as for instance C_{60} fullerenes encapsulated in SWCNT, constitutes promising routes towards the tunability of the CNT conductance. Among the wide variety of filled CNTs, peapods represent a pioneer hybrid structure discovered in 1998. Since that time, their electronic structures have been subjected to intense and controversial theoretical studies together with a limited number of experimental realizations. In this thesis the electronic properties of individual fullerene peapods have been investigated by combining micro-Raman spectroscopy and magnetotransport measurements on the same devices.

We bring evidence that the encapsulated C_{60} strongly modify the electronic band structure of semiconducting nanotubes in the vicinity of the charge neutrality point, including a rigid shift and a partial filling of the energy gap. Thus, individually connected peapods, which clearly exhibit a typical semiconducting resonant Raman spectrum with an energy band gap $\sim 0.5\ eV$, do not present a signature of an energy gap in the conductance spectrum. These results confirm the theoretical prediction of the appearance of the electronic states in the vicinity of the E_f, which are related to the C_{60} fullerenes.

A strong drop of the conductance was observed at high magnetic field, instead of the expected positive magnetoconductance due to the magneto-induced collapse of the energy gap. This unexpected effect could be the signature of the magnetic field squeezing of the electronic C_{60}s orbitals, which reduces the overlap with the SWCNT states and gives rise to the drop of the conductance, as the energy gap of the semiconducting shell is gradually restored.

In addition, applying a selective UV excitation ($\lambda = 335.8\ nm$) on the peapods, we demonstrate that the electronic coupling between the C_{60} and the CNT is strongly modified by the partial coalescence of the C_{60}s and their distribution inside the tube. The chosen wavelength do not affect the external SWCNT, as it is absorbed only by the C_{60} fullerenes. This partial coalescence of the fullerenes, con-

firmed by the Raman spectroscopy, leads to a considerable conductance reduction and semiconducting behaviour of the peapod FET. We tentatively explain this effect by the loss of the periodic distribution of the C_{60} inside the SWCNT, which leads to the loss of the conduction channel induced by the C_{60}s chain. These experimental results are supported by numerical simulations of the DOS and the conductance of CNTs with coalesced fullerenes inside, performed by K. Katin and M. Maslov (MEPhI).

As a perspective continuation of this part of the work we propose a challenging experiment of full transformation of peapod to DWCNT, performed on a single peapod. The idea is to study the electronic properties of the system all along the transformation by combining the transport experiment with the HRTEM observation and Raman spectroscopy. The individual peapod should be connected on a thin HRTEM transparent dielectric membrane in FET configuration with a lateral gate electrode. Technically the realization of such an experiment is possible, as it has been shown recently by Westenfelder et al. [Westenfelder 2011] using a SiN-based support for in situ high-resolution TEM electrical investigations. Thus, the transport properties of the peapods could be probed for the particular fullerenes distribution, monitored by the HRTEM.

Semiconductor nanowires (sc-NWs) are being the subject of intense researches that have started a decade ago. They represent model systems for the exploration of the electronic properties inerrant to the quasi-1D confinement. Moreover they offer the possibility to play with band structure tailoring and carrier doping. In this direction III-V sc-NWs such as InAs have played a particular role due to the small electron effective mass. We have studied the conductance of single InAs nanowires in a wide range of magnetic fields.

Investigations at zero magnetic field have evidenced the influence of the individual 1D electrical subbands on the electronic transport. The number of subbands being monitored by the gate voltage. The electron phase coherence length was estimated through the UCF behaviour versus applied gate voltage and low magnetic field. The achieved values of the $L_\varphi \sim 120$ nm and $L_\varphi \sim 200$ nm for 30 nm and 80 nm diameter InAs NWs, respectively, unveil the weakly diffusive regime of the carrier transport in these wires. The investigation of the UCF at different temperatures evidenced the Nyquist dephasing to be the major source of the electron phase decoherence. The study of the non-equilibrium UCF regime confirms the prediction of Ludwig et al. [Ludwig 2004], unveiling the prevalence of the electron-electron scattering over the inelastic scattering and, thus becoming the main phase decoherence mechanism in non-equilibrium regime.

Magnetotransport measurements were performed in both perpendicular and parallel orientations of the magnetic field with respect to the NW axis. At low magnetic field the magnetoconductance fluctuations were observed, their origin is originated from the phase modulation of the electronic wave functions induced by the magnetic field. The study of the correlation magnetic field B_c confirmed the validity of the application of the 1D dirty metal approximation. The observed WAL–WL

crossover fitted by a 1D dirty metal limit expression revealed the strong SO interaction. The contribution to the spin relaxations was found to be due Dyakonov-Perel and Elliott-Yafet mechanisms.

The high field investigations have revealed a drastic conductance drop above a critical field, which clearly rises with the Fermi energy. This effect is interpreted by the loss of conducting channels once all the magneto-electric subbands, shifted toward the high energy range by the magnetic field, have crossed the Fermi energy. Preliminary band structure calculations, performed by Y-M Niquet (CEA-INAC), taking into account the lateral and magnetic confinements, are in fairly good qualitative agreement with the observed result in the high field regime. To the best of our knowledge, this result is the first observation of band structure effects in magneto-transport experiments on sc.-NWs.

Appendix A

Appendix

A.1 Numerical simulation of the density of states and the conductance of C_{60} peapods

In this work Hückel Hamiltonian was calculated by K. Katin and M. Maslov from National Research Nuclear University (MEPhI) within the program package [Landrum 2006] (2S, 2P orbitals for carbon atoms and 6S, 5P, 5D orbitals for platinum atoms are considered). The parameters describing lengths and energies of these orbitals for carbon and platinum atoms were adopted from [Maslov 2009] and [Ditlevsen 1993], respectively. Influence of the contacts was involved through the self-energy functions [Tian 1998, Datta 1995]:

$$\Sigma_{R,L} = \tau^{+} g_{R,L} \tau \tag{A.1}$$

, where τ is the coupling matrix between extended peapod and the contact, g is a Green function of the contact, which can be non-iteratively extracted [Sanvito 1999]. Green function G of the extended system can be derived from the extended Hückel Hamiltonian [Datta 1995]

$$G = [IE - H - \Sigma_R - \Sigma_L]^{-1} \tag{A.2}$$

Transmission function T was estimated from [Datta 1995]:

$$T = trace\left[\Gamma_L \; G \; \Gamma_R \; G^{+}\right] \tag{A.3}$$

where

$$\Gamma_{L,R} = i\left(\Sigma_{R,L} - \Sigma_{R,L}^{+}\right) \tag{A.4}$$

We assumed that the zero-temperature ballistic conductivity is proportional to $T(E_f)$ in accordance with the Landauer formula, where E_f is the Fermi energy level.

A.2 InAs NWs band structure calculation methods

The band structure of the InAs NWs were computed with a sp^3d^5s* tight-binding model [Jancu 1998] along the lines of [Niquet 2006]. The orbital effect of the magnetic field was accounted for through Peierls substitution [Graf 1995], and the spin effect through the Zeeman Hamiltonian.

Spin-orbit coupling is taken into account in all simulations. The tight-binding calculations were performed with the TB_Sim code [TB_Sim] and **k.p** code, which are able deal with nanowires with diameters up to 80 nm.

A.3 Conductance correction and correlation magnetic field under pure metal approximation

The expression for the conductance correction in quasi-1D systems ($d \ll L_\varphi \ll L$) under pure metal approximation ($L_e \gg d$, d is a NW diameter) is obtained from following expression [Beenakker 1988]:

$$\Delta G(B) = -\frac{2e^2}{h}\frac{1}{L}\left[\frac{3}{2}\left(\frac{1}{L_\varphi^2}+\frac{4}{3L_{so}^2}+\frac{1}{L_B^2}\right)^{-1/2} - \frac{1}{2}\left(\frac{1}{L_\varphi^2}+\frac{1}{L_B^2}\right)^{-1/2} - \frac{3}{2}\left(\frac{1}{L_\varphi^2}+\frac{1}{L_e^2}+\frac{4}{3L_{so}^2}+\frac{1}{L_B^2}\right)^{-1/2} + \frac{1}{2}\left(\frac{1}{L_\varphi^2}+\frac{1}{L_e^2}+\frac{1}{L_B^2}\right)^{-1/2}\right] \quad \text{(A.5)}$$

The magnetic relaxation length L_B in this case is expressed as:

$$L_B^2 = \frac{C_1 L_m^4 L_e}{d_{eff}^3} + \frac{C_2 L_m^2 L_e^2}{d_{eff}^2} \quad \text{(A.6)}$$

Here d_{eff} is the effective diameter of the NW which:

$$d_{eff\perp} = \frac{2\sqrt{3}}{\pi d} \quad \text{for perpendicular magnetic field orientation} \quad \text{(A.7)}$$

$$d_{eff//} = \frac{2\sqrt{2}}{d} \quad \text{for parallel magnetic field orientation} \quad \text{(A.8)}$$

The constants C_1, C_2 and the diffusion coefficient D depend on whether the boundary scattering in the nanowires is diffusive or specular. In the heterostructures considered the scattering is predominantly specular, thus $C_1 \approx 9.5$, $C_2 \approx \frac{24}{5}$ and $D = \frac{1}{2} v_f l_e$.

The correlation magnetic field B_c in this case is expressed as [Beenakker 1988]:

$$B_c = \frac{0.38}{\beta}\frac{\Phi_0}{A_\varphi}\frac{l_e^2}{L_\varphi d}\left[1+\sqrt{1+3.3\beta\frac{L_\varphi^2 d}{l_e^3}}\right] \quad \text{(A.9)}$$

where $\Phi_0 = h/e$ is the magnetic flux quantum, β is a constant which equals $\frac{1}{3}$ for $L_\varphi \gg L_t$ and $1/(4^{1/3}-1) \approx 1.7$ for $L_\varphi \ll L_t$, and A_φ can be interpreted as a maximum area, perpendicular to B, which is enclosed phase coherently by electron waves during their diffusion through the sample.

One can see that in the regime $L_\varphi \gg l_e\sqrt{l_e/d}$ the correlation magnetic field can be estimated as:

$$B_c = B_{c(dirty)}\sqrt{\frac{l_e}{d}} \tag{A.10}$$

and for $l_e \ll L_\varphi \lesssim l_e\sqrt{l_e/d}$ as:

$$B_c = B_{c(dirty)}\frac{l_e}{d} \tag{A.11}$$

where $B_{c(dirty)}$ is a correlation magnetic field in a dirty limit 5.12. Should be noted that all above mentioned expressions are valid only for sufficiently small magnetic fields, such that $D\tau_B \gg d^2$ and $\tau_B \gg \tau_e$.

Appendix B

Annex

B.1 Publications

[3] **Magnetically induced quenching conductivity effect in InAs nanowires**, V. S. Prudkovskiy, F. Rossella, B. Raquet, M. Goiran, V. Bellani, R. Leturcq, P. Caroff, D. Ercolani, L. Sorba and Y. M. Niquet; in preparation.

[2] **Electronic coupling in fullerene-doped semiconducting carbon nanotubes probed by Raman spectroscopy and electronic transport**, V.S. Prudkovskiy, M. Berd, E.A. Pavlenko, K.P. Katin, M.M. Maslov, P. Puech, M. Monthioux, W. Escoffier, M. Goiran, and B. Raquet; *Carbon* **57**, 498 (2013).

[1] **NMR Investigation of the local diamagnetic properties of carbon structures with multilayer nanotubes**, G. Nikolaev, O.E. Omel'yanovskii, V. S. Prudkovskiy, A.V. Sadakov and V.I. Tsebro; *Low Temperature Physics* **35**, 123 (2009).

B.2 Oral and poster presentations

07/2012 **HMF20: High Magnetic Fields in Semiconductor Physics**, Chamonix (France), Magnetically induced conductivity quench in InAs nanowires, *Poster*.

07/2012 **RHMF 2012: The 10^{th} International Conference on Research in High Magnetic Fields**, Wuhan (China), Electronic transport properties of InAs nanowires in high pulsed magnetic field, *Poster*.

06/2012 **NT12: International Conference on the Science and Application of Nanotubes**, Brisbane, (Australia), Influence of the ultraviolet irradiation on the transport properties of individual C_{60} peapods, *Oral presentation*.

01/2012 **GDR-I GNT 2012: International Research Network on Graphene and nanotube**, Ecully (France), Electronic transport properties of individual C_{60} peapods, *Poster*.

06/2011 **Journée du RNT**, Toulouse (France), Investigation of the transport properties C_{60}@SWCNTs under high magnetic field, *Oral presentation*.

05/2011 **Journée du ED**, Toulouse (France), Investigation of the optical and transport properties of semiconducting nanostructures under high magnetic field, *Poster*.

09/2010 **2nd EuroMagNET Summer School Science in High Magnetic Fields**, Ameland, (Netherlands), Nanotechnological process for the electrical connection of individual nano-objects, *Poster*.

Appendix C

Résumé

Cette partie annexe résume le travail en langue française de façon complète. Le lecteur ne trouvera aucune information nouvelle dans cette partie et les figures utilisées sont également les mêmes que dans la partie principale. Cette partie a pour but d'informer le lecteur francophone des résultats, qui ont été obtenus pendant ce travail.

La thèse présente des mesures de transport électronique dans des systèmes quasi-unidimensionnels (quasi-1D) sous champ magnétique intense. Deux systèmes différents présentant un confinement électrique quasi-1D ont été considérés: les peapods de carbone (C_{60}@SWCNTs) et les nanofils d'InAs. L'objectif de ces travaux consiste à sonder les propriétés électroniques spécifiques de ces systèmes quasi-1D par les mesures de magnétotransport sur les nano-objets uniques. Dans les deux cas, les expériences sous champs magnétiques intenses ont été accompagnées par des caractérisations structurales et des mesures de conductance à champ magnétique nul. Le manuscrit de thèse se structure en quatre parties principales :

C.1 Les aspects théoriques du transport électronique

Dans cette partie, je décris les propriétés électroniques des systèmes de basses dimensionnalités. Je commence par un bref rappel des propriétés basiques de tels systèmes et de leur évolution en fonction des différents types de confinements. Ensuite je décris brièvement différentes méthodes utilisées pour créer ces systèmes. Je détaille enfin les régimes de transport électronique et de magnétotransport dans les systèmes unidimensionnels sont également détaillés. Une partie importante est consacrée à l'influence du champ magnétique sur les propriétés de transport de systèmes mésoscopiques.

C.2 Les méthodes de nanofabrication et de mesures expérimentales

Dans cette partie, je décris des nombreuses méthodes expérimentales utilisées pour la fabrication et la caractérisation des dispositifs étudiés. Je commence par décrire la fabrication des systèmes unidimensionnels (nanofils de InAs de 30 et 80 nm de diamètre et "peapods" C_{60}@SWCNTs), leur dépôt sur substrat ainsi que la création par lithographie des contacts électriques à l'échelle nanométrique, la caractérisation des dispositifs réalisés par MEB et AFM, et enfin la connexion électrique

des échantillons, cette fois-ci à l'échelle microscopique. Je décris les nombreuses difficultés techniques pour réaliser des contacts électriques qui présentent à la fois un comportement ohmic et de bonnes caractéristiques mécaniques, ainsi que pour manipuler ces dispositifs en évitant toute décharge électrostatique. Ce chapitre se poursuit par la présentation des dispositifs utilisés pour les mesures de transport électronique avec et sans champ magnétique. Enfin, il se termine par la description de la technique de spectroscopie Raman utilisée pour la caractérisation des nanotubes de carbone en mode Raman résonant. Cette technique peut être utilisée en combinaison avec les mesures de transport pour corréler les propriétés électroniques des nanotubes et leur structure.

C.3 Les résultats obtenus sur les nanotubes de carbone

Cette partie est consacrée aux propriétés électroniques de peapods (C_{60}@SWCNTs). L'encapsulation de diverses molécules à l'intérieur de nanotubes de carbone, comme par exemple les fullerènes C_{60}, constitue une des voies prometteuses vers l'accordabilité de la conductance des CNTs. Parmi la grande variété des nanotubes de carbone remplis, les peapods représentent une structure hybride novatrice découverte en 1998. Depuis lors, leur structure électronique a fait l'objet d'études théoriques controversées avec un nombre limité de réalisations expérimentales. Dans ce travail, les propriétés électroniques des peapods individuels ont été étudiées en combinant les mesures de spectroscopie micro-Raman et de magnétotransport sur les mêmes échantillons.

C.3.1 Les mesures de transport et la spectroscopie Raman

Les résultats sont représentés par quatre échantillons nommés ici A, B, C et D. Tous les paramètres des échantillons sont résumés dans le Tableau C.1.

L'échantillon	AFM ($\pm 0.5\ nm$)	RBM pic ($\pm 0.04\ nm$)	G bande ($\pm 0.04\ nm$)	E_g ($\pm 0.03\ eV$)
A	1.5	1.51	1.48	0.54
B	1.4	1.41	1.47	0.56
C	1.5	1.40	1.46	0.56
D	1.5	–	1.53	0.53

Table C.1: Diamètres des peapods obtenus à partir de mesures AFM et spectroscopie Raman (calculés à partir des positions des bandes RBM et G). La dernière colonne indique les valeurs des bandes interdites pour les SWCNTs semiconducteurs vides et avec les mêmes diamètres.

Les échantillons présentent les spectres Raman consistant avec un SWCNT semiconducteur (Figure C.1 a, c, e, g).

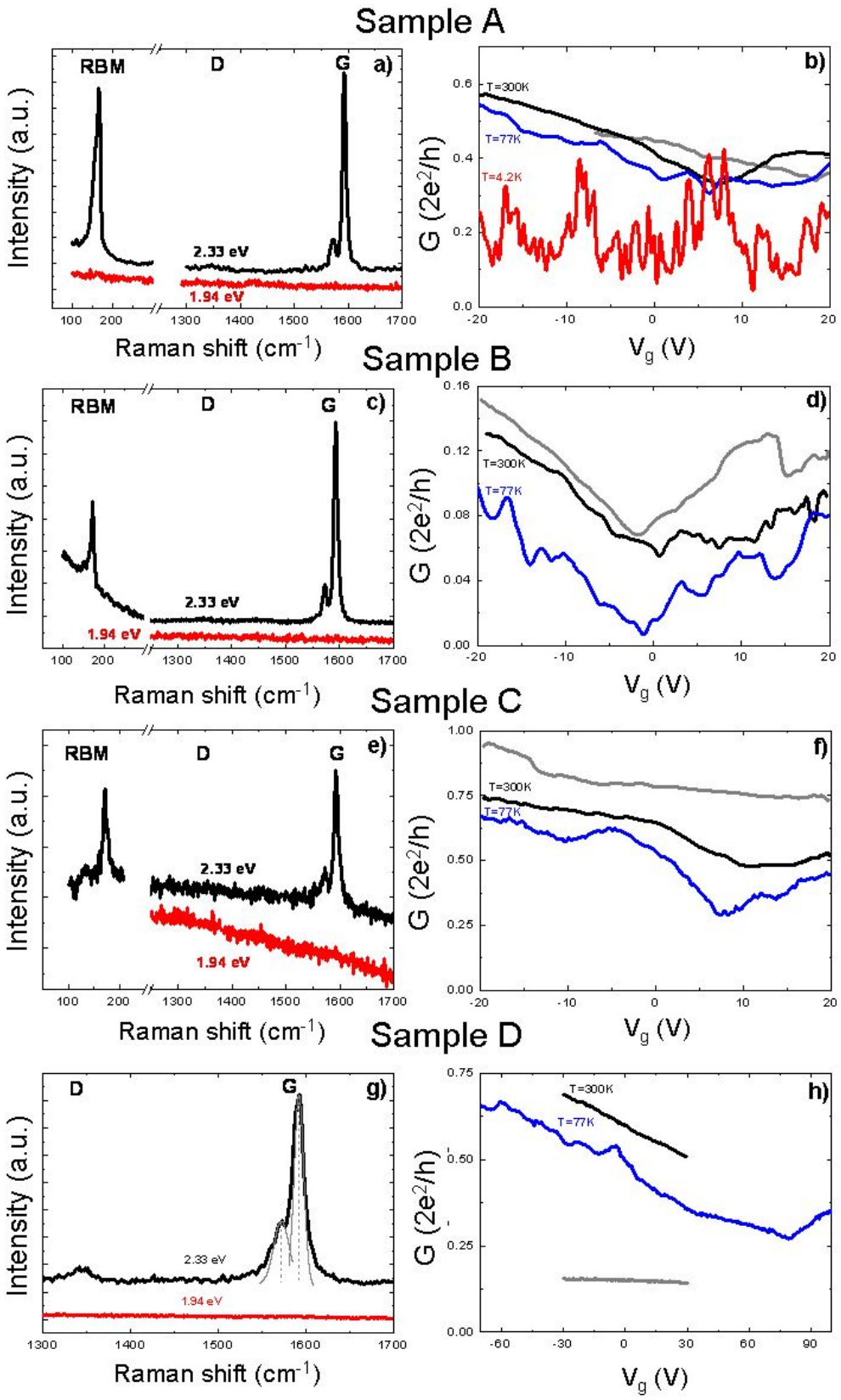

Figure C.1: Spectres Raman à 1,94 eV et 2,33 eV effectués sur les échantillons A (a), B (c), C (e) et D (g). Mesures de conductance des mêmes échantillons A (b), B (d), C (f) et D (h), en fonction de la tension de grille (densité de porteurs) à différentes températures. Les courbes grises représentent la conductance à température ambiante mesurée avant le recuit. Les autres mesures sont effectuées sous atmosphère d'hélium.

Chaque spectre présente des résonances Raman sous une excitation 2.33 eV (courbes noires), tandis que les spectres effectués à 1.94 eV (courbes rouges) et 1.58 eV (non représentées) restent plats. L'absence de signal Raman lors de l'utilisation des énergies d'excitation 1.94 eV et 1.58 eV traduit l'absence complète de CNT métallique. La présence d'une réponse Raman uniquement sous une excitation de 2.33 eV combinée avec le diamètre des peapods permet d'identifier (Kataura plot) le SWCNT externe comme un tube semi-conducteur avec une bande interdite E_g = 0,54 ± 0,02 eV. La même conclusion vaut pour tous les échantillons.

Les mesures de conductance $G(V_g)$ des quatre échantillons sont présentées dans la figure C.1 (b, d, f, h), à différentes températures. Les échantillons présentent une dépendance $G(V_g)$ modérée sans l'état bloqué du peapod-transistor, même à 4,2 K. Les courbes en forme de V à 300 K et à 77 K avec leurs minima de conductance ne sont pas compatibles avec la bande interdite E_g ∼0.5 eV déduite de la spectroscopie Raman.

C.3.2 Les calculs de la densité d'états

La simulation de DOS a été calculée par K.P. Katin et M.M. Maslov (MEPhI) pour le SWCNT dans deux cas : le nanotube vide et le nanotube partiellement rempli de fullerènes (Figure C.2). Le SWCNT calculé a des caractéristiques géométriques très proches par rapport aux peapods étudiés ici.

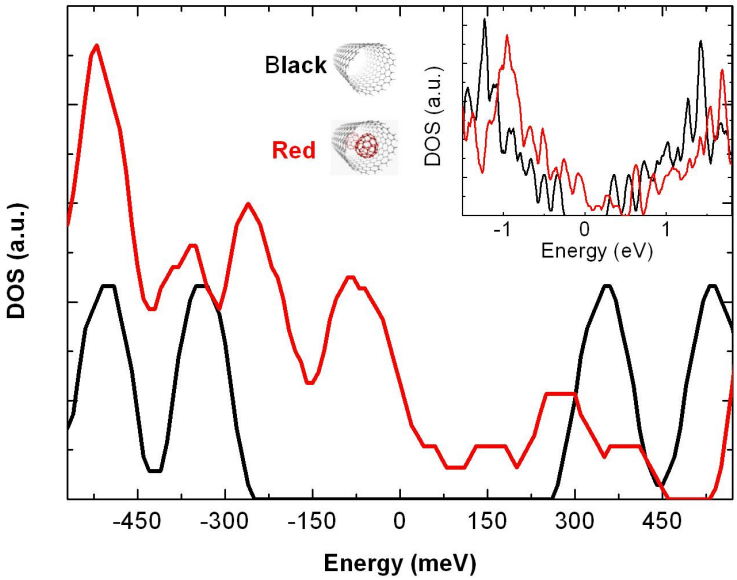

Figure C.2: La DOS calculée pour un SWCNT (12,10) vide (courbe noire) et pour le même tube rempli de deux C_{60} (courbe rouge). L'insert montre une échelle élargie.

Cette simulation montre que l'encapsulation de C_{60} influe considérablement sur le DOS, montrant à la fois un transfert de charge et l'apparition de nouveaux états, qui a remplissent partiellement la bande interdite du tube semi-conducteur. Le décalage de l'énergie induite par le transfert des électrons varie de 0,1 à 0,3 eV, en fonction du type d'isomère C_{60}. L'effet d'ajouter un fullerène supplémentaire dans le nanotube augmente cette tendance. En conséquence, la simulation soutient le déplacement de la structure électronique vers des énergies plus élevées avec l'apparition d'une bande d'impureté qui rétrécit considérablement la bande interdite du SWCNT, à la suite de l'encapsulation de C_{60}.

C.3.3 Le magnéto-transport

La structure de bande électronique de nos échantillons a été explorée par de magnéto-transport. Les mesures de la magnéto-résistance de CNT individuel sous champ magnétique parallèle à l'axe du tube révèlent des sous-bandes 1D électroniques et leurs modulations en champ magnétique, via l'effet Arahonov-Bohm (AB).

Dans notre étude (Figure C.3), une réduction drastique de la conductance dans le régime des champs magnétiques intense est observée proche du minimum de conductance, $V_g = 5\ V$ (Figure C.1b) et $V_g = 70\ V$ (Figure C.1h) pour l'échantillon A et D, respectivement.

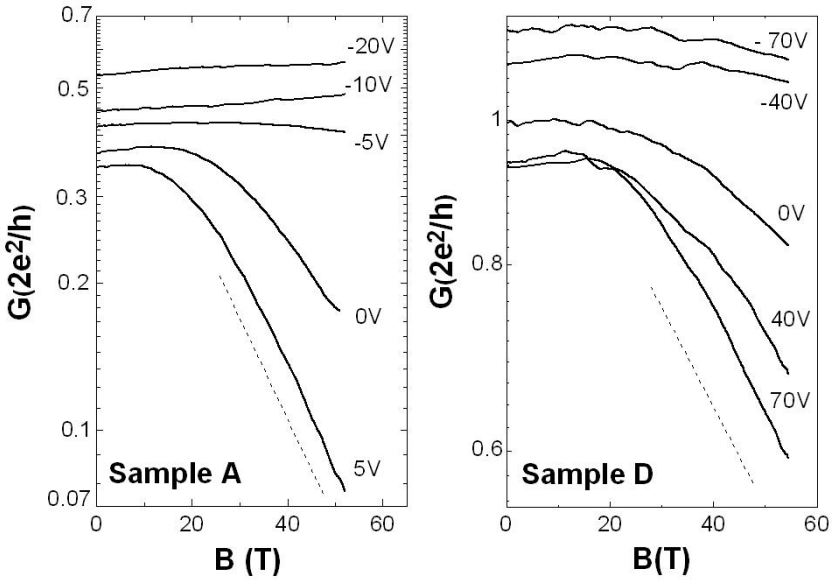

Figure C.3: Les mesures de magnéto-conductance sous champ magnétique parallèle à l'axe du tube, à 77 K pour différentes tensions de grille (les figures de gauche et de droite correspondent à l'échantillon A et D, respectivement). Les lignes en pointillés illustrent la diminution exponentielle de la conductance au voisinage de point neutralité de charge.

Le scénario Aharonov-Bohm pour un magnéto-conductance négative autour de point neutralité de charge nécessite un CNT métallique, ce qui est exclu de la spectroscopie Raman. Nous expliquons provisoirement la réduction de la magnéto-conductance par un rétrécissement des fonctions d'ondes des C_{60}s induite par un champ magnétique. Près du point neutralité de charge, la conduction se fait par les états électroniques induits par les C_{60}s encapsulées. Le champ magnétique comprime ses orbitales réduisant ainsi le recouvrement avec les états du CNT et donnant lieu à la décroissance exponentielle de la conductance, restaurant graduellement la bande interdite du tube semi-conducteur extérieur. Loin de point neutralité de charge, les états électroniques impliqués dans le processus de conduction sont des états de la bande qui sont beaucoup moins sensibles au champ magnétique.

C.3.4 Les effets de l'irradiation ultraviolette

La coalescence des C_{60}s induite par irradiation laser UV est un outil puissant pour la redistribution des fullerènes à l'intérieur du peapod. La configuration des C_{60}s a une forte influence sur les propriétés de transport électronique du peapod. Pour explorer cet effet, nous nous engageons à modifier la structure des fullerènes encapsulées par irradiation UV.

Les spectres Raman du peapod (l'échantillon A) avant et après l'irradiation sont présentés sur la Figure C.4.

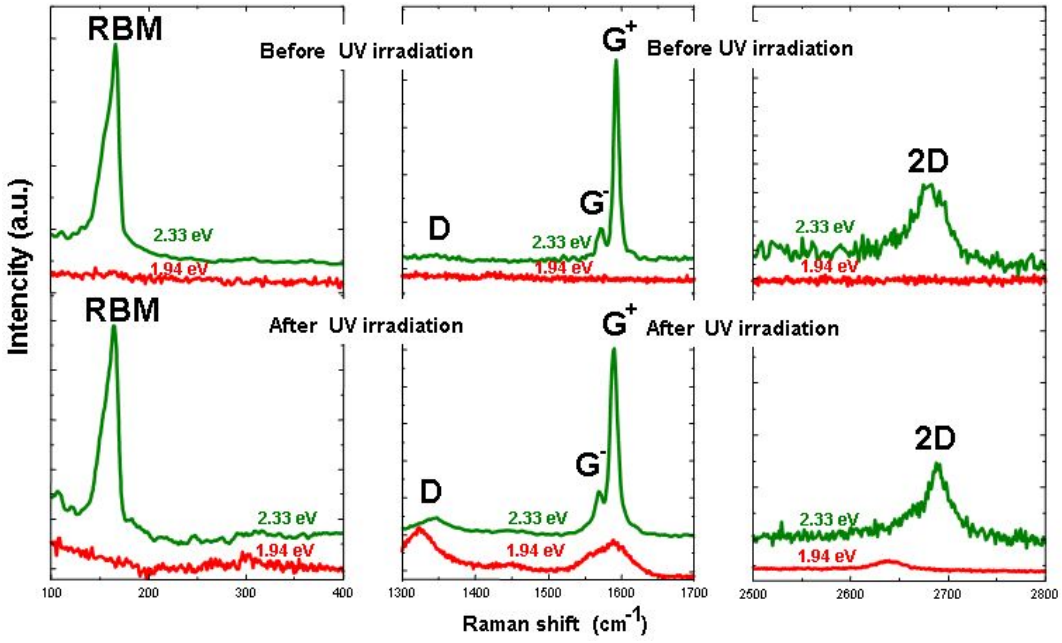

Figure C.4: Les spectres Raman à 2,33 eV (vert) et à 1,94 eV (rouge) avant et après l'irradiation UV, pour l'échantillon A.

Après l'irradiation, les spectres Raman pour l'énergie d'excitation 2.33 eV confirme la présence de tube semi-conducteur extérieur. Pour l'énergie d'excitation 2.33 eV, on constate le début de la fusion des bandes G^+ et G^-, ce qui témoigne d'une coalescence des fullerènes. Pour l'énergie d'excitation 1,94 eV, nous voyons l'apparition du signal Raman qui n'existait pas auparavant, associée à une modification des fullerènes. L'intensité de la bande D par rapport à la bande G indique le caractère incomplet et la défectuosité de cette structure.

Les échantillons irradiés présentent une chute importante de conductance en comparaison avec les mêmes échantillons avant l'irradiation (Figure C.5).

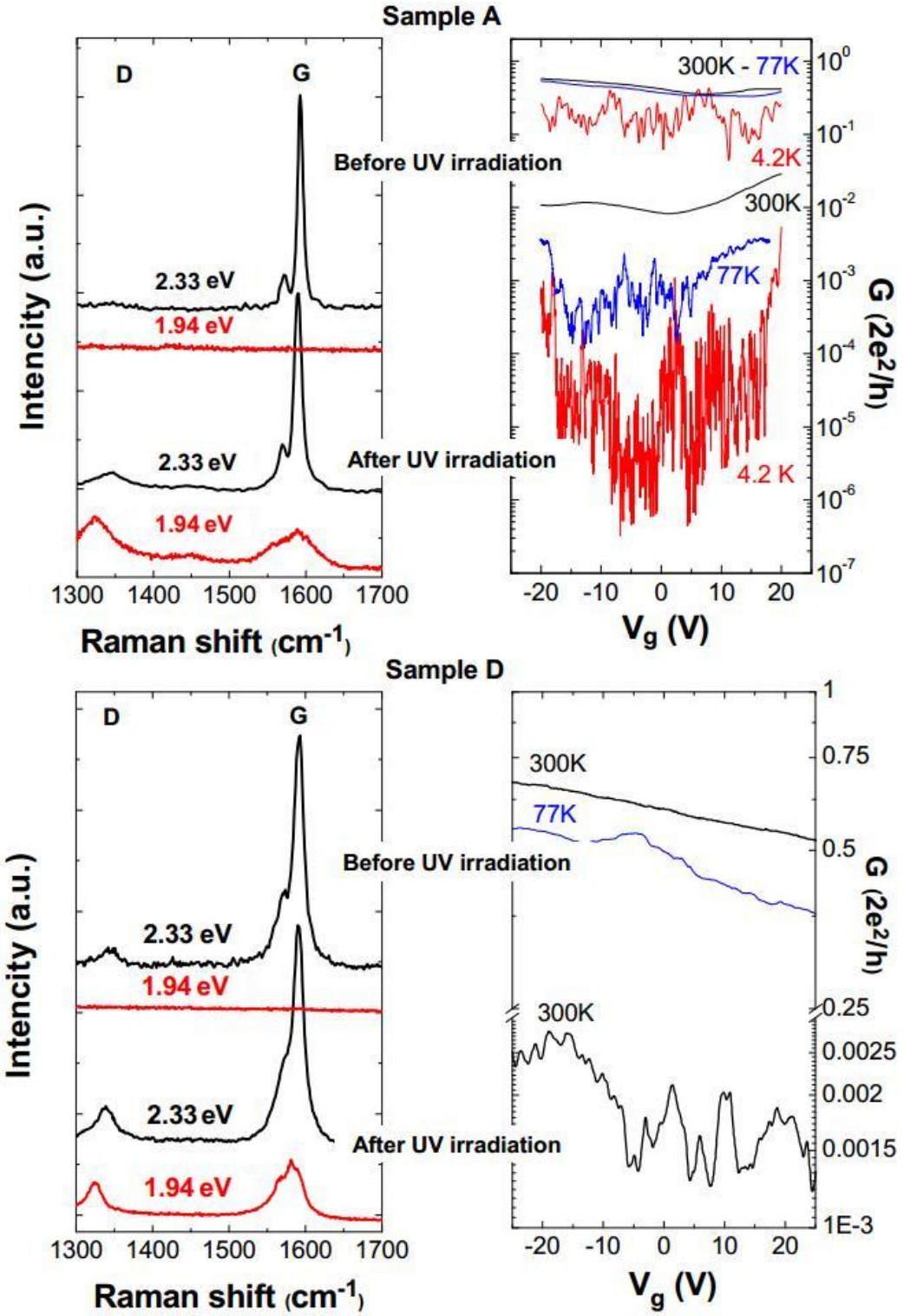

Figure C.5: Les spectres Raman à différentes énergies d'excitation et les mesures de conductance en fonction de la tension de grille à différentes températures, avant et après irradiation UV sur deux échantillons A et D (figures supérieurs et inférieurs, respectivement).

Pour l'échantillon A, le faible niveau de conductance accompagnée d'une dépendance en température plus prononcée est le signe d'un comportement ambipolaire en fonction de la tension de grille sur les bords de la fenêtre en énergie. Les résultats des simulations de conductance du peapod avant et après irradiation (fait par K.P. Katin et M.M. Maslov) confirment qualitativement la chute de conductance de deux ordres de grandeur.

C.3.5 Conclusion

Dans cette thèse, les propriétés électroniques des peapods individuels ont été étudiées en combinant les mesures de spectroscopie micro-Raman et de magnéto-transport sur les mêmes échantillons. Nous avons constaté que les C_{60}s encapsulés modifient fortement la structure de bande électronique des nanotubes semiconducteurs au voisinage du point de neutralité de charge. Cette modification comprend un déplacement rigide de la structure électronique et un remplissage partiel de la bande interdite. Nous avons aussi montré que l'excitation UV sélective des fullerènes conduit à une forte modification du couplage électronique entre les C_{60}s et le CNT induite par la coalescence partielle des C_{60}s et de leur distribution à l'intérieur du tube. Les résultats expérimentaux sont supportés par des simulations numériques de la densité d'états et de la conductance des nanotubes de carbone avec des fullerènes à l'intérieur (K. Katin, M. Maslov).

C.4 Les résultats obtenus sur les nanofils d'InAs

Cette partie est consacrée aux propriétés électroniques de nanofils d'InAs. Les nanofils semiconducteurs font l'objet de recherches actives depuis ces dix dernières années. Ils représentent des systèmes modèles pour l'étude des propriétés électroniques des objets quasi-1D. Ils représentent en outre des possibilités de modulation de la structure de bande ainsi que de contrôle de la densité de porteurs. Dans ce domaine de recherche, les nanofils semi-conducteurs à base de composes III-V tels que InAs, ont une place particulière en raison de la faible masse effective des porteurs de charge. Nous avons étudié la conductance de nanofils individuels dans une large gamme de champs magnétiques (jusqu'à 60 T).

C.4.1 La caractérisation de transport électronique à champ magnétique nul

Les résultats sont présentés par cinq échantillons, nommés ici A, B, C, D et E. Les paramètres de ces échantillons sont résumés dans le Tableau C.2.

L'échantillon	Diamètre ($\pm 0.5\ nm$)	Longueur ($\pm 5\ nm$)	Mobilité à 4.2 K ($cm^2/(Vs)$)	L_φ à 4.2 K ($\pm 5\ nm$)
A	33.1	377	3000	130
B	34.7	375	1000	120
C	29.8	386	900	125
D	37.8	372	1500	110
E	$80 \pm 5\ nm$	600	840	200

Table C.2: Dimensions géométriques et longueurs caractéristiques de transport des nanofils d'InAs.

La figure C.6 présente les mesures de conductance $G(V_g)$ de l'échantillon A pour différentes températures.

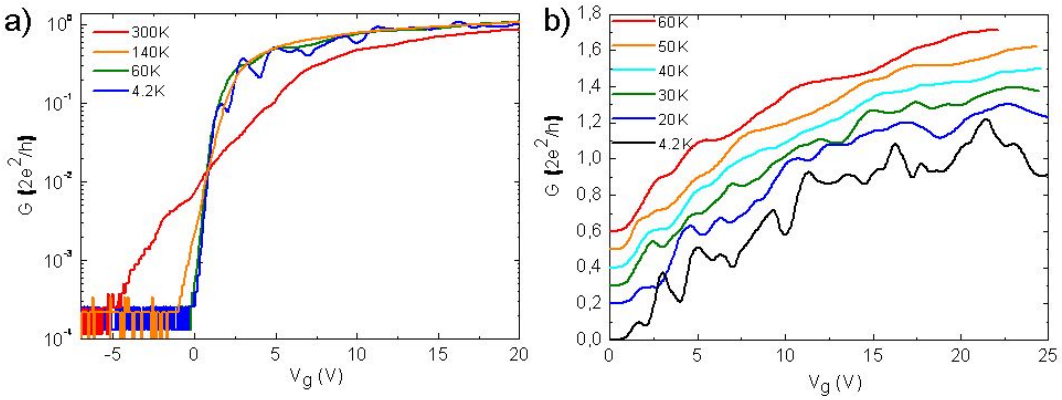

Figure C.6: L'échantillon A. Conductance en fonction de la tension de grille mesurée à des températures différentes. La tension drain-source est $V_{ds} = 1\ mV$ pour toutes les courbes. Sur la figure de droite, les courbes sont décalées pour plus de clarté.

Les transitions On/Off se révèlent plus abrupte avec la diminution de la température, montrant l'augmentation de la mobilité des électrons à basse température. La mobilité a été estimée à environ $\sim 10^3\ cm^2(Vs)^{-1}$ à basses températures (T = 4.2 K). Les modulations de la conductance à basse température sont constitués de deux composantes: les fluctuations, qui sont fortement dépendantes de la température, et les fluctuations en forme de marche, qui persistent jusqu'à T = 60 K et qui sont reproductibles pour différents cycles thermiques. L'origine physique de la première contribution est attribuée aux fluctuations universelles de conductance (UCF) provenant des changements d'interférence électronique. La deuxième contribution, les caractéristiques en forme de marche, est attribuée à la structure de bande 1-D des nanofils.

Grâce aux calculs de la structure de bande de nanofils d'InAs, qui a été faites

par Yann-Michel Niquet (Institut nanosciences et Cryogénie - INAC / CEA), nous avons calculé la DOS et tracer sa dépendance en fonction de la tension de grille (Figure C.7).

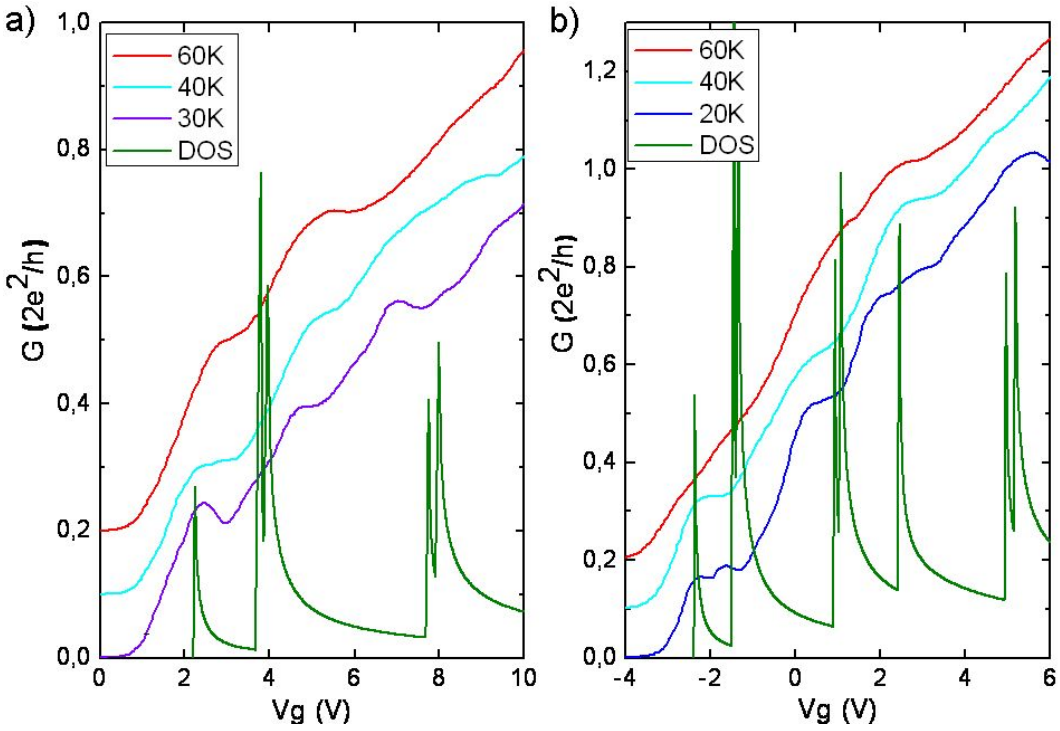

Figure C.7: Conductance en fonction de la tension de grille à températures modérées et la DOS (courbes vertes) en unité arbitraire pour a) l'échantillon A et b) l'échantillon D.

Les fluctuations en forme de marche (Figure 7) sont en bon accord avec la position des singularités de van Hove, calculée directement à partir de la loi de dispersion sans paramètre libre. Ainsi, nous observons l'influence des sous-bandes 1D individuelles sur le transport électronique.

De l'étude de l'UCF nous avons déduit la longueur de cohérence $L_\varphi = 120\ nm$, pour les nanofils $d = 33\ nm$, et $L_\varphi = 200\ nm$, pour les nanofils $d = 80\ nm$. Cette valeur a été confirmée par l'étude de l'UCF sous champ magnétique.

C.4.2 Les expériences de magnéto-transport sur les nanofils d'InAs

La figure C.8 présente, à une échelle semi-logarithmique, le comportement de magnétoconductance typique de nanofils d'InAs, mesuré à T = 4.2 K pour différentes valeurs de la tension de grille, et dans deux configurations du champ magnétique.

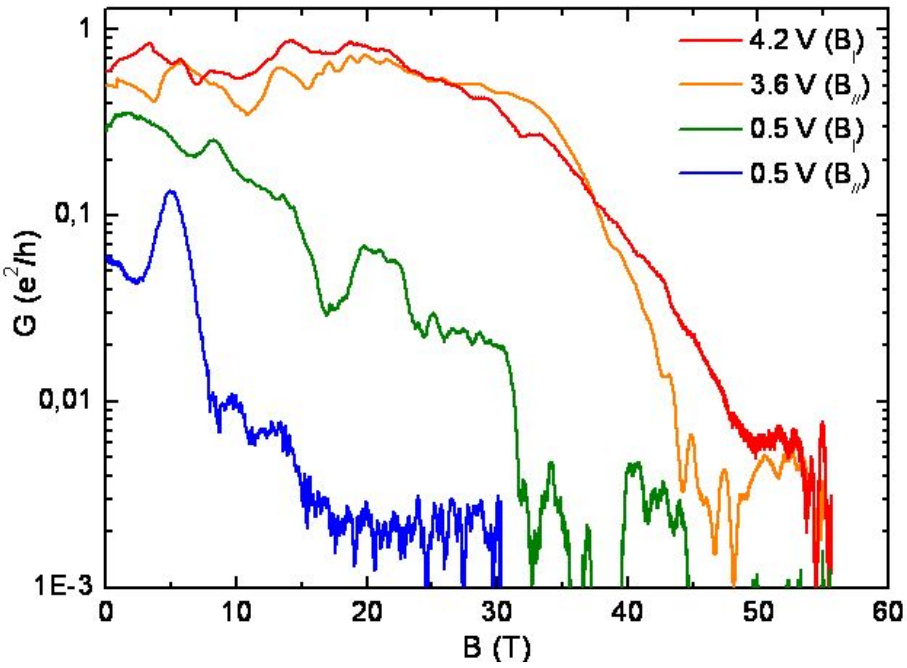

Figure C.8: Conductance en fonction du champ magnétique parallèle (orange et bleu) et perpendiculaire (rouge et vert) pour deux gammes de V_g correspondant à différentes positions de l'énergie de Fermi, T = 4.2 K, pour l'échantillon A.

Pour les deux configurations, à bas champ magnétique et sous champ intermédiaire, la conductance montre des fluctuations, suivies d'une suppression de conductance à champ magnétique fort. Au-delà d'un champ critique, qui augmente nettement avec l'énergie de Fermi, la conductance décroît rapidement jusqu'à des valeurs qui sont proches de la résolution expérimentale. Cet effet peut être associé à la perte de canaux de conduction une fois que toutes les sous-bandes magnétoélectriques, décalées vers les hautes énergies par le champ magnétique, ont traversé l'énergie de Fermi.

Pour comprendre ce comportement, les calculs de la structure de bandes des nanofils d'InAs ont été réalisés par Yann-Michel Niquet et ses collègues, en tenant compte des confinements latéral et magnétique. La figure C.9a présente les mesures de magnétotransport sur l'échantillon A sous champ magnétique. La figure C.9b présente les sous-bandes magnétoélectriques calculées en fonction du champ magnétique. L'orientation du champ magnétique est perpendiculaire à l'axe du nanofil.

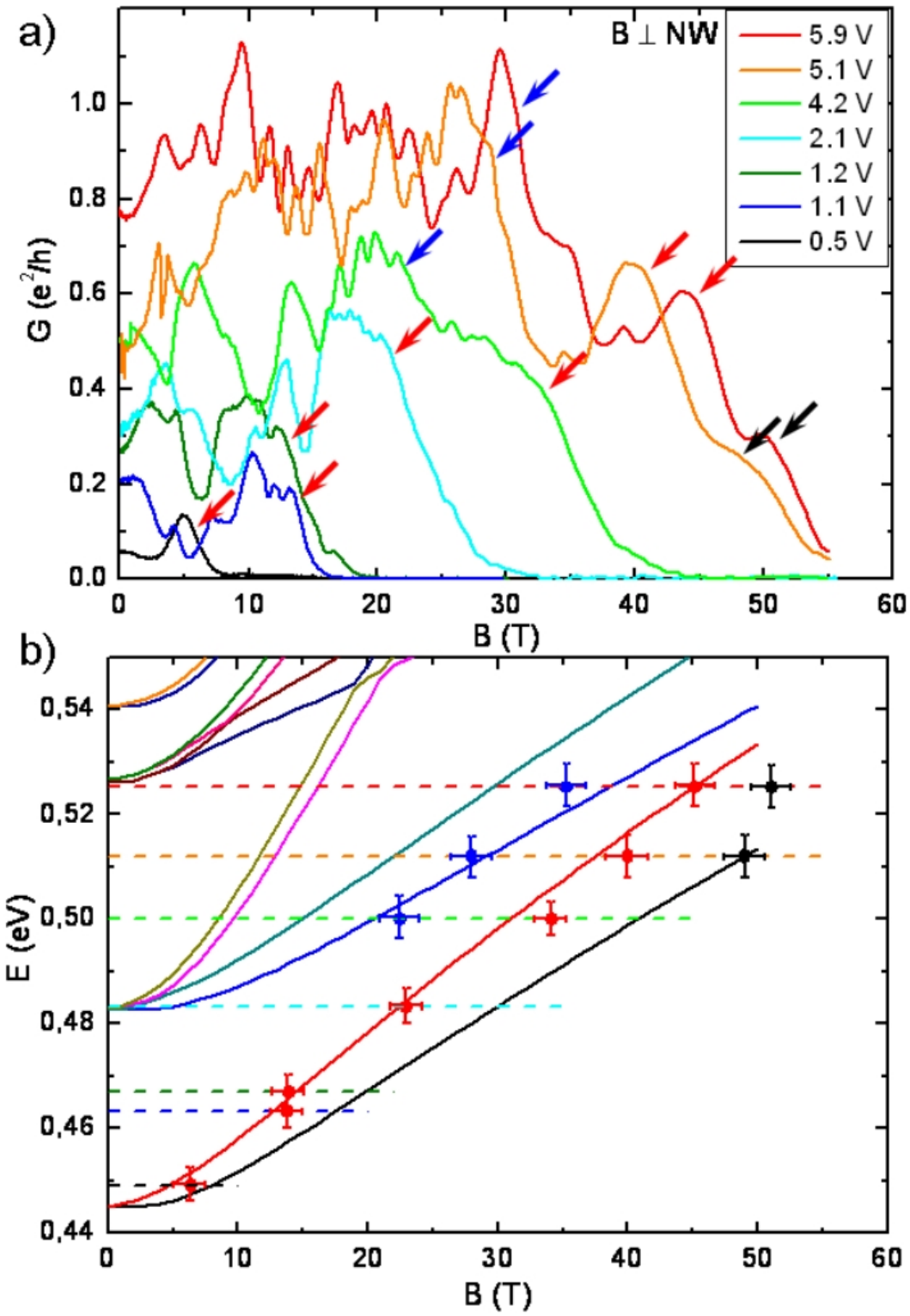

Figure C.9: L'échantillon A. a) Magnéto-conductance pour différentes tensions de grille sous un champ magnétique perpendiculaire à T = 4.2 K, les diminutions de conductance correspondant à la perte de des canaux de conduction sont marquées par les flèches. b) Les sous-bandes magnéto-électriques calculées en fonction du champ magnétique. Les lignes pointillées indiquent le niveau de Fermi pour les courbes $G(B)$, les couleurs correspondent de courbes $G(V_g)$. Les cercles pleins correspondent à la position des flèches sur la figure a) (la couleur correspond à la sous-bande perdue).

Nous avons obtenu un bon accord entre les chutes de conductance et les traversées du niveau de Fermi ($B = 0$) par les sous-bandes magnéto-électriques. Afin de faire ressortir cet effet, la couleur des flèches sur la Figure C.9a et des cercles sur la Figure C.9b correspondent à la couleur de la sous-bande, qui traverse le niveau de Fermi, pour une courbe $G(B)$ donnée. Ainsi, nous attribuons le comportement $G(B)$ à la perte de canaux de conduction, décalée vers les hautes énergies par le champ magnétique appliqué.

C.4.3 Conclusion

Nous avons étudié la conductance de nanofils individuels dans une large gamme de champs magnétiques (jusqu'à 60 T). Les mesures en champ nul et en champ faible ont démontré un transport faiblement diffusif dans ces nanofils. Les mesures de transport sous champ magnétique intense ont révélé une forte chute de la conductance au dessus d'un champ critique qui augmente clairement avec l'énergie de Fermi. Cet effet est interprété par la perte de canaux de conduction une fois que toutes les sous-bandes magnéto-électriques, décalés vers les hautes énergies par le champ magnétique, ont traversé l'énergie de Fermi. Les calculs de structure de bande préliminaires (Y-M. Niquet), en prenant en compte les confinements latéraux et magnétiques, sont en bon accord qualitatif avec les résultats observés dans le régime de champ magnétique intense. Ce résultat est la première observation des effets de structure de bande dans les expériences de magnéto-transport sur les nanofils semiconducteurs.

C.5 Conclusion générale

Cette thèse présente des mesures de transport électronique dans des nano-objets individuels quasi-unidimensionnels (quasi-1D) sous champ magnétique intense. Deux systèmes différents présentant un confinement quasi-1D ont été considérés: les peapods de carbone (C_{60}@SWCNTs) et les nanofils d'InAs. L'objectif de ces travaux consiste à sonder les états électroniques spécifiques de ces systèmes au voisinage de niveau de Fermi par des mesures de magnétotransport. Dans les deux cas, les expériences sous champs magnétiques intenses s'accompagnent d'un contrôle du nombre de porteurs de charge par dopage électrostatique ainsi que par des mesures complémentaires des propriétés structurales.

Nos travaux sur les C_{60}@SWCNTs ont relevé que les C_{60}s encapsulés dans un nanotube de carbone monoparoi semi-conducteur modifient fortement sa structure de bande électronique au voisinage du point de neutralité de charge impliquant un déplacement rigide de la structure électronique et un remplissage partiel de la bande interdite. Nous avons aussi montré que l'excitation UV sélective des fullerènes encapsulés conduit à une forte modification du transport électronique du peapod, attribuée à une coalescence partielle des C_{60}s et à leur redistribution à l'intérieur du tube.

Les mesures de magnétotransport sur des nanofils individuels d'InAs ont mis en évidence, pour la première fois, des transitions de l'état conducteur à l'état bloqué du nanofils en configuration transistor. Ces dernières sont induites par un champ magnétique intense et sont modulées par la densité de porteurs. Appuyés par des simulations de structures électroniques, nos résultats révèlent la formation de sous-bandes magnéto-électriques dans les nanofils et leurs signatures directes sur la magnéto-conductance.

Bibliography

[Altshuler 1981] B L Altshuler et A G Aronov. *Magnetoresistance of thin films and of wires in a longitudinal magnetic field.* JETP Lett., vol. 33, page 499, 1981. (Cited page 112.)

[Altshuler 1982] B L Altshuler, A G Aronov et D E Khmelnitsky. *Effects of electron-electron collisions with small energy transfers on quantum localisation.* Journal of Physics C: Solid State Physics, vol. 15, no. 36, page 7367, 1982. (Cited pages 107 and 111.)

[Anderson 1958] P. W. Anderson. *Absence of Diffusion in Certain Random Lattices.* Phys. Rev., vol. 109, pages 1492–1505, Mar 1958. (Cited page 17.)

[Antell 1959] G R Antell et D Effer. J. Electroanal. Chem. Soc., vol. 106, page 509, 1959. (Cited page 92.)

[Aronov 1987] A. G. Aronov et Yu. V. Sharvin. *Magnetic flux effects in disordered conductors.* Rev. Mod. Phys., vol. 59, pages 755–779, Jul 1987. (Cited page 114.)

[Arrondo 2005] C. Arrondo, M. Monthioux, K. Kishita et M. Le Lay. *In-situ coalescence of aligned C_{60} molecules in Peapods.* AIP Conference Proceedings, vol. 786, pages 329–332, 2005. (Cited page 75.)

[Atalla 1959] E.; Scheibner E.J. Atalla M.M.; Tannenbaum. *Stabilization of Silicon Surfaces by Thermally Grown Oxides.* Bell System Technical Journal, vol. 38, pages 749–783, 1959. (Cited page 1.)

[Bachtold 1999] Adrian Bachtold, Christoph Strunk, Jean-Paul Salvetat, Jean-Marc Bonard, Laszlo Forro, Thomas Nussbaumer et Christian Schonenberger. *Aharonov-Bohm oscillations in carbon nanotubes.* Nature, vol. 397, pages 673–675, 1999. (Cited page 83.)

[Bandow 2001] S. Bandow, M. Takizawa, K. Hirahara, M. Yudasaka et S. Iijima. *Raman scattering study of double-wall carbon nanotubes derived from the chains of fullerenes in single-wall carbon nanotubes.* Chemical Physics Letters, vol. 337, pages 48 – 54, 2001. (Cited page 75.)

[Bandow 2004] S. Bandow, T. Hiraoka, T. Yumura, K. Hirahara, H. Shinohara et S. Iijima. *Raman scattering study on fullerene derived intermediates formed within single-wall carbon nanotube: from peapod to double-wall carbon nanotube.* Chemical Physics Letters, vol. 384, pages 320 – 325, 2004. (Cited page 75.)

[Beenakker 1988] C. W. J. Beenakker et H. van Houten. *Flux-cancellation effect on narrow-channel magnetoresistance fluctuations.* Phys. Rev. B, vol. 37, pages 6544–6546, 1988. (Cited pages 81, 106, 110, 112, and 136.)

[Beenakker 1991] C.W.J. Beenakker et H. van Houten. *Quantum Transport in Semiconductor Nanostructures.* In Henry Ehrenreich et David Turnbull, editeurs, Semiconductor Heterostructures and Nanostructures, volume 44 of *Solid State Physics*, pages 1 – 228. Academic Press, 1991. (Cited pages 5, 13, 32, 33, and 34.)

[Berd 2012] Mourad Berd, Pascal Puech, Ariete Righi, Arezki Benfdila et Marc Monthioux. *Resonant Laser-Induced Formation of Double-Walled Carbon Nanotubes from Peapods under Ambient Conditions.* Small, vol. 8, pages 2045–2052, 2012. (Cited pages 75, 76, and 85.)

[Blömers 2011] Ch. Blömers, M. I. Lepsa, M. Luysberg, D. Grützmacher, H. Lüth et Th. Schäpers. *Electronic Phase Coherence in InAs Nanowires.* Nano Letters, vol. 11, no. 9, pages 3550–3556, 2011. (Cited pages 96, 98, 106, and 107.)

[Bogachek 1993] E. N. Bogachek, M. Jonson, R. I. Shekhter et T. Swahn. *Magnetic-flux-induced conductance steps in microwires.* Phys. Rev. B, vol. 47, pages 16635–16638, Jun 1993. (Cited pages 35, 36, and 98.)

[Bogachek 1994] E. N. Bogachek, M. Jonson, R. I Shekhter et T. Swahn. *Discrete electronic transport through a microwire in a longitudinal magnetic field.* Phys. Rev. B, vol. 50, pages 18341–18349, Dec 1994. (Cited pages 35, 36, and 98.)

[Bogachek 1996] E. N. Bogachek, A. G. Scherbakov et Uzi Landman. *Magnetic switching and thermal enhancement of quantum transport through nanowires.* Phys. Rev. B, vol. 53, pages R13246–R13249, May 1996. (Cited pages 35, 36, 37, 98, 99, and 116.)

[Boyko 1999] B. A. Boyko, A.I. Bykov, M.I. Dolotenko, N. P. Kolokolchikov, I. M. Markevtsev, O. M. Tatsenko et K. Shuvalov. *With record magnetic fields to the 21st Century.* In Pulsed Power Conference, 1999. Digest of Technical Papers. 12th IEEE International, volume 2, pages 746–749 vol.2, 1999. (Cited page 48.)

[Bryllert 2005] T. Bryllert, L. Samuelson, L.E. Jensen et L.E. Wernersson. *Vertical high mobility wrap-gated inas nanowire transistor.* Electron Devices Meeting, 2005. IEDM Technical Digest. IEEE International, vol. 1, pages 157 –158, 2005. (Cited pages 95 and 103.)

[Bychkov 1984a] Yu A Bychkov et E I Rashba. *Oscillatory effects and the magnetic susceptibility of carriers in inversion layers.* Journal of Physics C: Solid State Physics, vol. 17, no. 33, pages 6039–6045, 1984. (Cited pages 97 and 114.)

[Bychkov 1984b] Yu A Bychkov et E I Rashba. *Properties of a 2D electron-gas with lifted spectral degeneracy.* JETP, vol. 39, no. 33, pages 78–81, 1984. (Cited page 97.)

[Chazalviel 1975] J. N. Chazalviel. *Spin relaxation of conduction electrons in n-type indium antimonide at low temperature.* Phys. Rev. B, vol. 11, pages 1555–1562, Feb 1975. (Cited page 113.)

[Cho 2003] Youngmi Cho, Seungwu Han, Gunn Kim, Hosik Lee et Jisoon Ihm. *Orbital Hybridization and Charge Transfer in Carbon Nanopeapods.* Phys. Rev. Lett., vol. 90, page 106402, Mar 2003. (Cited pages 68, 70, and 73.)

[Cinke 2002] Martin Cinke, Jing Li, Bin Chen, Alan Cassell, Lance Delzeit, Jie Han et M Meyyappan. *Pore structure of raw and purified HiPco single-walled carbon nanotubes.* Chemical Physics Letters, vol. 365, pages 69 – 74, 2002. (Cited page 66.)

[Cui 2001] Yi Cui, Qingqiao Wei, Hongkun Park et Charles M. Lieber. *Nanowire Nanosensors for Highly Sensitive and Selective Detection of Biological and Chemical Species.* Science, vol. 293, pages 1289–1292, 2001. (Cited pages 91 and 96.)

[Datta 1995] Supriyo Datta. Electronic transport in mesoscopic systems. Cambridge University Press, 1995. (Cited pages 5, 18, 24, 26, 81, and 135.)

[Dayeh 2005] S A Dayeh, D Aplin, X Zhou, P K L Yu et E T Yuand D Wang. *47th TMS Annu. Electronic Materials Conf., Santa Barbara.* 2005. (Cited pages 95 and 103.)

[Dayeh 2007a] Shadi A. Dayeh, David P.R. Aplin, Xiaotian Zhou, Paul K.L. Yu, Edward T. Yu et Deli Wang. *High Electron Mobility InAs Nanowire Field-Effect Transistors.* Small, vol. 3, no. 2, pages 326–332, 2007. (Cited pages 95 and 103.)

[Dayeh 2007b] Shadi A. Dayeh, Cesare Soci, Paul K. L. Yu, Edward T. Yu et Deli Wang. *Influence of surface states on the extraction of transport parameters from InAs nanowire field effect transistors.* Applied Physics Letters, vol. 90, page 162112, 2007. (Cited page 96.)

[Dayeh 2009a] Shadi A. Dayeh, Cesare Soci, Xin-Yu Bao et Deli Wang. *Advances in the synthesis of InAs and GaAs nanowires for electronic applications.* Nano Today, vol. 4, pages 347 – 358, 2009. (Cited pages 93 and 95.)

[Dayeh 2009b] Shadi A. Dayeh, Edward T. Yu et Deli Wang. *Transport Coefficients of InAs Nanowires as a Function of Diameter.* Small, vol. 5, no. 1, pages 77–81, 2009. (Cited pages 95 and 115.)

[Dayeh 2010] Shadi A Dayeh. *Electron transport in indium arsenide nanowires.* Semiconductor Science and Technology, vol. 25, page 024004, 2010. (Cited page 92.)

[Debald 2005] S. Debald et B. Kramer. *Rashba effect and magnetic field in semiconductor quantum wires.* Phys. Rev. B, vol. 71, page 115322, Mar 2005. (Cited pages 35, 98, 99, and 116.)

[Dhara 2009] Sajal Dhara, Hari S. Solanki, Vibhor Singh, Arjun Narayanan, Prajakta Chaudhari, Mahesh Gokhale, Arnab Bhattacharya et Mandar M. Deshmukh. *Magnetotransport properties of individual InAs nanowires.* Phys. Rev. B, vol. 79, page 121311, 2009. (Cited pages 96, 98, 106, and 115.)

[Ditlevsen 1993] P.D. Ditlevsen, M.A. Van Hove et G.A. Somorjai. *Molecular modeling of ethylene decomposition on platinum surfaces.* Surface Science, vol. 292, pages 267 – 275, 1993. (Cited pages 88 and 135.)

[Doh 2005] Yong-Joo Doh, Jorden A. van Dam, Aarnoud L. Roest, Erik P. A. M. Bakkers, Leo P. Kouwenhoven et Silvano De Franceschi. *Tunable Supercurrent Through Semiconductor Nanowires.* Science, vol. 309, no. 5732, pages 272–275, 2005. (Cited page 91.)

[Dresselhaus 1955] G. Dresselhaus. *Spin-Orbit Coupling Effects in Zinc Blende Structures.* Phys. Rev., vol. 100, pages 580–586, Oct 1955. (Cited page 97.)

[Dresselhaus 1995] M. S. Dresselhaus, G. Dresselhaus et P.C. Eklund. Science of fullerenes and carbon nanotubes. CA: Academic Press, 1995. (Cited pages 40, 61, 62, and 63.)

[Dresselhaus 2005] M.S. Dresselhaus, G. Dresselhaus, R. Saito et A. Jorio. *Raman spectroscopy of carbon nanotubes.* Physics Reports, vol. 409, pages 47 – 99, 2005. (Cited pages 52, 55, and 56.)

[Dubay 2004] O. Dubay et G. Kresse. *Density functional calculations for C_{60} peapods.* Phys. Rev. B, vol. 70, page 165424, Oct 2004. (Cited page 71.)

[Eliasen 2010] Anders Eliasen, Jens Paaske, Karsten Flensberg, Sebastian Smerat, Martin Leijnse, Maarten R. Wegewijs, Henrik I. Jorgensen, Marc Monthioux et Jesper Nygard. *Transport via coupled states in a C_{60} peapod quantum dot.* Phys. Rev. B, vol. 81, page 155431, 2010. (Cited pages 60, 66, 73, and 74.)

[Elliott 1954] R. J. Elliott. *Theory of the Effect of Spin-Orbit Coupling on Magnetic Resonance in Some Semiconductors.* Phys. Rev., vol. 96, pages 266–279, Oct 1954. (Cited page 97.)

[Endo 1996] Morinubo Endo, Sumio Iijima et Mildred S. Dresselhaus. Carbon nanotubes. Elsevier, 1996. (Cited page 2.)

[Estévez Hernández 2010] S. Estévez Hernández, M. Akabori, K. Sladek, Ch. Volk, S. Alagha, H. Hardtdegen, M. G. Pala, N. Demarina, D. Grützmacher et Th. Schäpers. *Spin-orbit coupling and phase coherence in InAs nanowires.* Phys. Rev. B, vol. 82, page 235303, Dec 2010. (Cited page 98.)

[Fedorov 2007] Georgy Fedorov, Alexander Tselev, David Jimenez, Sylvain Latil, Nikolai G. Kalugin, Paola Barbara, Dmitry Smirnov et Stephan Roche. *Magnetically Induced Field Effect in Carbon Nanotube Devices.* Nano Letters, vol. 7, pages 960–964, 2007. (Cited page 84.)

[Ferry 1997] David K. Ferry et Stephen M. Goodnick. Transport in nanostructures. Cambridge University Press, 1997. (Cited pages 5 and 31.)

[Foldvari 2008] Marianna Foldvari et Mukasa Bagonluri. *Carbon nanotubes as functional excipients for nanomedicines: II. Drug delivery and biocompatibility issues.* Nanomedicine: Nanotechnology, Biology and Medicine, vol. 4, no. 3, pages 183 – 200, 2008. (Cited page 60.)

[Ford 2009] Alexandra C. Ford, Johnny C. Ho, Yu-Lun Chueh, Yu-Chih Tseng, Zhiyong Fan, Jing Guo, Jeffrey Bokor et Ali Javey. *Diameter-Dependent Electron Mobility of InAs Nanowires.* Nano Letters, vol. 9, pages 360–365, 2009. (Cited pages 95, 96, and 101.)

[Ford 2012] Alexandra C. Ford, S. Bala Kumar, Rehan Kapadia, Jing Guo et Ali Javey. *Observation of Degenerate One-Dimensional Sub-Bands in Cylindrical InAs Nanowires.* Nano Letters, vol. 12, no. 3, pages 1340–1343, 2012. (Cited page 103.)

[Georgakilas 2007] Vasilios Georgakilas, Dimitrios Gournis, Vasilios Tzitzios, Lucia Pasquato, Dirk M. Guldi et Maurizio Prato. *Decorating carbon nanotubes with metal or semiconductor nanoparticles.* J. Mater. Chem., vol. 17, pages 2679–2694, 2007. (Cited page 59.)

[Golubev 1985] V. G. Golubev, V. I. Ivanov-Omskii, I. G. Minervin, A. V. Osutin et D. G. Polyakov. *Nonparabolicity and anisotropy of the electron energy spectrum in GaAs.* Sov. Phys. JETP, vol. 61, pages 1214–1219, 1985. (Cited page 92.)

[Graf 1995] M. Graf et P. Vogl. *Electromagnetic fields and dielectric response in empirical tight-binding theory.* Phys. Rev. B, vol. 51, pages 4940–4949, 1995. (Cited page 135.)

[Gunnarsson 1997] O. Gunnarsson. *Superconductivity in fullerides.* Rev. Mod. Phys., vol. 69, pages 575–606, 1997. (Cited page 67.)

[Haluska 1993] M. Haluska, P. Fejdi, M. Vybornov et H. Kuzmany. *Structural and Morphological Characterization of Fullerite Crystals Prepared from the Vapor Phase.* In Electronic Properties of Fullerenes, volume 117 of *Springer Series in Solid-State Sciences*, pages 173–176. Springer Berlin Heidelberg, 1993. (Cited page 67.)

[Hansen 2005] A. E. Hansen, M. T. Björk, C. Fasth, C. Thelander et L. Samuelson. *Spin relaxation in InAs nanowires studied by tunable weak antilocalization.* Phys. Rev. B, vol. 71, page 205328, 2005. (Cited pages 96, 97, 98, 106, 111, and 115.)

[Heinrich 1988] H. Heinrich et G. Bauer. Physics and technology of submicron structures. Springer Series in Solid-State Sciences V83, 1988. (Cited page 17.)

[Hernandez 2003] E. Hernandez, V. Meunier, B. W. Smith, R. Rurali, H. Terrones, M. Buongiorno Nardelli, M. Terrones, D. E. Luzzi et J.-C. Charlier. *Fullerene Coalescence in Nanopeapods: A Path to Novel Tubular Carbon.* Nano Letters, vol. 3, pages 1037–1042, 2003. (Cited page 75.)

[Heun 2010] S. Heun, B. Radha, D. Ercolani, G. U. Kulkarni, F. Rossi, V. Grillo, G. Salviati, F. Beltram et L. Sorba. *Pd-Assisted Growth of InAs Nanowires.* Crystal Growth & Design, vol. 10, no. 9, pages 4197–4202, 2010. (Cited pages 40 and 100.)

[Hirahara 2000] K. Hirahara, K. Suenaga, S. Bandow, H. Kato, T. Okazaki, H. Shinohara et S. Iijima. *One-Dimensional Metallofullerene Crystal Generated*

Inside Single-Walled Carbon Nanotubes. Phys. Rev. Lett., vol. 85, pages 5384–5387, 2000. (Cited page 41.)

[Hoffmann 1963] Roald Hoffmann. *An Extended H[u-umlaut]ckel Theory. I. Hydrocarbons.* The Journal of Chemical Physics, vol. 39, no. 6, pages 1397–1412, 1963. (Cited page 81.)

[Hornbaker 2002] D. J. Hornbaker, S.-J. Kahng, S. Misra, B. W. Smith, A. T. Johnson, E. J. Mele, D. E. Luzzi et A. Yazdani. *Mapping the One-Dimensional Electronic States of Nanotube Peapod Structures.* Science, vol. 295, pages 828–831, 2002. (Cited pages 60, 66, and 72.)

[Iijima 1991] Sumio Iijima. *Helical microtubules of graphitic carbon.* Nature, vol. 354, page 56, 1991. (Cited pages 1 and 2.)

[Jancu 1998] Jean-Marc Jancu, Reinhard Scholz, Fabio Beltram et Franco Bassani. *Empirical spds∗ tight-binding calculation for cubic semiconductors: General method and material parameters.* Phys. Rev. B, vol. 57, pages 6493–6507, 1998. (Cited page 135.)

[Javey 2003] Ali Javey, Jing AU Guo, Qian Wang, Mark Lundstrom et Hongjie Dai. *Ballistic carbon nanotube field-effect transistors.* Nature, vol. 424, pages 654–657, 2003. (Cited page 65.)

[Jiang 2000] Jie Jiang, Jinming Dong et D. Y. Xing. *Zeeman effect on the electronic spectral properties of carbon nanotubes in an axial magnetic field.* Phys. Rev. B, vol. 62, pages 13209–13215, Nov 2000. (Cited page 83.)

[Jing Kong 2000] Chongwu Zhou Michael G. Chapline Shu Peng Kyeongjae Cho Hongjie Dai Jing Kong Nathan R. Franklin. *Nanotube Molecular Wires as Chemical Sensors.* Science, vol. 287, page 622, 2000. (Cited page 65.)

[Jorio 2002] A. Jorio, A. G. Souza Filho, G. Dresselhaus, M. S. Dresselhaus, A. K. Swan, M. S. Ünlü, B. B. Goldberg, M. A. Pimenta, J. H. Hafner, C. M. Lieber et R. Saito. *G-band resonant Raman study of 62 isolated single-wall carbon nanotubes.* Phys. Rev. B, vol. 65, page 155412, 2002. (Cited page 78.)

[Jorio 2008] Ado Jorio, Gene Dresselhaus et Mildred S. Dresselhaus. Carbon nanotubes: Advanced topics in the synthesis, structure, properties and applications (topics in applied physics). Springer-Verlag, Berlin, 2008. (Cited page 2.)

[Katz 2006] E. A. Katz. Fullerene thin films as photovoltaic material. Elsevier, 2006. (Cited page 67.)

[Klitzing 1980] K. v. Klitzing, G. Dorda et M. Pepper. *New Method for High-Accuracy Determination of the Fine-Structure Constant Based on Quantized Hall Resistance.* Phys. Rev. Lett., vol. 45, pages 494–497, 1980. (Cited page 1.)

[Koguchi 1992] Masanari Koguchi, Hiroshi Kakibayashi, Masamitsu Yazawa, Kenji Hiruma et Toshio Katsuyama. *Crystal Structure Change of GaAs and InAs Whiskers from Zinc-Blende to Wurtzite Type.* Japanese Journal of Applied Physics, vol. 31, pages 2061–2065, 1992. (Cited pages 93 and 94.)

[Kojima 2012] Takashi Kojima et Tomoya Ono. *First-principles study on transport property of peapods.* Current Applied Physics, vol. 12, no. 0, pages S100–S104, 2012. (Cited pages 71 and 73.)

[Kondo 2005] Hisashi Kondo, Hiori Kino et Takahisa Ohno. *Transport properties of carbon nanotubes encapsulating* C_{60} *and related materials.* Phys. Rev. B, vol. 71, page 115413, Mar 2005. (Cited pages 69, 85, and 88.)

[Kong 2001] Jing Kong, Erhan Yenilmez, Thomas W. Tombler, Woong Kim, Hongjie Dai, Robert B. Laughlin, Lei Liu, C. S. Jayanthi et S. Y. Wu. *Quantum Interference and Ballistic Transmission in Nanotube Electron Waveguides.* Phys. Rev. Lett., vol. 87, page 106801, 2001. (Cited page 65.)

[Kong 2007] Byung-Seon Kong, Dae-Hwan Jung, Sang-Keun Oh, Chang-Soo Han et Hee-Tae Jung. *Single-Walled Carbon Nanotube Gold Nanohybrids: Application in Highly Effective Transparent and Conductive Films.* The Journal of Physical Chemistry C, vol. 111, no. 23, pages 8377–8382, 2007. (Cited page 60.)

[Kongkanand 2007] Anusorn Kongkanand, Rebeca Martínez Domínguez et Prashant V. Kamat. *Single Wall Carbon Nanotube Scaffolds for Photoelectrochemical Solar Cells. Capture and Transport of Photogenerated Electrons.* Nano Letters, vol. 7, pages 676–680, 2007. (Cited page 60.)

[Krishtopenko 2012] S S Krishtopenko, V I Gavrilenko et M Goiran. *Exchange interaction effects in electron spin resonance: Larmor theorem violation in narrow-gap quantum well heterostructures.* Journal of Physics: Condensed Matter, vol. 24, page 252201, 2012. (Cited page 92.)

[Kroto 1985] H.W. Kroto, J.R. Heath, S.C. Obrien, R.F. Curl et R.E. Smalley. *C_{60}: Buckminsterfullerene.* Nature, vol. 318, page 162, 1985. (Cited pages 1 and 66.)

[Krupke 2003] Ralph Krupke, Frank Hennrich, Hilbert v. Löhneysen et Manfred M. Kappes. *Separation of Metallic from Semiconducting Single-Walled Carbon Nanotubes.* Science, vol. 301, pages 344–347, 2003. (Cited page 78.)

[Kubo 1966] R Kubo. *The fluctuation-dissipation theorem.* Reports on Progress in Physics, vol. 29, no. 1, page 255, 1966. (Cited page 35.)

[Kumar 2010] A. Kumar, G. A. Csáthy, M. J. Manfra, L. N. Pfeiffer et K. W. West. *Nonconventional Odd-Denominator Fractional Quantum Hall States in the Second Landau Level.* Phys. Rev. Lett., vol. 105, page 246808, Dec 2010. (Cited page 13.)

[Landauer 1970] Rolf Landauer. *Electrical resistance of disordered one-dimensional lattices.* Philosophical Magazine, vol. 21, pages 863–867, 1970. (Cited page 25.)

[Landrum 2006] G.A. Landrum et W.V. Glassey. *The YAeHMOP extended Hückel molecular orbital package.*, July 27 2006. (Cited pages 88 and 135.)

[Lee 1987] P. A. Lee, A. Douglas Stone et H. Fukuyama. *Universal conductance fluctuations in metals: Effects of finite temperature, interactions, and magnetic field.* Phys. Rev. B, vol. 35, pages 1039–1070, 1987. (Cited page 109.)

[Lee 2007] Hyunju Lee, Sang Won Yoon, Eun Joo Kim et Jeunghee Park. *In-Situ Growth of Copper Sulfide Nanocrystals on Multiwalled Carbon Nanotubes and Their Application as Novel Solar Cell and Amperometric Glucose Sensor Materials.* Nano Letters, vol. 7, pages 778–784, 2007. (Cited page 60.)

[Liang 2009] Dong Liang, Mohammed R. Sakr et Xuan P. A. Gao. *One-Dimensional Weak Localization of Electrons in a Single InAs Nanowire.* Nano Letters, vol. 9, no. 4, pages 1709–1712, 2009. (Cited page 98.)

[Liang 2010] Dong Liang, Juan Du et Xuan P. A. Gao. *Anisotropic magnetoconductance of a InAs nanowire: Angle-dependent suppression of one-dimensional weak localization.* Phys. Rev. B, vol. 81, page 153304, Apr 2010. (Cited pages 98, 106, 112, and 114.)

[Liang 2012] Dong Liang et Xuan P.A. Gao. *Strong Tuning of Rashba Spin-Orbit Interaction in Single InAs Nanowires.* Nano Letters, vol. 12, pages 3263–3267, 2012. (Cited pages 96, 98, 106, and 115.)

[Liu 2012] Xian-Ming Liu, Zhen dong Huang, Sei woon Oh, Biao Zhang, Peng-Cheng Ma, Matthew M.F. Yuen et Jang-Kyo Kim. *Carbon nanotube (CNT)-based composites as electrode material for rechargeable Li-ion batteries: A review.* Composites Science and Technology, vol. 72, pages 121 – 144, 2012. (Cited page 60.)

[Lu 2003] Jing Lu, Shigeru Nagase, Shuang Zhang et Lianmao Peng. *Strongly size-dependent electronic properties in C_{60}-encapsulated zigzag nanotubes and lower size limit of carbon nanopeapods.* Phys. Rev. B, vol. 68, page 121402, 2003. (Cited pages 68, 69, 70, and 73.)

[Lu 2009] Ganhua Lu, Leonidas E. Ocola et Junhong Chen. *Room-Temperature Gas Sensing Based on Electron Transfer between Discrete Tin Oxide Nanocrystals and Multiwalled Carbon Nanotubes.* Advanced Materials, vol. 21, pages 2487–2491, 2009. (Cited page 60.)

[Ludwig 2004] T. Ludwig, Ya. M. Blanter et A. D. Mirlin. *Nonequilibrium mesoscopic conductance fluctuations.* Phys. Rev. B, vol. 70, page 235315, 2004. (Cited pages 108, 129, and 132.)

[Luzzi 2000] David E. Luzzi et Brian W. Smith. *Carbon cage structures in single wall carbon nanotubes: a new class of materials.* Carbon, vol. 38, pages 1751 – 1756, 2000. (Cited page 75.)

[Maslov 2009] M.M. Maslov, A.I. Podlivaev et L.A. Openov. *Nonorthogonal tight-binding model for hydrocarbons.* Physics Letters A, vol. 373, pages 1653 – 1657, 2009. (Cited pages 81, 88, and 135.)

[Mikoshiba 1962] Nobuo Mikoshiba et Shun-ichi Gonda. *Weak-Field Magnetoresistance of Impurity Conduction in n-Type Germanium.* Phys. Rev., vol. 127, pages 1954–1961, 1962. (Cited page 84.)

[Mintmire 1998] J. W. Mintmire et C. T. White. *Universal Density of States for Carbon Nanotubes.* Phys. Rev. Lett., vol. 81, pages 2506–2509, 1998. (Cited page 63.)

[Miyake 2002] Takashi Miyake et Susumu Saito. *Electronic structure of potassium-doped carbon nanotubes.* Phys. Rev. B, vol. 65, page 165419, 2002. (Cited page 59.)

[Monthioux 2001] M. Monthioux, B.W. Smith, B. Burteaux, A. Claye, J.E. Fischer et D.E. Luzzi. *Sensitivity of single-wall carbon nanotubes to chemical processing: an electron microscopy investigation.* Carbon, vol. 39, pages 1251 – 1272, 2001. (Cited pages 40 and 41.)

[Monthioux 2002] M Monthioux. *Filling single-wall carbon nanotubes.* Carbon, vol. 40, pages 1809 – 1823, 2002. (Cited page 40.)

[Nanot 2009] Sébastien Nanot. *Structure de bandes et transport électronique dans les nanotubes de carbone sous champ magnétique intense.* PhD thesis, 2009. (Cited pages 49, 50, 65, and 79.)

[Niquet 2006] Y. M. Niquet, A. Lherbier, N. H. Quang, M. V. Fernández-Serra, X. Blase et C. Delerue. *Electronic structure of semiconductor nanowires.* Phys. Rev. B, vol. 73, page 165319, 2006. (Cited page 135.)

[Novoselov 2004] K. S. Novoselov, A. K. Geim, S. V. Morozov, D. Jiang, Y. Zhang, S. V. Dubonos, I. V. Grigorieva et A. A. Firsov. *Electric Field Effect in Atomically Thin Carbon Films.* Science, vol. 306, no. 5696, pages 666–669, 2004. (Cited page 1.)

[Ohlsson 2002] B.J Ohlsson, M.T Björk, A.I Persson, C Thelander, L.R Wallenberg, M.H Magnusson, K Deppert et L Samuelson. *Growth and characterization of GaAs and InAs nano-whiskers and InAs/GaAs heterostructures.* Physica E: Low-dimensional Systems and Nanostructures, vol. 13, pages 1126 – 1130, 2002. (Cited pages 91 and 94.)

[Okada 2001] Susumu Okada, Susumu Saito et Atsushi Oshiyama. *Energetics and Electronic Structures of Encapsulated C_{60} in a Carbon Nanotube.* Phys. Rev. Lett., vol. 86, pages 3835–3838, 2001. (Cited pages 68 and 73.)

[Okazaki 2008] Toshiya Okazaki, Shingo Okubo, Takeshi Nakanishi, Soon-Kil Joung, Takeshi Saito, Minoru Otani, Susumu Okada, Shunji Bandow et Sumio Iijima. *Optical Band Gap Modification of Single-Walled Carbon Nanotubes by Encapsulated Fullerenes.* Journal of the American Chemical Society, vol. 130, pages 4122–4128, 2008. (Cited page 73.)

[Pawel Utko 2010] Ilya V Krive Robert I Shekhter Mats Jonson Marc Monthioux Laure Noe & Jesper Nygard Pawel Utko Raffaello Ferone. *Nanoelectromechanical coupling in fullerene peapods probed by resonant electrical transport experiments.* Nature Communications, vol. 1, page 37, 2010. (Cited page 74.)

[Peng 2009] Xiaohui Peng, Jingyi Chen, James A. Misewich et Stanislaus S. Wong. *Carbon nanotube-nanocrystal heterostructures.* Chem. Soc. Rev., vol. 38, pages 1076–1098, 2009. (Cited page 60.)

[Pfund 2006] Andreas Pfund, Ivan Shorubalko, Renaud Leturcq, Magnus T. Borgstrom, Fabian Gramm, Elisabeth Muller et Klaus Ensslin. *Fabrication of Semiconductor Nanowires for Electronic Transport Measurements.* CHIMIA International Journal for Chemistry, vol. 60, pages 729–734, 2006. (Cited pages 40 and 100.)

[Philip G. Collins 2000] Masa Ishigami A. Zettl Philip G. Collins Keith Bradley. *Extreme Oxygen Sensitivity of Electronic Properties of Carbon Nanotubes.* Science, vol. 287, page 1801, 2000. (Cited page 65.)

[Pichler 2001] T. Pichler, H. Kuzmany, H. Kataura et Y. Achiba. *Metallic Polymers of C_{60} Inside Single-Walled Carbon Nanotubes.* Phys. Rev. Lett., vol. 87, page 267401, 2001. (Cited page 73.)

[Pichler 2003] T. Pichler, A. Kukovecz, H. Kuzmany, H. Kataura et Y. Achiba. *Quasicontinuous electron and hole doping of C_{60} peapods.* Phys. Rev. B, vol. 67, page 125416, 2003. (Cited pages 60 and 66.)

[Podlivaev 2011] A. Podlivaev et L. Openov. *On the thermal stability of graphone.* Semiconductors, vol. 45, pages 958–961, 2011. (Cited page 81.)

[Ponomarenko 2010] L. A. Ponomarenko, R. Yang, R. V. Gorbachev, P. Blake, A. S. Mayorov, K. S. Novoselov, M. I. Katsnelson et A. K. Geim. *Density of States and Zero Landau Level Probed through Capacitance of Graphene.* Phys. Rev. Lett., vol. 105, page 136801, Sep 2010. (Cited page 127.)

[Puech 2007] P. Puech, F. Puccianti, R. Bacsa, C. Arrondo, M. Monthioux, W. Bacsa, V. Paillard, A. Bassil et F. Barde. *Thermal transfer in SWNTs and peapods under UV-irradiation.* physica status solidi (b), vol. 244, pages 4064–4068, 2007. (Cited page 86.)

[Quay 2007] C. H. L. Quay, John Cumings, S. J. Gamble, A. Yazdani, H. Kataura et D. Goldhaber-Gordon. *Transport properties of carbon nanotube C_{60} peapods.* Phys. Rev. B, vol. 76, page 073404, 2007. (Cited pages 73 and 74.)

[Rafailov 2003] P. M. Rafailov, C. Thomsen et H. Kataura. *Resonance and high-pressure Raman studies on carbon peapods.* Phys. Rev. B, vol. 68, page 193411, Nov 2003. (Cited page 78.)

[Rai-Choudhury 1997] P. Rai-Choudhury. Handbook of microlithography, micromachining, and microfabrication. SPIE Press Monograph, 1997. (Cited page 2.)

[Rao A. M. 1997] Shunji Bandow Bruce Chase P. C. Eklund K. A. Williams S. Fang K. R. Subbaswamy M. Menon A. Thess R. E. Smalley G. Dresselhaus Dresselhaus M. S. Rao A. M. Richter E. *Diameter-Selective Raman Scat tering from Vibrational Modes in Carbon Nanotubes.* Science, vol. 275, pages 187–191, 1997. (Cited page 54.)

[Rashba 1960] E I Rashba. *Properties of semiconductors with an extremum loop. First Cyclotron and combinational resonance in a magnetic field perpendicular to the plane of the loop.* Sov. Phys. Solid State, vol. 2, pages 1224–1238, 1960. (Cited page 97.)

[Richter 2008] Thomas Richter, Christian Blömers, Hans Lüth, Raffaella Calarco, Michael Indlekofer, Michel Marso et Thomas Schäpers. *Flux Quantization Effects in InN Nanowires.* Nano Letters, vol. 8, pages 2834–2838, 2008. (Cited page 95.)

[Robel 2006] Istvan Robel, G. Girishkumar, Bruce A. Bunker, Prashant V. Kamat et K. Vinodgopal. *Structural changes and catalytic activity of platinum nanoparticles supported on C_{60} and carbon nanotube films during the operation of direct methanol fuel cells.* Applied Physics Letters, vol. 88, page 073113, 2006. (Cited page 60.)

[Rochefort 2003] A. Rochefort. *Electronic and transport properties of carbon nanotube peapods.* Phys. Rev. B, vol. 67, page 115401, Mar 2003. (Cited page 71.)

[Roulleau 2010] P. Roulleau, T. Choi, S. Riedi, T. Heinzel, I. Shorubalko, T. Ihn et K. Ensslin. *Suppression of weak antilocalization in InAs nanowires.* Phys. Rev. B, vol. 81, page 155449, Apr 2010. (Cited pages 96, 97, 98, 111, 115, and 116.)

[Saito 1998] R. Saito, G. Dresselhaus et M. S. Dresselhaus. Physical properties of carbon nanotubes. Imperial College Presse, 1998. (Cited pages 52 and 60.)

[Sakurabayashi 2003] Yasunori Sakurabayashi, Marc Monthioux, Keisuke Kishita, Yoshinao Suzuki, Takuya Kondo et Mikako Le Lay. *Tailoring double-wall carbon nanotubes?* AIP Conference Proceedings, vol. 685, pages 302–305, 2003. (Cited page 75.)

[Sanvito 1999] S. Sanvito, C. J. Lambert, J. H. Jefferson et A. M. Bratkovsky. *General Green's-function formalism for transport calculations with* spd *Hamiltonians and giant magnetoresistance in Co- and Ni-based magnetic multilayers.* Phys. Rev. B, vol. 59, pages 11936–11948, May 1999. (Cited page 135.)

[Schäpers 2006] Th. Schäpers, V. A. Guzenko, M. G. Pala, U. Zülicke, M. Governale, J. Knobbe et H. Hardtdegen. *Suppression of weak antilocalization in $Ga_xIn_{1-x}As/InP$ narrow quantum wires.* Phys. Rev. B, vol. 74, page 081301, Aug 2006. (Cited page 116.)

[Scherbakov 1996] A. G. Scherbakov, E. N. Bogachek et Uzi Landman. *Quantum electronic transport through three-dimensional microconstrictions with variable shapes.* Phys. Rev. B, vol. 53, pages 4054–4064, Feb 1996. (Cited pages 35 and 98.)

[Shen 2012] Jun Shen, Pascal Puech, Thierry Ondarcuhu, Walter Escoffier, Bertrand Raquet et Marc Monthioux. *The effect of adsorbed species and exposure to sulfuric acid on the electrical conductance of individual single-wall carbon nanotube transistors.* Carbon, vol. 50, no. 10, pages 3953 – 3956, 2012. (Cited page 77.)

[Shiozawa 2006] H. Shiozawa, H. Ishii, H. Kihara, N. Sasaki, S. Nakamura, T. Yoshida, Y. Takayama, T. Miyahara, S. Suzuki, Y. Achiba, T. Kodama, M. Higashiguchi, X. Y. Chi, M. Nakatake, K. Shimada, H. Namatame,

M. Taniguchi et H. Kataura. *Photoemission and inverse photoemission study of the electronic structure of C_{60} fullerenes encapsulated in single-walled carbon nanotubes.* Phys. Rev. B, vol. 73, page 075406, Feb 2006. (Cited page 73.)

[Shklovskii 1984] B. I. Shklovskii et A. L. Efros. Electronic properties of doped semiconductors. Springer-Verlag, Berlin, 1984. (Cited page 84.)

[Smith 1998] B. W. Smith, M. Monthioux et D. E. Luzzi. *Encapsulated C_{60} in carbon nanotubes.* Nature, vol. 396, page 323, 1998. (Cited pages 66 and 75.)

[Suarez-Martinez 2010] I. Suarez-Martinez, P.J. Higginbottom et N.A. Marks. *Molecular dynamics simulations of the transformation of carbon peapods into double-walled carbon nanotubes.* Carbon, vol. 48, pages 3592 – 3598, 2010. (Cited page 75.)

[Takahashi 1966] Kiyoshi Takahashi et Toyosaka Morizumi. *Growth of InAs Whiskers in Wurtzite Structure.* Japanese Journal of Applied Physics, vol. 5, pages 657–662, 1966. (Cited page 92.)

[Tans 1997] Sander J. Tans, Michel H. Devoret, Hongjie Dai, Andreas Thess, Richard E. Smalley, L. J. Geerligs et Cees Dekker. *Individual single-wall carbon nanotubes as quantum wires.* Nature, vol. 386, pages 474–477, 1997. (Cited page 2.)

[Thouless 1977] D. J. Thouless. *Maximum Metallic Resistance in Thin Wires.* Phys. Rev. Lett., vol. 39, pages 1167–1169, Oct 1977. (Cited page 25.)

[Tian 1998] Weidong Tian, Supriyo Datta, Seunghun Hong, R. Reifenberger, Jason I. Henderson et Clifford P. Kubiak. *Conductance spectra of molecular wires.* The Journal of Chemical Physics, vol. 109, pages 2874–2882, 1998. (Cited pages 81 and 135.)

[Tserkovnyak 2006] Yaroslav Tserkovnyak et Bertrand I. Halperin. *Magnetoconductance oscillations in quasiballistic multimode nanowires.* Phys. Rev. B, vol. 74, page 245327, Dec 2006. (Cited pages 35, 98, 99, and 116.)

[Utko 2006] Pawel Utko, Jesper Nygard, Marc Monthioux et Laure Noe. *Sub-Kelvin transport spectroscopy of fullerene peapod quantum dots.* Applied Physics Letters, vol. 89, no. 23, page 233118, 2006. (Cited page 73.)

[van Wees 1988] B. J. van Wees, H. van Houten, C. W. J. Beenakker, J. G. Williamson, L. P. Kouwenhoven, D. van der Marel et C. T. Foxon. *Quantized conductance of point contacts in a two-dimensional electron gas.* Phys. Rev. Lett., vol. 60, pages 848–850, Feb 1988. (Cited pages 35 and 98.)

[Vavro 2002] J. Vavro, M. C. Llaguno, B. C. Satishkumar, D. E. Luzzi et J. E. Fischer. *Electrical and thermal properties of C_{60}-filled single-wall carbon nanotubes.* Applied Physics Letters, vol. 80, pages 1450–1452, 2002. (Cited page 73.)

[Žutić 2004] Igor Žutić, Jaroslav Fabian et S. Das Sarma. *Spintronics: Fundamentals and applications.* Rev. Mod. Phys., vol. 76, pages 323–410, Apr 2004. (Cited page 97.)

[Wagner 1964] R. S. Wagner et W. C. Ellis. *Vapor-Liquid-Solid machanism of sigle crystal growth.* Applied Physics Letters, vol. 4, pages 89–90, 1964. (Cited page 93.)

[Wang 2005] Joseph Wang. *Carbon-Nanotube Based Electrochemical Biosensors: A Review.* Electroanalysis, vol. 17, no. 1, pages 7–14, 2005. (Cited page 60.)

[Westenfelder 2011] B Westenfelder, J C Meyer, J Biskupek, G Algara-Siller, L G Lechner, J Kusterer, U Kaiser, C E Krill III, E Kohn et F Scholz. *Graphene-based sample supports for in situ high-resolution TEM electrical investigations.* Journal of Physics D: Applied Physics, vol. 44, page 055502, 2011. (Cited page 132.)

[Yazawa 1993] Masamitsu Yazawa, Masanari Koguchi, Akiko Muto et Kenji Hiruma. *Semiconductor nanowhiskers.* Advanced Materials, vol. 5, pages 577–580, 1993. (Cited page 93.)

[Yildirim 2005] T. Yildirim et S. Ciraci. *Titanium-Decorated Carbon Nanotubes as a Potential High-Capacity Hydrogen Storage Medium.* Phys. Rev. Lett., vol. 94, page 175501, May 2005. (Cited page 60.)

[Zawadzki 2004] W Zawadzki et P Pfeffer. *Spin splitting of subband energies due to inversion asymmetry in semiconductor heterostructures.* Semiconductor Science and Technology, vol. 19, no. 1, page R1, 2004. (Cited page 92.)

[Zhang 2011] Rufan Zhang, Qian Wen, Weizhong Qian, Dang Sheng Su, Qiang Zhang et Fei Wei. *Superstrong Ultralong Carbon Nanotubes for Mechanical Energy Storage.* Advanced Materials, vol. 23, pages 3387–3391, 2011. (Cited page 2.)

Auteur : Vladimir PRUDKOVSKIY
Titre : Propriétés électroniques des systèmes quasi-unidimensionnels (C_{60}@SWCNTs et nanofils d'InAs) étudiés par le transport électronique sous champ magnétique intense.
Directeurs de thèse : Michel GOIRAN et Bertrand RAQUET
Spécialité : Nanophysique

Lieu et date de soutenance : Salle de séminaire du LNCMI, 14 Juin 2013
Intitulé et adresse du laboratoire : Laboratoire National des Champs Magnétiques Intenses (LNCMI-T), CNRS-UPR 3228, 143 avenue de Rangueil, 31400 Toulouse, France

Résumé :

Cette thèse présente des mesures de transport électronique dans des systèmes quasi-unidimensionnels (quasi-1D) sous champ magnétique intense. Deux systèmes différents présentant un confinement électrique quasi-1D ont été considérés: les peapods de carbone (C_{60}@SWCNTs) et les nanofils d'InAs. L'objectif de ces travaux consiste à sonder les propriétés électroniques spécifiques de ces systèmes quasi-1D par les mesures de magnétotransport sur les nano-objets uniques. Dans les deux cas, les expériences sous champs magnétiques intenses ont été accompagnée par des caractérisations structurales et des mesures de conductance à champ magnétique nul.

L'encapsulation de diverses molécules à l'intérieur de nanotubes de carbone (CNTs), comme par exemple les fullerènes C_{60}, constitue une des voies prometteuses vers l'accordabilité de la conductance des CNTs. Parmi la grande variété des nanotubes de carbone remplis, les peapods représentent une structure hybride pionnière découvert en 1998. Depuis lors, leur structure électronique a fait l'objet d'études théoriques controversées avec un nombre limité de réalisations expérimentales. Dans cette thèse, les propriétés électroniques des peapods individuels ont été étudiés en combinant les mesures de spectroscopie micro-Raman et de magnétotransport sur les mêmes échantillons. Nous avons constaté que les C_{60} encapsulés modifient fortement la structure de bande électronique des nanotubes semi-conducteurs au voisinage du point de neutralité de charge. Cette modification comprend un déplacement rigide de la structure électronique et un remplissage partiel de la bande interdite. Nous avons aussi montré que l'excitation UV sélective des fullerènes conduit à une forte modification du couplage électronique entre les C_{60} et le CNT induite par la coalescence partielle des C_{60} et de leur distribution à l'intérieur du tube. Les résultats expérimentaux sont supportés par des simulations numériques de la densité d'états et de la conductance des nanotubes de carbone avec des fullerènes fusionnés à l'intérieur (K. Katin, M. Maslov).

Les nanofils semiconducteurs (sc-NWs) font l'objet de recherches actives depuis ces dix dernières années. Ils représentent des systèmes modèles pour l'étude des propriété électronique objet quasi-1D. Ils représentent en outre des possibilités de modulation de la structure de bande aussi que de contrôle de la densité de porteurs. Dans ce domaine de recherche, les nanofils semi-conducteurs à base de composes III-V tel que InAs, ont une place particulière en raison de la faible masse effective des porteurs de charge. Nous avons étudié la conductance de nanofils individuels dans une large gamme de champs magnétiques (jusqu'à 60T). Les mesures en champ nul et en champ faible ont démontré un transport faiblement diffusif dans ces nanofils. Les mesures de transport sous champ magnétique intense ont révélé une forte chute de la conductance au dessus d'un champ critique qui s'élève clairement avec l'énergie de Fermi. Cet effet est interprété par la perte de canaux de conduction une fois que toutes les sous-bandes magnéto-électriques, décalés vers les hautes énergies par le champ magnétique, ont traversé l'énergie de Fermi. Les calculs de structure de bande préliminaires (Y-M. Niquet), en prenant en compte les confinements latéraux et magnétiques, sont en bon accord qualitatif avec les résultats observés dans le régime de champ magnétique intense. Ce résultat est la première observation des effets de structure de bande dans les expériences de magnéto-transport sur les sc-NWs.

Mots-clefs: Système 1D, magnétotransport, structure électronique, champs magnétiques intenses, peapods, nanofils semiconducteurs.

Author : Vladimir PRUDKOVSKIY
Title : Electronic transport of quasi-one-dimensional systems (C_{60}@SWCNTs and InAs nanowires) studied under high magnetic field
Supervisors : Michel GOIRAN and Bertrand RAQUET
Speciality : Nanophysics

Place and date of the PhD defense : Salle de séminaire du LNCMI, 14 June 2013
Laboratory : Laboratoire National des Champs Magnétiques Intenses (LNCMI-T), CNRS-UPR 3228, 143 avenue de Rangueil, 31400 Toulouse, France

Abstract :

The scope of this thesis is related to the electronic properties of quasi 1D systems probed by high field magnetotransport. Two different systems exhibiting quasi-1D confinement have been considered: carbon C_{60} peapods (C_{60}@SWCNTs) and InAs semiconductor nanowires. The magnetotransport measurements on single nano-objets have been used to investigate the specific electronic structure of these 1D systems. In both cases, the high magnetic fields experiments have been supported by structural characterisation and conductance measurements at zero field.

The encapsulation of various molecules inside carbon nanotubes (CNTs), as for instance C_{60} fullerenes encapsulated in SWCNT, constitutes promising routes towards the tunability of the CNT conductance. Among the wide variety of filled CNTs, peapods represent a pioneer hybrid structure discovered in 1998. Since that time, their electronic structure has been subjected to intense and controversial theoretical studies together with a limited number of experimental realizations. In this thesis the electronic properties of individual fullerene peapods have been investigated by combining micro-Raman spectroscopy and magnetotransport measurements on the same devices. We bring evidence that the encapsulated C_{60} strongly modify the electronic band structure of semiconducting nanotubes in the vicinity of the charge neutrality point, including a rigid shift and a partial filling of the energy gap. In addition by playing with a selective UV excitation of the fullerene, we demonstrate that the electronic coupling between the C_{60} and the CNT is strongly modified by the partial coalescence of the C_{60} and their distribution inside the tube. The experimental results are supported by numerical simulations of the Density of States and the conductance of CNTs with coalesced fullerenes inside (K. Katin, M. Maslov).

Semiconductor nanowires (sc-NWs) are being the subject of intense researches started a decade ago. They represent model systems for the exploration of the electronic properties inerrant to the quasi1-D confinement. Moreover they offer the possibility to play with band structure tailoring and carrier doping. In this direction III-V sc-NWs such as InAs NWs have played a particular role due to the small electron effective mass. We have studied the high magnetic field conductance of single nanowires. Prior to the high field measurements, the zero and low field investigations have demonstrated a weakly diffusive regime of the carrier transport in these wires. The high field investigations have revealed a drastic conductance drop above a critical field, which clearly rises with the Fermi energy. This effect is interpreted by the loss of conducting channels once all the magneto-electric subbands, shifted toward the high energy range by the magnetic field, have crossed the Fermi energy. Preliminary band structure calculations (Y-M. Niquet), taking into account the lateral and magnetic confinements, are in fairly good qualitative agreement with the observed result in the high field regime. This result is the first observation of band structure effects in magneto-transport experiments on sc-NWs.

Keywords : 1D systems, magnetotransport, electronic structure, high magnetic field, peapods, semiconductor nanowires.